© Copyright 2019

Matthew Bonnema

Understanding the Impacts of Reservoirs in Developing Regions using Satellite
Remote Sensing

Matthew Bonnema

A dissertation

submitted in partial fulfillment of the

requirements for the degree of

Doctor of Philosophy

University of Washington

2019

Reading Committee:

Faisal Hossain, Chair

Bart Nijssen

Erkan Istanbulluoglu

Tamlin Pavelsky

Program Authorized to Offer Degree:

Department of Civil and Environmental Engineering

University of Washington

Abstract

Understanding the Impacts of Reservoirs in Developing Regions using Satellite
Remote Sensing

Matthew Bonnema

Chair of the Supervisory Committee:
Professor Faisal Hossain
Department of Civil and Environmental Engineering

Dams provide immense societal benefits in the form of hydropower generation, flood control,

and water supply. However, they also cause significant negative environmental impacts by

altering the timing and magnitude of natural streamflow, limiting the transport of sediment,

nutrients, and biota upstream and downstream, and altering aspects of water quality such as

sediment concentration and water temperature. Dam development in developing regions has been

increasing in the last 30 years and will continue to intensify in the coming decades. This is

leading to rapid hydrologic transformations of developing river basins, with potentially dire

consequences for local populations dependent on the natural river systems for food and

livelihood. In-situ hydrologic observations in such regions are limiting, making satellite remote

sensing the only viable option for studying the impacts of this rapid dam development. This

dissertation aims to advance our ability to study the impacts of reservoirs in data limited regions. First, a method for estimating reservoir outflow using purely remote sensing observations was developed and tested on reservoirs in the United States and Bangladesh. This method was then applied to ungauged reservoirs in the Mekong River Basin and their impact the river system was evaluated in terms of flow alteration and residence time. It was found that smaller reservoirs on upper tributaries exerted a higher degree of flow alteration and residence time on the rivers they impound than larger, more downstream reservoirs. However, the reservoirs on larger rivers exert their impacts on significantly larger volumes of streamflow, so their contribution to the overall flow alteration and residence time of the river system was found to be more significant. Looking towards upcoming satellite missions, the applicability and usefulness of the Surface Water and Ocean Topography (SWOT) Mission for monitoring reservoir outflow and river discharge was tested using by generating synthetic observations based on the expected performance of the SWOT instrument. It was found that SWOT is expected to observe reservoir storage change with higher accuracy than methods from existing sensors in most cases. However, some reservoirs were unable to be accurately observed by simulated SWOT observations, indicating a cooperative multi-sensor approach may be useful. The performance of SWOT observations of river discharge was found to be satisfactory given there are currently no satellite sensors capable of estimating discharge. However, the dramatic differences between wet season and dry season discharge in monsoonal rivers proved difficult and some adjustments to the discharge estimation methods may be needed. Finally, impacts on river temperature downstream of major dam development in the 3S Basin, the largest tributary to the Mekong River, were observed using satellite remote sensing. Dam construction in the basin coincided with significant temperature decreases downstream, providing clear evidence of hydropower induced river cooling. The

findings of this dissertation and the remote sensing methods employed here represent valuable

steps towards understanding the hydrologic impacts of dams and predicting the impacts of

further dam development in developing basins around the world.

TABLE OF CONTENTS

LIST OF FIGURES

10

LIST OF TABLES

ACKNOWLEDGEMENTS

I would like to thank my advisor, Dr. Faisal Hossain, who made this work possible with his support and guidance. He allowed me the freedom needed to pursue research that I enjoyed and brought a contagious passion to everything we worked on together. The opportunities he provided allowed me to develop the skills I needed for my long term career goals.

I would also like thank my committee members, Bart Njissen, Erkan Istanbulluoglu, and Tamlin Pavelsky for their valuable time and thoughtful insight. Their feedback was critical in shaping this dissertation. I also want to thank LuAnne Thompson for her time as my Graduate School Representative.

I would like to give a special thank you to the past and current members of the SASWE research group. Their support, encouragement and willingness to help and collaborate was energizing.

I am grateful for the NASA Earth and Space Science Fellowship for providing financial support during my last two years of studies.

Lastly, I would like to thank my wife, Gwyn. Without her support, patience, and love, this dissertation would not be possible.

At the time of writing, Chapters 2, 3, 4, and 5 have been published in *Water Resources Research* and Chapter 6 is in review for publication in *Environmental Research Letters.* These articles are:

Chapter 2:

Bonnema, Matthew, Safat Sikder, Yabin Miao, Xiaodong Chen, Faisal Hossain, Ismat Ara
      Pervin, S. M. Mahbubur Rahman, and Hyongki Lee. 2016. "Understanding Satellite-
      Based Monthly-to-Seasonal Reservoir Outflow Estimation as a Function of Hydrologic
      Controls." Water Resources Research 52 (5): 4095–4115.
      https://doi.org/10.1002/2015WR017830.

Chapter 3:

Bonnema, Matthew, and Faisal Hossain. 2017. "Inferring Reservoir Operating Patterns across
      the Mekong Basin Using Only Space Observations." Water Resources Research 53 (5):
      3791–3810. https://doi.org/10.1002/2016WR019978.

Chapter 4:

Bonnema, Matthew, and Faisal Hossain. 2019. "Assessing the Potential of the Surface Water and Ocean Topography Mission for Reservoir Monitoring in the Mekong River Basin." Water Resources Research 55 (1): 444–61. https://doi.org/10.1029/2018WR023743.

Chapter 5:

Bonnema, Matthew G., Safat Sikder, Faisal Hossain, Michael Durand, Colin J. Gleason, and David M. Bjerklie. 2016. "Benchmarking Wide Swath Altimetry-Based River Discharge Estimation Algorithms for the Ganges River System." Water Resources Research 52 (4): 2439–61. https://doi.org/10.1002/2015WR017296.

Chapter 6:

Bonnema, Matthew, Faisal Hossain, Bart Nijssen and Gordon Holtgrieve (2019) Hydropower's Hidden Transformation of Rivers in the Mekong, Environmental Research Letters (in review).

Chapter 1: Introduction

1.1   STATE OF DAM DEVELOPMENT AROUND THE WORLD

Dams have been an essential element of human development throughout the last century. By controlling the flow of rivers and forming reservoirs, they allow us to deliver water where and when it is needed. Dams provide numerous societal benefits. The facilitate valuable hydroelectric power generation, the largest source of clean energy. By 2012, hydropower accounted for 16.2% of the world's electricity generation (IEA 2016). Dams also provide protection from one of the most damaging natural disasters, floods, by storing the flood pulse and releasing it gradually over a safe period of time. This ability to store water and selectively release it at a later time makes dams invaluable for providing water for agricultural, industrial, and domestic uses.

However, these benefits come with severe environmental costs as dams impose wide reaching modifications to hydrologic systems (Biemans et al. 2011; Y. N. Pokhrel et al. 2012; C. Vörösmarty et al. 2004). Dams disconnect rivers, limiting transport of sediment, nutrients, and biota, with damaging consequences to the upstream and downstream river ecosystems (Pringle 2003; Graf 2006; Ligon, Dietrich, and Trush 1995)This disconnection lead to the capture of sediment in reservoirs. As much as 30% of the annual global sediment discharge is currently being trapped by reservoirs (C. Vörösmarty et al. 2004). Additionally, the altering of streamflow imposed by dams in order to mitigate floods or provide hydroelectricity, or water supply, disrupts the natural streamflow patterns of river systems, patterns that many river ecological systems have adapted to and depend on. Dams can also play a role in altering river water temperature, again disrupting downstream ecological systems. These impacts extend beyond the

aquatic environment. Sediment carries valuable nutrients, essential to floodplain agriculture. Additionally, fishing is a major source of nutrition and livelihood in many regions.

Large scale dam development began in the United States and many other developed nations in first half of the 20th Century. By the later half of the 20th Century, dam building in these regions slowed as many of the most beneficial locations for dams had already been used and growing environmental concerns slowed the desire to further regulate river systems. Now, in the 21st Century, many developing regions are going through a similar period of rapid dam construction. One global study identified at least 3700 major dams that are either under construction now or planned for construction in the future in the hydropower sector alone, with a majority of these located in developing nations (Zarfl et al. 2014). Figure 1.1 shows a map of these dams along with a map of existing major dams (Lehner et al. 2011). Region specific datasets also reveal dramatic dam development in major basins such as the Amazon and the Mekong. These planned dams are not only numerous, they are increasingly ambitious in their size and as a result, their hydrologic impact. For example, the Grand Ethiopian Renaissance Dam, under construction in the Nile River Basin, will be large enough to store 1.5 times the annual flow of the Blue Nile River it will impound (Wheeler et al. 2016). Similarly, there are plans in the next 20 years for the construction of 9 major dams on the main stem of the Mekong River in the lower Mekong River Basin, which is not currently impounded (WLE 2017). Ultimately, these developing regions are set to experience rapid hydrologic transformations with wide reaching environmental and societal impacts. Understanding these impacts will be critical for these regions in the coming decades.
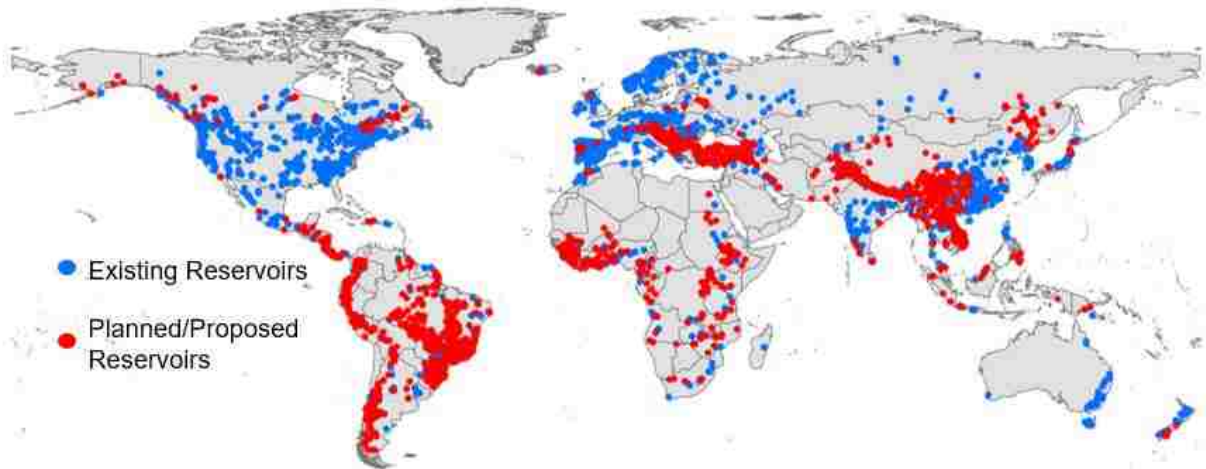
Figure 1.1. Map of existing large dams from the GRanD Dam Database (Lehner et al. 2011) and planned/proposed hydropower dams (Zarfl et al. 2014)

1.2 SATELLITE REMOTE SENSING OF RESERVOIRS

Unfortunately, in-situ hydrologic observations in the developing regions where the recent dam construction activity is occurring are largely unavailable due to two primary factors. National agencies in these regions lack the capacity to routinely collect hydrologic information such as streamflow or water quality parameters such as sediment concentration or water temperature. Even when data is collected, there an unwillingness of agencies to share the data openly. This is especially true of transboundary river systems, where multiple nations or agencies are competing over limited water resources. This fundamental lack of in situ data is likely to persist or worsen in future (A. Gebregiorgis and Hossain 2014). Thus, observations from satellite remote sensing platforms are the only viable methods for understanding reservoir impacts.

Evaluating the hydrologic impacts of reservoirs begins with understanding the dynamics of the reservoirs themselves. The amount of water stored in a reservoir (reservoir storage) fluctuates throughout a typical year, in order to maximize the benefits the reservoir provides (flood control, hydropower, water supply, etc.). These storage change fluctuations reveal how the reservoir is interacting with the river system. For example, decreasing reservoir storage indicates that the amount of water input into the reservoir is less than the amount of water leaving the reservoir, suggesting that the reservoir is releasing more water than it is taking in. Estimating reservoir storage changes over time from satellite observations requires simultaneous estimates of water surface elevation changes and water surface area changes (Huilin Gao 2015). Methods for estimating these parameters independently from satellite observations have been well established.

Nadir radar altimeters measuring water surface elevation, originally designed to measure sea surface heights, were first applied to lakes in 1994 (C. M. Birkett 1994).Since then, satellite radar altimeters have been used to monitor water height changes for a number of lakes and reservoirs around the world, for example, the Great Lakes (Morris and Gill 1994); Lake Chad (Coe and Birkett 2004; H. Gao et al. 2011); lakes and reservoirs in the United States, Brazil, and Nigeria (Okeowo et al. 2017); and a reservoir in the Amazon (D. E. Alsdorf, Rodríguez, and Lettenmaier 2007). A major limitation of satellite radar altimeters is their poor spatial coverage. Radar altimeters only measure water elevation directly beneath the satellite with footprints from 3–5 km wide and a spacing between orbital tracks typically greater than 100km (Huilin Gao 2015). As a result, they miss a large amount of surface waterbodies. Visible and infrared satellite imagery can be used to observe the water surface extent of reservoirs and estimate reservoir surface area. This technique has been applied to monitor numerous lakes and reservoirs (Huilin

18

Gao, Birkett, and Lettenmaier 2012; González-Jorge et al. 2018; S. Zhang, Gao, and Naz 2014). However, visible and infrared satellite imagery is blocked by clouds, meaning observation of reservoirs in cloudy conditions by visible sensors is impossible. Synthetic Aperture Radar (SAR), such as the instrument on board Sentinel-1, can be used to overcome this deficiency, as the radar signal used by these sensors penetrates clouds and can provide reservoir surface area in cloudy conditions (Huang et al. 2018).

Standard methods for estimating storage change from satellite based observations of reservoir surface area and/or water surface elevation have several limitations that hinder their applicability to reservoir sin data limited regions, by requiring in-situ observations (J. Zhang et al. 2006; Smith and Pavelsky 2009), or nadir altimeter observations, which have poor spatial coverage (C. M. Birkett 2000; Duan and Bastiaanssen 2013). These limitations mean there are no suitable methods for estimating reservoir storage change using traditional approaches in ungauged river basins. Furthermore, current satellite based estimation of reservoir outflow is also limited, requiring in-situ observations (Muala et al. 2014) and thus cannot be applied to data limited developing regions. Monitoring the water quality impacts of reservoirs from satellite observations is also in its infancy. Suspended sediment concentration can be estimated from visible/infrared imagery, but requires in-situ observations for calibration (Umar, Rhoads, and Greenberg 2018). Thermal infrared imagery of rivers has been shown to accurately monitor river temperature, but despite this, its application to the thermal impacts of reservoirs has been limited (Dugdale 2016; Tavares et al. 2019).

The upcoming Surface Water and Ocean Topography (SWOT) Mission, launching in 2021, is expected to improve upon the surface water observing deficiencies of past and current satellite missions and greatly expand understanding of surface water dynamics (Biancamaria,

Lettenmaier, and Pavelsky 2016). For lakes and reservoirs, SWOT will observe water surface elevation and reservoir surface area, providing more direct estimates of reservoir storage change. Furthermore, SWOT will provide estimates of river discharge, allowing for the impacts of reservoirs on streamflow to be more directly assessed. Given the potential of the SWOT mission, and the novelty of the interferometric SAR instrument it will employ, there is much interest in understanding the potential accuracy of its observations and its potential applicability to reservoir monitoring. Despite the improvement SWOT represents over current remote sensing platforms, there is still value in developing reservoir monitoring methods using traditional sensors, both for the long historical record of traditional sensors and for potential multi-sensor cooperation between traditional sensors and SWOT.

1.3   RESEARCH OBJECTIVES

The objectives of this dissertation are twofold, to develop and test satellite based methods that help better assess the impacts of reservoirs in developing regions, and to apply those methods to ungauged regions in order to provide a deeper understanding of the impacts of reservoirs in those regions. More specifically, the research objectives are as follows:

1. Develop and test a method for estimating reservoir outflow, relying entirely on remotely sensed observations.

2. Apply the reservoir outflow estimation method to reservoirs in the Mekong River Basin and use the resulting outflow to evaluate the impacts of reservoirs on downstream streamflow in terms of two measures of impact, residence time and flow alteration.

3. Evaluate the potential of the SWOT mission for estimating reservoir storage and outflow in the Mekong River Basin. Additionally, evaluate the capabilities of SWOT river discharge estimation in tropical monsoonal climates.

4. Utilize satellite-based thermal infrared observations to understand the impacts of reservoirs on river temperature in the 3S Basin, a major tributary to the Mekong River.

1.4   APPROACH

This dissertation is organized as follows:

Chapter 2 introduces a mass balance approach for estimating reservoir outflow from only satellite based observations. This chapter also explores the role of several hydrologic controls in the mass balance approach. Chapter 3 applies the mass balance approach to 20 reservoirs in the Mekong River Basin and uses the resulting outflow estimates to evaluate the hydrologic impact of the reservoirs in terms of two factors, residence time and flow alteration. Chapter 4 evaluates the accuracy of SWOT storage change and outflow estimates for the same 20 Mekong Basin reservoirs by simulated SWOT observations of the reservoirs. Chapter 5 evaluates the accuracy of three different SWOT based discharge estimation approaches in the Ganges-Brahmaputra Delta. Chapter 6 uses satellite based thermal infrared observations to understand the impact of reservoirs in the 3S basin on downstream river temperature and evaluates the overall thermal impact of these reservoirs on the Mekong River.

Chapter 2: Understanding Reservoir Discharge as a Function of Hydrologic Controls

Abstract: Growing population and increased demand for water is causing an increase in dam and reservoir construction in developing nations. When rivers cross international boundaries, the downstream stakeholders often have little knowledge of upstream reservoir operation practices. Satellite remote sensing in the form of radar altimetry and multi-sensor precipitation products can be used as a practical way to provide downstream stakeholders with the fundamentally elusive upstream information on reservoir outflow needed to make important and proactive water management decisions. This study uses a mass balance approach of three hydrologic controls to estimate reservoir outflow from satellite data at monthly and annual time scales: precipitation-induced inflow, evaporation, and reservoir storage change. Furthermore, this study explores the importance of each of these hydrologic controls to the accuracy of outflow estimation. The hydrologic controls found to be unimportant could potentially be neglected from similar future studies. Two reservoirs were examined in contrasting regions of the world, the Hungry Horse Reservoir in a mountainous region in northwest U.S. and the Kaptai Reservoir in a low-lying, forested region of Bangladesh. It was found that this mass balance method estimated the annual outflow of both reservoirs with reasonable skill. The estimation of monthly outflow from both reservoirs was however less accurate. The Kaptai basin exhibited a shift in basin behavior resulting in variable accuracy across the 9 year study period. Monthly outflow estimation from

Hungry Horse Reservoir was compounded by snow accumulation and melt processes, reflected by relatively low accuracy in summer and fall, when snow processes control runoff. Furthermore, it was found that the important hydrologic controls for reservoir outflow estimation at the monthly time scale differs between the two reservoirs, with precipitation-induced inflow being the most important control for the Kaptai Reservoir and storage change being the most important for Hungry Horse Reservoir.

2.1 INTRODUCTION

The estimation of reservoir outflow from satellite observations is an important first step towards understanding the impacts of reservoirs on streamflow. In this chapter, a combination of satellite altimetry and a satellite precipitation product was used to determine reservoir outflow (Figure 2.1) through the use of a simple mass balance between hydrologic controls (2.1) where reservoir outflow (O) is balanced by changes in reservoir storage (ΔS), precipitation-induced runoff flowing into the reservoir (I), and evaporative losses (E). Due to the revisit period of the satellite observations being longer than a week, the mass balance was resolved on approximately monthly time scales.

$$O = I - E - \Delta S \qquad (2.1)$$
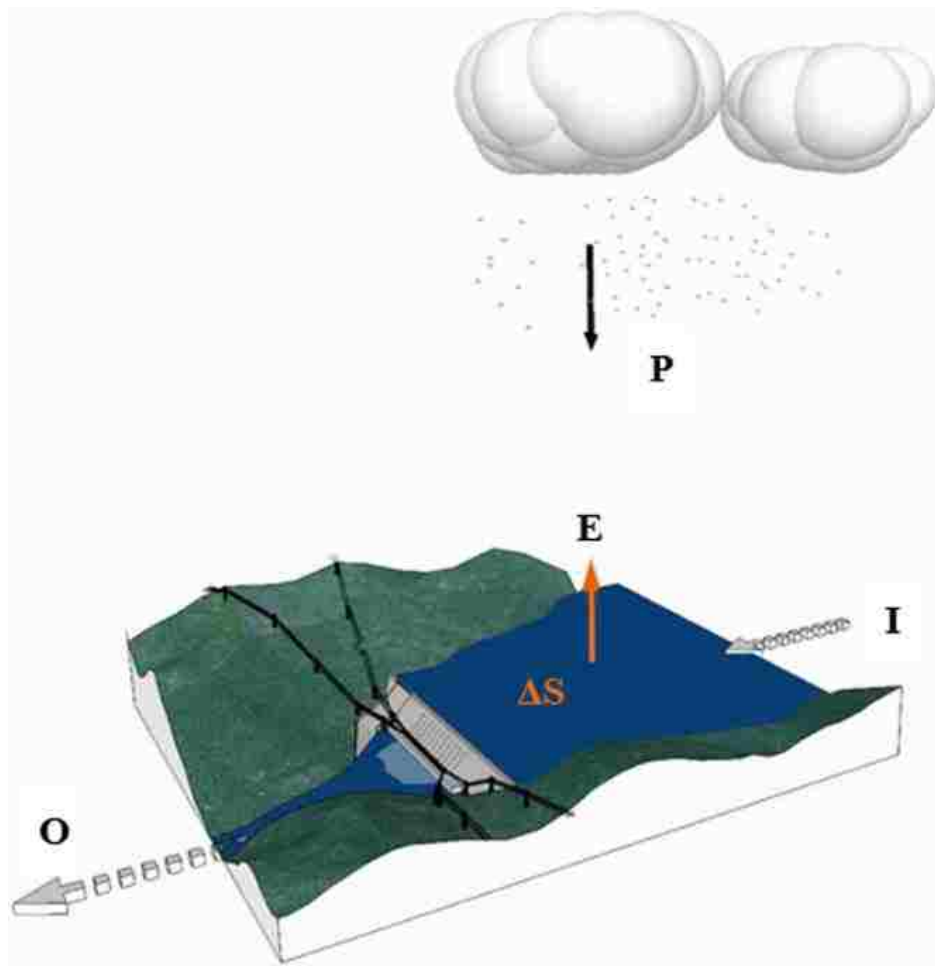
Figure 2.1. Schematic of mass balance between reservoir outflow (O), evaporation (E), changes in reservoir storage (ΔS), and runoff-derived inflow (I) driven by precipitation (P).

The total change in reservoir storage can be estimated by combining radar altimetry measurements of reservoir surface elevation with remotely sensed reservoir surface area (Huilin Gao 2015). Initially designed for oceanic observations, radar altimetry has been used to accurately measure lake and reservoir elevations since the early 1980s (Corp. et al., n.d.; Mason et al., n.d.; C. M. Birkett 1995; J. Zhang et al. 2006; Lee et al. 2011). More recent efforts have combined altimetry with various methods of determining reservoir surface area. (C. M. Birkett 2000) used TOPEX/POSEIDON altimetry measurements with NOAA/AVHRR radiometer images to develop a simultaneous time series of the elevation and water surface extent of Lake Chad. Additionally, (Huilin Gao, Birkett, and Lettenmaier 2012) used the Moderate Resolution

24

Imaging Spectroradiometer (MODIS) along with satellite radar altimetry to estimate storage changes in 34 global reservoirs. Furthermore, (Yunus D. Salami 2012) combined altimeter measurements from multiple sources with existing storage-elevation curves and validated their results with a mass balance similar to equation 1 (in their case, outflow was measured with a streamflow gauge and the equation was solved for storage change). A wide array of satellite altimeter missions, both current (JASON-2, AltiKa, Sentinel-1 & 2, Envisat) and future (JASON-3 and Sentinel-3) can be leveraged for the estimation of storage changes (Lambin et al. 2010; Verron et al. 2015; D. E. Alsdorf, Rodríguez, and Lettenmaier 2007).

Precipitation-induced runoff flowing into a reservoir can also be estimated using satellite remote sensing of precipitation. This involves using a satellite precipitation product such as the Tropical Rainfall Measurement Mission (TRMM, now deactivated) or its successor, the Global Precipitation Mission (GPM), to provide an estimate of precipitation over the basin contributing to the reservoir (Huffman et al. 2007; Hou et al. 2014). This precipitation can then be fed into a runoff model of appropriate complexity to determine the runoff generated.

Few studies have attempted to use satellite estimated volume changes to estimate reservoir outflow, which is an important geophysical variable for a wide variety of scientific investigations and applications. (Swenson and Wahr 2009) used satellite-derived storage changes of a small lake downstream of Lake Victoria to estimate the outflow of Lake Victoria. This approach had high success at the monthly and seasonal time scales, but is specific to Lake Victoria or other systems with a small lake directly downstream of a large reservoir. (Muala et al. 2014) used altimetry-derived storage changes and in situ inflow measurements to estimate the discharge from Lake Nasser and Rosaries Reservoir in the Nile Basin. They were able to estimate outflow from Rosaries Reservoir to within 18% of observed outflow, while outflow

from Lake Nasser was more difficult to predict. It is clear that more investigation into satellite-based reservoir discharge estimation is needed.

Improved knowledge of reservoir outflow provides a greater understanding of the human impacts on the terrestrial water cycle, compared to only reservoir storage. Reservoirs and irrigation water supply withdrawals have decreased annual global discharge into oceans by 2.1% and reservoirs have increased the residence time of surface water by 3 months (C. Vörösmarty and Sahagian 2000; Biemans et al. 2011). Both of these conclusions have huge implications for downstream ecosystem health, reservoir sedimentation, and water supply. However, a limitation of such global reservoir studies is the absence of observations of reservoir outflow. (Döll, Fiedler, and Zhang 2009) cites high uncertainties in reservoir operations (which are incidental to reservoir discharges) as a limitation of their global river flow impacts study. Reservoir discharge estimates could be used to refine or localize such studies to more accurately assess regionally specific reservoir impacts.

Additionally, there is value in observing reservoir outflow, rather than reservoir storage change alone from a water management perspective. Knowledge of the amount of water flowing out of an upstream and transboundary reservoir provides downstream stakeholders with a more direct proxy of the amount of water flowing into their region, which has implications for downstream reservoir operations, flood forecasting, and water supply management.

The goals of this study are twofold. First, this study presents a practical method tailored for operationalization of estimating reservoir outflow using the mass balance approach shown in equation 1 and Figure 1, and evaluates this method against observed outflow from two reservoirs in regions with different climates. Second, this study explores the sensitivity of the hydrologic

26

controls included in the mass balance approach for each reservoir and determines which, if any, controls can be reasonably ignored at monthly time scales to enable practical operations.

2.2   STUDY REGION AND DATA

The interaction between hydrologic controls is a function of climate, geography, and size and function of the reservoir. Here the role of climate and geography was explored while keeping function and size relatively constant. As such, this study examined two similarly sized hydropower reservoirs in contrasting climate and geographic settings, Hungry Horse Reservoir and Kaptai Reservoir. Hungry Horse is located in the Rocky Mountains of western Montana. It captures water from a 6067 km2 drainage area primarily made up of mountainous forest and has a total water storage capacity of 4.28 km^3. Figure 2.2 shows a map of the watershed draining into the reservoir. There are no dams or other flow regulatory structures upstream of Hungry Horse Dam, but a significant portion of the basin builds up a snowpack in Winter that can act like a natural reservoir until spring snowmelt begins. Constructed from 1948 to 1953, the dam's principal function has been hydroelectric generation with secondary utility as a flood control structure. In contrast, Kaptai Reservoir is located on the Karnaphuli River in the Rangamati District of Bangladesh. It should be noted that there are no regulatory structures upstream of Kaptai Reservoir. A map of this reservoir's watershed is also shown in Figure 2.2. It has a maximum water storage capacity of 6.48 km3 and captures water from a 11,080 km2 area. Construction of Kaptai Dam finished in 1955 and its primary function to date has been hydropower generation. It is the only hydropower dam in Bangladesh.

27
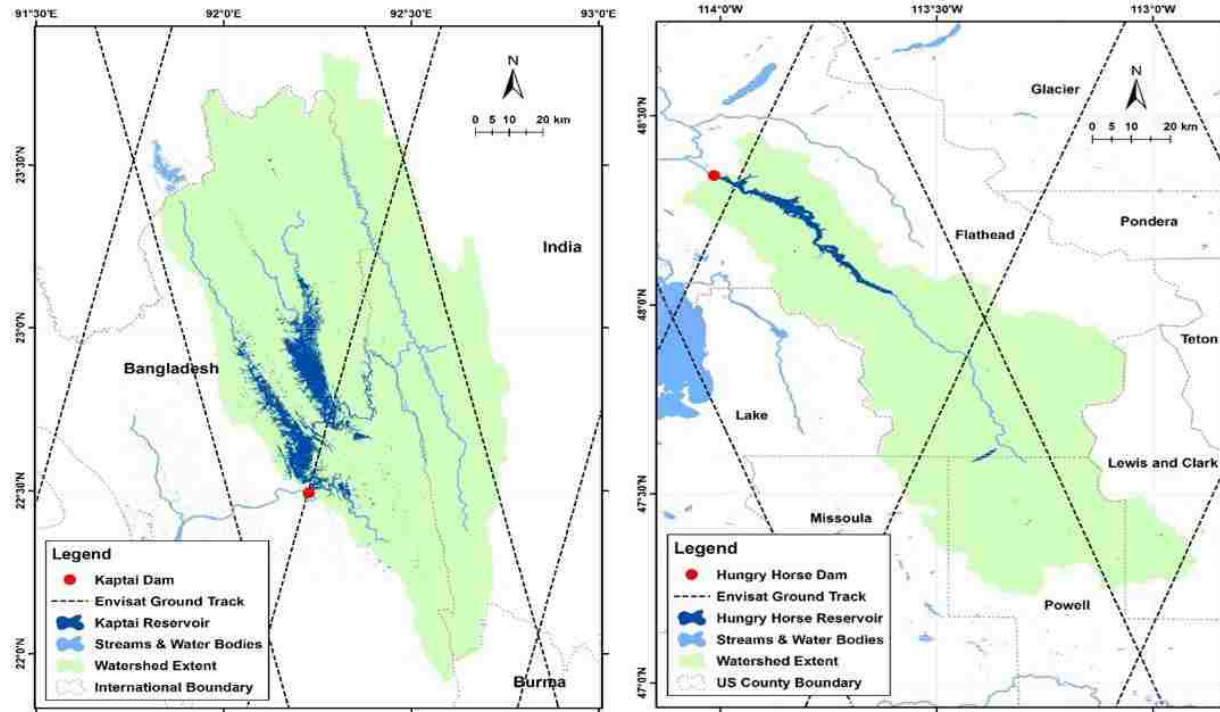
Figure 2.2. Map of the drainage area contributing runoff to the reservoirs as well as the ground track of the Envisat altimeter for (right) Hungry Horse Reservoir and (left) Kaptai Reservoir.

All altimeter measurements of both reservoirs were taken by the satellite altimeter Envisat from 21 October 2002 to 4 October 2010 for Hungry Horse Reservoir and 29 October 2002 to 12 October 2010 for Kaptai Reservoir on a 35 day repeat cycle. Envisat (Environmental Satellite) provided 18 Hz retracked data (~350 m along-track sampling) to estimate water elevation. Interested readers are referred to (Benveniste et al. 2002)for further details on remote sensing techniques and to (Siddique-E-Akbor et al. 2011) for an application over inland waters. The locations where the satellite ground tracks cross the reservoirs are shown in Figure 2.2. Daily precipitation estimates were provided by the 3B42v7 TRMM product (Huffman et al. 2007) for the same time period. This TRMM product has been calibrated against rain gauge observations. These precipitation estimates were conservatively regridded to 0.5° resolution for use in the VIC hydrologic model (section 3.1.2). Digital Elevation Models (DEMs) of each

28

reservoir were obtained from the Shuttle Radar Topography Mission (SRTM), taken from when the reservoirs were at their lowest point observed by the mission (Farr and Kobrick 2000). Observed outflow for the Hungry Horse Reservoir was measured at USGS streamflow station #12362500, located directly downstream of Hungry Horse Dam. Outflow and river level measurements were available at a gauge station located immediately downstream of the Kaptai Dam and maintained by Bangladesh Water Development Board (BWDB). These data were made available as part of a 5 year Memorandum of Understanding between the Institute of Water Modeling (IWM)-Bangladesh and University of Washington.

2.3 METHODS

2.3.1 *Mass Balance*

In this study, reservoir outflow was calculated as the mass balance of all the inflow and outflow fluxes from the reservoir system, represented by precipitation-induced reservoir inflow (I), changes in reservoir storage (ΔS), evaporation (E), and reservoir outflow (O) outlined in Equation 2.1. It was assumed that groundwater seepage would not be a major factor contributing to reservoir outflow and was ignored.

Two different hydrologic characterizations of reservoir inflow were used here, the curve number (CN) method and the Variable Infiltration Capacity (VIC) model (Woodward et al. 2003; Liang et al. 1994). Although ease of operation was a key goal of this study, the comparative use of a simple approach like CN and a more complex approach, using a macroscale hydrologic model like VIC, allowed the sensitivity of hydrologic process controls on outflow estimation accuracy to be explored. This is elaborated further in the following sections.

29

For the application of the CN method, the catchment of each reservoir was delineated from 30 m Digital Elevation Models (DEMs) obtained from the Shuttle Radar Topography Mission (SRTM). The resulting watershed delineations are shown in Figure 2.2. Soil type for the Hungry Horse Watershed was obtained from the NRCS Web Soil Survey. Soil data for the Kaptai basin were obtained from the Food and Agriculture Organization of the United Nations Harmonized World Soil Database v 1.2 (Fischer et al. 2008). Land cover of both basins at 1 km resolution was obtained from USGS Land Cover Characterization data (Loveland et al. 2000). From the soil type and land cover data, AMC II (antecedent moisture condition II, referring to average soil moisture) curve numbers for each 1 km grid cell of data were estimated using curve number lookup tables provided by the NRCS Conservation Engineering Division. The composite curve number (CN) of each basin was calculated as an area weighted average of each curve number. A dynamic curve number approach was used, where the CN alternates among AMC I (dry), AMC II (moderate), and AMC III (wet) conditions, depending on the rainfall (in inches) over the previous 5 days (P5):

$$CN = \begin{cases} AMC\ I & 0 < P_5 \le 0.5 \\ AMC\ II & 0.5 < P_5 \le 1.1 \\ AMC\ III & P_5 > 1.1 \end{cases} \tag{2.2}$$

A similar dynamic CN approach has been used in TRMM-based flood monitoring applications (Hong et al. 2007). Once the curve number was known, the daily watershed runoff was estimated from TRMM precipitation data using standard curve number equations.

The VIC hydrologic model is a gridded land surface model (LSM) that characterizes the land cover and soil types and solves energy and mass balance at each grid cell to determine evapotranspiration, interception, surface runoff, subsurface runoff, aerodynamic water fluxes, and snow. VIC models the land surface as flat grid cells. Subgrid heterogeneity in elevation and

30

soil and surface parameters are characterized by statistical distributions. All fluxes and model states are updated at a daily or subdaily time step and each grid cell is simulated independently. Water is only allowed to flow between cells after it has been routed into a channel, and once in the channel, it is not allowed to reenter the soil. The ARNO recession curve is used to characterize the soil moisture balance and the base flow of the lowest soil layer (Todini 1996). The generation of runoff is determined by the soil saturation excess, calculated by the Xinanjing variable infiltration curve (Zhao et al. 1980). The Penman-Monteith equation is employed to calculate the evapotranspiration. Snow pack is modeled in a two-layer approach, with the upper layer solved separately in the energy balance (Andreadis, Storck, and Lettenmaier 2009). The routing model is based on the model described in (LOHMANN, NOLTE-HOLUBE, and RASCHKE 1996). Interested readers are referred to (Liang et al. 1994) for a more detailed description of VIC.

The model has since been updated to model additional processes to improve its performance in a wide range of basins. Of particular importance to this study is the inclusion of frozen soil parameterizations (Cherkauer and Lettenmaier 1999) and snow accumulation and ablation algorithms and updates to cold land processes (Cherkauer, Bowling, and Lettenmaier 2003). (Haddeland, Lettenmaier, and Skaugen 2006) used VIC to study the effects of irrigation on the Colorado and Mekong River basins, demonstrating that VIC can be applied to both mountainous basins in the central United States and tropical monsoon basins in Southeast Asia. (Zhu and Lettenmaier 2007) utilized VIC to study long-term climate trends in the North American monsoon system. (Hamlet and Lettenmaier 1999) studied climate change and ENSO effects on the snow-dominated Columbia River Basin using a VIC hydrologic model. An

31

important limitation of VIC is its inability to model groundwater. (Wenger et al. 2010) reports high errors from VIC modeling in basins with strong groundwater influences.

Here a modified 0.5° resolution VIC model with a daily time step, based on the one used in (Zhou et al. 2016) to study reservoir contributions to global surface water storage variations, was used with the Sheffield global meteorological data set as forcing (Sheffield, Goteti, and Wood 2006). The Sheffield data were regridded to 0.5° resolution for use in the model, using a first-order conservative remapping approach. This model was calibrated against streamflow observations around the world (Zhou et al. 2016). The precipitation component of the Sheffield data set was replaced with TRMM 3B42v7 precipitation data for both the Hungry Horse and Kaptai basins. The routing model employed by this VIC model used 0.5° resolution river network data from (Wu et al. 2011).

A standard energy balance method (Chow, Maidment, and Mays 1988) was used to estimate evaporation from both reservoirs. The average evaporation of each calendar day of the year was used in the mass balance (i.e., the evaporation values on 1 January for all years were averaged to find the typical evaporation on 1 January). The required climatological data for the evaporation estimates of Kaptai Reservoir were provided by the NCDC (National Climatic Data Center) station at Rangamati near Kaptai Lake. Daily evaporation was estimated for the time period of the study using climatological data available from 2011 to 2014. For the Hungry Horse Reservoir, daily evaporation was estimated using a historical record of climate data, from 1948 to 1972. This climatic approach was favored over a more localized weather-scale approach, because this study aimed to explore the feasibility for operational applications around the world, requiring minimal input data.

The storage change of both reservoirs was estimated as follows. First, the relationship between reservoir water surface elevation and surface area was derived from 30 m resolution DEMs provided by SRTM. The SRTM observations used were those taken when the reservoirs were at their lowest (base water surface elevation), so that the largest portion of reservoir bathymetry was observed. Landsat images over the reservoirs were used to get a better understanding of the minimum reservoir extent. This allowed for knowledge of the bathymetry of the reservoir above this base water surface elevation. From this bathymetry, a relationship between water surface elevation and surface area was determined by classifying the elevation data into 1 m elevation bands and calculating the surface area of each band. A power law function was fitted to the lower elevation-area data of each reservoir to provide an estimate of the elevation area relationship below the water surface elevation at the time the SRTM overpassed the region (during 11–21 February 2000). These curves are shown in Figure 2.3. This allowed for the calculation of storage volume change using only one type of satellite measurement (elevation) instead of two (elevation and surface area).
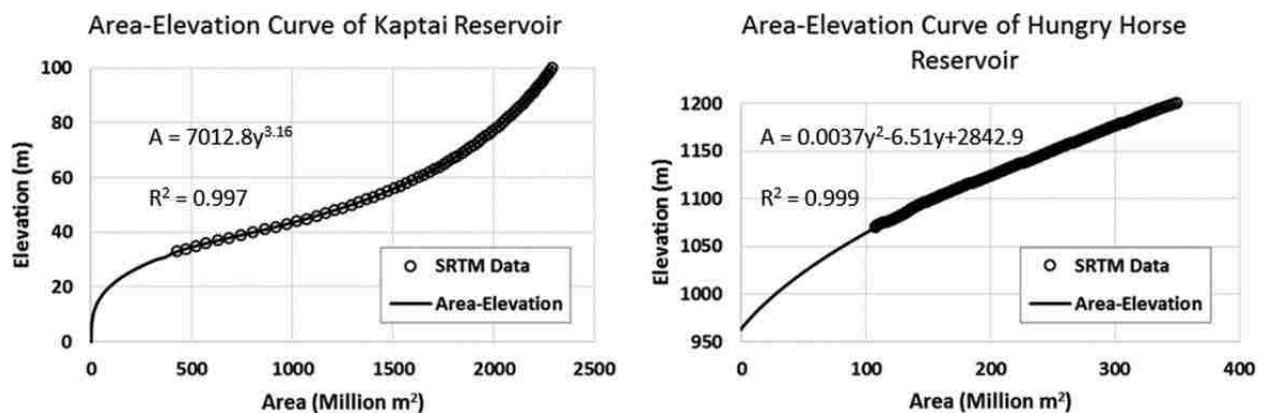
Figure 2.3. Area-Elevation curves for (left) the Kaptai Reservoir and the (right) Hungry Horse Reservoir. Note that the datums of both elevation measurements are the same and that Hungry Horse Reservoir is approximately 1000 m higher in elevation than Kaptai Reservoir.

These storage-elevation curves were then used, along with radar altimeter measurements of water surface elevation, to derive a time series of water storage changes by approximating the

33

volume of water between two elevations as the average area multiplied by the difference in elevation:

$$\Delta S = A_{avg} * \Delta h = \frac{(A_2 + A_1)}{2} * (h_2 - h_1) \qquad (2.3)$$

Where A_{avg} is the average of surface area at two elevations, Δh is the difference in elevation (between water levels 1 and 2), $h_{1,2}$ are the elevation measurements at water levels 1 and 2, respectively, $A_{1,2}$ are the surface areas corresponding to h_1 and h_2 and ΔS is the change in reservoir storage between the time when h1 and h2 were observed.

These changes in reservoir storage provide the ΔS in the mass balance (Equation 2.1) for estimating reservoir discharge. A time series of the estimated storage changes for both reservoirs is shown in Figure 2.4 along with the precipitation into each basin.
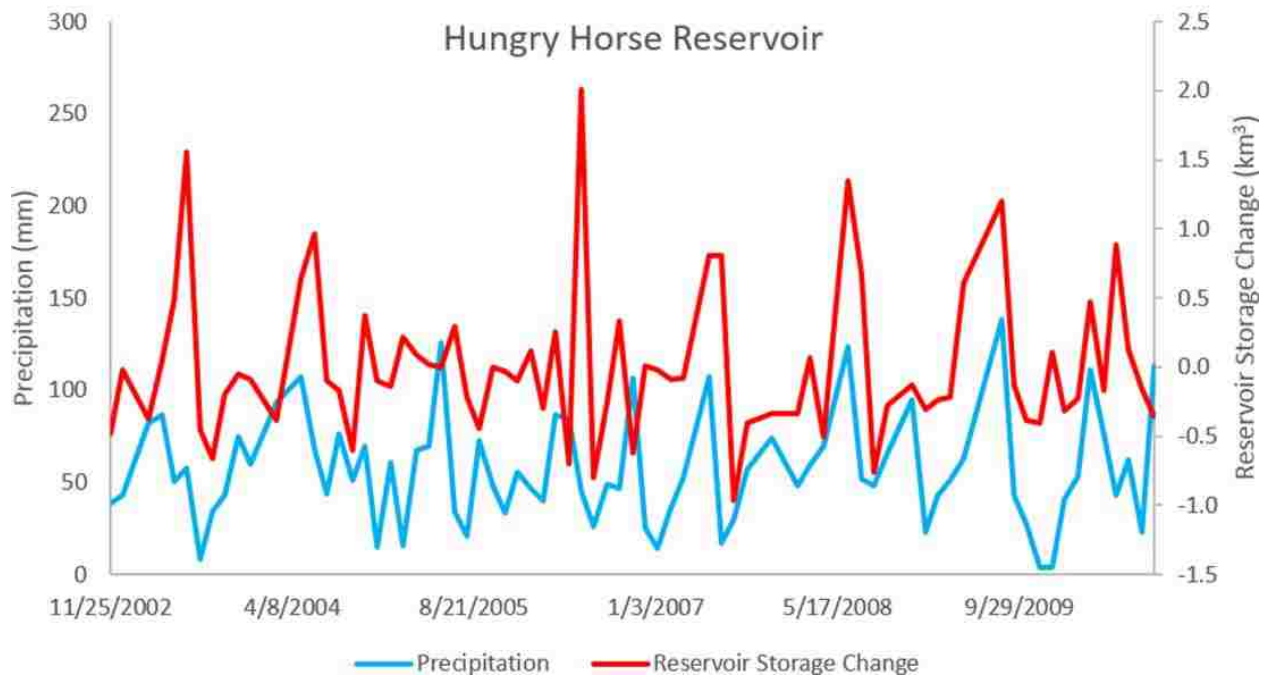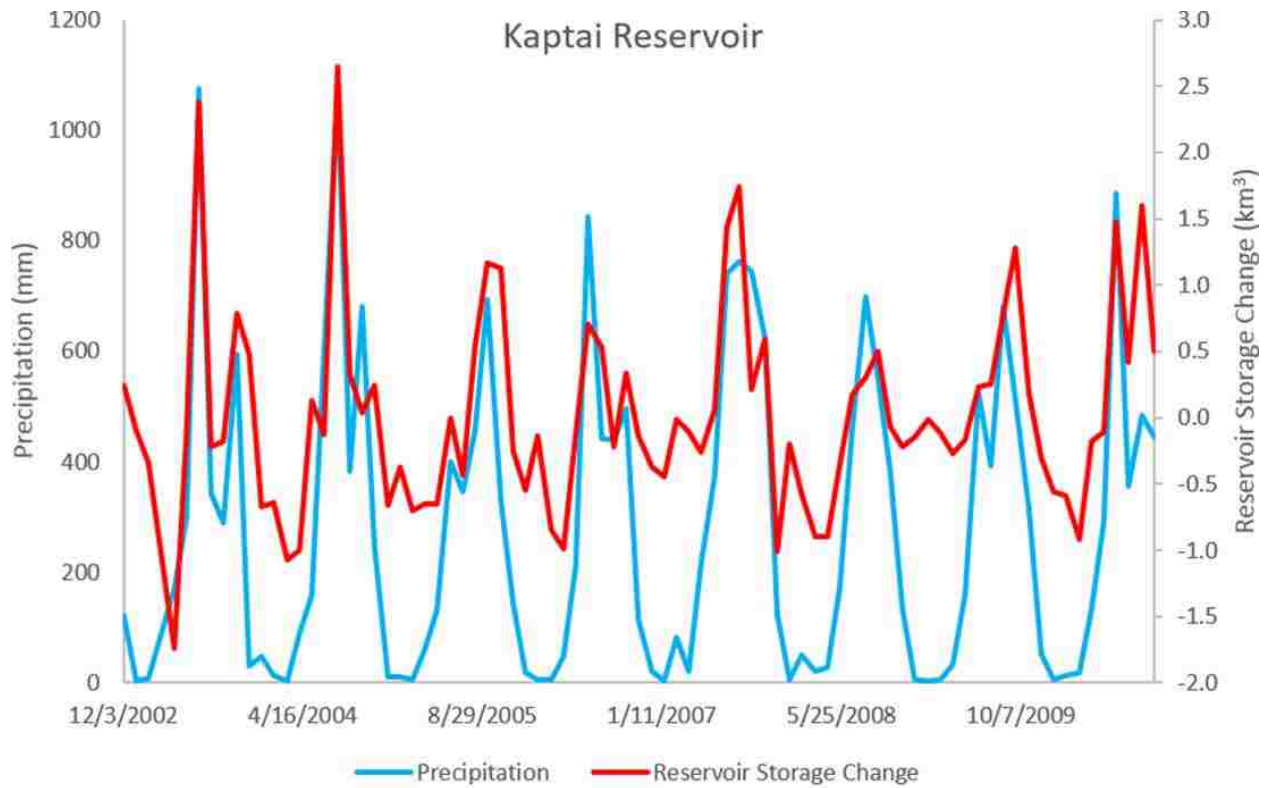
Figure 2.4. Precipitation and reservoir storage change for (top) Kaptai Reservoir and (bottom) Hungry Horse Reservoir. Precipitation is summed over the 35 day period between satellite overpasses. Storage change is the difference between the total amounts of water in the reservoir between two consecutive satellite overpasses, every 35 days.

This approach is similar to the approach used by (J. Zhang et al. 2006) to measure water storage in Lake Dongting in China. They reported a correlation coefficient (R) of 0.96 between in situ observations and altimetry-based storage fluctuations. (Yunus D. Salami 2012) applied a similar technique to Kainji Reservoir in Nigeria and found an R2 of 0.93 between in situ and altimetry-based storage changes.

2.3.2   *Hydrologic Controls*

The importance of the hydrologic controls (I, E, and ΔS) to the estimation of reservoir outflow was assessed based on the outflow accuracy from different combinations of controls in the mass balance. The combinations explored here were IES, IS, ES, and S. Near monthly (35 day), reservoir outflow was calculated using the mass balance described in section 3.1 for each of these combinations of hydrologic controls. By comparing the accuracy of estimated outflow between each combination, the relative impact each control had on the mass balance was estimated.

2.3.3   *Inflow Error Assessment*

Of the three hydrologic controls described in section 3.2, the method of estimating inflow into the reservoir using the VIC hydrologic model is considerably more complex than the estimation of evaporation, storage change, or inflow with the curve number method. This study explores how precipitation errors propagate through the VIC model in order to gain a better understanding of the sources of error in the resulting reservoir outflow estimate. Because of the varying availability of precipitation data, the method for exploring inflow errors was different for each basin.

Daily precipitation from a rain gage in the Kaptai basin, located on Kaptai Reservoir, was compared to daily precipitation from the 0.25° TRMM grid cell containing the gage to understand how accurate TRMM precipitation estimates were, compared to trusted, ground-based precipitation measurements. TRMM precipitation over the Kaptai basin was also compared with the Sheffield global data set precipitation. Then, both TRMM and Sheffield precipitation were used as forcings in the VIC model of the basin. The resulting runoffs (which served as inflow into the reservoir) were also compared, to provide as sense of how error in precipitation propagates through the VIC model.

The TRMM precipitation data were compared to precipitation from the PRISM data set (PRISM Climate Group, Oregon State University. The PRISM data were conservatively regridded to match the 0.25° resolution of the TRMM precipitation data. These two precipitation data sets were then used to force the VIC model of the Hungry Horse Basin and the resulting runoffs (inflows into the reservoir) were compared. Because snow processes play an important role in the hydrology of this basin, the snow water equivalent (SWE) outputs from each VIC model run were compared.

2.4   RESULTS

Hydrographs comparing the mass balance estimated outflow for various combinations of hydrologic controls with observed outflow for the Kaptai Reservoir are shown in Figure 2.5, for both the CN method and the VIC model. Similar comparison hydrographs for the Hungry Horse Reservoir are shown in Figure 2.6. Outflow is presented as the total volume of water that passed through the reservoir every 35 days between satellite overpasses. The corresponding error statistics are shown in Table 2.1 for Kaptai Reservoir and Table 2.2 for

37

Hungry Horse. These statistics are the root-mean-squared error (RMSE), relative root-mean-squared error (RRMSE), relative bias, and the Nash-Sutcliffe model efficiency coefficient (NSE). It should be noted that Winter refers to December, January, and February; Spring refers to March, April, and May; Summer refers to June, July, and August; and Fall refers to September, October, and November. The annual discharge was also estimated for each reservoir for 2003–2009. The years 2002 and 2010 were excluded from this portion of the analysis because the period of study used at monthly time scales does not include the entirety of 2002 or 2010. A comparison between this estimated annual outflow and observed annual outflow is given in Table 2.3 as a percent difference between estimated and observed outflow. Here negative percent difference indicates that the estimate was an under prediction of the observed. Table 2.3 also provides RMSE, RRMSE, relative bias, and NSE for the annual outflow estimates. The annual estimates were examined in conjunction with yearly precipitation totals, but no clear correlation between accuracy and bias of the estimates and precipitation amount was found.

Table 2.1. Error Statistics for Kaptai Reservoir Discharge Estimations Including Different Hydrologic Controls, Changes in Storage (S), Runoff Inflow (I), and Evaporation (E)

		I,S,E (CN)	I,S (CN)	I,S,E (VIC)	I,S (VIC)	E,S	S
Overall	RMSE [km^3]	1.39	1.32	0.78	0.80	1.72	1.70
	RRMSE [%]	83.2	79.3	46.8	47.8	103.4	101.7
	Relative Bias [%]	-67.89	-63.20	-1.15	6.2	-86.78	-84.13
	NSE	-1.50	-1.27	0.22	0.19	-2.87	-2.74
Winter	RMSE [km^3]	0.89	0.83	0.60	0.57	0.94	0.88
	RRMSE [%]	82.2	76.9	54.4	52.0	86.8	81.4
	Relative Bias [%]	-68.31	-62.23	-20.55	-14.60	-72.96	-66.98
	NSE	-1.29	-1.01	0.03	0.09	-1.56	-1.25
Spring	RMSE [km^3]	0.90	0.85	0.82	0.80	0.98	0.93
	RRMSE [%]	65.5	61.5	59.7	57.2	70.9	67.3
	Relative Bias [%]	-55.46	-50.36	-26.89	-22.04	-63.49	-58.83
	NSE	-0.49	-0.32	-0.20	-0.13	-0.75	-0.58
Summer	RMSE [km^3]	1.59	1.52	0.93	0.97	2.15	2.13
	RRMSE [%]	80.6	77.0	46.5	49.0	108.6	107.6
	Relative Bias [%]	-66.37	-61.86	8.21	14.29	-98.46	-97.46
	NSE	-2.10	-1.83	-0.05	-0.14	-4.63	-4.53
Fall	RMSE [km^3]	1.91	1.85	0.72	0.85	2.52	2.50
	RRMSE [%]	81.5	76.0	30.9	35.0	103.8	102.9
	Relative Bias [%]	-76.27	-68.90	16.99	25.07	-99.52	-98.67
	NSE	-9.34	-8.53	-0.48	-0.83	-14.98	-14.69

39

Table 2.2. Error Statistics for Hungry Horse Reservoir Discharge Estimations Including
Different Hydrologic Controls, Changes in Storage (S), Runoff Inflow (I), and Evaporation (E)

		I,S,E (CN)	I,S (CN)	I,S,E (VIC)	I,S (VIC)	E,S	S
Overall	RMSE [km³]	0.27	0.27	0.20	0.20	0.27	0.27
	RRMSE [%]	86.0	86.4	62.7	64.3	86.4	86.8
	Relative Bias [%]	-28.07	-24.43	15.23	17.68	-28.58	-24.69
	NSE	-1.02	-1.04	-0.08	-0.13	-1.05	-1.06
Winter	RMSE [km³]	0.10	0.10	0.09	0.09	0.11	0.11
	RRMSE [%]	44.0	42.1	39.8	39.2	48.6	46.7
	Relative Bias [%]	-21.75	-20.04	8.83	10.80	-21.96	-20.09
	NSE	0.14	0.22	0.30	0.32	-0.05	0.03
Spring	RMSE [km³]	0.27	0.27	0.20	0.20	0.27	0.27
	RRMSE [%]	88.7	88.6	67.9	66.8	88.6	88.5
	Relative Bias [%]	-40.87	-38.98	-7.47	-3.74	-42.61	-40.72
	NSE	-0.30	-0.30	0.24	0.26	-0.30	-0.29
Summer	RMSE [km³]	0.42	0.42	0.23	0.23	0.42	0.42
	RRMSE [%]	88.9	89.0	48.1	48.4	89.2	89.3
	Relative Bias [%]	-50.90	-46.58	4.11	2.34	-51.72	-47.41
	NSE	-5.22	-5.24	-0.82	-0.85	-5.27	-5.28
Fall	RMSE [km³]	0.16	0.17	0.22	0.24	0.16	0.17
	RRMSE [%]	66.5	70.4	92.1	99.7	66.1	70.0
	Relative Bias [%]	26.20	32.22	69.17	78.72	27.50	34.65
	NSE	-1.67	-1.99	-4.12	-5.00	-1.64	-1.96

Table 2.3. Percent difference between observed and estimated annual total flows. A negative percent difference represents an under prediction in the estimate.

	Percent Difference by year [%]							Overall Error			
Year	2003	2004	2005	2006	2007	2008	2009	RMSE [km^3]	RRMSE [%]	Rel. Bias [%]	NSE
Kaptai (VIC)	-17.8	-25.9	-13.9	-13.5	28.0	15.8	16.0	3.66	20.4	-5.98	0.30
Kaptai (CN)	-68.5	-67.1	-79.1	-68.1	-51.2	-63.0	-74.4	12.73	71.1	-68.01	-7.47
Hungry Horse (VIC)	29.9	22.7	-7.7	48.0	-15.0	5.2	23.6	0.75	26.4	14.99	-1.63
Hungry Horse (CN)	-12.3	-31.6	-60.4	19.7	-29.4	-35.8	-19.1	0.98	34.2	-23.75	-3.41

2.4.1   *Kaptai Reservoir*

Using the CN method to provide inflow, the I, E,S estimated outflow had an overall RRMSE of 83.2% and an NSE of −1.50 at the monthly time scale across all seasons. Replacing the inflow estimation method with the VIC model, the I,E,S estimated outflow improved, with an overall RRMSE of 46.8% and an NSE of 0.22. Removing the evaporation component from these monthly estimates slightly increased the accuracy of outflow estimates using CN-derived inflow and slightly decreased the accuracy of outflow estimates using VIC-derived inflow. The two estimates that exclude inflow showed considerably lower accuracy than both inflow methods and large negative biases. Monthly outflow predictions made using CN-derived inflow during the dry season (Winter and Spring) exhibited small gains in accuracy over predictions made without inflow. Predictions utilizing VIC inflow showed larger gains in accuracy in the Winter months. The I,S outflow estimate using VIC was the most accurate dry season estimate, with the I,E,S estimate using VIC performing only slightly worse. Including CN-based inflow in the mass balance resulted in larger increases in accuracy in the wet season than the dry season. Replacing

CN-derived inflow with VIC modeled inflow provided another significant improvement in outflow estimation accuracy, with the lowest seasonal RRMSE occurring in the Fall. Similar to the dry season, the E,S and S outflow estimates were considerably less accurate compared to other estimates in the Fall. The NSE of the VIC I,E,S outflow estimation for each season ranged from 0.03 to −0.48, while the NSE for the overall estimate was 0.22. This indicates that the mass balance estimate utilizing VIC modeled inflow was a better predictor of monthly outflow than the average monthly outflow from 2002 to 2010 would be, while seasonal average outflow would be a more accurate predictor of monthly outflow than the mass balance estimate.

The difference between outflow estimate accuracy of the two inflow methods was smaller in the dry season (Winter and Spring), with less than 10% RRMSE differences in the spring. However, in the dry season, CN-driven outflow estimates more closely match outflow estimates derived from storage change only, with differences in RRMSE around 5%. This trend can be seen in the hydrograph in Figure 2.5. Conversely, wet season CN-driven outflow estimates showed a significant increase in accuracy over estimates excluding the inflow component, as shown by decreases in RRMSE between 28.0% and 20.6% during this period. VIC model-driven outflow estimates exhibit even higher accuracy improvements over the CN-driven estimate in the wet season than in the dry season, with RRMSE differences as high as 50.6%. CN-driven outflow estimates exhibited large negative relative biases across all seasons, which is reflected in the hydrograph (Figure 2.5).

Comparison between observed and estimated total outflow using the VIC model at annual time scales reveals a shift from underestimation to overestimation of annual outflow between 2006 and 2007. Pre-2006 outflow estimates match the wet season peaks, but underestimate dry season low flows. In contrast, post-2006 outflow estimates over predict peak wet season

42

discharge, but better capture dry season low flows. This shift is reflected by the low overall relative bias, where the overestimates compensated for the underestimates. The percent difference between estimated and observed annual outflow ranged from 13.9% to 28.0% in magnitude with no clear trend over time. With an RRMSE of 20.4% and NSE of 0.30, the mass balance performed with higher accuracy at the annual time scale than the monthly time scale at this reservoir.

The CN-driven annual outflow estimates did not follow this pattern and the percent difference between observed and estimated outflow remained between −51.2% and −79.1%, with no clear trend over time. An RRMSE of 71.1% indicates that the mass balance using CN inflow estimated annual outflow with more skill than monthly outflow. However, it performed significantly worse than the mass balance using the VIC model inflow as illustrated by the drastic difference between RRMSE and NSE of the two annual outflow estimates.
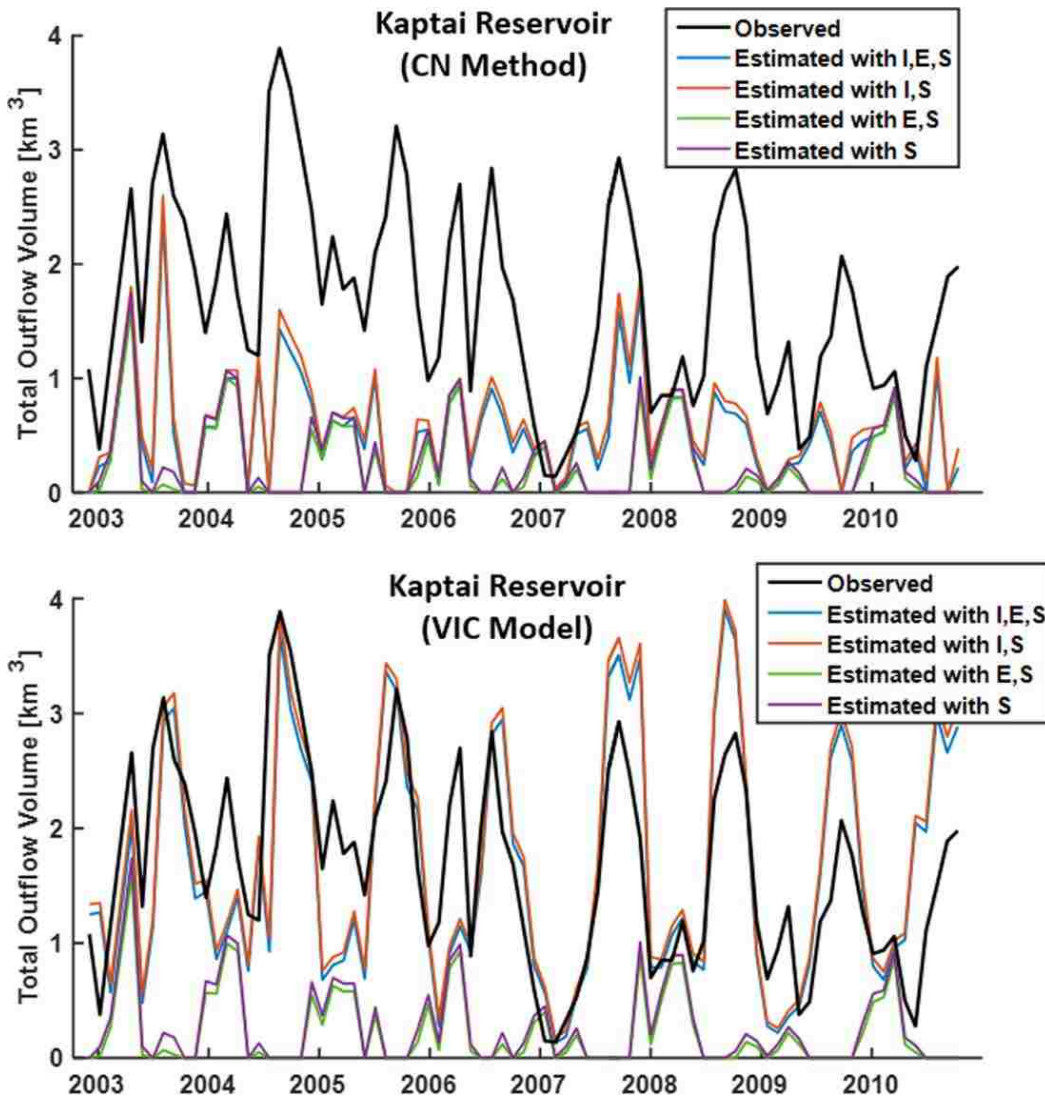
Figure 2.5. Hydrographs comparing Kaptai Reservoir discharge observations to discharge estimates using different components of the mass balance, changes in storage (S), runoff inflow (I), and evaporation (E). The inflow in the top graph uses the CN method while the inflow in the bottom graph uses the VIC model.

2.4.2   *Hungry Horse Reservoir*

Estimations of outflow from the Hungry Horse Reservoir resulted in instances of outflow considerably lower than expected. These instances occurred fewer than once a year on average. It is clear that a hydrologic process was not properly represented, even by the VIC model, however

the exact reason for these errors is unclear. Given the small number of these errors in estimates made using VIC model inflow, a minimum flow threshold was implemented here to correct for these errors. This threshold was provided by a State of Montana operation constraints report and set at 8.5 m3/s (to meet environmental flow requirements downstream), which corresponds to 0.026 km3 in a 35 day period. Outflow estimates that violated this limit were instead taken as the average of the previous and subsequent outflow estimates. Outflow estimates generated with CN-derived inflow or generated without considering inflow experienced more frequent errors of this nature, with multiple erroneous outflow estimates occurring in subsequent time steps. In these instances, the averaging correction could not be applied and the discharge values were set at 0.25 km3. This corrective approach requires reservoir-specific and river-specific data and thus might not be applicable to other reservoirs. However, a minimum threshold of no flow can be applied to all reservoirs if negative outflow becomes an issue.

Outflow estimates that used CN-derived inflow were nearly identical to estimates that excluded the inflow component across all seasons. This is reflected by similar error statistics between estimates with and without the CN-derived inflow component, and can be clearly seen in Figure 6. From Table 2, the I,E,S estimated outflow with inflow derived from the VIC model was most accurate overall with an RRMSE of 62.7%, followed closely by the I,S estimates with 64.3%. Outflow estimates that utilized CN-derived inflow and those that excluded inflow were less accurate, ranging from 86.0% and 86.8% RRMSE. Estimates that included VIC modeled inflow tended to overpredict discharge as shown by positive relative bias. Estimates utilizing CN-derived inflow or lacking the inflow component exhibited negative relative bias with higher magnitude.
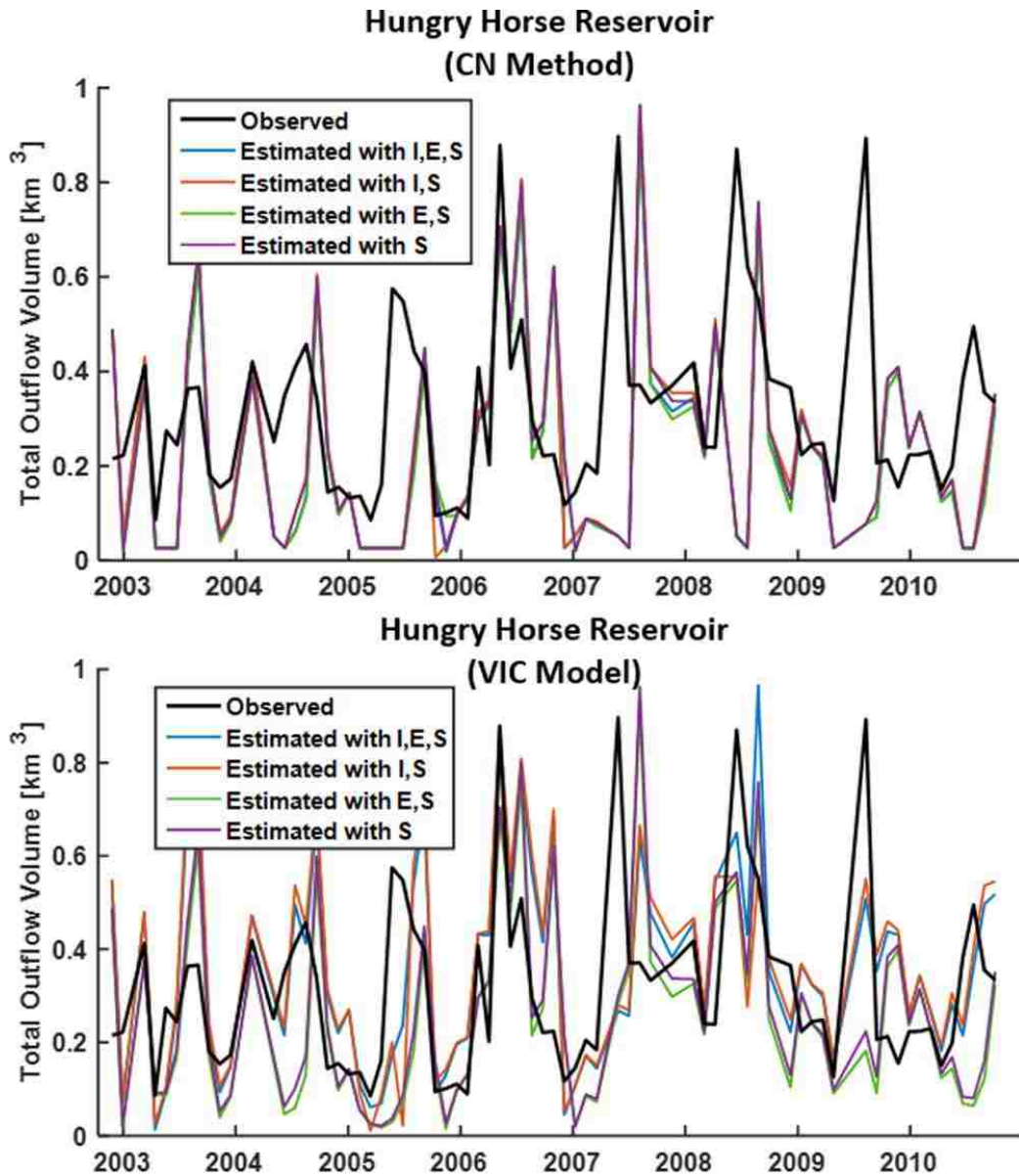
Figure 2.6. Hydrographs comparing Hungry Horse Reservoir discharge observations to discharge estimates using different components of the mass balance, changes in storage (S), runoff inflow (I), and evaporation (E). The inflow in the top graph uses the CN method while the inflow in the bottom graph uses the VIC model.

Winter outflow estimation was considerably more accurate. Outflow estimates using CN-derived inflow showed small gains in accuracy over estimates that excluded inflow. Outflow estimates utilizing VIC modeled inflow were the most accurate here with RRMSEs of 39.8% and 39.2% for I,E,S and I,E estimates, respectively. Spring discharge estimates provided RRMSE

similar to the overall RRMSE for all mass balance component combinations, but with lower relative bias. The lowest relative bias (2.34%) occurred in the summer with VIC providing inflow. Summer RRMSE for this estimate was 48.1%. In contrast to the other seasons, fall estimates without inflow exhibited higher accuracy than estimates including inflow, with an RRMSE of 66.4% for the E,S estimate and a relative bias of 25.25%. Based on the overall NSE, the mass balance estimates were not better predictors of monthly discharge than the 2002–2010 mean flow would be. Seasonally, the mass balance predicted flows more accurately than the seasonal mean outflow in the Winter and Spring, and less accurately in the Summer and Fall.

With an RRMSE of 34.2%, the mass balance including CN inflow estimated annual reservoir outflow more skillfully than monthly inflow. Annual outflow estimates that used CN-derived inflow consistently underestimated observed annual outflow (represented by negative percent difference), with the exception of 2006. In contrast, the mass balance consistently overestimated annual outflow (represented by positive percent difference) when utilizing the VIC model inflow component, with underprediction only occurring in 2005 and 2007. Percent differences between observed and estimated annual outflow utilizing VIC inflow ranged in magnitude from 5.2% in 2007 to 48% in 2006. There is no clear trend in the accuracy of the discharge estimates over time. An RRMSE of 26.4% suggests that the mass balance estimated discharge with higher skill at the annual time scale than the monthly time scale. However, an NSE of −1.63 indicates that the mass balance is a worse predictor of annual outflow than the 2003–2009 average annual outflow.

2.4.3 *Inflow Error Assessment Results*

Table 2.4 shows the RMSE, hit bias, probability of missed precipitation, and probability of false precipitation for the comparison between TRMM precipitation and Sheffield precipitation and

between TRMM and the rainfall gage station at Kaptai Reservoir. Interested readers are referred to (Tian and Peters-Lidard 2010) for more information regarding hit bias, missed precipitation, and false precipitation, and to (A. S. Gebregiorgis et al. 2012) for more information on how these errors propagate. These statistics are shown for the entire study period as well was for consecutive 3 month seasons (i.e., precipitation errors from every December, January, and February were considered for the statistics listed under "DJF"). The pattern in RMSE is the same for both comparisons, with the lowest occurring in DJF and the highest in JJA. TRMM appears negatively biased when compared to the gage, but positively biased when compared to Sheffield. Additionally, the season distribution of missed precipitation is different, but the overall missed precipitation for both comparisons is similar. The rainfall gage comparison indicates that TRMM falsely identifies precipitation over twice as much as the Sheffield comparison. Some differences between these two comparisons are expected however, because the comparison with the rainfall gage only takes into account one TRMM grid cell, while the Sheffield comparison examines the entire domain.

Table 2.4. Comparison between TRMM precipitation and the Kaptai Reservoir rainfall gage as well as between TRMM and the Sheffield global dataset precipitation.

TRMM and Kaptai Reservoir Rainfall Gage					
	Overall	DJF	MAM	JJA	SON
RMSE [mm/day]	15.39	1.93	6.65	25.4	15.87
Hit Bias [mm/day]	-3.39	-0.11	-0.46	-8.55	-4.28
Missed Precipitation [%]	6.87	0.56	1.31	18.3	7.14
False Precipitation [%]	15.94	3.33	22.88	23.08	15.93
TRMM and Sheffield					
	Overall	DJF	MAM	JJA	SON
RMSE [mm/day]	9.78	4.26	8.53	13.13	10.87
Hit Bias [mm/day]	1.86	-0.51	0.70	3.78	0.86
Missed precipitation [%]	6.47	8.43	7.95	3.27	6.26
False precipitation [%]	35.87	12.40	30.41	62.45	37.74

The resulting daily inflow generated from the VIC model forced with TRMM precipitation is compared to the inflow generated from the VIC model forced with Sheffield precipitation in Figure 2.7. From this graph, it can be seen that inflow produced with TRMM and Sheffield precipitation follow similar seasonal patterns with similar magnitude in peak flows. However, the timing of these peak flows appears to be different in many cases. This leads to a high error between the two inflows, but a low bias. When these daily inflows are aggregated into monthly inflows, these timing errors are eliminated and result in an RRMSE between the two monthly inflows of less than 10%.

Kaptai Reservoir VIC Modeled Inflow
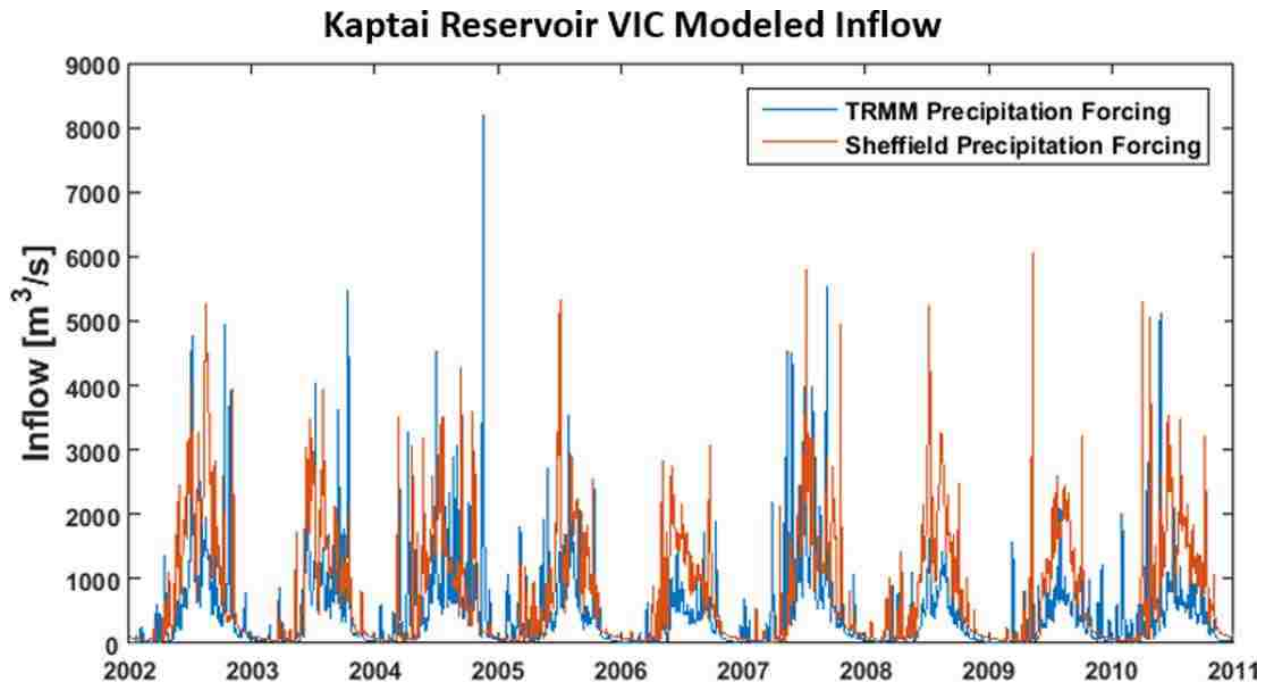
Figure 2.7. Comparison between daily Kaptai Reservoir inflow generated by the VIC model forced by TRMM and Sheffield precipitation data.

Table 2.5 shows the RMSE, hit bias, probability of missed precipitation, and probability of false precipitation for the comparison between TRMM precipitation and PRISM precipitation over the Hungry Horse basin. TRMM has the highest RMSE, hit bias, and missed precipitation in the DJF when most of the precipitation is snow. TRMM is also negatively biased across all seasons, indicating an underrepresentation of precipitation in this basin. Figure 2.8 shows the daily basin average snow water equivalent (SWE) in the basin generated using the VIC model with both sets of precipitation forcings (TRMM and PRISM). Figure 8 also shows the resulting inflow generated by the VIC model using both precipitation forcings. From the SWE comparison, it is clear that TRMM precipitation causes consistently lower SWE than PRISM. This leads to the consistently lower spring and summer peak inflows shown in the inflow comparison graph.

Table 2.5. Comparison between daily TRMM and PRISM precipitation from 2002 to 2010 over the Hungry Horse basin.

	Overall	DJF	MAM	JJA	SON
RMSE [mm/day]	4.25	4.67	4.15	3.85	4.30
Hit Bias [mm/day]	-1.58	-2.17	-1.65	-0.97	-1.55
Missed precipitation [%]	31.2	50.2	27.8	14.8	32.2
False precipitation [%]	11.6	3.0	19.0	16.5	7.8
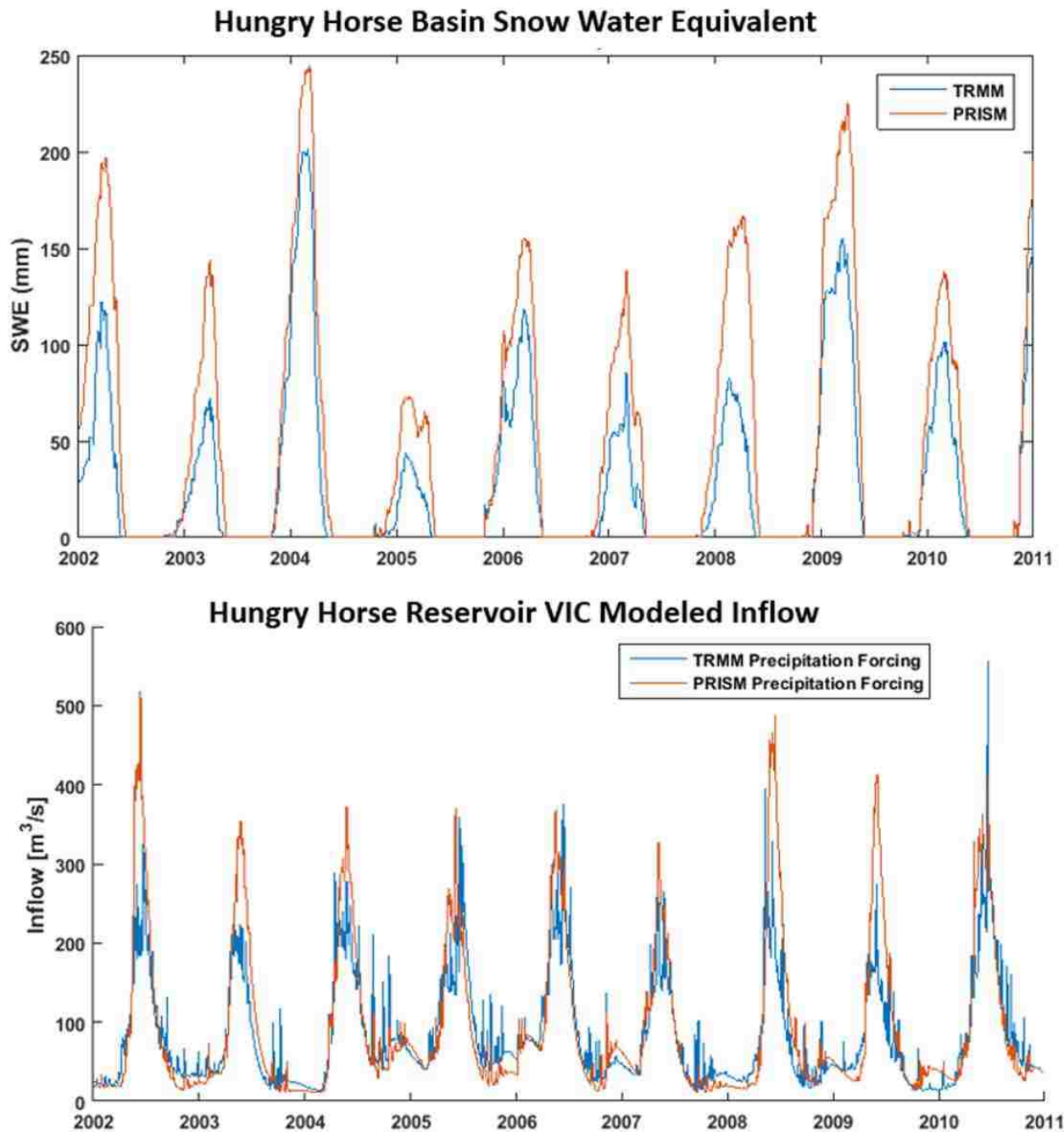
Figure 2.8. Comparison between VIC model outputs generated using TRMM and PRISM precipitation as forcings, (top) average snow water equivelent and (bottom) inflow into the Hungry Horse Reservoir.

2.5   Discussion and Conclusions

The mass balance approach utilizing CN-derived inflow demonstrated small gains in monthly Kaptai Reservoir outflow estimation over mass balance approaches that excluded inflow. Conversely, the mass balance approach utilizing VIC modeled inflow yielded fairly accurate monthly outflow estimates. The outflow estimation accuracy improvements achieved by utilizing the VIC model to derive inflow over the CN method suggest that improved modeling of the hydrologic inflow processes led to more accurate outflow estimates. Furthermore, examination of the seasonal differences in monthly outflow estimation revealed higher accuracies in the wet season than the dry season. This indicates that the mass balance and VIC inflow model better represent the hydrological processes during the wet season. A seasonal shift in the relative bias from negative (underestimations) in the dry season to positive (overestimation) in the wet season is observed for VIC inflow-based estimations. However, the hydrograph in Figure 2.5 reveals that overestimation of wet season outflow only occurred from 2007 to 2010. During 2002–2006, wet season outflow estimates appear to match observed outflow. Similarly, dry season underestimation occurred primarily in 2002–2006, while dry season estimates in 2007–2010 match observations more closely. This indicates a shift in the conditions of this basin that caused outflow estimates to increase in all seasons. One possible explanation is a change in basin characteristics through land cover or land use changes, such as an increase in vegetation, which would cause a larger portion of precipitation to be intercepted leading to less runoff flowing into the reservoir than predicted. This highlights the vulnerability of this method to changing basin conditions, as any changes would have to be accounted for in the runoff model. Estimates that utilized CN inflow did not appear to follow this pattern, indicating that the process that caused this shift is poorly represented by the curve number method.

Comparison between observed outflow and outflow estimated using different components of the mass balance showed that the accuracy of the outflow estimate was highly variable and depended on which hydrologic controls were considered. For the Kaptai Reservoir, the two most accurate combinations of controls were I,E,S (inflow, evaporation, and storage change) and I,S (inflow and storage change), when the VIC model was used to provide inflow. The difference in accuracy between these two cases was relatively small. This, in conjunction with the high error in estimated outflow in both cases where inflow was not included, indicated that precipitation-induced inflow is the most important hydrologic control to consider for this reservoir, which is consistent with the region's high precipitation. This is reflected by the significant accuracy improvements achieved utilizing a more complex, process-based approach (VIC) over a simpler, more empirical approach (CN). This is further supported by the size of the reservoir relative to the inflow. The Kaptai Reservoir has the capacity to store only 33% of the average annual runoff of this time period. This indicates that inflow and outflow should be considerably larger than storage change in this reservoir. However, storage change was also an important control to consider, particularly during periods of low precipitation. While including evaporation in the mass balance resulted in an overall lower relative bias, the effects on outflow estimation accuracy were minimal. At this time, it is unclear if evaporation is an insignificant control for this reservoir, or if the climatologic evaporation approach used here is insufficient and a more localized, weather-based approach is needed.

 As a source of error for the Kaptai Reservoir, the precipitation input likely had little effect. The error and bias present when comparing TRMM precipitation to Sheffield precipitation were reduced when these precipitation data sets were used as forcings in the VIC

model, and were further reduced when the resulting runoff (inflow into the reservoir) was aggregated over monthly time scales.

The mass balance approach for the Hungry Horse Reservoir provided less accurate monthly outflow overall. However, Winter outflows from Hungry Horse were estimated with a significant degree of accuracy and compelling NSE, when the VIC model provided the inflow component. Utilizing the CN method to provide inflow did little to improve accuracy over simply excluding inflow. This suggests that the VIC model captures one or more hydrological processes that control the runoff in this basin that are otherwise poorly represented by the CN method. This important process is likely snow accumulation/melt, characteristic of high-elevation basins such as the Hungry Horse basin. The VIC model, through energy balance, can represent the timing and magnitude of snow accumulation/melt while the CN method has no capacity to represent snow processes. Winter is the only season where inflow is typically not effected by snowmelt, as a majority of the basin remains below freezing throughout the Winter. The relatively lower accuracy during the other seasons could be caused by difficulties in estimating the quantity and timing of snow accumulation/melt. This is supported by the findings of the inflow error analysis, where differences in Winter SWE (resulting from two different precipitation forcings) caused similar differences in spring and summer runoff. Including inflow in the mass balance provided an increase in outflow estimation accuracy, indicating that inflow is an important hydrologic control in this basin. However, the magnitude of the storage change was considerably larger relative to inflow. This is supported by the Hungry Horse Reservoir's size relative to annual runoff. The reservoir has the capacity to store 144% of the average annual flow during the study period. This suggests storage change is the most important hydrologic control in this basin. Representing inflow properly was also important in generating accurate outflow

55

estimates as demonstrated by the differences between the I,E,S (VIC) estimate, the E,S estimate, and the I,E,S (CN) estimate. However, excluding inflow improved the accuracy in the fall. A possible source of this anomaly is an overestimation of inflow and runoff during this time as suggested by the high relative bias associated with the I,E,S (VIC) estimate. The partition between the forms of precipitation (rain or snow) into the basin in the fall is highly sensitive to the climate. It is possible that the model forcing does not accurately reflect the conditions at the higher elevation points in the basin, causing the VIC model to erroneously treat fall snow precipitation as rain. Furthermore, slight inaccuracies in the VIC model's partitioning between snow accumulation and melt would have high impacts on the resulting inflow. This could lead to the overestimated Fall outflows generated with inflow included in the mass balance.

Unlike the Kaptai Reservoir, outflow estimation for the Hungry Horse Reservoir was significantly impacted by errors in the TRMM precipitation input. The negative bias of TRMM precipitation compared to PRISM precipitation, particularly in the Winter, propagated through the VIC model and resulted in negatively biased inflow. A similar negative bias is seen in spring outflow estimation, when runoff is at a peak due to snowmelt. Additionally, groundwater effects in the basin, which are not modeled by VIC, could significantly affect inflow.

Annual outflow totals of both reservoirs were estimated more accurately than monthly outflow, indicating that the mass balance approach for annual estimations has more value than for monthly estimations. These annual estimates once again illustrate which hydrologic controls were important for each basin. The difference in accuracy between Kaptai Reservoir annual outflow estimated from VIC inflow and CN inflow was extreme, identifying inflow as a key component of outflow estimation in this basin. In contrast, the difference in accuracy between Hungry Horse Reservoir annual outflow estimated from VIC inflow and CN inflow was less

56

pronounced. This signifies that while inflow is a significant hydrologic control, it is not the dominant control. However, the low NSE for the annual Hungry Horse outflow indicates that even at yearly time scales, some source of error is hindering the mass balance's effectiveness. This could be errors in TRMM precipitation propagating through the VIC model, or high connectivity with the groundwater table.

What emerges from this study is that understanding the dominant hydrologic controls governing reservoir outflow is key to improving reservoir outflow estimations. The dramatic difference in hydrologic controls between the two reservoirs used in this study indicates that the results from these reservoirs are not transferable to regions with differing climate and geography. For example, evaporation was found to have little effect on the two reservoirs studied here, but other regions such as the Middle East or a semiarid region (e.g., Lake Mead in U.S.) would have higher evaporation rates and the importance of this hydrologic control would need to be reassessed. Furthermore, reservoirs of varying sizes and functions may also behave differently in terms of hydrologic controls. As seen here, reservoirs that can store a smaller percentage of their annual inflow tend to be more dynamically operated than larger reservoirs. In more extreme cases, these reservoir dynamics may occur more often at time scales shorter than monthly. This influences which hydrologic controls are important in estimating the reservoir outflow between satellite overpasses. Additionally, the purpose of the reservoir might dictate its response to different hydrologic controls. Further work needs to be conducted to determine how reservoir size and use affects the hydrologic controls of this mass balance. This involves scaling up the method used here to multiple reservoirs of varying conditions, regulations and storage capacity. Additional studies should also examine reservoirs on a global scale to determine how well this method works in a wide variety of climates and geographies. In Chapter 3, this method is

adapted to work for reservoirs that do not lie under nadir radar altimeters and then applied to a system of reservoirs in the Mekong River Basin.

Chapter 3: Inferring reservoir operating patterns across the Mekong Basin using only space observations

Note: This chapter has been published mostly in its current form in *Water Resources Research* (M. Bonnema and Hossain 2017b); Used with permission.

Abstract: This chapter explores the operating pattern of artificial reservoirs by examining their impact on streamflow through two parameters, residence time and flow alteration, using a purely satellite-based technique for the Mekong Basin. Overall residence times of individual reservoirs ranged from 0.09 to 4.04 years, while streamflow was altered between 11 and 130% of its natural variability. The current set of reservoirs appears to have increased the residence time of the entire Mekong basin by about 1 month. However, if subbasin variability is considered, the satellite-based method depicts a different picture. Residence time increases to 4 months when only regulated flows are considered. If low residence time reservoirs on major rivers are excluded and reservoirs on higher stream-order rivers considered, residence time increases to 1.3 years. Predictable strong seasonal patterns emerged in residence time, where reservoirs experience higher residence time in the dry season and lower residence time in the wet season and residence time varies inversely with precipitation. High variability in reservoir effects on streamflow between reservoirs could not be explained by any reservoir properties (e.g., size, use, location, etc.), highlighting the variability in the human decisions operating these reservoirs. The take-home message of this chapter is that satellite observations, in combination with physical models forced with satellite data, can elucidate the spatiotemporal variability of reservoir behavior in ungauged basins of the developing world. We demonstrate in this study that the requirement for ground data to monitor current or historical behavior of dams is not necessary.

3.1 INTRODUCTION

Chapter 2 established a suitable method for satellite-based reservoir outflow estimation, laying the groundwork for a deeper understanding of the impacts of reservoirs on the timing and magnitude of downstream flows. This chapter applies the mass balance approach to 20 reservoirs in the Mekong River Basin, in order to estimate two key measures of reservoir impacts, residence time and flow alteration.

Residence time, as defined in (Monsen et al. 2002), is "*how long a parcel, starting from a specified location within a waterbody, will remain in the waterbody*". For reservoirs, the specified starting location is typically the point in which water enters the reservoir from upstream. The residence time of a reservoir is in essence, a measure of the time delay between when water enters the reservoir and when it is released by human operating decisions. Residence time controls biochemical processes such as nutrient accumulation and eutrophication processes (Ambrosetti, Barbanti, and Sala 2002) as well as sedimentation ((M Kummu et al. 2010)) and fish population dynamics (Beamesderfer et al. 1990). The residence time of a reservoir can be used to obtain first order approximations of these and other complex processes, which dictate some impacts the reservoir has on the river system. In short, time varying residence time can be considered as an important 'piece of the puzzle' when attempting to reveal a reservoir's multi-faceted impact on hydrology, geomorphology and ecosystem function.

Flow alteration refers to the short term effects of reservoir operation on downstream streamflow. That is, it is a measure of the instantaneous change in streamflow imposed by a reservoir. The degree to which flow is changed dictates the change in water supply the downstream population must manage. Altered river flows also impact ecosystem health and biodiversity (Bunn and Arthington 2002). While estimating the impact altered streamflows have

on specific species is difficult, understanding the extent of reservoir imposed flow alteration is an important step in estimating these effects.

Past studies have characterized reservoir residence time as the volume of the reservoir divided by the mean annual inflow (Vorosmarty 1997), which is more indicative of the design feature of a dam. This method also makes the assumption of steady state conditions within the reservoirs, where volume remains constant and inflow is equal to outflow. This may be valid when studying long time scales, where annual inflow and outflow are equal. However, residence time can fluctuate greatly at shorter time scales due to variations in inflow, outflow, volume changes and mixing processes (Rueda et al. 2006). Accounting for this temporal variability in reservoirs requires observing these time varying parameters.

Understanding the impacts of reservoirs in the Mekong River Basin is critical. The Mekong River Basin (Figure 3.1) is currently going through a transformation (Molle, Foran, and Käkönen 2009) that is emblematic of dam development in developing regions. Growing demand for clean, renewable energy and the economic benefits it brings has driven dramatic hydropower development in the MRB over the last 20 years and continues into the coming decades (WLE 2017). As Laos vies to be the "battery of Asia", with plans to build an unprecedented nine dams on the currently free flowing main stem of the Mekong River, the region is poised to drastically increase its ability to produce renewable energy. However, with the economic benefits that hydropower provides comes environmental costs (Winemiller et al. 2016). Dams in the MRB have already significantly altered sediment transport (Matti Kummu and Varis 2007; Lu and Siew 2006; K. D. Fu, He, and Lu 2008), river connectivity (Grill et al. 2014), and streamflow (Lu et al. 2014; M. Bonnema and Hossain 2017a). These and other alterations to the natural river system threaten downstream fish and rice production, and by extension, the food security of

61

millions of inhabitants of the region (Kondolf, Rubin, and Minear 2014; Lauri et al. 2012; Ziv et al. 2012).

Understanding how dams in the Mekong River Basin impact residence time and streamflow is a key step towards understanding the impacts of future dams. Such a study can provide the foundation for studying reservoirs in other developing basins undergoing rapid change due to dam construction such as the Irrawaddy, Yangtze, Zambesi, Congo, or Amazon (Winemiller et al. 2016). The benefit of a satellite based approach is that it is unhindered by lack of availability of in-situ data and has global applicability. Satellite-based reservoir technique can therefore be scaled regionally or globally to answer for diverse set of stakeholders and scientific communities fundamental questions that have not been answered before. Some of these questions are: *What are the impacts of dam operations on ecosystem services and flood risk in river basins? How are the impacts on regulated river systems likely to change in the future due to climate change, increasing development pressures and aggressive dam building plans by the developing world?*

3.2   STUDY REGION AND DATA

This study focused on 20 large reservoirs in the Mekong River Basin, identified by the Global Reservoir and Dam (GRanD) Database (Lehner et al. 2011). Figure 3.1 shows a map of the Mekong Basin with these 20 dams as well as all existing and future (planned or proposed dams) as identified in WLE 2017. Table 3.1 lists the dam/reservoir name along with their capacity and degree of regulation (capacity volume divided by annual inflow volume), taken from the GRanD Database. The capacity of these reservoirs ranges from 22.8 million m^3 to 7030 million m^3 with an average of 961 million m^3. Degree of regulation (DOR) is the reservoir

62

capacity expressed as a percentage of the mean annual inflow into the reservoir, which can be assumed as the 'design' residence time of the reservoir.

For validation of the satellite-based technique, daily time series of in-situ reservoir water levels was acquired for specific reservoir sites via our institutional agreement with Vietnam. In other cases, daily time series of reservoir volumes of some reservoir sites was acquired from publicly available websites (e.g. Thaiwater.net). Further validation was carried out on the Oroville Reservoir in California.
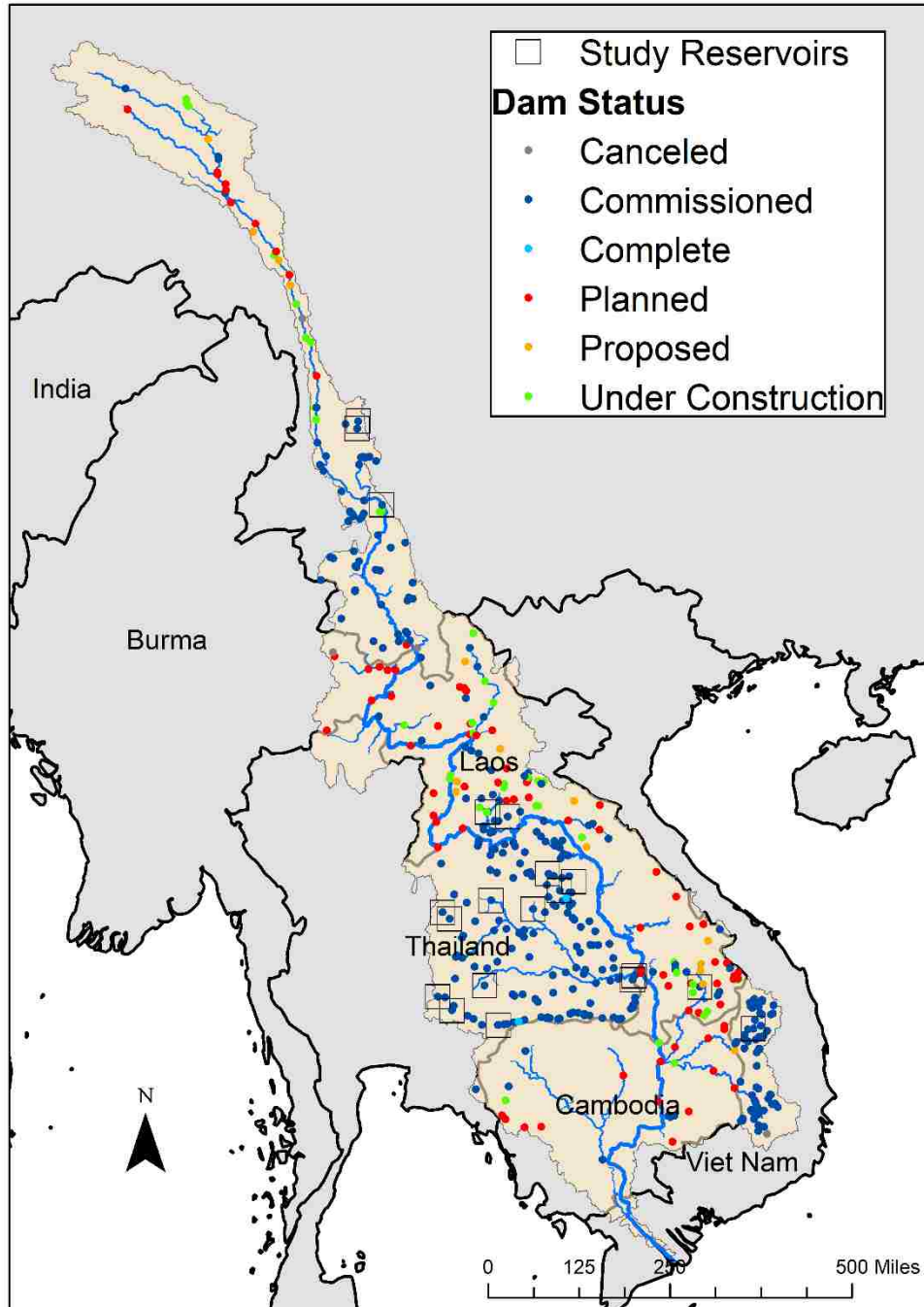
Figure 3.1. Map of Mekong River Basin with current and future dams (WLE 2017). The location of the 20 dams studied in this chapter are highlighted by boxes.

Table 3.1. List of dams examined in this study and their capacities and degrees of regulation

(Lehner et al. 2011)

Dam/Reservoir Name	Capacity [million m^3]	Degree of Regulation (%)
Haixihai	61.9	197.7
Zibihe	93.2	131.6
Manwan	920	3.2
Nam Ngum	7030	87.5
Nam Leuk	185	72.3
Nam Oun	520	70.4
Nong Han Lake	1873.9	155.6
Nam Pung	165.5	102
Ubol Ratana	2263	83.2
Lam Pao	1430	48
Chulabhorn	188	198.1
Huai Kum	22.8	15.7
Lam Chang Han	26	156.4
Lamtakhong	310	189.8
Lamphraphloeng	152	86.7
Lamnangrong	150	161.6
Pak Mun	229	0.7
Sirindhorn	1966	142.7
Houayho	596	395.6
Yali	1037	17.1

3.3 METHODS

3.3.1 *Residence Time*

The key ingredients for estimating residence time are derived from the mass balance equation explored in Chapter 2 (Equation 2.1), inflow (I), storage (S), and outflow (O). In Chapter 2, it was found that evaporation was several magnitudes smaller than the other terms and played relatively little role in the mass balance for a reservoir in a similar, tropical monsoon climate. In this chapter, evaporation is excluded, resulting in Equation 3.1, where I is inflow, O is outflow, and ΔS is the change in reservoir storage over a duration of time.

$$O = I - \Delta S \qquad (3.1)$$

With the water in reservoirs obeying mass balance, several basic assumptions can be made in order to simplify the calculation of reservoir residence time:

1. A water parcel which enter the reservoir over a specific duration does not mix with other water parcels within the reservoir.

2. Water parcels exit the reservoir in order from oldest to newest.

Note that this is equivalent to assuming the reservoirs behave as plug flow reactors. With these two assumptions, the length of time a parcel of water spends in the reservoir can be identified. Generally speaking, a monthly time step was used, so the residence time of the inflow entering a reservoir during one month is the amount of time until all of the water is released that was in the reservoir just after the monthly inflow parcel arrived. This is expressed by Equation 2, where t_0 denotes the time step of interest, $\theta(t_0)$ is the residence time of the water entering the reservoir at time t_0, and t_R is the time step in which the water that entered at time t_0 is released from the reservoir. This time of release is calculated by summing the amount of water exiting the reservoir

in each time step, O(t), beginning at t_0 and ending when the sum is equal to the volume of the

reservoir, $V(t_0)$ plus the amount of inflow, $I(t_0)$, at the time step of interest, t_0.

$$\theta(t_0) = t_R - t_0$$
$$I(t_0) + V(t_0) = \sum_t^{t_R} O(t) \tag{3.2}$$

To average residence time of a single reservoir across time, an inflow weighted approach was

used, as shown in Equation 3.3.

$$\theta_{t-avg,r} = \frac{\sum_{t=1}^{T} I_{t,r} \theta_{t,r}}{\sum_{t=1}^{T} I_{t,r}} \tag{3.3}$$

Where $I_{t,r}$ is the inflow to reservoir r at time t, $\theta_{t,r}$ is the residence time of reservoir r at time t, and

$\theta_{t-avg,r}$ is the time-averaged residence time of reservoir r over T time steps.

In order to estimate the collective effects of these reservoirs on the residence time of the

basin as a whole, a similar averaging technique was used, shown in Equation 3.4.

$$\theta_{b-avg} = \frac{\sum_{r=1}^{R} \left(\sum_{t=1}^{T} I_{t,r} \right) \theta_{t-avg,r}}{\sum_{t=1}^{R} \left(\sum_{t=1}^{T} I_{t,r} \right)} \tag{3.4}$$

Where θ_{b-avg} is the basin-average residence time over R reservoir and all other terms are as

defined previously.

3.3.2   *Flow Alteration*

Reservoir imposed flow alteration (FA) is defined here as the percent difference between I and

O. Substituting the mass balance between O, I, and ΔS (Equation 3.1), shows that this is

equivalent to the ratio between ΔS and I, shown in Equation 3.5.

$$FA = \frac{O - I}{I} = \frac{-\Delta S}{I} \tag{3.5}$$

Note that positive FA indicates streamflow was increased by reservoir operations and negative FA indicates streamflow was decreased by reservoir operations. When averaging FA across longer time scales, the result should be close to 0, due to the principle of mass balance employed here. Thus, to derive meaningful information about a reservoir's overall effect on downstream flow, the absolute value of FA is used when averaging. This averaging process is inflow weighted, similarly to residence time, shown in Equations 3.6 (time average) and 3.7 (basin average).

$$FA_{t-avg,r} = \frac{\sum_{t=1}^{T} I_{t,r} |FA_{t,r}|}{\sum_{t=1}^{T} I_{t,r}} \tag{3.6}$$

$$FA_{b-avg} = \frac{\sum_{r=1}^{R} \left(\sum_{t=1}^{T} I_{t,r}\right) FA_{t-avg,r}}{\sum_{t=1}^{R} \left(\sum_{t=1}^{T} I_{t,r}\right)} \tag{3.7}$$

where $FA_{t-avg,r}$ is the time-averaged flow alteration of reservoir r over T time steps, $FA_{r,t}$ is the flow alteration of reservoir r at time t, FA_{b-avg} is the flow alteration, is the basin-average flow alteration over R reservoir and all other terms are as defined previously.

3.3.3 *Reservoir Outflow*

To estimate reservoir outflow, the mass balance introduced in Chapter 2 was applied to each of the 20 reservoirs. Again, evaporation was excluded here based on the findings of Chapter 2. For inflow, a 0.1 degree resolution Variable Infiltration Capacity (VIC) Model of the MRB was employed (Liang et al. 1994). The model was constructed using land cover data from the Global Land Cover Characterization (GLCC) dataset and soil data prepared by the Harmonized World Soil Database (HWSD) (Loveland et al. 2000). Monthly leaf area index and albedo were provided by the Moderate Resolution Imaging Spectroradiometer (MODIS) mission and topography information was obtained from SRTM. The meteorological forcings such as temperature (minimum and maximum), wind speed and precipitation were obtained from 237

68

weather station records archived as Global Summary of the Day (GSOD) by National Climatic

Data Center (NCDC). This model was calibrated using streamflow observations from 13 in-situ

gage stations from 2003-2008. Validation of the calibrated model with data from the same gage

stations from 2009-2013 resulted in model bias ranging from -17.8% to 27.1% (Table 2). Figure

3.2 shows the fit of the calibration and validation for 4 of these stations, corresponding to the

error statistics shown in Table 3.2.

Table 3.2. VIC model calibration error statistics. Base represents the uncalibrated model
performance for 2003-2008, calibration represents the performance of the calibrated model
during the calibration period (2003-2008) and validation represents calibrated model
performance from 2009-2013.

Basin	Category	Bias (%)	NRMSE (%)	Efficiency	Correlation
Chiang Sean	Base	-52.6	70.6	0.64	0.80
	Calibration	-6.3	35.5	0.80	0.90
	Validation	8.6	42.5	0.57	0.87
Luang Prabang	Base	-37.2	63.1	0.69	0.84
	Calibration	6.6	37.5	0.84	0.92
	Validation	27.1	52.8	0.70	0.92
Vientiane	Base	-42.5	63.3	0.71	0.84
	Calibration	-4.8	35.3	0.84	0.92
	Validation	15.3	41.3	0.78	0.92
Nakhon Phanom	Base	-21.1	63.3	0.71	0.84
	Calibration	-29.3	52.4	0.78	0.93
	Validation	-17.8	36.3	0.88	0.95
Pakse	Base	-18.6	63.3	0.71	0.84
	Calibration	-3.2	38.7	0.86	0.93
	Validation	8.0	34.2	0.89	0.95
Kampong Cham	Base	-12.9	63.3	0.71	0.84
	Calibration	-16.7	45.3	0.84	0.93
	Validation	-4.3	40.9	0.85	0.92
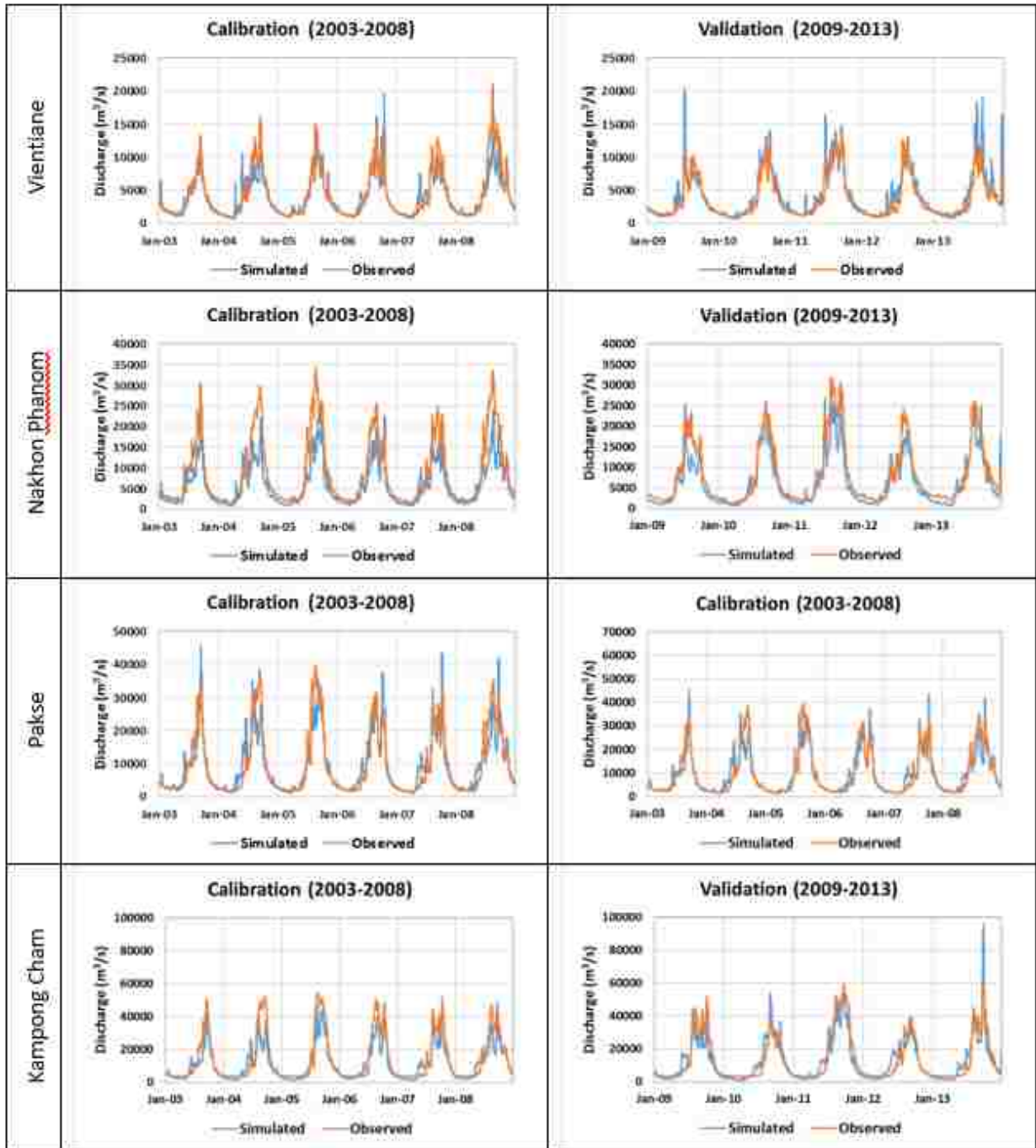
Figure 3.2. Calibration and validation of VIC model at four selected streamflow gaging stations on the main stem of the Mekong River. Note: the calibration and validation was carried out at all the streamflow locations shown in Figure 3.1, but only a sample of 4 locations are shown herein.

This model was run at the daily time step from 2002 through 2015 (14 years), providing surface water fluxes for each 0.1 degree grid cell. These modeled fluxes were then re-gridded to

0.01 degree resolution, because 0.1 degree cells did not properly resolve the correct stream channels feeding into the reservoirs. The re-gridding was performed by assigning all 0.01 degree cells the value of the 0.1 degree cell containing them. These fluxes were then run through a streamflow routing model of the basin to obtain daily inflow into each reservoir (Lohmann et al. 1996). The re-gridding was necessary to simulate reservoir inflow at the appropriate resolution because some of the reservoirs are built on smaller rivers that would not appear in 0.1 degree resolution topography. The routing model used estimates of surface runoff from the VIC model and routed this water to river channels according to input topographical information. The daily flows were then aggregated into average monthly inflow. The upper panel of Figure 3.3 shows monthly averaged basin precipitation and basin outflow at the MRB delta (i.e. the basin outlet), averaged across the entire 2002 through 2015 time period. Precipitation and outflow are both seen to increase from May through September, decrease from September through December, and then remain stably low from January through April. This pattern is fairly representative of the local inflow behavior at each reservoir, with the exception that lag between precipitation and inflow being much shorter than 1-2 months for smaller basins. The lower panel of Figure 3.3 shows the annual average basin precipitation and basin outflow from 2002 through 2015. A point to note is that the VIC model represents natural stream flows and does not take the effects of reservoir operations into account. Therefore, the inflow of reservoirs downstream of other reservoirs was adjusted according the outflow of each upstream reservoir.
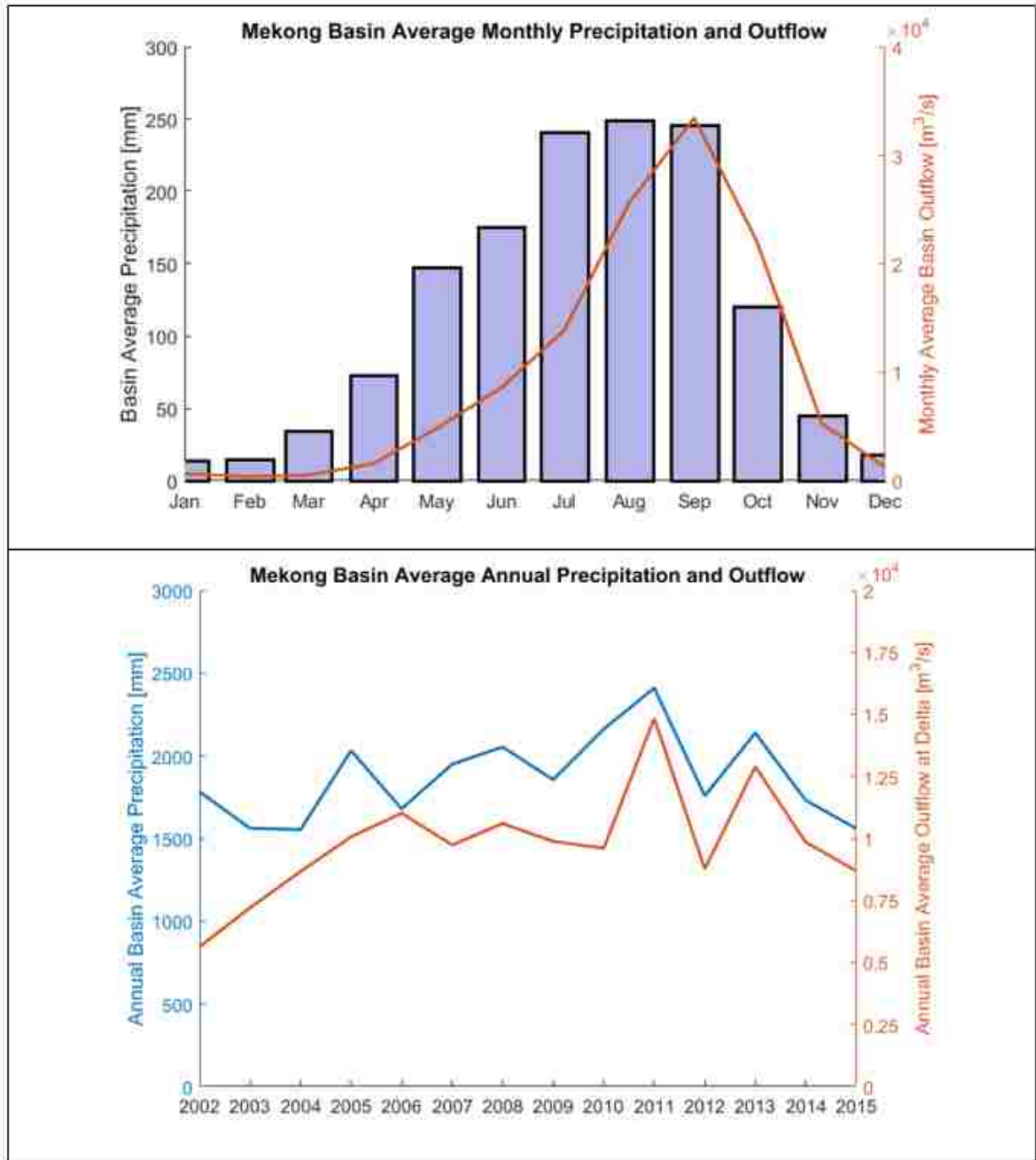
Figure 3.3. Monthly averaged basin precipitation and outflow at the MRB delta from VIC model (top) and annual average basin precipitation and outflow at delta from 2002 through 2015 from VIC model (bottom).

3.3.4   *Reservoir Storage*

Unlike the reservoirs in Chapter 2, a majority of the 20 reservoirs examined in this chapter do not lie under a radar nadir altimeter path. Therefore, the method used in Chapter 2 was adapted to work with a different kind of satellite measurement, visible and near infrared imagery. The methodology follows a three-step process similar to the approach explored in Chapter 2. First, a relationship between reservoir surface area and elevation was established for each reservoir. This relationship is derived from SRTM DEM in the exact manner described in Chapter 2. Next, the area-elevation curve was used to convert satellite measurements of either water surface elevation or surface area into reservoir volume (known as the area-volume curve). Finally, a monthly operations curve (i.e. operating policy) was established from a long record of satellite observations and used to fill gaps in the satellite record. Each of these processes is described in greater detail below.

The volume of a reservoir is then computed using either radar altimetry-based water surface elevations or spectral (visible) band-based water surface area from Landsat. The Sirindhorn Reservoir is the only reservoir of the 20 examined here that is observed by a satellite altimeter. For this reservoir, elevations obtained from the Jason-2 satellite altimetry mission were used. Using the area-elevation curve, the reservoir surface area corresponding to the observed elevation was identified. For all other reservoirs, Landsat images were used to estimate reservoir surface area. Specifically, the normalized difference water index (NDWI) was used to classify water pixels from 30 m resolution Landsat spectral images (McFeeters 1996). This method identifies which pixels of a Landsat image likely contain water by calculating the NDWI for each pixel, according to Equation 3.8:

73

$$NDWI = \frac{X_{green} - X_{nir}}{X_{green} + X_{nir}}$$ (3.8)

Where X_{green} and X_{nir} are the reflectance values in the green and near infrared wavelengths, respectively. The green wavelength corresponds to Band 3 from Landsat 8 and Band 2 from Landsat 4,5, and 7. The near infrared wavelength corresponds to Band 5 from Landsat 8 and Band 4 from Landsat 4,5, and 7. Pixels with NDWI greater than 0 were classified as water pixels and pixels with NDWI less than 0 were assumed to not contain surface water (McFeeters 1996). The surface area of the water pixels is then the estimate of the reservoir surface area at the time of the Landsat overpass. Again, using the area-elevation curve, the corresponding water surface elevation was identified.

With both water elevation and surface area known, the volume of the reservoir can be computed by estimating the volume of water required to fill the reservoir to the storage capacity listed in the GRanD Database (Huilin Gao, Birkett, and Lettenmaier 2012). This is done using a trapezoidal approximation (Equation 3.9), where *V* is the volume of the reservoir, *A* is the reservoir surface area, *h* is the reservoir elevation and the subscript *c* denotes these quantities at reservoir capacity.

$$V = V_c - (A_c + A)(h_c - h)/2$$ (3.9)

A significant issue with building a time series of reservoir surface areas with Landsat images is the potential for unusable images due to cloud cover, which can lead to long temporal gaps in data. This was overcome here by employing a method similar to the approach outlined in Yoon and Beighley (2015). Here, the assumption is made that reservoirs are operated at a relatively stable level on a sub monthly scale and when looked over a long record, variability of reservoir operation at sub-monthly scales remains within a narrow range. This is a fairly realistic

assumption as most reservoirs strive to follow the rule curve and make release and storage decisions according to a pre-defined standard operating procedure (SOP).

The reservoir volumes estimated from the entire record of Landsat images were thus grouped by month and the average reservoir volume for each month was calculated. This formed an approximation of the reservoir operations curve. This process is illustrated by Figure 3.4. The utilization of green and NIR Landsat bands to estimate water surface is depicted in the upper panels and the derivation of the area-elevation curve is shown in the lower left panel. A single water surface area estimate, when paired with the area-elevation curve, led to a single point on the operations curve in the lower right panel. With a long record of Landsat images, the average reservoir volume for each month can be estimated. This monthly average is the approximation of the operations curve, which was then used to fill gaps in the time series of reservoir volume generated from Landsat images. For each monthly time step where no cloudless Landsat image exists, reservoir volume from the approximated operations curve was used. The operations curve was completely disregarded in favor of Landsat based volume estimates, when available. Figure 3.5 shows the fraction of months without any usable Landsat images from 2002 through 2015, averaged across all reservoirs, as well as the range of unobserved months of all reservoirs. Unsurprisingly, the months with the least amount of usable Landsat images occur when precipitation is the highest (see Figure 3.3).
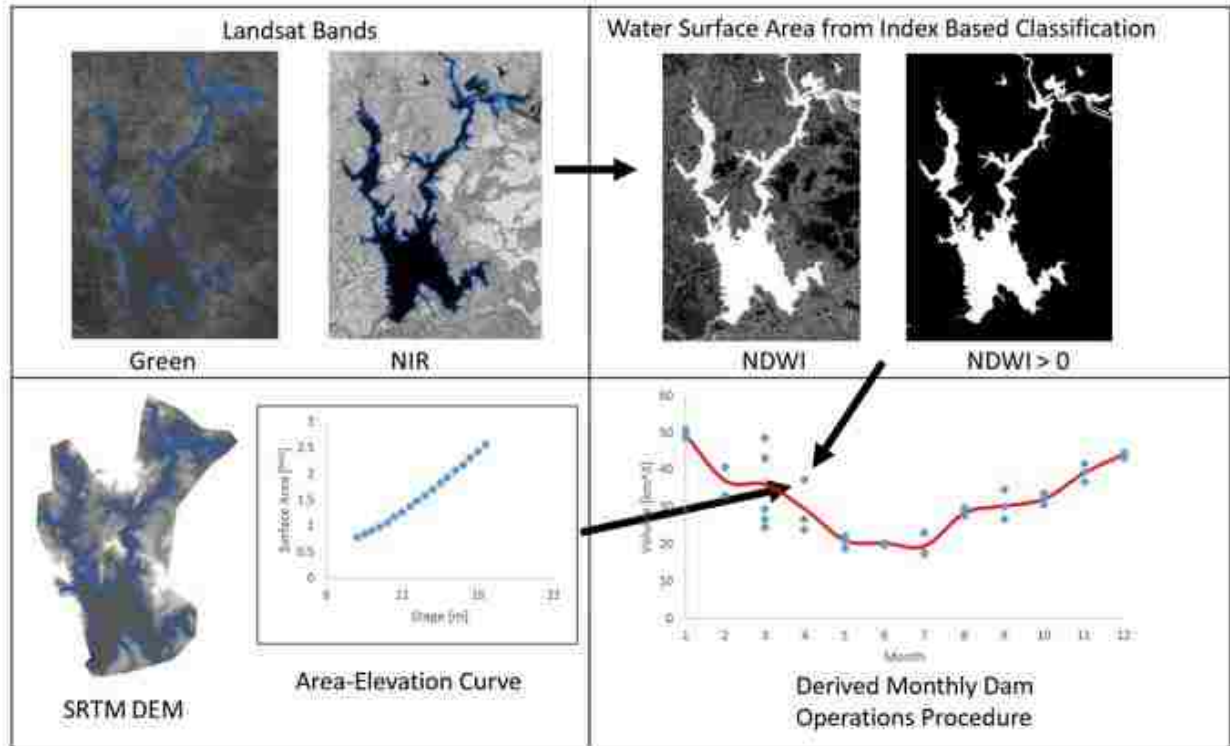
Figure 3.4. Flow chart depicting process of approximating reservoir operations curve. Upper left panel shows the green and NIR Landsat bands. Upper right panel shows the Normalized Difference Water Index (NDWI) and the classified water pixels. Lower left panel shows an area-elevation curve and the SRTM 30m DEM it was derived from. Lower right panel shows the derived operations curve (monthly averages of reservoir volume). A single point on the curve is the result of the combination of one NDWI classified image with the area-elevation curve.
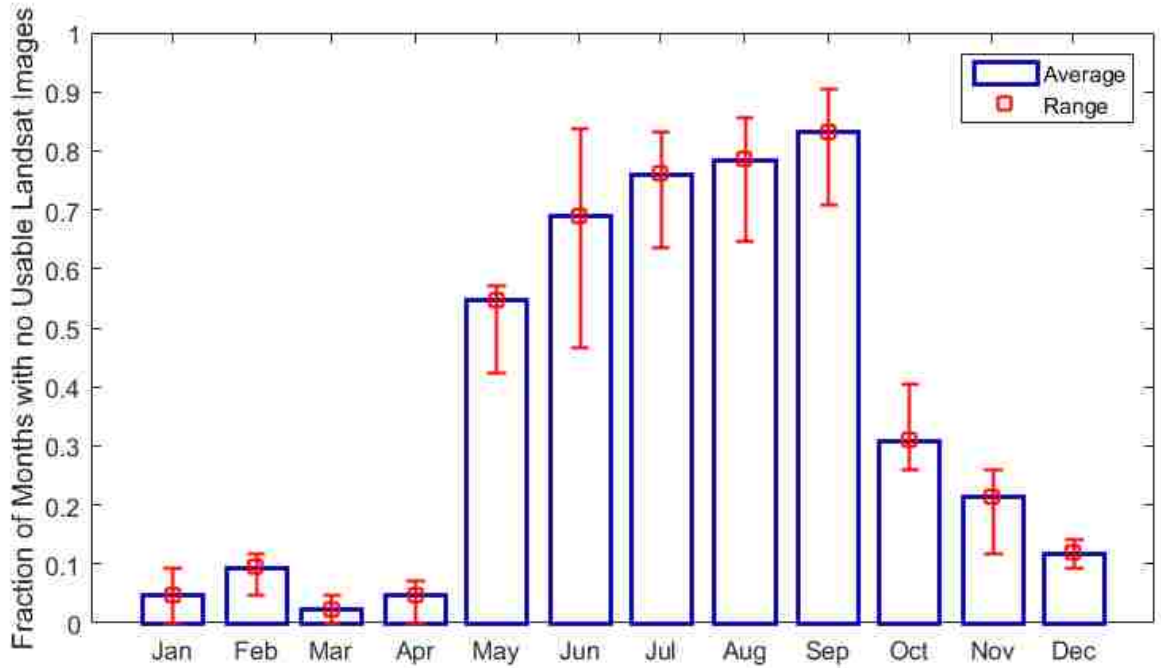
Figure 3.5. Average and range of fractions of months with usable Landsat observations, by month over the 14 year period.

Reservoir outflow was estimated using the same mass balance described in Chapter 2, excluding evaporation (Equation 3.1) As previously stated, these outflows were used to correct the inflows of downstream reservoirs. Since the routing model conserves water in the river network, the downstream inflows are adjusted by the amount of total storage change in upstream reservoirs (Equation 3.10) where I_{adj} is the adjusted inflow, I is the natural inflow (modeled by VIC), and ΔS_{up} is the storage change of upstream reservoirs.

$$I_{adj} = I - \sum \Delta S_{up} \tag{3.10}$$

3.4 RESULTS AND DISCUSSION

3.4.1 *Validation of Satellite Based Volume Estimates*

There are several limitations in the satellite based approach employed here, such as long sampling frequency (relative to ground based approaches), interference from clouds and other atmospheric effects, and uncertainties associated with deriving water surface area from spectral data. Thus, validating these methods to ground based measurements is essential. The top panel of Figure 3.6 shows reservoir volumes estimated by ground observations (in-situ), altimeter water height data, Landsat surface area and derived operations curve for the Sirindorn reservoir. Comparison between the altimeter and in-situ volumes and taking the ground observed value as the true volume results in a root mean squared error (RMSE) of 0.27 km^3, which is 19% of the average reservoir volume in this time period. Similarly, comparisons between the Landsat and in-situ volumes agree to within 20% of RRMSE. This indicates that the altimetry and Landsat based methods of estimating reservoir volume are both successful (within a 20% error range) in capturing the month-to-month reservoir volume fluctuations. Furthermore, when the in-situ observations were used to estimate residence time, the resulting residence times agreed with altimeter and Landsat derived residence times to within 15% and 17% RRMSE, respectively.
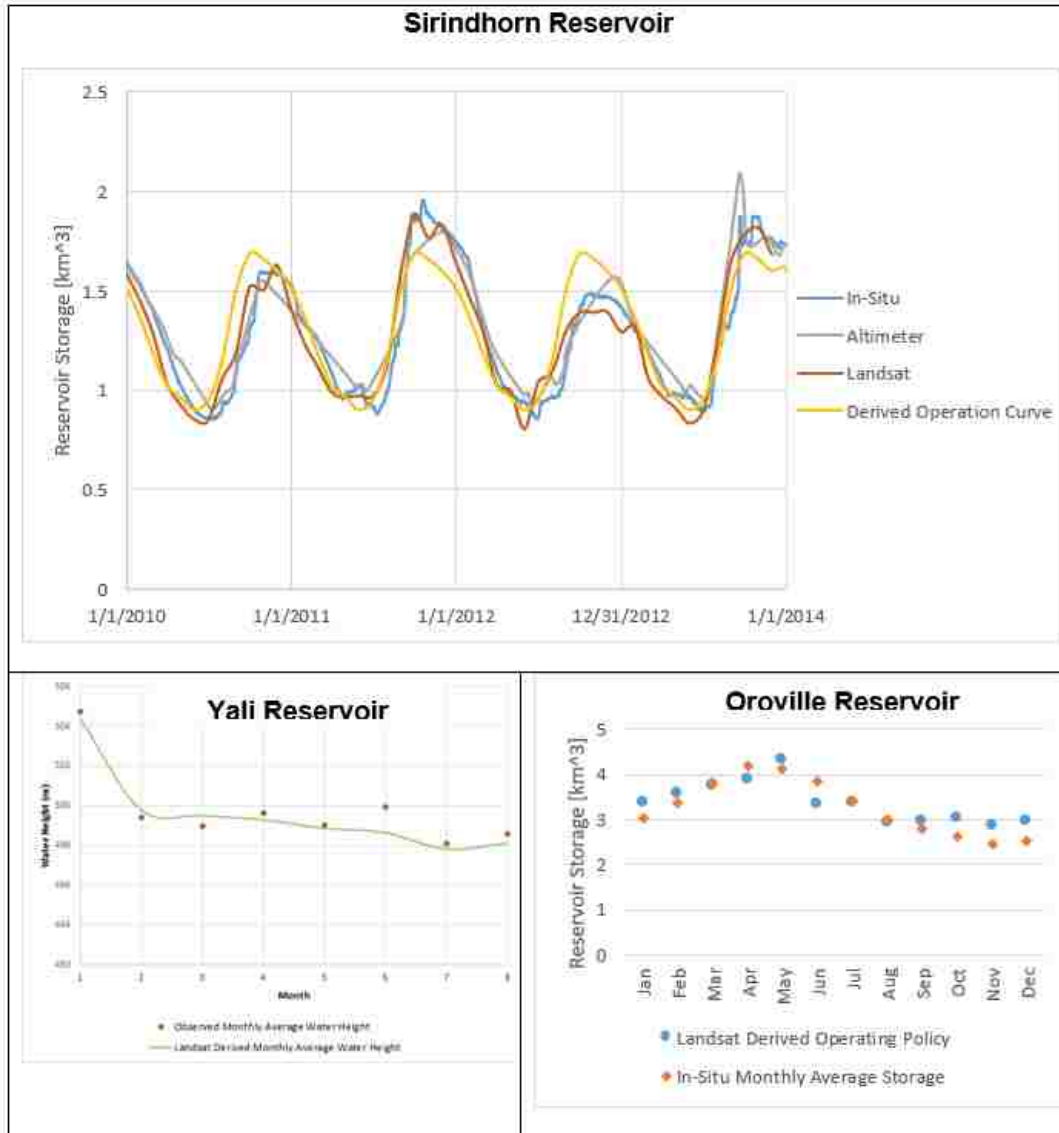
Figure 3.6. Comparison between ground observed, altimeter derived, Landsat derived, and approximated operating policy estimated reservoir volume for the Sirindhorn Reservoir (top), comparison between observed monthly average water height and Landsat derived water height for the Yali Reservoir for 8 months in 2016 (bottom left), and comparison between Landsat derived operating policy and in-situ monthly average storage of the Oroville Reservoir (bottom right).

Due to the linear relationship between flow alteration and storage, a 19% RRMSE in altimeter based volume results in 19% RRMSE in FA and 20% RRMSE in Landsat volume results in 20% RRMSE in FA. Comparison between volumes estimated from the derived monthly operations curve and the in-situ resulted in 32% error. While this is substantially worse than Landsat or altimeter methods, it is important to note that this method is only employed at times when Landsat data is unavailable, primarily occurring during the wet season. Based on the results from the Sirindhorn Reservoir, this would result in an overestimation of storage during wet seasons. Such overestimations would lead to underestimations of wet season outflows, potentially increasing flow alteration and leading to longer residence times. Subsequently, overestimations of wet season storage would increase flows during the transition from wet to dry season, which would decrease flow alteration and residence time.

Unfortunately, the Sirindhorn Reservoir is the only reservoir studied here that was overpassed by a satellite altimeter to provide skillful height variations. Nevertheless, the close agreement between satellite-based volume and the in-situ volume established a good level of trustworthiness in our comprehensive satellite-based approach that synthesizes multiple platforms for other reservoirs of the MRB. The lower left panel of Figure 6 compares the actual monthly water level elevations of the Yali Reservoir to elevations derived from the visible Landsat images. This Landsat derived water surface elevations exhibit an RMSE of 0.57 m, which is 8.6% of the range in actual water surface elevations observed during this time period. The lower right panel of Figure 6 shows a comparison between a Landsat derived operations curve and the average monthly volume of the Oroville reservoir from 2010 to 2016. These two monthly averaged volumes agree to within 17% RRMSE and compares well with the well-known design rule curve of Oroville dam. Overall, these results signify that both the Landsat

80

based method and the altimeter-based method are certainly capable of accurately estimating water surface heights and consequential volume changes. These results also demonstrate the skill of average operating policy estimation and its usefulness to estimate volume when no other sources of data are available.

3.4.2   *Reservoir Residence Time and Flow Alteration*

Figure 3.7 shows the average and range of the estimated reservoir operations curves, normalized by their maximum storage so that comparisons can be made between reservoirs of different volumes. While there is variation among the different reservoirs, as evident by the large range, a dominant trend can be gleaned, of higher volume at the beginning of the dry season, followed by decline into the wet season. At the end of the wet season, the reservoirs fill again. This trend is highlighted by the average normalized operations curve which is shown in black.
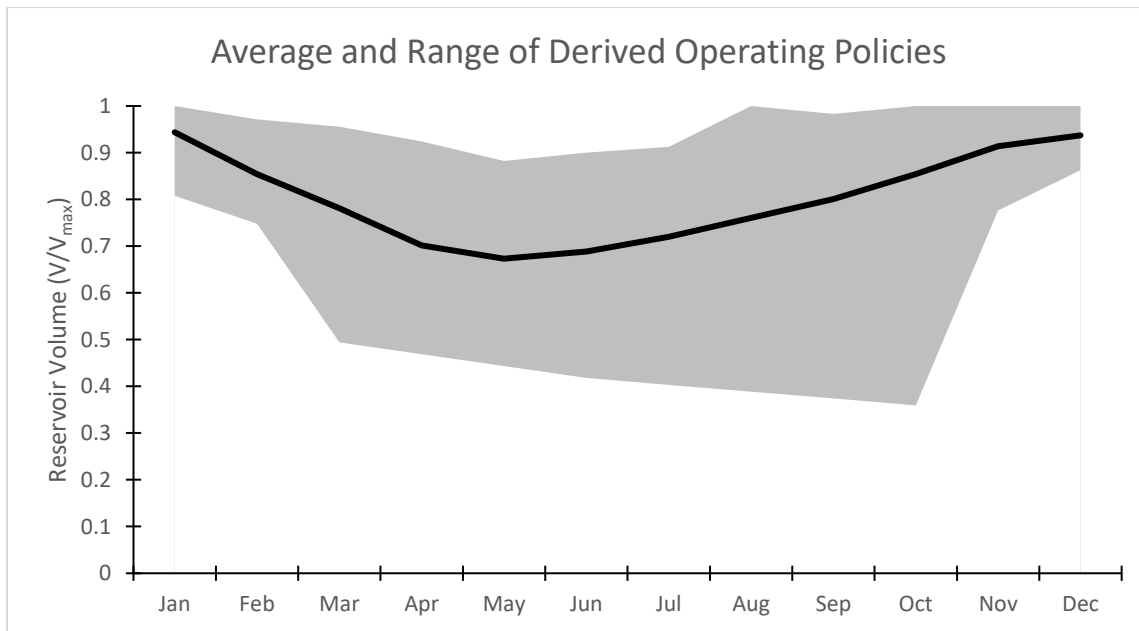
Figure 3.7. Average and range of derived reservoir operations curves (i.e. 'effective') for all reservoirs, normalized by reservoir maximum volume. Average shown in black.

Figure 3.8 displays how the resulting residence times are distributed throughout the MRB. Figure 3.8 also shows the resulting average absolute flow alterations for each reservoir in the MRB. These residence time and FA values are also shown in Table 3.3 broken down as a function of season: wet season (June through October) and the dry season (November through May). Residence times ranged from 0.09 years to 4.04 years and FA ranged from 11% to 131%. Note that the overall average FA is the average of the magnitudes of monthly FA, while the wet and dry season FA preserved the sign, in an attempt to characterize the nature of the flow alterations. FA was largely negative in the wet season and positive in the dry season, reinforcing the trend exhibited by the operations curves. Reservoirs with low residence time also exhibited low FA.
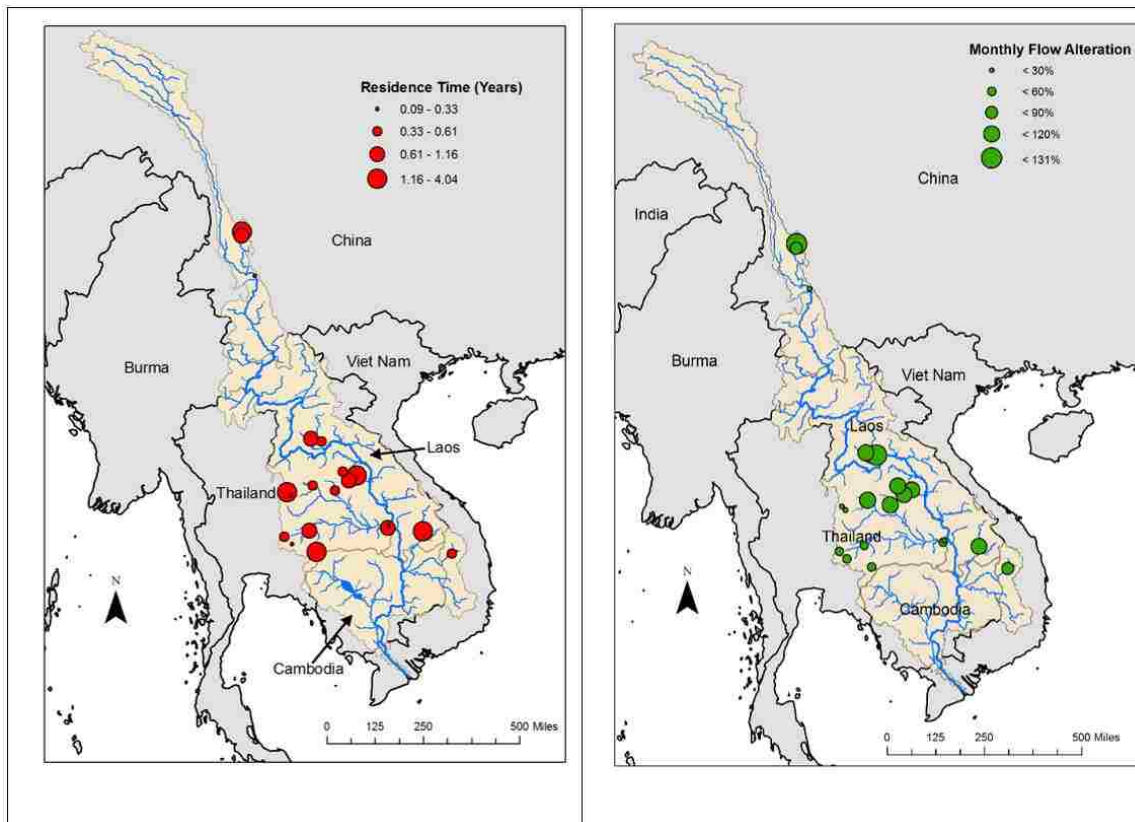
Figure 3.8. Map displaying the residence time (left) and flow alteration (right) of reservoirs in the Mekong Basin.

Table 3.3. Estimated overall and seasonal residence time and flow alteration for each

reservoir

Dam Name	Overall Residence Time (yr)	Dry Season Residence Time (yr)	Wet Season Residence Time (yr)	Overall Absolute FA (%)	Dry Season FA (%)	Wet Season FA (%)
Haixihai	2.07	2.08	2.05	131.0	142.6	-81.1
Zibihe	1.15	1.15	1.13	72.6	65.9	-26.5
Manwan	0.12	0.18	0.07	17.2	16.2	
Nam Ngum	1.16	1.18	1.15	108.2	56.3	-36.3
Nam Leuk	0.58	0.59	0.45	125.4	114.1	-96.1
Nam Oun	0.61	0.63	0.57	99.2	103.5	-58.0
Nong Han Lake	2.33	2.35	2.32	118.2	1.6	-31.0
Nam Pung	0.95	1.05	0.93	106.9	7.5	-31.6
Ubol Ratana	0.56	0.61	0.50	112.3	25.5	-24.6
Lam Pao	0.53	0.53	0.43	101.9	47.8	-21.6
Chulabhorn	2.08	2.09	2.05	26.2	40.1	-4.1
Huai Kum	0.22	0.30	0.21	11.1	20.6	-.05
Lam Chang Han	0.89	0.92	0.84	39.3	57.3	-2.1
Lamtakhong	0.58	0.59	0.49	50.8	24.2	-5.4
Lamphraphloeng	0.33	0.33	0.33	57.1	3.9	-.05
Lamnangrong	1.94	1.96	1.93	48.5	21.7	-4.7
Pak Mun	0.09	0.25	0.06	11.5	12.3	-1.2
Sirindhorn	0.96	1.04	0.91	58.4	61.7	-15.4
Houayho	4.04	4.05	3.98	99.7	15.6	-4.6
Yali	0.44	0.66	0.38	74.6	10.4	-18.5

Figure 3.9 shows a comparison between the residence time estimated in this study and the

DOR estimated in the GRanD Database. DOR was estimated in Lehner et al. (2011)by dividing

reservoir capacity by long term average annual inflow. It should be noted that the time frame

from which this average annual inflow represents is different from the time frame examined in

this study. DOR is essentially the reservoir capacity expressed as a percentage of the annual

average inflow, and is similar to residence time, as calculated using a similar method than the

one employed here. Thus, it is a good point of comparison for the resulting residence times from

this study. Figure 3.9 presents DOR as the number of years of inflow which can be stored within

a reservoir. This figure shows some agreement between the simple to obtain DOR and the temporally varying approach employed here, however other reservoirs show significant differences. No correlation between the capacity, stream order, or reservoir use could be established that would explain this difference, although a larger sample size of reservoirs could provide greater clarity.
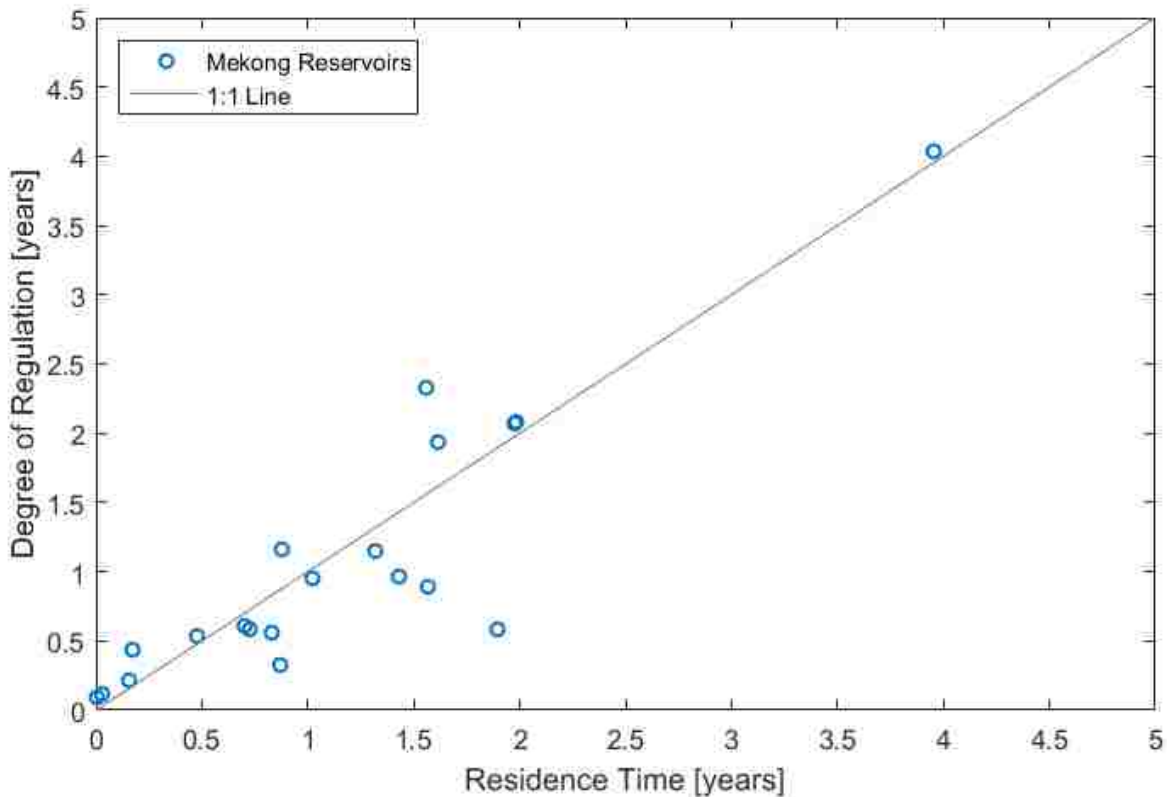
Figure 3.9. Comparison between residence time estimated in this study and degree of regulation (DOR) from the GRanD Database. Here, DOR is the reservoir capacity expressed in years of average annual inflow. 1:1 line shown in grey.

As seen in Table 3.3, residence time was typically larger during dry season than wet season. This agrees with what is known about seasonal variations in stream flow and reservoir operations. Figure 3.7 illustrates the typical seasonal trend observed in reservoir volume, where

reservoirs are kept low during the start of the wet season and allowed to fill towards the end of the wet season. This is followed by high reservoir volume in the beginning of the dry season, as reservoirs are then being used to store water and release it in a controlled fashion throughout the wet season. The low inflows in the dry season led to a decrease as water is discharged for irrigation, water supply or hydropower generation. It is this long, slow release of water in the dry season that causes residence time to increase. Similarly, the rapid outflows and lower volume combined in the wet season lead to lower residence time. Figure 3.10 plots the average monthly residence time of all reservoirs, each normalized by the reservoir's average residence time. This plot further elucidates the seasonal trend in residence time.
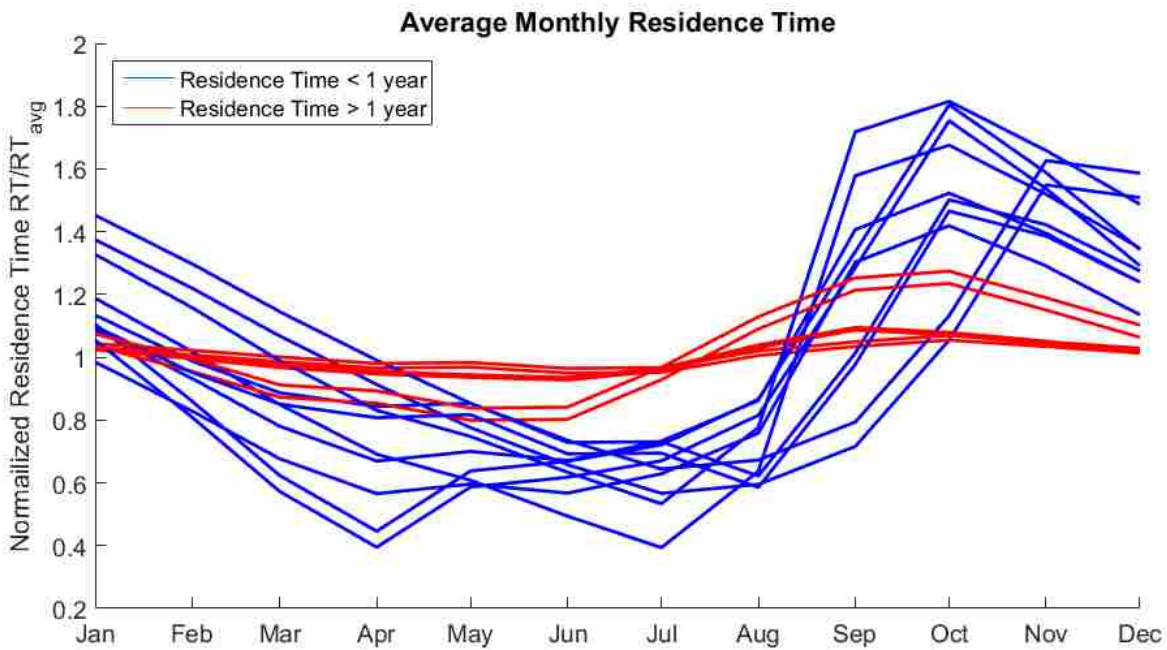
Figure 3.10. Average monthly residence time for each reservoir, normalized by each reservoir's average residence time. Reservoirs with residence time less than 1 year are shown in blue. Reservoirs with residence time greater than 1 year are shown in red.

It also reveals that reservoirs with higher average residence time exhibit less seasonal fluctuation in residence time (reservoirs with residence time greater than 1 year are shown in red in Figure 3.10). Similarly, reservoirs with lower average residence time have more pronounced seasonal variations than reservoirs with higher residence time. A likely explanation for this pattern is that these reservoirs in the MRB with higher average residence time tend to have higher storage capacity relative to their inflow. This indicates that such reservoirs would be inherently less sensitive to fluctuations in inflow, resulting in a more consistent residence time. For example, water entering the Houayho Reservoir is estimated to stay within the reservoir for approximately 4 years before being released. This water resides in the reservoir over the course of multiple wet and dry seasons, dampening the seasonal trend described earlier. In contrast, water entering the Sirindhorn Reservoir is only estimated to stay in the reservoir just under 1 year, resulting in single seasons or months have more of an effect on residence time.

Figure 3.11 shows the yearly average residence time for each reservoir from 2002 through 2015, grouped by average residence time. Note that since the method employed here estimates residence time by following a parcel of water from reservoir entry to exit, it is incapable of estimating residence time of parcels which do not exit reservoirs within the time period. For this reason, reservoirs with higher residence time do not have residence time estimates for the entire time period. While there are some variations among the reservoirs, there are also clear trends. Most reservoirs experience rises in residence time in 2009, 2012, and 2014. Normalizing theses residence times by reservoir averages, averaging across all reservoirs, and plotting with precipitation reveals a possible source of these yearly fluctuations. Figure 3.11 also shows basin averaged precipitation, revealing a negative relationship between average annual precipitation and basin averaged residence time, where residence time increases when

86

precipitation decreases. Similarly, residence time decreases when precipitation increases. This trend is made evident by a correlation coefficient of -0.65 between annual average precipitation and annual basin averaged residence time. Logically, when there is more water in the river system, reservoirs typically have higher releases, which lead to lower residence times. Conversely, when there is less water in the river system, inflows and outflows are lower, leading to higher residence time. Additionally, in drier time periods, reservoirs may be operated in such a way to withhold more water than usual to provide additional security in water supply for the uncertain future.
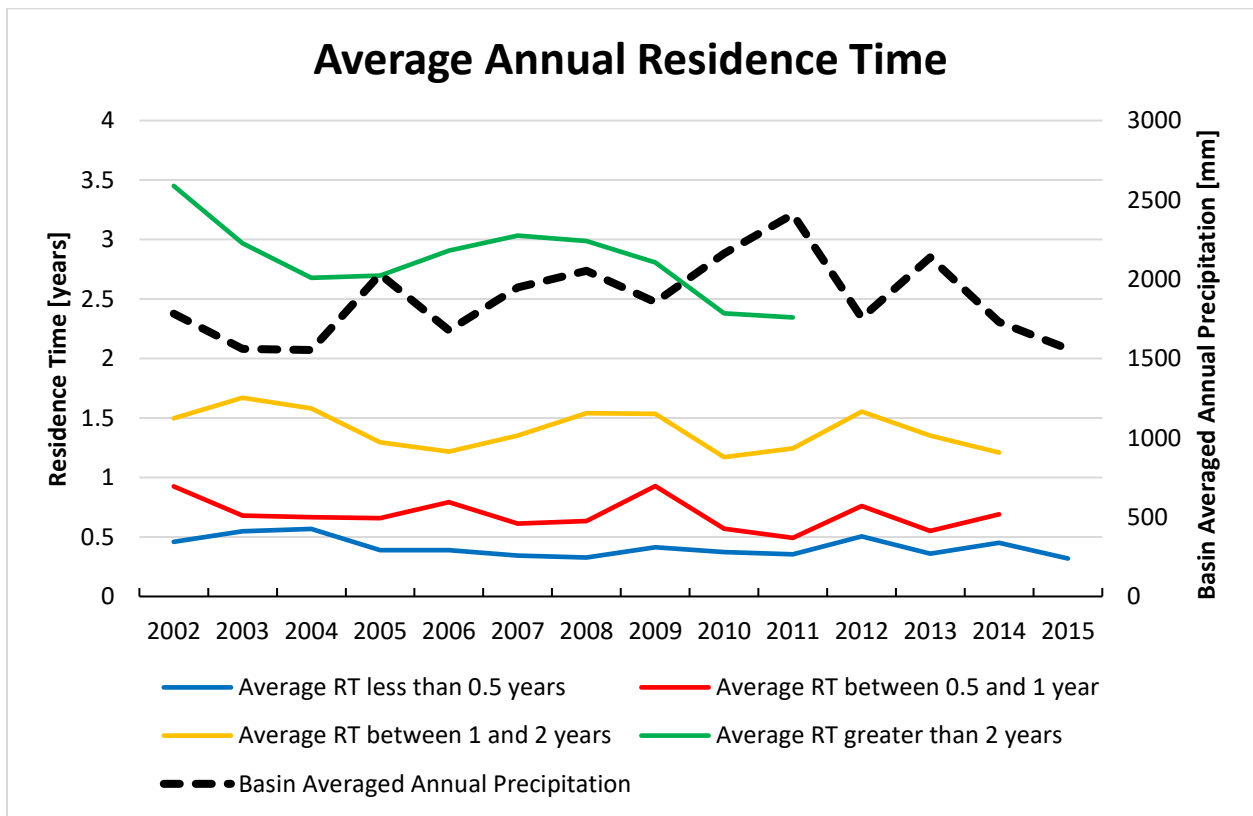
Figure 3.11. Average annual residence time, grouped by residence time ranges and plotted with basin averaged annual precipitation. Each colored line represents the average annual residence time of all reservoirs with average overall residence time within the listed range.

87

Figure 3.12 shows the monthly average variation of flow alteration and the range of monthly averages across all reservoirs. This plot highlights the high variability in FA among the reservoirs in the MRB, particularly in transitional months between dry and wet seasons. In November for example, nearly half the reservoirs exhibit high positive FA and the other half exhibit high negative FA. These patterns do not correlate with size, location or reservoir function, indicating that accurately predicting these alterations is difficult without direct observations of storage change. Figure 3.13, showing the yearly average FA grouped by overall average FA, exhibits similar variability. While year to year variations largely remain consistent for low FA reservoirs, a sharp decrease in FA of all reservoirs with average FA greater than 80% during 2008. The exact cause of this is unknown. Examination of reservoir volume reveals that reservoirs delayed in filling slightly longer in the 2008 wet season than in other years, resulting in part of the wet season flows to release more freely. It is unclear at this time why this trend is only present in the more impactful reservoirs.
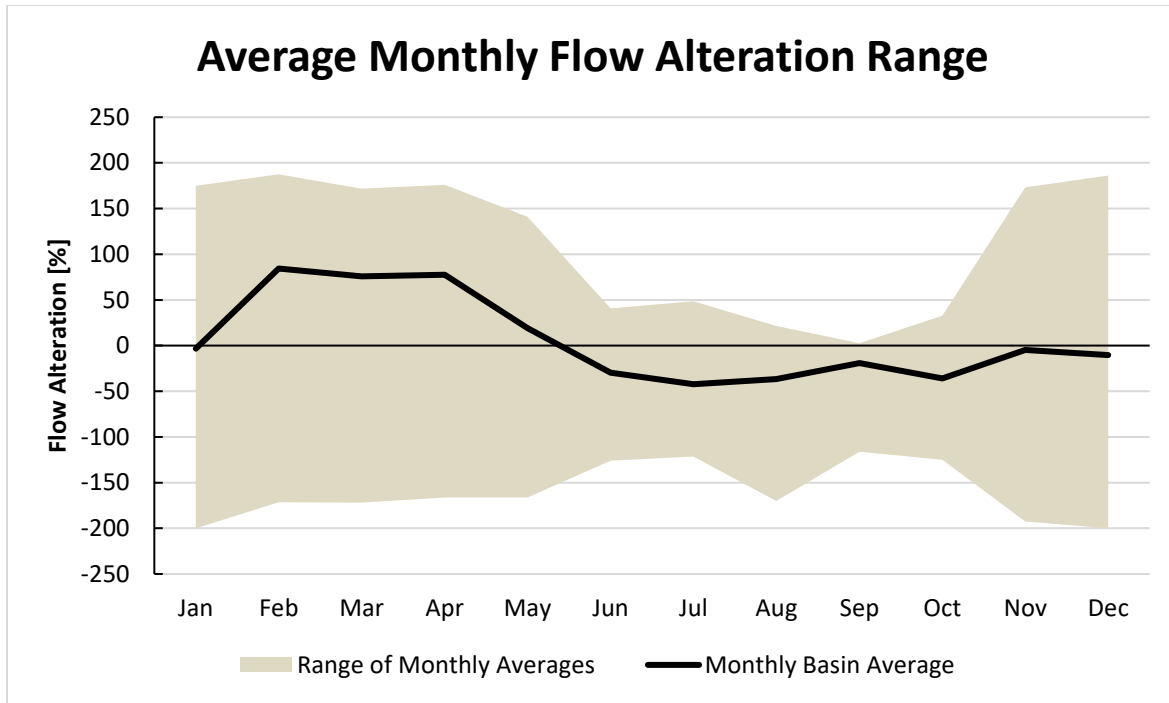
Figure 3.12. Average monthly flow alteration across basin and range of values from individual reservoirs.

Average Annual Flow Alteration
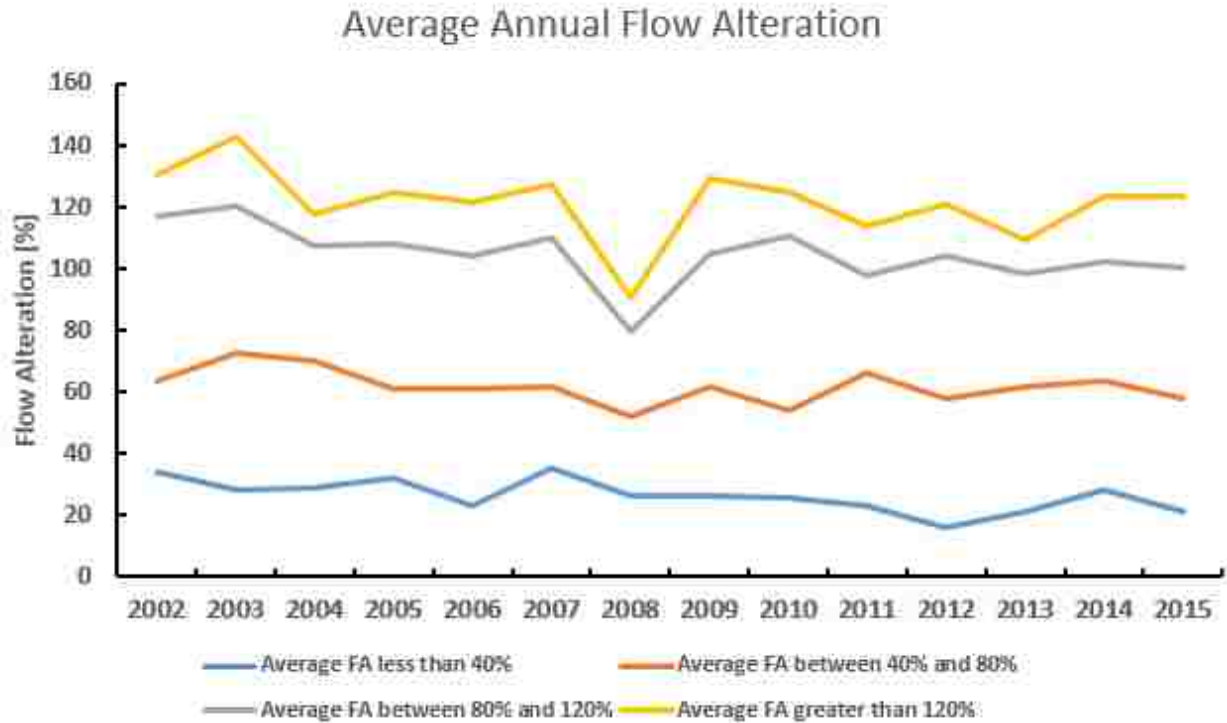
Figure 3.13. Annual average flow alteration, grouped by flow alteration ranges. Each line represents the average annual FA of all reservoirs with overall average FA within the specified range.

    One issue associated with the method of filling data gaps using the derived operations curve is that the temporal trends in reservoir storage may be dampened by the temporal trends exhibited by the reservoir operations curve. During larger temporal gaps in useable Landsat images, this would result in the operating policy prescribing its own temporal variability to a time period where the temporal variability is unknown. This is most concerning in the wet season, when the number of useable Landsat images is significantly lower (Figure 3.5). However, based on the results of the Sirindhorn Reservoir (Figure 3.6), it is only the magnitude of storage that appears erroneous, and not timing, resulting in preserved monthly trends. This mechanism would seek to dampen annual variability, particularly in wet season storage. However, the fact that such drastic annual variability is present in flow alteration and that

90

patterns emerge which appear independent from inflow variations (such as the decrease in annual FA in 2008), suggests that a fair amount of the temporal patterns in storage fluctuation are captured in spite of potential temporal dampening.

Figure 3.8 qualitatively suggests that reservoir residence time is equally distributed across the basin and there appears to be no correlation between reservoir location and residence time. While this may be the case, the location of the reservoir within the river network plays an important role in the overall effect of the reservoir on basin residence time. Considering the Mekong basin as a whole, the reservoirs studied here caused an average increase in the length of time water spends in the river network by only 3 weeks (0.059 years). When considering only the portion of the overall flow that is regulated by these reservoirs (totaling 17% of basin runoff), the average increase in residence time rises to just over 4 months (0.35 years). Most of the regulated discharge passes through two reservoirs, the Manwan Reservoir on the main stem of the Mekong in China and the Pak Mun Reservoir on the Mun River, a major tributary of the Mekong in Thailand. While neither of these reservoirs are particularly small, they both experience significantly large flows, leading to the extremely short residence times observed in this study. Because of their low residence times, their impact on the overall residence time of the basin is limited. If these dams are excluded, and only regulated discharge from higher order rivers is considered, the average increase in residence of this discharge becomes 1.3 years. This flow only makes up 3.5% of the total basin discharge, so while these reservoirs have little impact on the basin as a whole, they do have significant impact on local hydrology, specifically, on lower order streams within the river network. These results are similar to the conclusions drawn by Grill et al. (2014), in which the most severe reservoir impacts on streamflow occur in higher tributaries.

91

These impacted waters are diluted as they join flow from unregulated streams, resulting in little impact on the main stem.

Similarly, examining the reservoir's collective impact on MRB outflows at the delta revealed that they have little effect on river basin flow, with an average flow alteration of just 5%. Reducing the scope to only rivers regulated by these reservoirs, the average flow alteration increases to 23%. Removing the Manwan and Pak Mun Reservoirs, which also have the lowest flow alteration, results in an average flow alteration of 89% across the remaining regulated rivers.

The role of stream order is further explored in Figure 3.14, where residence time is plotted against stream order for the Mekong reservoirs studied here, as well as for all reservoirs in the GRanD Database and the average of each stream order. GRanD Database reservoir residence time was taken as their DOR expressed in years. Note that there are some reservoirs in the GranD database with residence times higher than 5 years. These were excluded from the plot so that the Mekong reservoirs could be compared with the global situation in better detail. The averages shown include reservoirs beyond the extent of the plot, but exclude database entries labeled as fair or poor quality. There is a clear negative trend between residence time and stream order in the global set of reservoirs from GranD, which appears to be mirrored in the Mekong reservoirs. This trend suggests that the most impactful reservoirs in terms of residence time increase tend to be built on lower order rivers. However, higher order reservoirs impact a larger amount of flow. As stream order increases, so does river flow and it becomes increasingly difficult or infeasible to build a reservoir that retains water for long periods of time under such high flows. Greater control of smaller flows in lower order streams can be imposed by smaller reservoirs that can be more feasible to build.
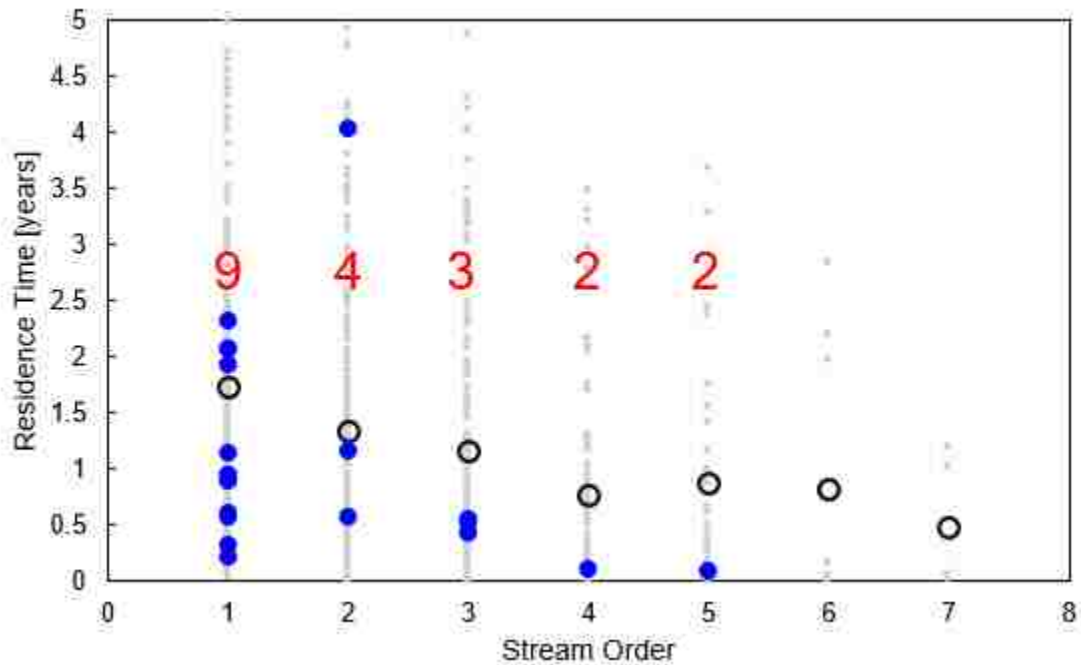
Figure 3.14. Stream order versus residence time for the MRB reservoirs as well as all GRanD Database reservoirs and their averages by stream order. GRanD Database residence time taken as the DOR expressed in years. The red numbers signify the number of MRB reservoirs in each stream order.

3.5   CONCLUSIONS

This chapter utilized an array of remote sensing data to observe the operations of reservoirs in the MRB. These reservoir operations were then paired with a hydrologic model and used to derive the impacts these reservoirs have on the streamflow. These impacts were characterized by two parameters: residence time as a measure of how long reservoirs store water, and flow alteration as a measure of the near instantaneous impact on streamflow. Examination of these

parameters revealed insightful temporal and spatial patterns. Some patterns are self-evident, such as reservoirs experiencing higher residence time in the dry season than the wet season.

The presence of such an intuitive trend expected of river basins dominated by monsoonal hydrology, adds credibility to the satellite based method. The fact that satellite observations and physical hydrological model alone are able to elucidate such a trend without any help from in-situ observations is notable for ungauged river basins in the developing world. Other less obvious trends provide insights into reservoir operations in the MRB. One such trend is the pattern of highly impactful small reservoirs on smaller tributaries and lower impact larger reservoirs on larger tributaries. Current reservoirs collectively have insignificant impact on the overall MRB system if the MRB is assumed as one single control volume. However, there are two caveats to this 'systems' approach. First – the systems approach of a single residence time for the entire basin is valuable for water balance studies only when all riparian nations are working together on a shared vision for integrated water resources management. Second – the single basin-wide metric does not paint the real picture of spatially and temporally diverse human impacts of reservoirs within a basin to identify appropriate and local water management strategies. For example, many reservoirs on lower stream-order rivers have significant impact on the localized streamflow.

Future plans for MRB development involve tripling the number of dams currently in the basin. Basin-wide reservoir impacts on residence time and flow alteration will no longer remain insignificant (Grill et al. 2014; 2015). Another interesting point that emerged is the complete lack of trend in monthly reservoir imposed flow alteration. The fact that no reservoir properties (e.g. size, location, use, etc.) can be used to characterize monthly flow alteration highlights the

94

importance of satellite based observations to understand how humans operate the reservoirs to maximize benefit.

The key take home message of this chapter is that satellites can indeed pick out the diverse variability of reservoir operations in ungauged and international river basins that is otherwise intractable. As satellite observations of the water cycle (surface water inundation, height; (Biancamaria, Lettenmaier, and Pavelsky 2016)), precipitation, soil moisture become increasingly more widespread in the near future, it appears that the scientific community will be able to rely on space observations to understand the potential impact of reservoir development planned by each riparian nation that lacks ground-based observations or data sharing mechanisms. The hope is that the availability of such understanding across a basin will counter the secrecy or the lack of capacity that is typically common among riparian nations of international river basins, and result in a more cooperative environment for the benefit of all the stakeholders of the basin.

With the upcoming launch of the Surface Water and Ocean Topography (SWOT) Mission, our ability to monitor surface water remotely is expected to greatly improve. Chapter 4 seeks to quantify this improvement by simulating SWOT observations of the same 20 Mekong reservoirs studied in Chapter 3 and comparing the accuracy of these synthetic observations to real observations made by past and current satellite sensors.

Chapter 4: Assessing the Potential of the Surface Water and Ocean Topography Mission for Reservoir Monitoring in the Mekong River Basin

Abstract: The planned Surface Water and Ocean Topography (SWOT) mission, scheduled to launch in 2021, is designed to significantly improve on current lake and reservoir remote monitoring capacity. These improvements are especially important for the Mekong River Basin (MRB), where rapid dam construction puts downstream food security at risk and upstream dam operations are largely unknown to downstream water managers due to lack of upstream hydrologic information. This study aims to answer: How accurately will SWOT estimate reservoir storage change in the MRB? A physically based simulation tool developed by NASA Jet Propulsion Laboratory to mimic SWOT-like observations of water bodies was applied to 20 reservoirs in the MRB and for 17 of those reservoirs, synthetic SWOT-based storage change estimates demonstrated high skill, with errors typically less than 8%. The remaining three reservoirs showed higher errors due to complex neighboring topography or long narrow reservoir shape. In comparison with current satellite observations of six reservoirs in the MRB, the synthetic SWOT observations showed between 4% and 10% lower storage change normalized root-mean-square error. Finally, the simulated elevation and surface area was successfully used to estimate the area-elevation relationships for each reservoir, with a median percent difference of 6.9%. These relationships are a potential avenue for multisensor cooperation toward improved understanding of reservoir dynamics. Such cooperation, where observations from many difference remote sensors are synthesized to provide a more complete view of human

interactions on the river system, is vital for the MRB as more dams as human influence over the system increases.

4.1 INTRODUCTION

The Surface Water and Ocean Topography (SWOT) Mission, planned to launch in 2021, shows promise to improve satellite based reservoir monitoring (Biancamaria, Lettenmaier, and Pavelsky 2016). SWOT will use interferometric synthetic aperture radar (InSAR) to provide estimates of reservoir water surface area and elevation simultaneously in wide swaths with global coverage (L.-L. Fu et al. 2012). This will allow for the estimation of reservoir storage directly from SWOT observations. SWOT has a return period of 20.9 days, with many locations observed more than once within this time period, meaning storage changes can potential be resolved at sub-monthly time scales (Solander, Reager, and Famiglietti 2016). Additionally, repeat SWOT observations of reservoir surface area and elevation could be used to estimate reservoir area-elevation relationships, which may help improve current reservoir monitoring techniques.

Given the great potential of SWOT for reservoir monitoring and the innovativeness of the Ka band radar interferometer SWOT will employ (Fjørtoft et al. 2014), it is critical to make efforts before SWOT launches to understand how skillfully SWOT will observe reservoirs. There are no current satellites equipped with similar sensors and while AirSWOT (a SWOT like instrument mounted on an aircraft) has provided valuable insight into the expected performance of SWOT (Moller et al., n.d.; Altenau et al. 2017), it is only applicable to the limited locations it has operated in. In order to elucidate the applicability of SWOT in data limited regions like MRB, simulation of SWOT observations is the only feasible option. Lee et al. (2010) used a combination of satellite altimetry, satellite imagery, and lake gauges to simulate realistic water

97

elevation changes and corrupted them with random errors, which represented conservative estimates of expected SWOT instrument errors. They found that lakes larger than 1 km^2 typically exhibited relative storage change errors less than 5% and one-hectare lakes have relative storage change errors around 20%. NASA Jet Propulsion Laboratory (JPL) developed a SWOT simulation tool, here after referred to as the SWOT Hydrology Simulator, which generates realistic SWOT observations based on the planned orbit and expected performance of SWOT (Rodriguez and Moller 2004). Solander, Reager, and Famiglietti (2016) applied the SWOT Hydrology Simulator to reservoirs in California and they found that surface area and height errors were typically minimal for reservoirs larger than 1 km^2, with <5% area error and <15 cm height error. However, reservoirs in mountainous terrain or with strong elliptical shape were found to have higher errors.

This chapter aims to build on the work of these past studies by applying the SWOT Hydrology Simulator to a set of reservoirs in the MRB. Because of the potential usefulness of SWOT observations in the MRB, where data is limited and hydrologic changes due to dam development are rapid, it is imperative that SWOT's potential capabilities be analyzed in this region. Such a study demonstrates SWOT's usefulness and applicability to potential end users, and creates realistic expectations of SWOT's performance, both of which are important for the adoption of SWOT observations into scientific and water management communities that stand to benefit from them. This study assesses the skillfulness of SWOT reservoir observations and seeks to answer the following research questions: *1) How accurately will SWOT estimate reservoir storage change in the MRB and 2) will the accuracy of SWOT observations be sufficient for estimating reservoir area-elevation relationships and for reservoir outflow modelling?* By comparing simulated SWOT observations with reservoir observations from

98

currently operating satellite missions such as Landsat and Sentinel, this study provides a valuable first step towards creating a multi-sensor reservoir monitoring approach. Leveraging observations from different sensors can mitigate deficiencies in accuracy, sampling frequency, or coverage of a single sensor and improve overall reservoir monitoring capacity. For example, Sentinel-1, Sentinel-2, Sentinel-3, Landsat-8, AltiKa, and Jason-3 all take observations of reservoir water levels or extent. By taking observations from all of these sensors along with SWOT into account, a more complete view of upstream reservoir operations could be provided to a downstream water management decision maker. This study also explores multi-sensor synergy with SWOT observations in providing bathymetric information (area-elevation relationship), which could be used to improve traditional satellite based reservoir monitoring techniques. Finally, this chapter investigates the applicability of SWOT storage change estimates as inputs into a simple reservoir model to estimate reservoir outflow, which is key for understanding reservoir interactions with the river system and a largely unknown quantity of importance to those living downstream.

4.2   STUDY REGION AND DATA

This study focuses on the same set of 20 MRB reservoirs studied in Chapter 3. A list of the reservoirs along with information about the country location, average surface area, capacity, and primary use (if available) is shown in Table 3.1, all taken from the GRanD Database (Lehner et al. 2011). Figure 4.1 shows the locations of these reservoirs in the MRB, along with the planned observational swaths of SWOT Mission. These 20 reservoirs are fairly representative of the variety of reservoirs found in the basin. They range in capacity from 22.8 million m^3 to 7030 million m^3, while the average capacity of current reservoirs in the basin is 1116 million m^3

(WLE 2017). The distribution of country location among the set of 20 reservoirs is also similar to the distribution of all reservoirs throughout the basin, with Thailand slightly over represented here and Vietnam slightly under represented. This distribution of location means that geographic variabilities that could affect SWOT observations such as terrain type, reservoir shape, or sampling frequency are represented by the set of study reservoirs. Six reservoirs (Sirindhorn, Yali, Chulabhorn, Lam Pao, Nam Oun, and Ubol Ratana) have daily in-situ storage change data available for 2016. These six reservoirs are highlighted in Figure 4.1. This allows for the investigation of how well SWOT sampling frequency captures daily reservoir operations. For the other reservoirs, the only available data are surface area estimates based on satellite observations.
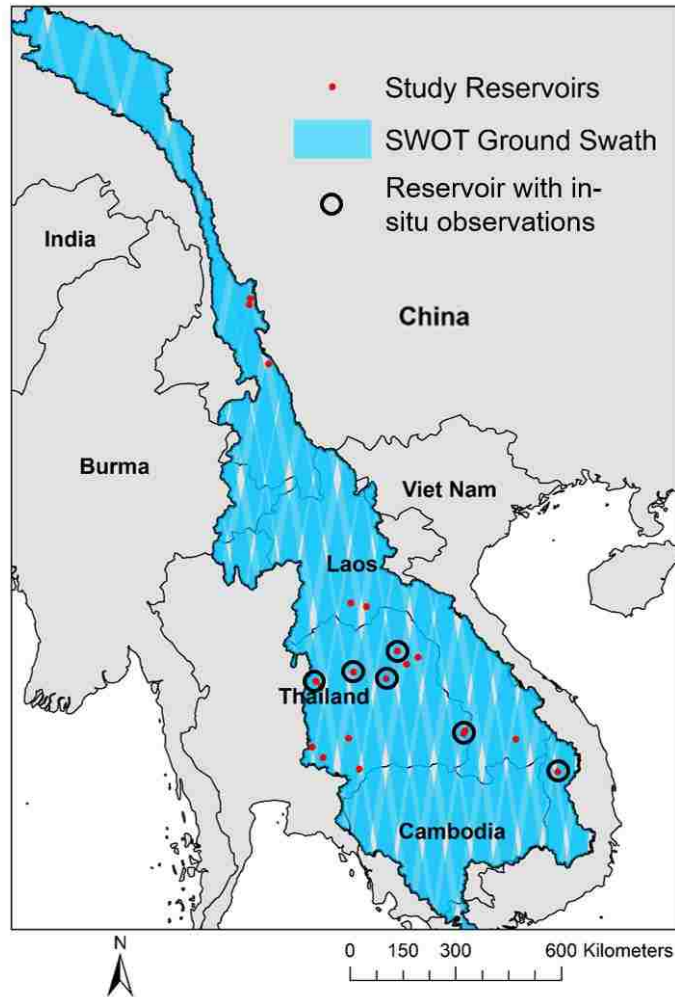
Figure 4.1. Map of Mekong River Basin showing study reservoirs and SWOT observational swaths. Dam locations taken from GRanD Database [Lehner et al., 2012]. The six reservoirs with in-situ observations are highlighted.

4.3 METHODS

The general methodology of this study involves a hypothetical scenario where SWOT was operational for the year 2016. First, a reference dataset representative of the real conditions of the 20 Mekong reservoirs during 2016 is created. This dataset is then run through the SWOT Hydrology Simulator and the output is used to derive reservoir water surface elevation and water

surface area. These quantities are then used to estimate reservoir storage change. Finally, the storage change is input into a simple mass balance model and the impacts of SWOT storage change errors on reservoir outflow estimation are analyzed. The following subsections describe these processes in greater detail.

4.3.1   *SWOT Hydrology Simulator*

The SWOT Hydrology Simulator developed by NASA JPL is a tool that attempts to mimic the characteristics of SWOT's Ka band interferometry instrument over surface water features such as lakes and rivers (Rodriguez and Moller 2004). The tool takes a digital elevation model (DEM) of a water feature and the surrounding topography as input and simulates a SWOT observation of the water feature (Peral et al. 2014). The simulator does this by first converting the geographic coordinates of the DEM into radar coordinates, and assigns radar reflectiveness properties to the DEM depending on land type (water or land) and water surface roughness, which is approximated by the simulator using a wind field, another simulator input. The simulator then approximates the radar signals returned to SWOT based on the planned orbit relative to the location of the water feature, and based on the expected characteristics of the radar interferometry instrument. The simulator then processes these synthetic radar returns and generates a pixel cloud of water heights as output. From the pixel cloud, reservoir water surface elevation, reservoir surface area, and storage change are calculated. Figure 4.2 shows a flowchart illustrating the simulation process from simulator inputs to reservoir storage change estimation. Each step of this process is described in greater detail in the following sections.
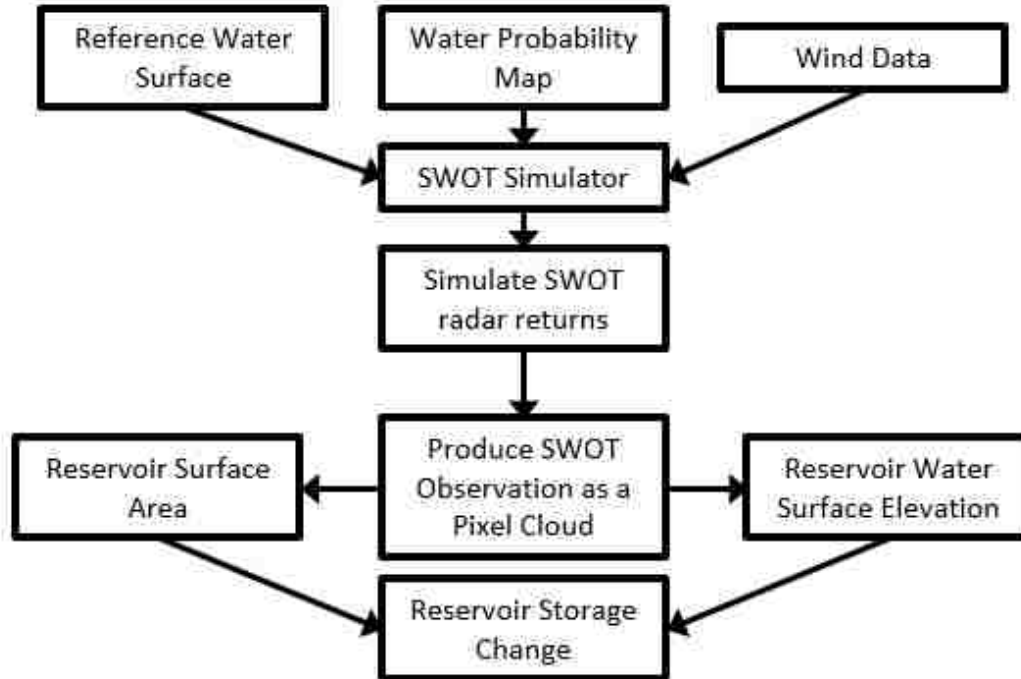
Figure 4.2. Flow chart illustrating the SWOT simulation process, from the inputs (reference water surface, water probability map, wind data) to the simulator output (pixel cloud) which is then used to estimate surface area and water surface elevation.

Two important sources of error included in the simulator are dark water and layover. Dark water occurs when a pixel containing water becomes misclassified as land, due to dark radar returns and its occurrence depends on the roughness of the water surface and incidence angle between the interferometer and the water surface. Smooth water surfaces can cause the radar signal to be reflected away from the satellite, instead of scattered back towards it, resulting in water that appears to be of similar brightness to land. Layover occurs when a location on land and a location in the water surface have the same range from the SAR instrument, resulting in signals returning from both locations at the same time. When the contrast between the land and water radar return is low, it becomes difficult to distinguish which signal came from which

103

location, resulting in elevation errors. The simulator also accounts for thermal noise, instrument height error, and classification error. Wet tropospheric errors are also simulated, but in a simplistic manner that does not take into account any atmospheric information. The simulator merely applies spatially correlated errors such that the tropospheric error equals 4.0 cm when averaged over a 1 km^2 area, which coincides with the wet tropospheric error budget in the SWOT Project and Mission Performance and Error Budget (Esteban-Fernandez, 2017).

4.3.2   *SWOT Hydrology Simulator Input Preparation*

The simulator requires a 3-dimensional model of the water surface to be simulated and of the surrounding topography, a water probability map, and surface level wind fields. The water probability map is used by the simulator to flag areas where dark water effects are present. For example, if a pixel in the pixel cloud is classified as land, but is located in a pixel of the water probability map that likely contains water, it is flagged as dark water. The water probability map used here was taken from the Global Surface Water Explorer, which was generated using 32 years of Landsat imagery (Pekel et al. 2016). Wind fields are used by the simulator to simulate roughness characteristics of the water surface. The wind fields used here were taken from the 10 m wind speed components from the ERA-Interim global atmospheric 80 km reanalysis data produced by the European Centre for Medium-Range Weather Forecasts (ECMWF). Note that the actual water surface roughness, which controls dark water occurrence, is dependent on the localized surface wind field and the 10 m wind field is a crude approximation of this, however, it is the best option available for simulations in this region.

The water surface models for each reservoir were created by pairing water classified satellite imagery with a Digital Elevation Model (DEM) generated by the Shuttle Radar and

104

Topography Mission (SRTM). Figure 4.3 shows a flowchart illustrating the process of creating the reference dataset of true water surfaces. First, Landsat and Sentinel-2 visible and infrared images are cropped first by the reservoir extent (provided by the GRanD Database) with a 1 km buffer, and then by the reservoir watershed (delineated using the SRTM DEM). This cropped region is then checked for clouds using the quality control flags of the satellite products. Images with greater than 5% clouds within the vicinity of the reservoir were removed. The remaining images were classified for water by calculating the Normalized Difference Water Index (NDWI) and identifying pixels with NDWI greater than 0 as containing water (McFeeters 1996). Sentinel-1 Synthetic Aperture Radar (SAR) radar backscatter images were also classified for water by identifying pixels with VV polarization backscatter less than -14 decibels (dB) as containing water. Note that Pham-Duc, Prigent, and Aires (2017) found that -15 dB was suitable for Sentinel-1 VV polarization water classification in the Mekong Delta. This threshold was adjusted to -14 dB because it resulted in water surface areas similar to the Landsat-8 and Sentinel-2 water classifications. The reservoir surface area was calculated for each classified image by multiplying the number of water pixels by the pixel size, 30 m for Landsat, 15 m for Sentinel-2, and 10 m for Sentinel-1. Each image was then assigned an elevation based on the relationship between surface area and water surface elevation, derived for each reservoir from neighboring topography provided by the SRTM DEM, the same method developed in Chapter 2.
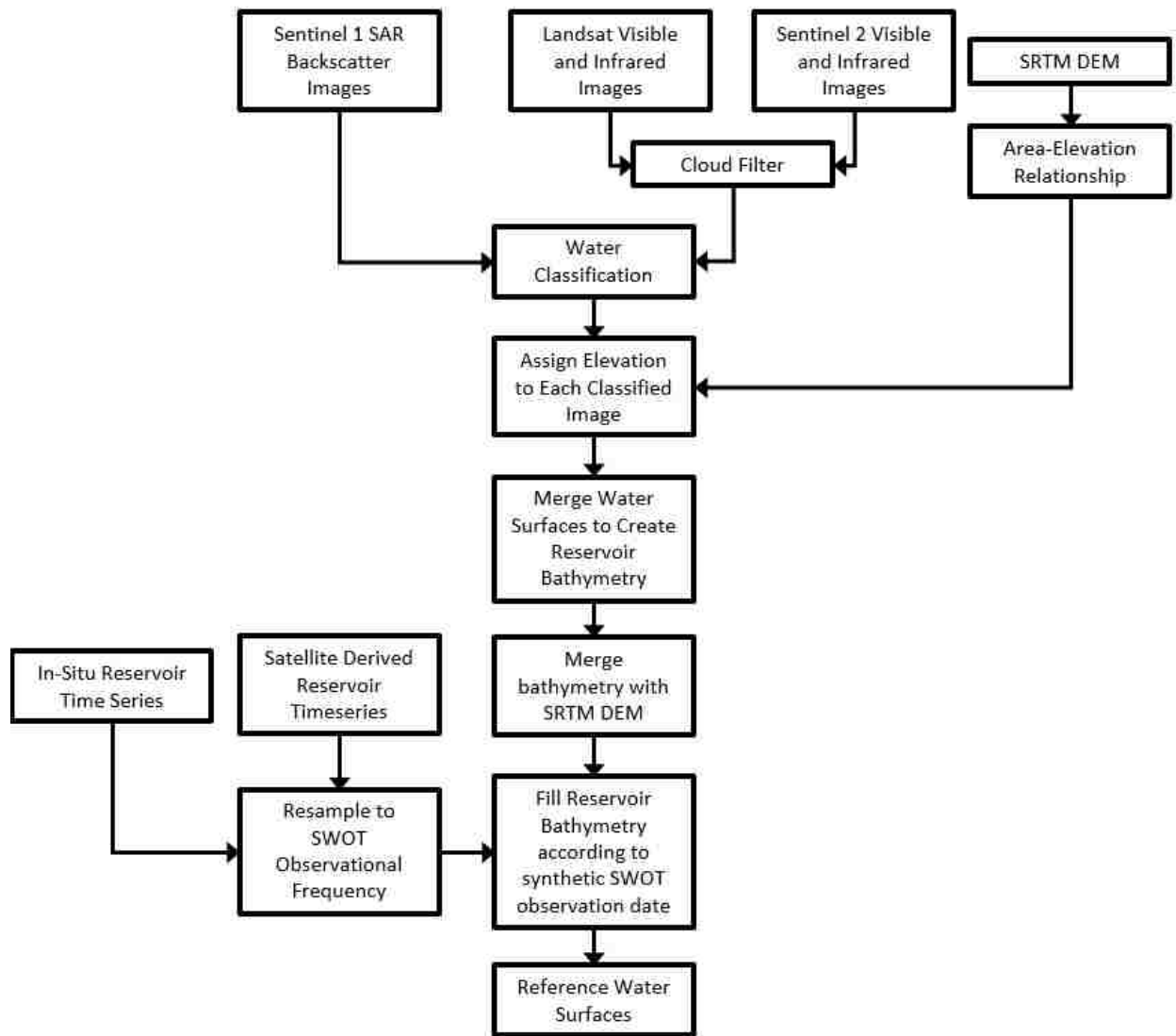
Figure 4.3. Flow chart illustrating the reference water surface creation process, which involves using satellite imagery to estimate reservoir bathymetry and then filling that bathymetry to a desired water level.

These water surfaces are then merged together based on their elevation, so that minimum elevation water pixels take precedence. This results in an approximation of the reservoir bathymetry above the minimum water elevation observed. This bathymetry is merged with the SRTM DEM. The resulting DEM was resampled to 10 m using bilinear interpolation. This was

106

done to avoid any false layover that may occur from the coarsely spaced 30 m pixels. Note that this results in a land surface that is smoother than the real land surface, which may cause lower layover errors than would be expected. The reservoirs are then filled to certain elevations based on in-situ water level or storage data for the six reservoirs with in-situ data available and satellite based monthly surface area and storage estimates for the rest, calculated from Landsat images in the same manner as in Chapter 3. Water surfaces are only generated for days which correspond to hypothetical SWOT observation days, based on SWOT's 20.9-day return time, assuming a start time of 12:00am local time January 1st, 2016. The result is a 3-dimensional water surface, representative of the true water surface during each hypothetical SWOT overpass for all 20 reservoirs. These water surfaces are treated as reference, by which the accuracy of SWOT observations are assessed.

4.3.3 *SWOT Hydrology Simulator Output Processing and Storage Change Calculation*

Each water surface is individually run through the SWOT Hydrology Simulator. Within the simulator, radar returns from the land and water surface are generated based on expected instrument performance. These synthetic radar observations are then processed to generate a pixel cloud, containing latitude, longitude, elevation, and surface area of water pixels. Also contained in the pixel cloud is a flag for the presence of dark water. The simulator flags dark water that occurs in locations likely to contain water based on the water probability map and places these pixels in their own dark water classification. Another flag present in the pixel cloud identified pixels impacted by layover, typically caused by complex nearby topography, which can result in high elevation errors.

Water surface elevation for each reservoir for each synthetic SWOT observation is derived from the pixel cloud by first filtering pixels classified as water from those classified as

107

land. Then, pixels flagged with layover or dark water are also filtered out. Only pixels in or within 1km of the original water surface are considered, with the rest filtered. Water surface elevation is then calculated by taking the median elevation of all remaining pixels. Similarly, land classified pixels and pixels greater than 1 km outside the original water surface are filtered for the water surface area calculation, but dark water and layover pixels are not removed. The water surface area is then calculated as the sum of the surface area of all remaining pixels. Storage change between subsequent synthetic SWOT observations is calculated using the trapezoidal approximation used in Chapter 2 (Equation 2.3). For the set of six reservoirs with available daily in-situ storage change data, daily in-situ storage changes are estimated by evenly distributing the storage change between two subsequent SWOT observations across each day between the observations.

Some SWOT passes only partially observe reservoirs. In these cases, surface area accuracy is evaluated by comparison with the region of the reference water mask that lies within the swath of the particular SWOT pass. Storage change for these partial passes is calculated by using the relationship between surface area and elevation derived from one or more passes when the reservoirs is completely observed to estimate total surface area based on observed elevation. For the Manwan Reservoir, a significant portion of its surface area lies in a region of no SWOT observations. For this reservoir, partial storage change was computed from the reference water surface for the regions of the reservoir lying within the SWOT swath and this was used to evaluate storage change.

The calculated storage change estimates are then input into the mass balance model employed in Chapter 3 (Equation 3.1). The synthetic SWOT storage change estimates along with

the reference dataset storage changes are input into the same outflow model to determine the effects of SWOT storage change errors on the efficacy of reservoir outflow estimation.

4.3.4   *Storage Change Estimation from Current Satellite Sensors*

In order to assess the performance of the synthetic SWOT reservoir observations in the context of traditional satellite based reservoir monitoring techniques, observations from four currently operating satellite missions are used to estimate the storage change of the six reservoirs with in-situ data available for 2016. Visible and infrared images from Landsat-8 and Sentinel-2 are cloud filtered and classified using NDWI, as described previously, to estimate water surface area. Sentinel-1 SAR radar backscatter images are also classified as previously described, using a -14 dB threshold. Landsat-8, Sentinel-2, and Sentinel-1 observations are applied to all six reservoirs. Jason-3 altimeter observations are only available for the Sirindhorn Reservoir and water surface anomalies provided by the altimeter observations are taken from USDA's Global Reservoir and Lake Monitor (G-REALM) (C. Birkett et al. 2011). Area-elevation relationships for each of the six reservoirs are derived from the SRTM DEM, as described in Chapter 2. Observed surface areas are then matched with their corresponding elevations based on the area-elevation relationship, and vice versa for elevation observations. Storage change between each observation of each sensor is then computed using Equation 2.3.

4.4 RESULTS

4.4.1 *Reservoir Water Surface Elevation and Surface Area Accuracy*

Overall, synthetic SWOT observations of reservoir water surface elevation exhibited high accuracy, with most reservoirs showing root mean squared errors (RMSE) lower than 0.1 m (Table 4.1). The primary factor determining the accuracy of SWOT based water surface elevation observations was reservoir size, with larger reservoirs exhibiting lower elevation RMSE (Figure 4.4). All four reservoirs with average surface area greater than 200 km^2 had elevation RMSE lower than 0.04 m. Smaller reservoirs showed a wider range of elevation accuracy, with RMSE typically between 0.1 m and 0.008 m.

Table 4.1. Simulated SWOT elevation, surface area, and storage change errors.

Dam Name	Elevation RMSE [m]	Area Error [km^2]	Area Error [%]	Storage change RMSE [km^3]	Storage Change NRMSE [%]
Haixihai	0.090	0.16	3.94	0.0040	6.46
Zibihe	0.087	0.25	3.16	0.0022	2.36
Manwan	0.722	2.82	7.63	1.0330	112.28
Nam Ngum	0.020	2.25	0.51	0.2490	3.54
Nam Leuk	0.075	0.38	4.13	0.0285	15.41
Nam Oun	0.021	1.20	3.13	0.0252	4.85
Nong Han Lake	0.043	3.10	4.23	0.1333	7.11
Nam Pung	0.065	0.20	1.27	0.0130	7.85
Ubol Ratana	0.013	19.60	6.26	0.1048	4.63
Lam Pao	0.028	7.80	3.85	0.0180	1.26
Chulabhorn	0.008	0.99	14.20	0.0080	4.26
Huai Kum	0.095	0.14	7.78	0.0014	6.32
Lam Chang Han	0.008	0.20	4.17	0.0016	6.08
Lamtakhong	0.078	1.87	6.95	0.0146	4.71
Lamphraphloeng	0.098	0.20	2.08	0.0196	12.89
Lamnangrong	0.055	0.17	1.47	0.0094	6.23
Pak Mun	0.484	9.00	10.36	0.2178	95.11
Sirindhorn	0.003	2.17	0.92	0.0009	0.45
Houayho	0.530	2.80	9.03	0.2742	42.25
Yali	0.012	1.50	3.30	0.0180	1.74
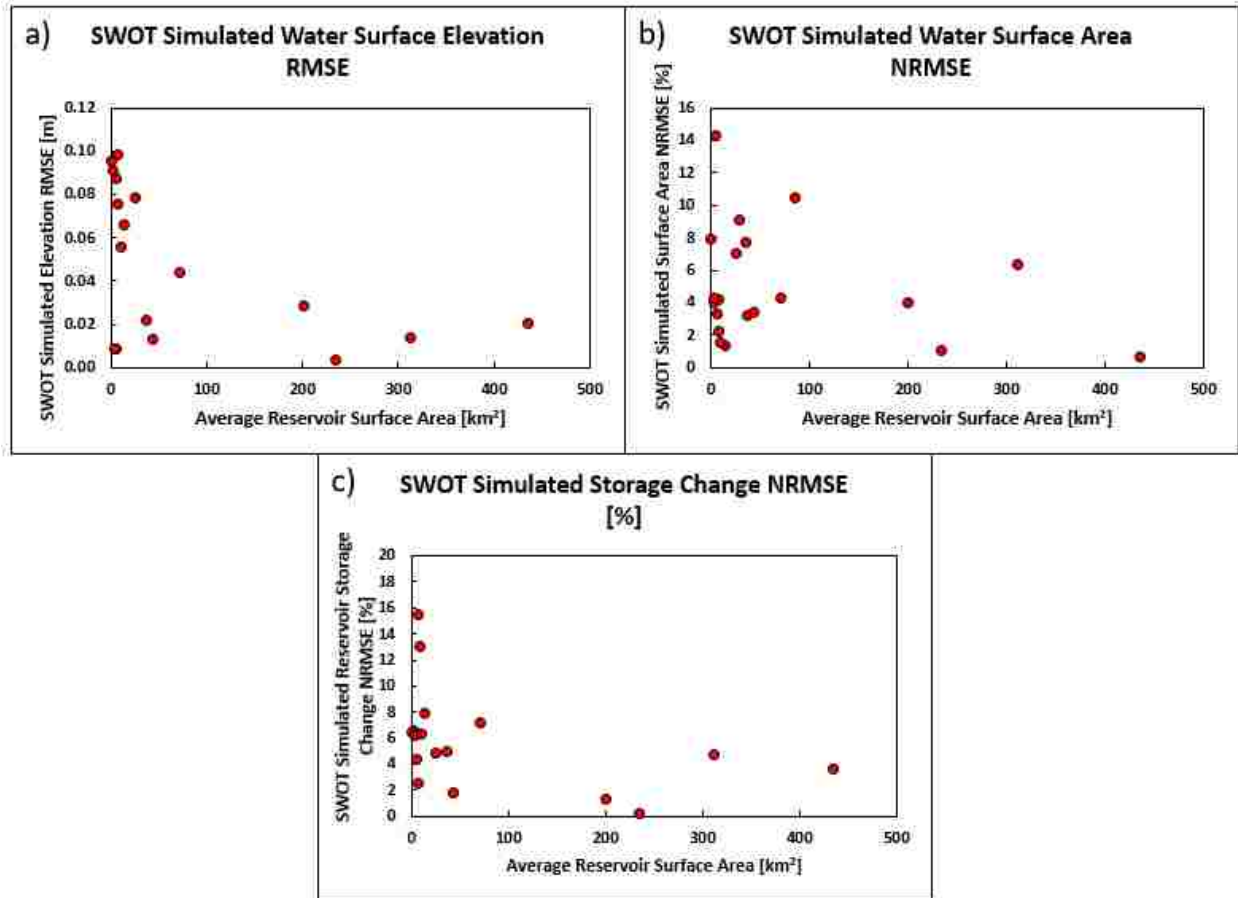
Figure 4.4. Plots showing the inverse relationships between average reservoir surface area and simulated SWOT (a) water surface elevation errors, (b) water surface area errors, and (c) storage change errors. Y-axis limits have been set to exclude the 3 reservoirs with the largest elevation and surface area errors.

Three reservoirs, Manwan, Pak Mun, and Houayho, all showed significantly higher elevation errors, with elevation RMSE between 0.484 m and 0.722 m. All three of these reservoirs experienced significant layover effects. Most reservoirs experienced some layover, but these effects were typically limited to reservoir edges and effected relatively few pixels. Manwan and Pak Mun are long, narrow reservoirs (as low as 100 m wide in some locations), and the layover effects typically occurring near the water edge made up a much more significant area of these reservoirs. Manwan is also located in an approximately 2 km wide valley, surrounded by

111

mountains that rise up to 1900 m above the water surface. Such mountainous terrain exacerbates layover. The Houayho Reservoir, is made up of multiple long, narrow channels (typically 0.5 km wide), and also located in mountainous terrain, with a 1000 m high ridge located 0.5 km to the east, the likely primary source of the high layover effects Because all three reservoirs were heavily impacted by layover, filtering layover pixels was infeasible and that step of the elevation estimation calculation was skipped.

Reservoir surface area was also estimated from the synthetic SWOT observations with high skill overall, with normalized root mean squared error (NRMSE) ranging from 0.5% to 14.2%, expressed as a percentage of total surface area (Table 4.1). The accuracy of reservoir surface area also followed a pattern with reservoir size (Figure 4.4). Larger reservoirs showed lower surface area NRMSE than smaller reservoirs. It should be noted that the surface area RMSE increases for larger reservoirs, but when the errors are expressed as a percentage of surface area, errors for larger reservoirs are significantly lower.

Dark water that occurred in the interior of the reservoirs had little impact on reservoir surface area estimates because it was properly identified by the water probability map and reclassified as water. However, dark water near the reservoir's edge was a larger source of error. Any dark water that occurred in areas that the water probability map did not identify as likely containing water, was misclassified as land. This causes an underestimate of surface area. In other cases, such as the Lamphraphloeng Reservoir, lower water levels caused false positive identification of dark water. Because the actual water level receded beyond regions that the water probability map identified as likely to contain water, some land pixels were miss-classified as dark water. This causes an overestimate in surface area.

By plotting SWOT estimated water surface area against water surface elevation, approximations of each reservoir's area-elevation relationship were created. When compared to the area-elevation relationships of the reference dataset, it is found that one year of SWOT data can relatively accurately reproduce a reservoir's area-elevation relationship. With the highly seasonal rainfall in the MRB, reservoirs experience seasonal emptying and filling. This means that over the course of a typical year, reservoirs will be observed by SWOT at a wide range of water levels. For reservoirs observed only once per SWOT cycle, this amounts to 17-18 observations per year. For the 6 reservoirs with in-situ observations, the simulated SWOT observations captured between 80% and 94% of the range of elevations the reservoirs experienced between 2012 and 2017.This results in a wide variety of area-elevation observations, which completes a significant portion of the area-elevation relationships. Table 4.2 shows the accuracy of the area-elevation relationships, derived by linearly interpolating between synthetic SWOT area-elevation pairs, as percent difference from the reference area-elevation relationship. Errors ranged from 1.42% to 17.34%, excluding the three reservoir affected by layover. Figure 4.5 shows an example of the Sirindhorn Reservoir, which has an area-elevation percent difference of 5.12%. Unsurprisingly, the three reservoirs impacted by layover experience significantly higher errors than all other reservoirs.

Table 4.2. The errors of the estimated area-elevation relationships and outflow estimated from

mass balance outflow model.

Dam Name	Area-Elevation Relationship Percent difference [%]	Outflow Percent Difference [%]
Haixihai	7.27	4.03
Zibihe	2.66	0.98
Manwan	126.40	1.13
Nam Ngum	3.99	0.98
Nam Leuk	17.34	3.51
Nam Oun	5.46	1.08
Nong Han Lake	8.01	3.49
Nam Pung	8.84	2.53
Ubol Ratana	5.21	1.21
Lam Pao	1.42	0.19
Chulabhorn	4.79	2.66
Huai Kum	7.11	0.31
Lam Chang Han	6.84	3.00
Lamtakhong	5.30	2.82
Lamphraphloeng	14.52	3.53
Lamnangrong	7.02	3.18
Pak Mun	107.07	0.20
Sirindhorn	5.12	0.02
Houayho	47.56	52.71
Yali	1.95	0.09

Sirindhorn Reservoir Area-Elevation Relationship
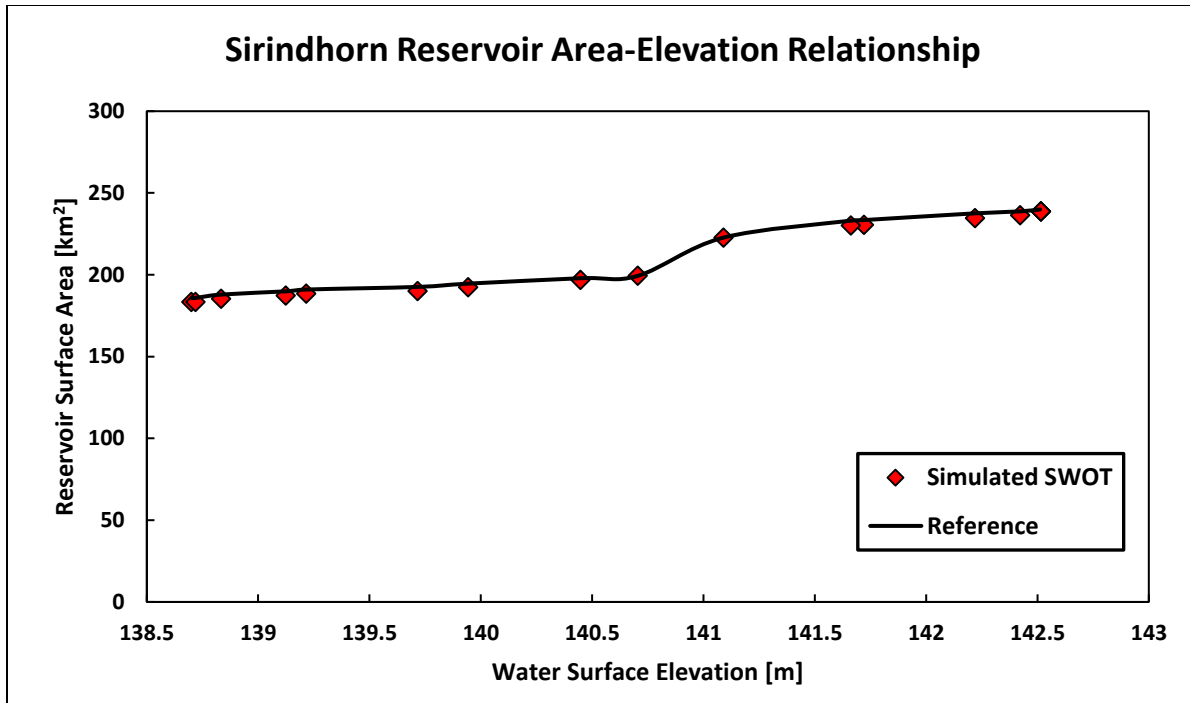
Figure 4.5. Example of surface area-elevation relationship estimation from the simulated SWOT observations along with the area-elevation relationship used to create the reference dataset.

4.4.2 *Storage Change Accuracy*

The synthetic SWOT observations estimate storage change with high skill, with NRMSE lower than 8% (Table 4.1), with the exception of the three layover impacted reservoirs. Figure 4.6 displays the reservoir storage change NRMSE [%] and how they are distributed throughout the basin. Again, accuracy appears interrelated with reservoir size, with larger reservoirs showing more accuracy storage change observations (Figure 4.4). This is consistent with the patterns seen in the components of storage change, surface area and elevation. In general, higher elevation errors and higher surface errors both tended to increase storage change error, but surface area errors tended to have higher correlation with storage change errors. This phenomenon occurs because storage change is calculated using surface area directly, but does

115

not rely on elevation, only elevation changes. This means that errors in elevation do not necessarily cause errors in storage change. As long as the elevation change between two observations is correct, storage change remains unaffected. This trend is made clear by examining how the accuracy of elevation, surface area, and storage change vary temporally. Figure 4.7 shows box plots of monthly elevation, surface area, and storage change errors across 17 reservoirs (with the 3 layover impacted reservoirs removed), averaged by month for reservoirs observed multiple times per month. The simulated water surface elevations tended to overestimate when reservoirs were at higher levels (October-March) and underestimate when reservoir levels were lower (April-September). This seasonality is not present in the monthly average surface area error, which remained fairly constant throughout the year. This seasonality is also mostly absent from the monthly average storage change error, with only slight increases between March and April, and September and October. These are the times when elevation errors typically switched between under and over estimating, resulting in larger elevation change errors. Except for those specific transitions, surface area errors represent a larger portion of the storage change errors than do elevation errors.
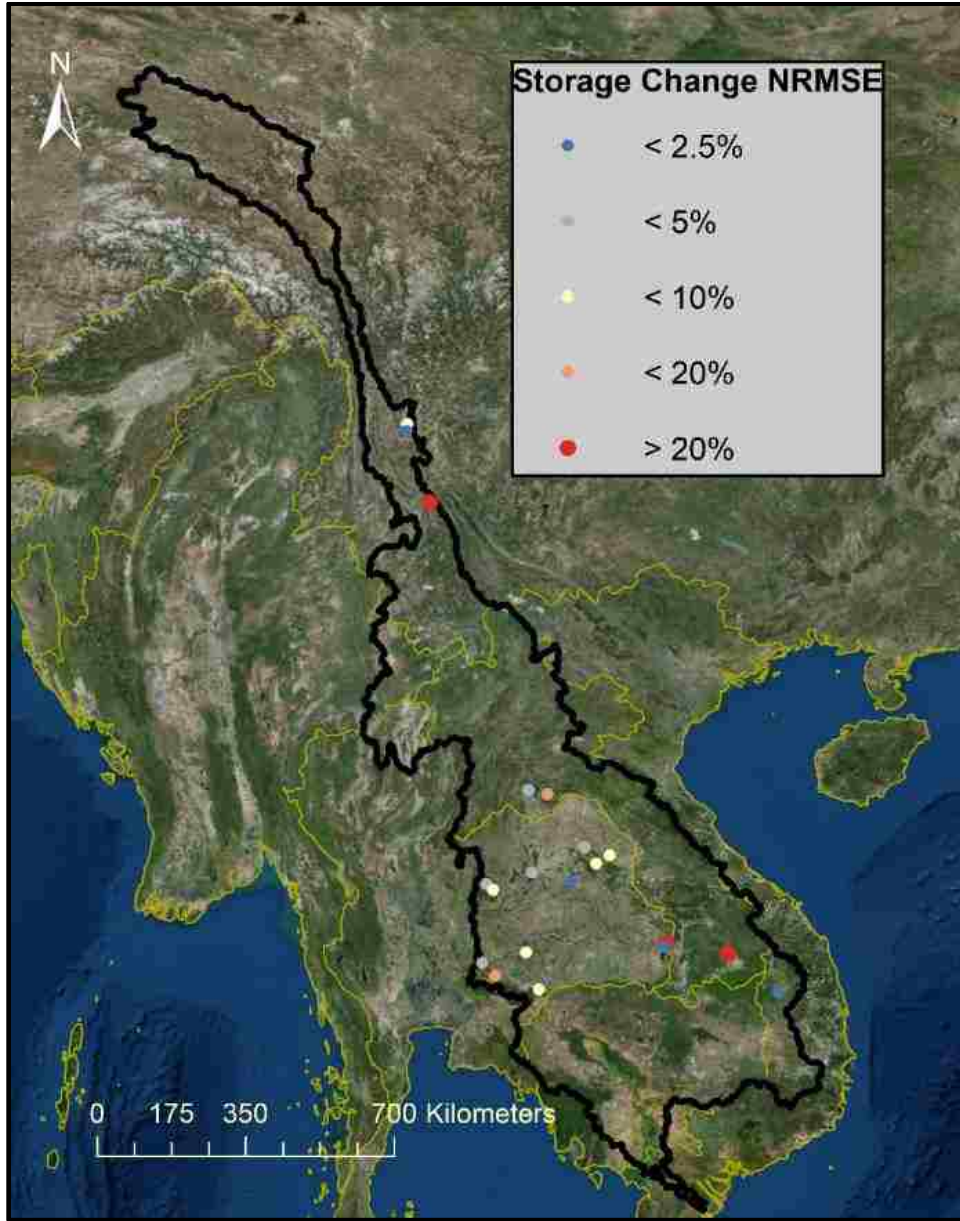
Figure 4.6. Map showing the SWOT storage change NRMSE [%] of each reservoir and their
location within the MRB.
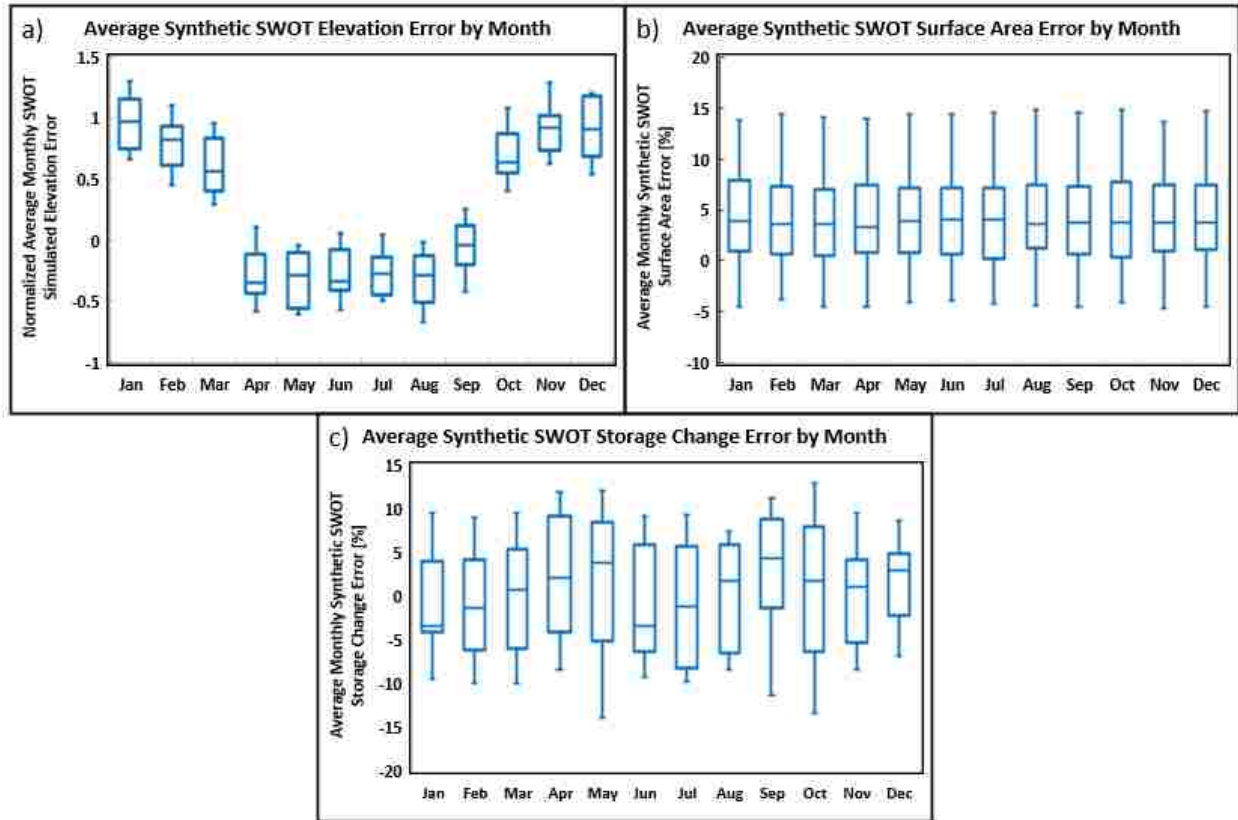
Figure 4.7. Boxplots showing the monthly variation of synthetic SWOT (a) elevation errors, (b) surface area errors, and (c) storage change errors.

For the six reservoirs with daily in-situ storage change observations available, the synthetic SWOT storage change estimates were extrapolated to daily storage change by evenly distributing them across all days between observations. These synthetic daily storage change values were compared to daily in-situ storage change observations, shown in Table 4.3. In terms of NRMSE, the Sirindhorn reservoir performed the worst, with 44.3%. This is likely a result of the Sirindhorn reservoir only having one SWOT observation per cycle where the other reservoirs have two, effectively decreasing the temporal resolution by half compared to the other reservoirs. Figure 4.8 (upper panel) compares the estimated and in-situ storage change of the Sirindhorn reservoir to illustrate that the temporal spacing of SWOT observations cannot capture daily peaks in reservoir storage change. Of particular note is the 62 million m^3 storage change

118

occurring on June 28, where interpolated SWOT observations only suggest a storage change of 6 million m^3. However, within the three weeks prior to this extreme storage change event, interpolated SWOT storage vastly over predicts storage change. These effects counteract each other as shown by the low storage change error when only considering storage change between subsequent SWOT observations. This is further illustrated by Figure 4.8 (lower panel), which shows the storage of the Sirindhorn reservoir, demonstrating how these temporal sampling errors manifest in overall reservoir storage. Since SWOT would have no prior knowledge of an anonymous reservoir's total storage, the synthetic SWOT storage simply starts at the in-situ storage on January 13 (the first SWOT overpass of the reservoir) and then uses the daily storage change to estimate the next day's storage change. Ultimately, while SWOT fails to capture the exact timing of rapid storage changes, its temporal resolution is sufficient for capturing overall reservoir dynamics.

Table 4.3. Results of daily storage change interpolation for the six reservoirs with in-situ observations.

Dam Name	Number of SWOT Observations per Cycle	Daily Storage Change RMSE [million m^3/day]	Daily Storage Change NRMSE [%]
Sirindhorn	1	6.91	44.3
Yali	2	4.82	27.6
Chulabhorn	2	0.48	37.2
Ubol Ratana	2	5.96	34.8
Nam Oun	2	0.94	33.7
Lam Pao	2	4.31	22.8
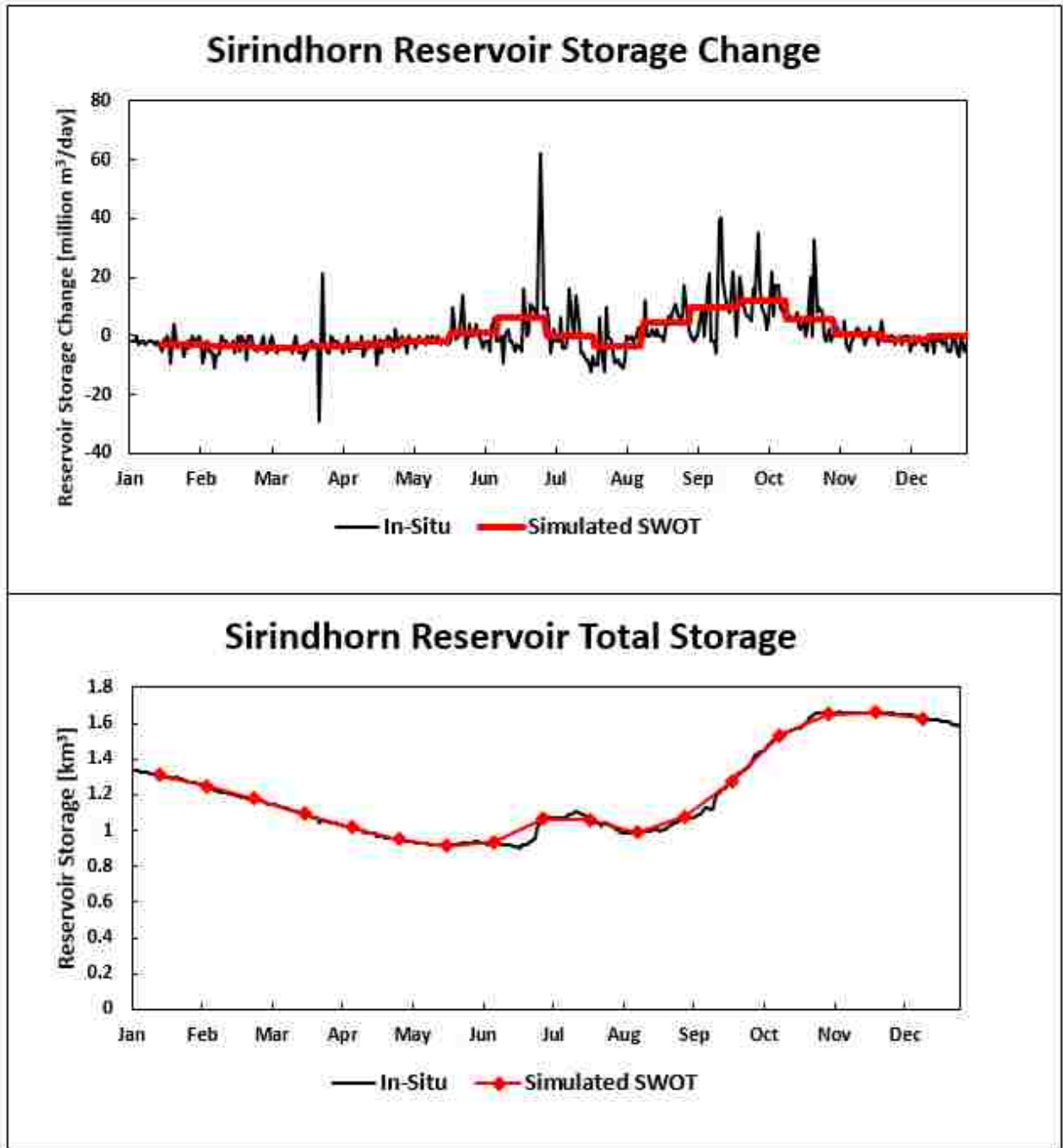
Figure 4.8. Results of the daily storage change interpolation from simulated SWOT observations for the Sirindhorn Reservoir (upper panel) and plot showing how those errors manifest when considering total storage (lower panel)

4.4.3   *Comparison with Current Satellite Sensors*

In comparison with the accuracy of traditional satellite based monitoring methods, the synthetic SWOT observations performed favorably. Table 4.4 summarizes the accuracy of each method across all 6 reservoirs when compared to in-situ data, as well as showing the average number of observations per reservoir for each of the sensors. Jason-3 only crosses the Sirindhorn reservoir, so the statistics presented are only representative of observations of that reservoir. Figure 4.9 shows a comparison of the storage change errors from different satellites for each of the six reservoirs. While Jason-3 provides higher accuracy, its observational capacity is limited to only 1 out of the 20 reservoirs studied, hindering its usefulness. The surface area based methods (Sentinel-1, Sentinel-2, and Landsat-8) all performed similarly. The simulated SWOT observations consistently outperform current capabilities, with synthetic SWOT errors typically less than half of the errors of current methods. Landsat-8 and Sentinel-2 are visible sensors and are completely blocked by cloud cover, which is the reason for their low average number of observations. Sentinel-1 and Jason-3 penetrate clouds (as does SWOT) and result in more frequent useable observations. In fact, Sentinel-1 observed these reservoirs almost as frequently as SWOT will and in the case of Sirindhorn, more frequently than SWOT will. The errors in reservoir storage of the current methods range from 6.48% to 12.34%, with the synthetic SWOT observations achieving average error across the six reservoirs of 2.86%. It should be noted that the errors observed are also related to the accuracy of the area-elevation curve derived from the SRTM DEM and a better approximation of this relationship (such as from SWOT observations as demonstrated in Figure earlier) could improve the accuracy of these methods.

Table 4.4. Summary of current satellite sensors and their reservoir monitoring capabilities over the six reservoirs with available in-situ data. Note that Jason-3 statistics are only calculated for the Sirindhorn Reservoir because that is the only reservoir of the six that it observes.

Satellite Mission	Reservoir Observations Provided	Average Number of Useable Observations in 2016	Average Storage NRMSE [%]
Landsat-8	Surface Area	6.3	12.34
Sentinel-1	Surface Area	27.1	9.35
Sentinel-2	Surface Area	7.7	10.64
Jason-3	Elevation	35	6.48
Simulated SWOT	Elevation and Surface Area	31.4	2.86
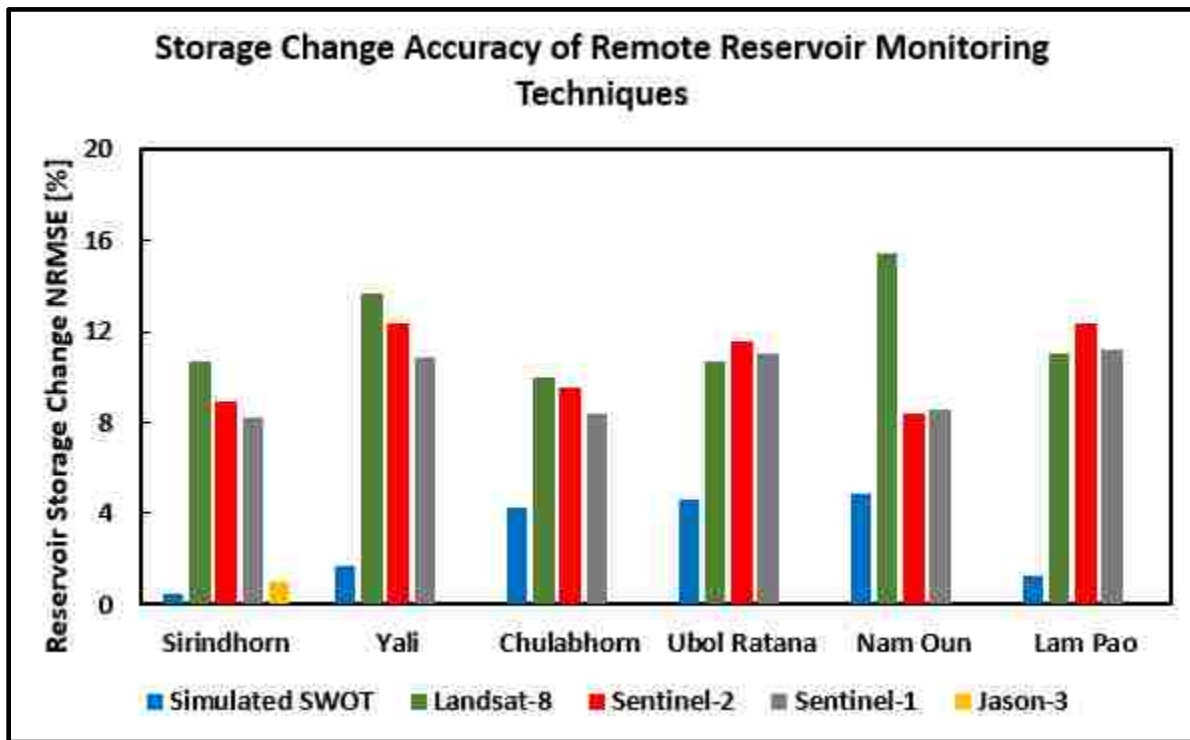
Figure 4.9. Comparison of satellite based reservoir storage change accuracy between synthetic SWOT observations and observations from Landsat-8, Sentinel-2, Sentinel-1, and Jason-3.

4.4.4   *Outflow Accuracy*

Table 4.2 shows the accuracy of reservoir outflow estimated from the simple mass balance model using synthetic SWOT storage changes compared to outflow estimated using the reference storage changes. Except for a single outlier, the Houayho Reservoir, the impacts of SWOT storage change errors on mass balance based outflow estimation were minimal, less than 4.1% difference. Manwan and Pak Mun showed low percent difference here (1.13% and 0.20%, respectively) despite their poor storage change accuracy because the volume of water flowing through these two reservoirs is magnitudes higher than their storage changes. Due to the linear nature of the mass balance model, this effect dampens the impacts of SWOT errors for all 20 reservoirs, but is most prominent on Manwan and Pak Mun because those reservoirs experience the largest inflows relative to their capacity.

4.5   DISCUSSION AND CONCLUSIONS

The SWOT based elevation, surface area, and storage change accuracy results are consistent with those of past studies of lakes and reservoirs larger than 1 km^2, with typical surface area errors around 5% and typical elevation errors <0.01 m. Furthermore, the characteristics of the three problematic reservoirs (narrow, in mountainous terrain) match those of reservoirs with high errors studied in Solander, Reager, and Famiglietti (2016). The result that SWOT is predicted to accurately capture storage change dynamics of 17 of the 20 reservoirs is promising for the application of SWOT on reservoirs in the MRB. Further supporting the applicational usefulness of SWOT storage change observations is their successful use in the mass balance outflow model. The low outflow errors due to errors in simulated SWOT storage change provides a real world proof of concept for using SWOT observations to drive a reservoir model.

123

The accurate estimation of reservoir area-elevation relationships from one year of SWOT observations highlights the potential of SWOT observations to improve the reservoir monitoring capacity of current satellite based reservoir monitoring techniques. Building these relationships from direct, simultaneous observations of reservoir surface area and water surface elevation could allow for the application of other satellite remote sensors to reservoirs in the MRB otherwise infeasible for remote monitoring. The accuracy of the relationships found here are suitable for this purpose, except when high layover effects are present. While the accuracy of the existing sensors is suitable for many applications, there is room for improvement and increasing the accuracy of the area-elevation relationship is one potential avenue for improvement. The merits of a multi-sensor approach is further reinforced when comparing existing satellite missions to the synthetic SWOT observations generated here. Because the synthetic SWOT storage change observations consistently outperformed current sensors, there is potential for SWOT observations to be used to correct errors in other sensors. Still, the advantages of current satellite sensors cannot be overlooked. While SWOT will observe the set of six reservoirs more frequently than Landsat-8, Sentinel-1, and Sentinel-2, if all four sensors are used cooperatively, the average number of observations per year would be double what SWOT alone can provide. Such cooperation has the potential to mitigate the issues with SWOT temporal sampling over reservoirs such as the Sirindhorn and better capture rapid storage change events, seen in Figure 4.8.

There are several limitations of this study that must be taken into account when extrapolating from the results. First, the synthetic SWOT observations were created using a software tool and not a real world instrument. While great effort has been made by JPL to create a tool that best mimics the expected performance of SWOT, it cannot account for all real world

124

conditions. The SWOT Hydrology Simulator is in ongoing development to make it more realistic and more reservoir simulations should be done as improvements to the simulator are made. Second, the resolution (30 m) of the SRTM DEM used to provide the simulator with topography information may be too coarse to simulate all influences of topography on SWOT observations. The SRTM DEM is however, the most precise openly available DEM of the region and thus represents the most realistic option for simulating SWOT in the MRB. Finally, the influence of rain on SWOT observations is not taken into account here. High rain rates are expected to interfere with SWOT's wide swath altimetry, but the degree of this influence has not been quantified. The MRB experiences extensive rainfall during the wet season (roughly between May and October), which could increase SWOT observation errors during a period when most reservoirs in the lower basin undergo rapid filling. Even with these limitations, this study represents a useful prediction of the expected performance of SWOT reservoir storage change estimation.

SWOT represents a potential significant step forward for satellite based reservoir monitoring capabilities and hydrologic prediction in ungauged river basins. This study uses the most realistic SWOT simulation tool available to quantify this potential on reservoirs in the Mekong River Basin. It was found that storage change can be accurately estimated from SWOT observations for all reservoirs tested except those with long narrow shapes or those set in mountainous terrain. The accuracy of these storage changes was sufficient for use in a simple reservoir outflow model, providing an early look at a potential application of SWOT observations to sub-basin scale hydrologic modeling. The ability to monitor not just reservoir storage change, but reservoir outflow, has many applications in water management in the transboundary, data limited Mekong River Basin.

125

Looking beyond what SWOT observations can achieve alone, this study also showed that reservoir surface area-elevation relationship estimation from SWOT observations is feasible after only a single year of SWOT orbits. Simulated SWOT storage changes performed with higher accuracy than current satellite sensors, indicating that these area-elevation relationships could improve the skill of current satellite based reservoir monitoring techniques. When SWOT launches in 2021, it will join an already impressive constellation of earth observing sensors. By leveraging observations from a suite of satellite missions (such as Landsat, Sentinel, and Jason) with observations from SWOT, there is potential to improve worldwide reservoir monitoring capabilities beyond what SWOT is capable of alone.

Observations of reservoir storage change are not the only surface water measurement relevant to understanding reservoir impacts on river systems that SWOT will make. SWOT will also measure river width, water surface elevation, and slope. From these observations, instantaneous river discharge can be estimated, providing valuable information from which the hydrologic changes imposed by reservoirs can be assessed. Chapter 5 examines this aspect of SWOT observations by making an assessment of the accuracy of three different methods for estimating river discharge from SWOT observables in a tropical monsoonal river basin.

126

Chapter 5: Benchmarking wide swath altimetry-based river discharge estimation algorithms for the Ganges river system

Note: This chapter has been published mostly in its current form in *Water Resources Research* (M. G. Bonnema et al. 2016); Used with permission.

Abstract: The objective of this chapter is to compare the effectiveness of three algorithms that estimate discharge from remotely sensed observables (river width, water surface height, and water surface slope) in anticipation of the forthcoming NASA/CNES Surface Water and Ocean Topography (SWOT) mission. SWOT promises to provide these measurements simultaneously, and the river discharge algorithms included here are designed to work with these data. Two algorithms were built around Manning's equation, the Metropolis Manning (MetroMan) method, and the Mean Flow and Geomorphology (MFG) method, and one approach uses hydraulic geometry to estimate discharge, the at-many-stations hydraulic geometry (AMHG) method. A well-calibrated and ground-truthed hydrodynamic model of the Ganges river system (HEC-RAS) was used as reference for three rivers from the Ganges River Delta: the main stem of Ganges, the Arial-Khan, and the Mohananda Rivers. The high seasonal variability of these rivers due to the Monsoon presented a unique opportunity to thoroughly assess the discharge algorithms in light of typical monsoon regime rivers. It was found that the MFG method provides the most accurate discharge estimations in most cases, with an average relative root-mean-squared error (RRMSE) across all three reaches of 35.5%. It is followed closely by the Metropolis Manning algorithm, with an average RRMSE of 51.5%. However, the MFG method's reliance on knowledge of prior river discharge limits its application on ungauged rivers. In terms of input data requirement at ungauged regions with no prior records, the Metropolis Manning algorithm provides a more practical alternative over a region that is lacking in historical observations as the algorithm

requires less ancillary data. The AMHG algorithm, while requiring the least prior river data, provided the least accurate discharge measurements with an average wet and dry season RRMSE of 79.8% and 119.1%, respectively, across all rivers studied. This poor performance is directly traced to poor estimation of AMHG via a remotely sensed proxy, and results improve commensurate with MFG and MetroMan when prior AMHG information is given to the method. Therefore, we cannot recommend use of AMHG without inclusion of this prior information, at least for the studied rivers. The dry season discharge (within-bank flow) was captured well by all methods, while the wet season (floodplain flow) appeared more challenging. The picture that emerges from this study is that a multialgorithm approach may be appropriate during flood inundation periods in Ganges Delta.

5.1 INTRODUCTION

Chapter 4 showed that SWOT is expected to provide useful estimates of reservoir storage change and that these storage change estimates can be paired with a hydrologic model to accurately estimate reservoir outflow. However, a key innovation of SWOT is that it will provide discharge estimates of large rivers. This will provide and independent assessment of the influence of reservoir operations on downstream streamflow. The discharge estimation process involves utilizing river width, water surface elevation, and water surface slope observed by SWOT and the application of discharge algorithms that are tailored for such inputs (D. E. Alsdorf, Rodríguez, and Lettenmaier 2007).

Three such algorithms, with global applicability are the at-many-stations hydraulic geometry (AMHG) algorithm, the mean flow and geomorphology (MFG) algorithm, and the Metropolis Manning (MetroMan) algorithm. The mechanics of each algorithm are presented in

Section 3. Gleason, Smith, and Lee (2014) recently tested the AMHG algorithm on 34 rivers around the world. They found that under most circumstances, the algorithm discharges had 26% to 41% relative root mean squared error (RRMSE) agreement with gauged flow rates. However, for braided river conditions and situations where changes in river discharge have a very small effect on river width the algorithm performs considerably less skillfully with median RRMSE greater than 70% (Gleason, Smith, and Lee 2014). Gleason and Hamdan (2017) applied AMHG to the Ganges using Landsat images, and found a dry-season RRMSE of 28%, suggesting that the AMHG method could be well-suited to the river. Durand et al. (2014) has reported 19% RRMSE from the MetroMan algorithm on the River Severn in the UK. Another study found that the Metropolis Manning algorithm overestimates the discharge of the Garonne River (Berthon et al. 2014). There has been no formal test of the MFG algorithm at the time of writing.

The discharge of rivers with high seasonal variability, meandering and braided nature and a tendency to change course, may be more difficult to extract than more stable rivers seen in most places. Such challenging set of river characteristics are often seen in deltas located at the downstream end of large river systems, such as Ganges-Brahmaputra, Nile, Zambesi, Niger, Indus, Salween and Mekong rivers. Given the economic and societal importance of most deltas for supporting the food and water needs of large populations, it is important to assess discharge estimation approaches in these locations (C. J. Vörösmarty et al. 2009).

Assessment of different discharge estimation methods takes particular importance in this decade as satellite observations on river width and heights are expected to become more widely available. There are currently several concurrently flying nadir altimeters that can measure river heights, such as JASON-1, JASON-2, ENVISAT (this mission ended in May 2012), CryoSat-2 and SARAL/AltiKa. With JASON-2 nearing its phasing out, JASON-3 was launched January

129

2016. In addition, the first satellite in European Space Agency (ESA)'s Sentinel-3 2-satellite constellation launched in February 2016 (Sentinel-3A) and Sentinel-3B will be launched in 2017. The planned Surface Water and Ocean Topography (SWOT) wide-swath radar interferometric altimetry mission (D. Alsdorf and Mognard 2011; Pavelsky and Durand 2012; L.-L. Fu et al. 2012) is scheduled for launch in 2021. Of these planned missions, JASON-3 and Sentinel-3 are actually designated operational missions, dedicated to providing near-real time data to the general public. Thus, there is an anticipated abundance of satellite water missions that measure height well into the foreseeable future. With such data continuity and declining latency, it is worthwhile to assess discharge algorithms that are amenable to handling remotely-sensed inputs of heights, widths and slope. The first step to this assessment, which is the primary motivation of this study, is to assess the algorithmic (or model-based) uncertainty of each approach. Such a study allows us to understand the various error interactions and provide further guidance on development of discharge estimation methods in preparation of future satellite missions.

5.2 STUDY REGION AND DATA

5.2.1 *Ganges River Delta*

The region of interest for this chapter is the Ganges River delta. The massive difference in river flow rates between the wet (Monsoon) and dry seasons makes this region unique for testing the ability of the algorithms to handle large seasonal variability. It is also a water-sensitive delta hosting two mega cities (Kolkata and Dhaka) and the water and food needs of over 200 million people in a changing climate. A majority of the non-Monsoonal flow originates from the Himalayan glaciers and snowpack that sustains the dry season (base) flow and groundwater stocks for water supply and crop production (Dyurgerov and Meier 2005)

Three rivers from the delta region were selected for the study, the Arial-Khan River, Mohananda River, and main stem of the Ganges River. Figure 5.1 shows the locations of these three rivers within the river system of Bangladesh. The Ganges River was selected for study because it is the major river in this system. The Mohananda and Arial Khan Rivers were selected because they are a tributary and distributary of the Ganges, respectively, and are representative of the many smaller rivers in the delta. These reaches of the Arial Khan and the Mohananda Rivers are single channel, while the Ganges River reach has a few braided sections.

131
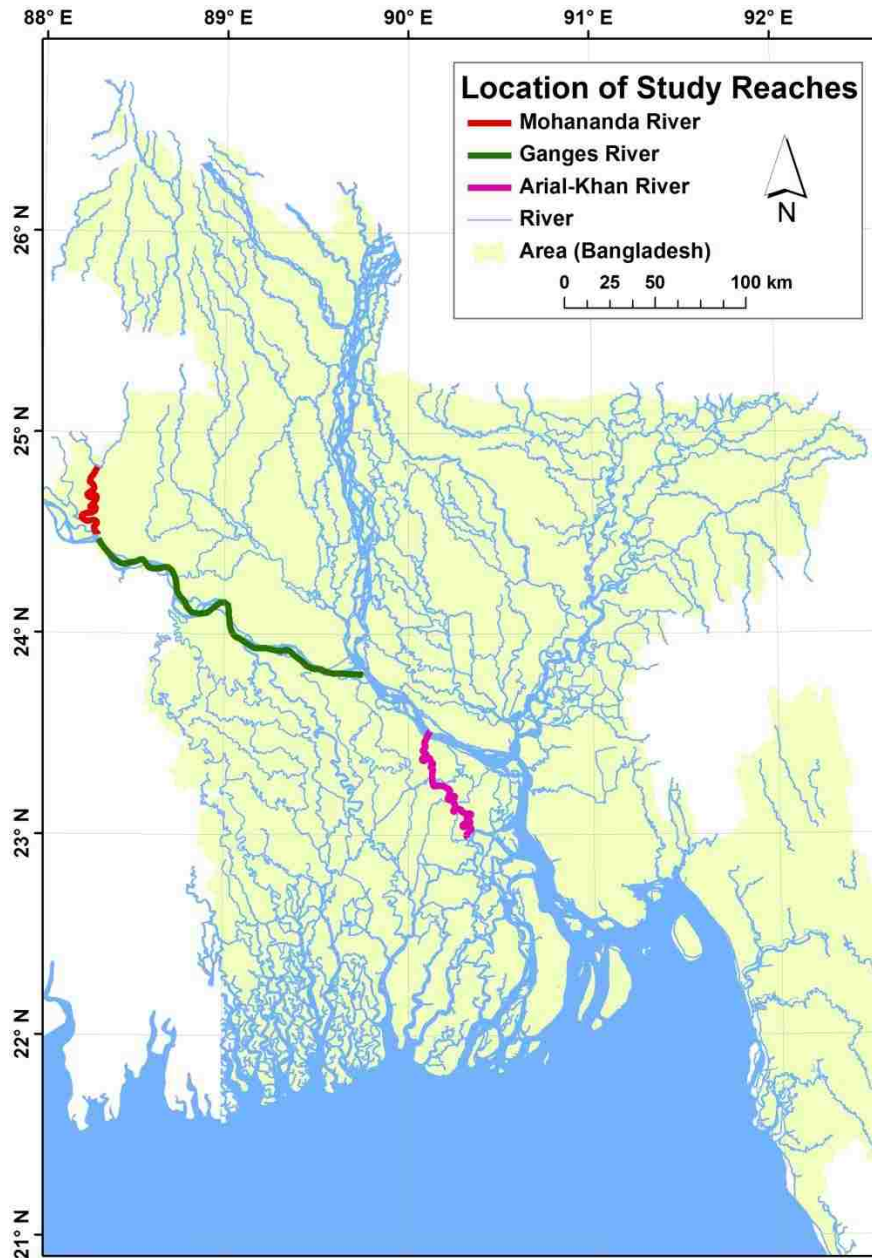
Figure 5.1. The Ganges Delta showing the selected river reaches that were studied.

There are some significant differences in the hydraulic characteristics of the selected river reaches. The Ganges River is an order of magnitude wider than the other two rivers studied here. The Arial-Khan River experiences tidal effects which, during the dry season causes the river flow direction to reverse during high tides. This behavior is characteristic of delta rivers emptying into an ocean. In spite of their differences, all three rivers experience the sharp change

132

in river flow characteristics during the Monsoon season which is characteristic of most rivers of humid deltas.

5.2.2 *Hydrodynamic Model*

Because the SWOT mission will not fly until 2020, a hydrodynamic model of the Ganges delta created with the Hydrologic Engineering Center River Analysis Software (HEC-RAS) was used to simulate the three rivers studied here and to provide the proxy remote sensing variables. This model has been previously calibrated and used for studying satellite river observations of the Ganges delta system (Sikder and Hossain 2015; Siddique-E-Akbor et al. 2014; Maswood and Hossain 2016). The Manning's roughness parameter at each cross section in the HEC-RAS model (located approximately every 10 km) was previously calibrated based on direct measurements of river height from gauge stations within the delta with boundary conditions specified by upstream gauged discharge and downstream water level. River bathymetry at each cross section was obtained from surveys of the river bed. All modeled cross sections of the Ganges are in locations where the river is single channel. Because of this, the model treats the entire river as single channel. The gauging stations along the selected river reaches are shown as red squares in Figure 5.2, while the performance of the HEC RAS model on each of these rivers is shown in Figure 5.3.
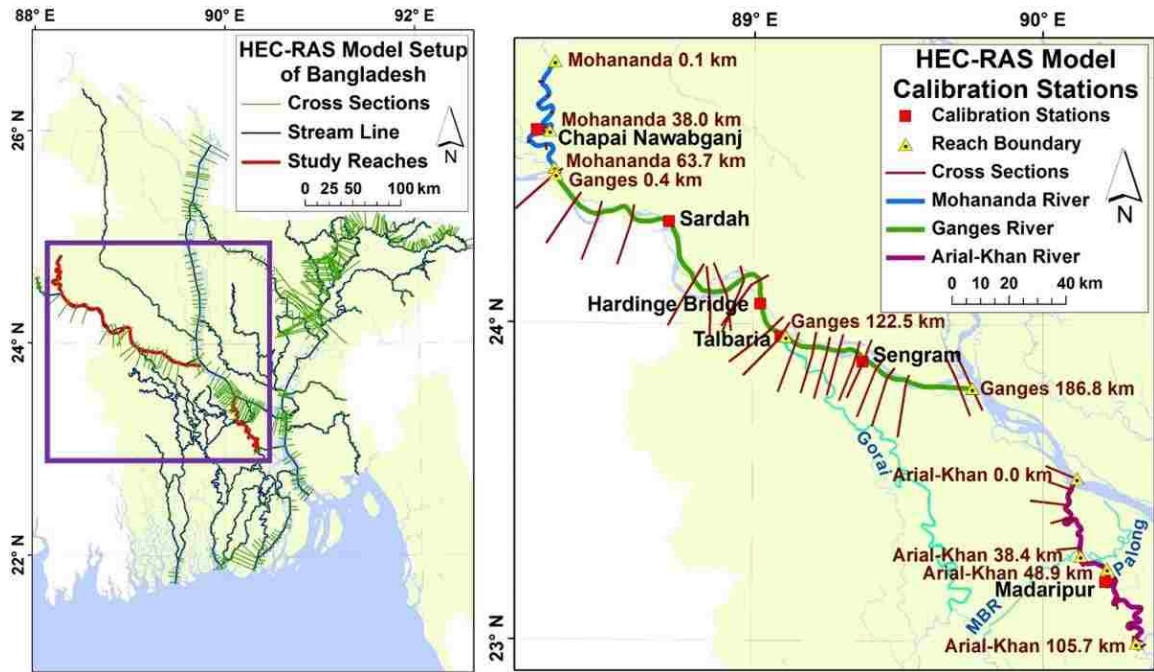
Figure 5.2. HEC-RAS river hydrodynamic model setup on the Ganges Delta and the calibration

station locations within the selected study reaches. The highlighted rivers are study reaches used

to delineate reach segments and the box in the left figure indicates the boundaries of the right

figure.
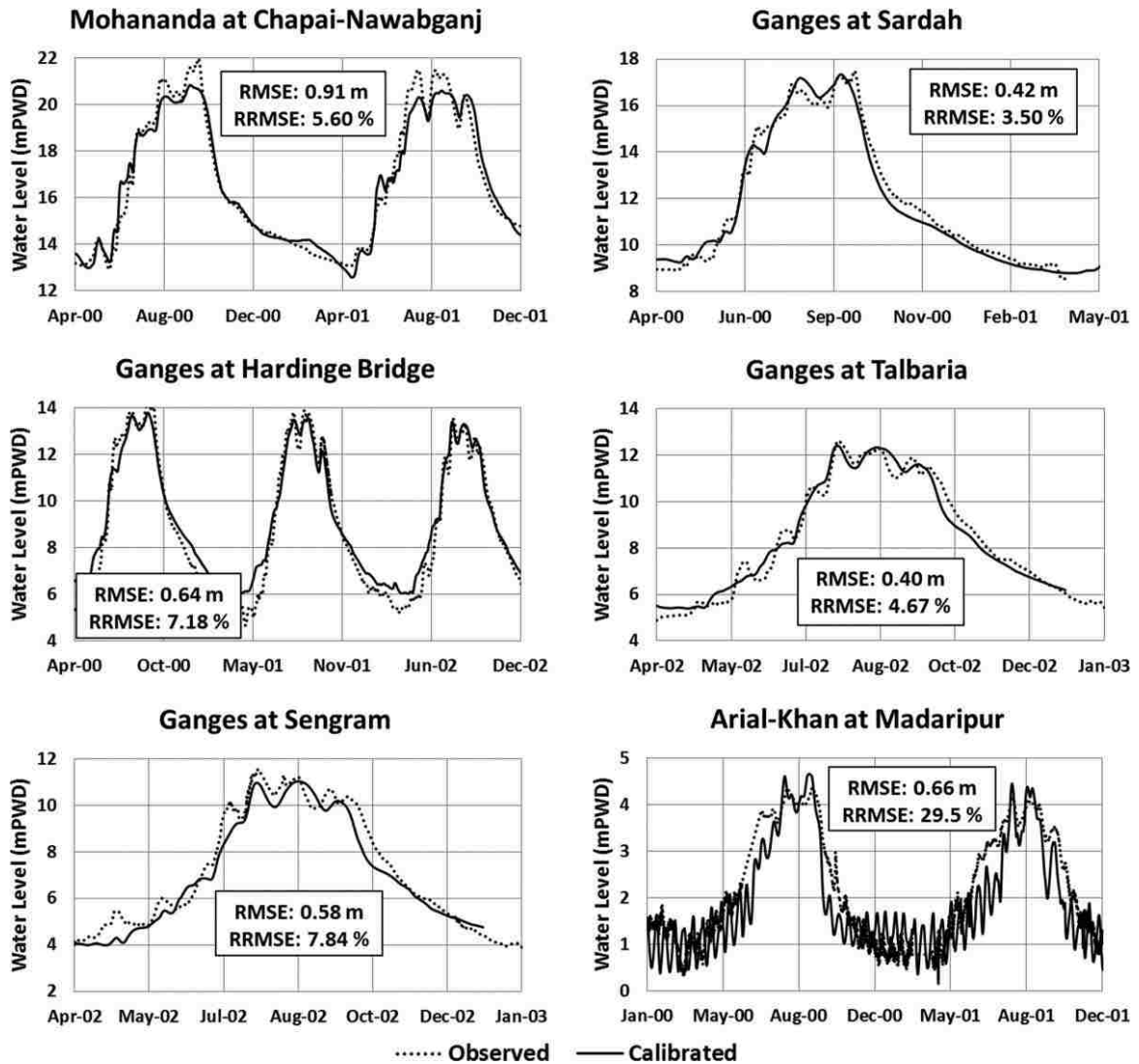
Figure 5.3. Time-series of observed and HEC-RAS simulated water level at gauging stations. Herein RMSE is Root Mean Squared Error while RRMSE is the RMSE relative to the average water level and expressed as a %.

Each study reach was subdivided into two or more reaches due to changes in river conditions resulting in significant differences in river hydrodynamics or discharge marked by specific locations. This was done so that the discharge algorithms could be applied to reaches with consistent discharge (i.e. reaches without abrupt changes in discharge or hydrodynamics). For the Ganges and Arial-Khan Rivers, this subdivision was determined using the location of

135

tributaries and distributaries along the channel. A sharp change in the slope of the Mohananda River marks the location of its subdivision. These subdivision locations are shown in Figure 5.4. The length of the resulting reaches ranges from 10 km to 100 km. Slope was calculated for each reach segment using the least-squares method. These calculated slopes are also depicted in Figure 5.4.

Mohananda Reaches

Ganges Reaches

Arial Khan Reaches
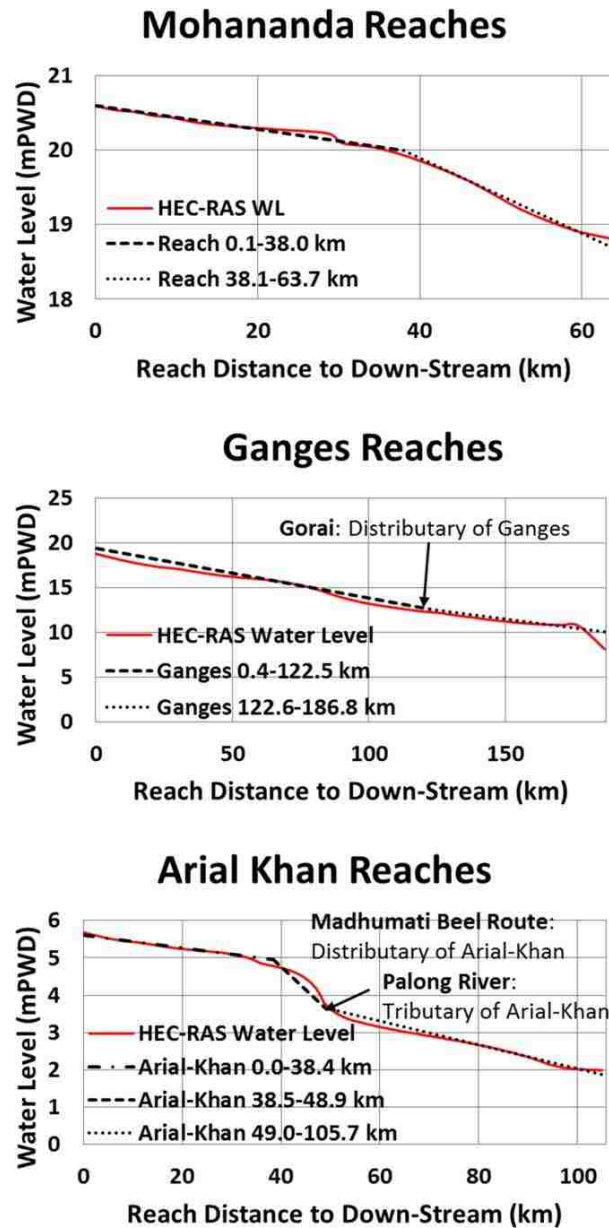
Figure 5.4. Water level of the Study Reaches on August 15, 2001. This illustrates the slope of each reach and the locations of the reach boundaries.

5.3 METHODS

The general methodology behind this study was to first generate river width and water surface elevation data as well as discharge for the three study rivers using the HEC-RAS model of the Ganges delta. Then, use this river width and water surface elevation data as input into each

137

algorithm in a consistent framework and compare the estimated daily discharges with the discharges generated by HEC-RAS model. The 5th, 15th, and 25th of each month from the year 2001 for a total of 36 days were used to assess the performance of each algorithm. This is similar to the sampling frequency expected from the SWOT mission. Daily river data of the entire year 2000 were treated as *a priori* knowledge and used to calibrate the MFG algorithm parameters and provide the prior parameter estimates for the Metropolis Manning algorithm.

Next, SWOT mission observations were simulated by passing the HEC-RAS model output through the SWOT simulator and use these river observations as inputs into the algorithms to understand how SWOT uncertainties affect discharge estimation. To help understand how each algorithm works, Figure 5 shows a depiction of an arbitrary river cross section (left) and profile (right) with remote sensing observables of width, depth (above a minimum or reference water depth), and slope.
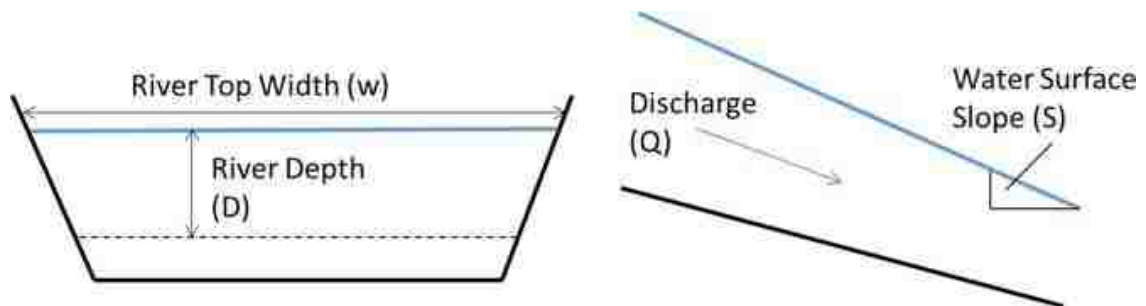
Figure 5.5. Representation of remote sensing observables of hydraulic features: width, depth, cross sectional area, and reach-averaged slope on a generic cross section.

5.3.1   *Data Processing*

In order to derive the river width, water surface elevation and water slope for use in each algorithm, 10 m resolution water depth rasters were created for the 2000-2001 period using HEC-Geo-RAS (Ackerman 2009). To generate these rasters, first the HEC-RAS model was used

138

to produce river cross sections at 100 m increments using a built in HEC-RAS interpolation tool. These cross sections were imported into GIS from HEC-RAS with the help of HEC-GeoRAS, resulting in 10 m resolution river bathymetry rasters. The generated river bathymetry was merged with 300 m resolution dry land DEMs of the study reaches provided by the Bangladesh Water Development Board (BWDB) and resampled to 10 m. These dry land DEMs were used because their elevations are based off the same local datum, mPWD (meter Public Work Datum), as the HEC-RAS model. Figure 5.6 shows the 300 m BWDB DEM and the HEC-RAS generated bathymetry (left), as well as the resulting 10 m merged DEM with river bathymetry (right) for the Mohananda River. Next, river depth data output taken from the HEC-RAS model of the study reaches were imported into GIS using HEC-Geo-RAS, resulting in 10 m resolution water depth rasters. These water depth rasters were then merged with the dry land DEMs with river bathymetry to convert them into water surface elevation layers.
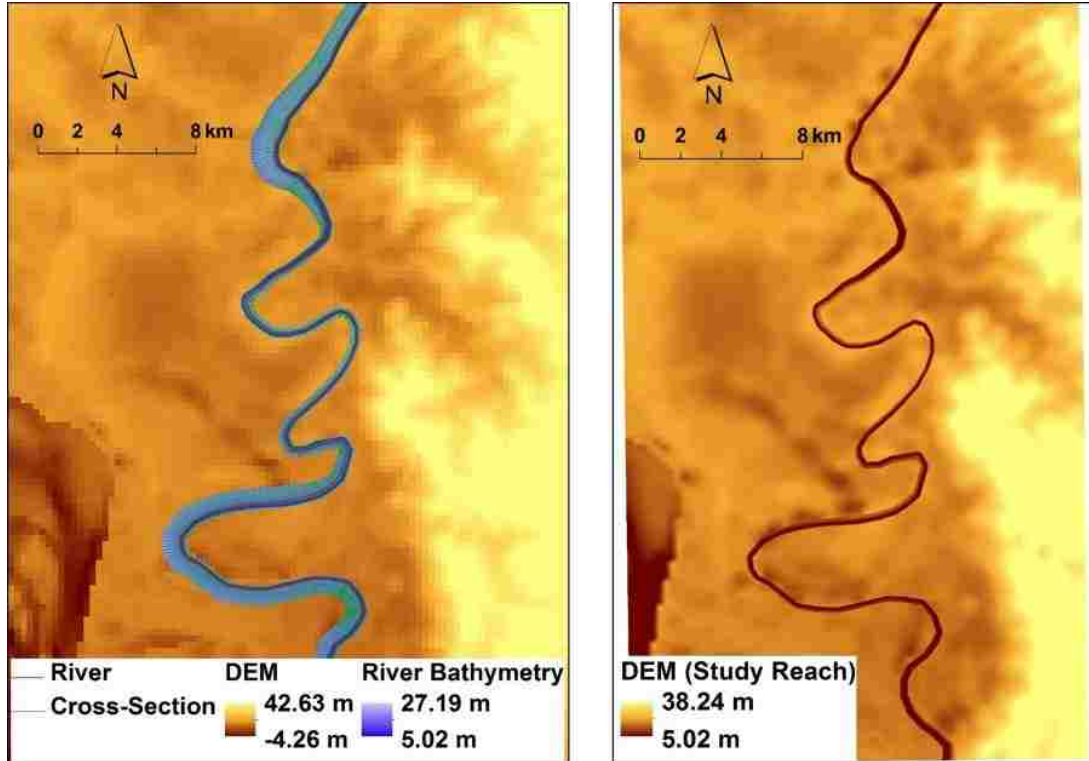
Figure 5.6. 300 m dry land DEM from the Bangladesh Water Development Board and river bathymetry from HEC-RAS model before merging (left) and 10 m merged dry land DEM with river bathymetry (right).

River width and height were extracted from the water surface raster by first dividing the raster into 100 m lengths (along river centerline) according to each cells proximity to points on the river centerline corresponding to 100 m increments (i.e. pixels were grouped with their nearest centerline point). River height in each 100 m increment was taken as the average height of all pixels within the 100 m length. River width in each 100 m increment was calculated by dividing the surface area of each increment (number of pixels multiplied by pixel area) by 100 m (the length of the increment). Figure 5.7 illustrates this data extraction process, from the combination of dry land DEMs with water surface DEMs, to averaging in 100 m increments to generate width, elevation, and slope along the entire reach. River heights and widths were

140

averaged across each increment for each of the selected 36 days of the study period in 2001 for the comparison between algorithms. These reach averaged observations are shown in Figure 5.8. In this study, it was assumed that the water slope, width and height data extracted from the water surface DEMs are a perfect representation of actual river conditions.
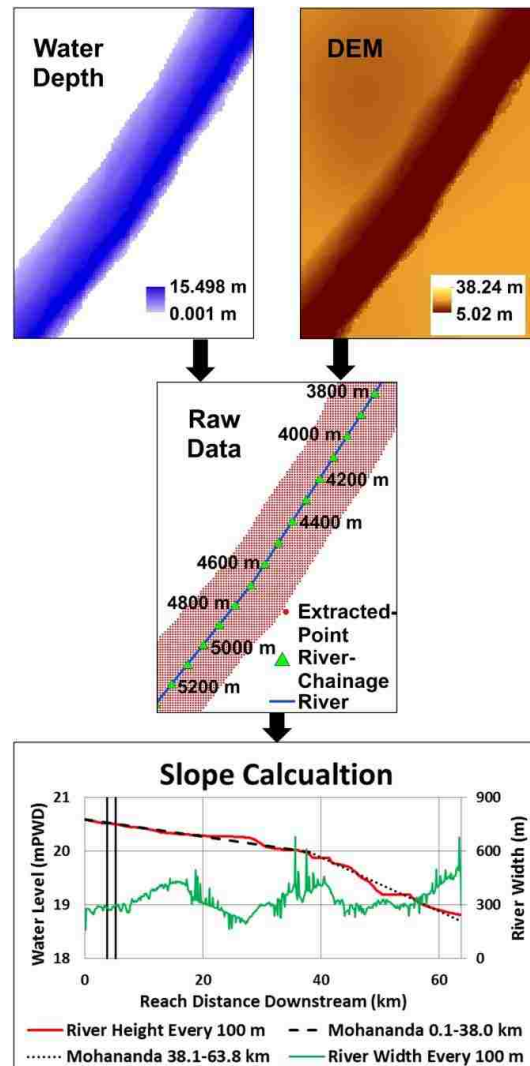
Figure 5.7. Data processing technique to determine slope of a reach and river width. The 'DEM' in the upper right panel represents the dry land (without water) elevation model. This DEM was merged with the water depth layer (upper left) to generate the water elevation layer (middle). From the water surface elevation layer, width, elevation and slope were extracted (bottom). The

black vertical lines in the bottom figure show the location along the reach of the data shown in the top and middle figures. Elevation of water surface is relative to a local datum called meter Public Water Datum (mPWD) which is about 0.45 m above local mean sea level.
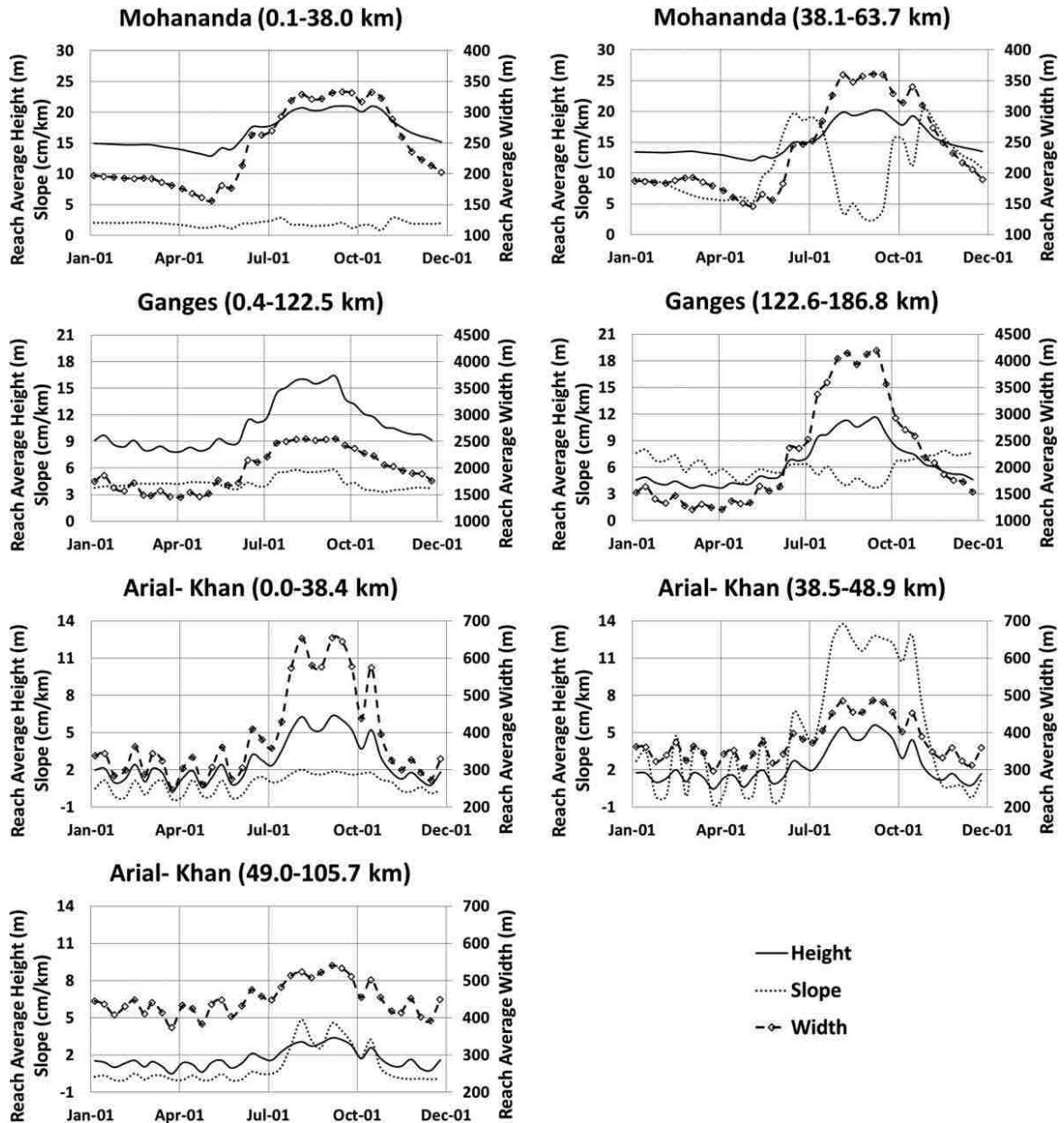
Figure 5.8. Reach averaged water surface height, width and slope (slope is positive at downward direction) of study reaches for 36 days of the independent validation period in 2001.

Preliminary tests of the AMHG method showed that it exhibited inadequate skill when applied over the entire year of the study period in 2001. Because of the high variability of both river width and discharge between the dry and wet seasons and a change in flow regime (within-bank flow versus floodplain flow), we separated the test into two periods: dry season and wet season. To properly compare the performance of the AMHG method to the other two approaches, similar time-period specific error statistics for the MFG and Metropolis Manning algorithm were calculated. The dry season of 2001 was defined as January 5th through May 15th and the wet season was defined as May 25th through December 25th. May 15th was chosen because in all three rivers, it marks the beginning of sharp increases in flow rate as well as height and width. Shifting this date earlier or later by a few days did not have a significant impact on the results.

5.3.2   *Application of the SWOT Simulator*

In order to better understand how the algorithms will perform with real observations, the SWOT simulator (introduced in Chapter 4) was applied in a manner that allowed the exploration of SWOT uncertainty on discharge estimation for Mohananda River. Here, river elevation measurements were simulated for each of the 36 days from 2001 using the HEC-RAS generated water depth files. These water heights were averaged within each 100 m long increment and used to determine the slope. The width was taken from the raster file generated from HEC-RAS output, because at the time of writing, estimating river width amongst SWOT location error had not been well established. No uncertainty was considered for width observations in this study.

The 10 m dry land DEMs with river bathymetry described earlier provided the floodplain topography and river bathymetry needed for the simulator. Additionally, the water surface elevation layers generated from HEC-GeoRAS were used as inputs in to the simulator. The

143

simulator applied random and topographical errors to these water surface elevation layers and created new water surface layers representative of expected SWOT measurements (Figure 5.9). Since river surface extent could not be extracted from the simulator output, only height errors occurring within the original water surface were considered. Simulated elevation measurements with high vertical error also exhibit high geolocation error, causing them to be located outside the water surface mask. Thus, excluding these points lead to an underestimation of the overall SWOT error. Additionally, it was assumed that no rainfall occurred during SWOT observations and tropospheric errors were neglected.
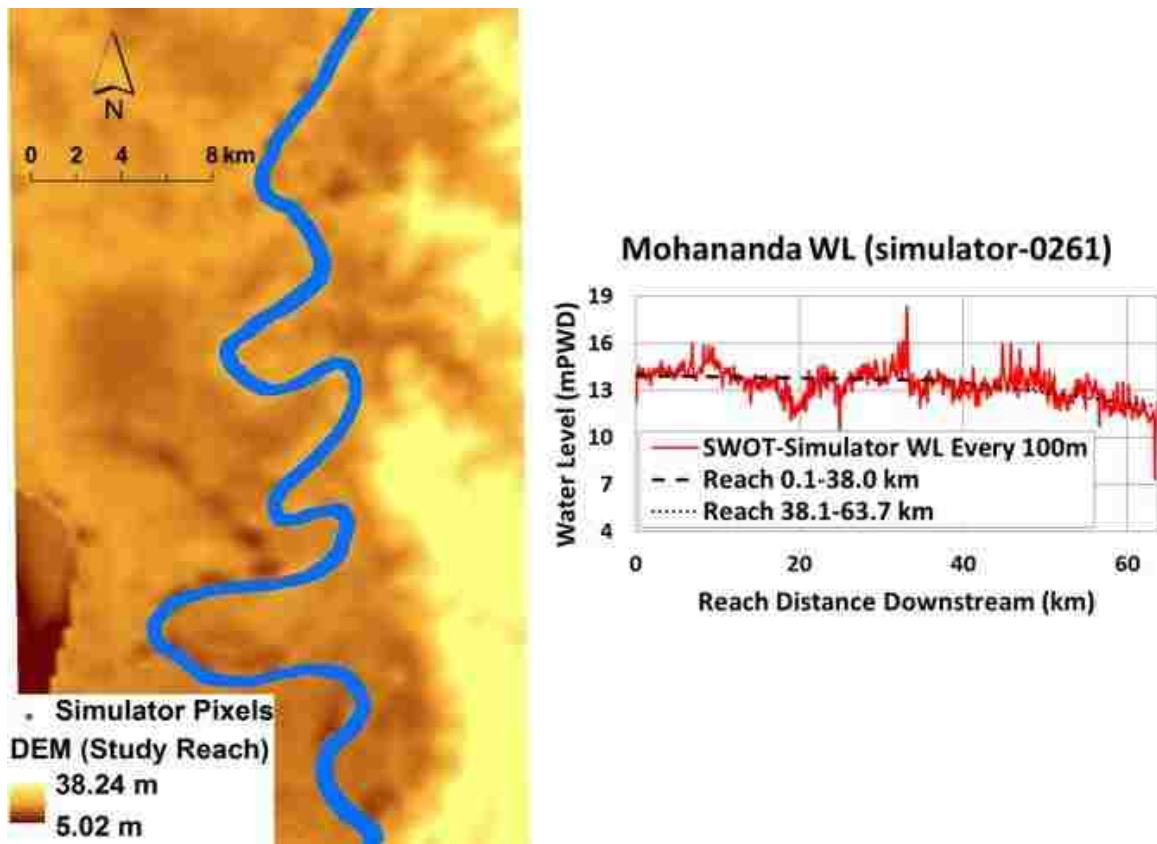
Figure 5.9. Application of the SWOT simulator. Water surface elevation raster generated by the SWOT simulator (Left); Averaged SWOT simulator WL at each 100 m increment of the Mohananda river (Right) on 15th April, 2001 (Orbit-0261).

The SWOT simulator typically runs for a complete cycle of 21 days (i.e. the simulated satellite flies over the same location on the earth every 21 days). Within this cycle, a river reach is expected to be covered at least once by the wide swath of the SWOT orbit. In higher latitudes the frequency of the coverage will be higher. The Mohananda river reach is entirely covered twice within a cycle by two orbits, once by the right swath of orbit-0261 and again by the left swath of orbit-0498 (Figure 5.10). The reach is passed by the orbit-0261 and orbit-0498 9.3 days and 17.8 days respectively from the cycle's starting date. Note that these different orbits result in slightly different simulated water surfaces due to differences in the location of the reach relative to the satellite (e.g. errors at the outer edges of the swath are different than errors at the inner edges of the swath). Here, discharge was estimated for both overpasses and averaged.
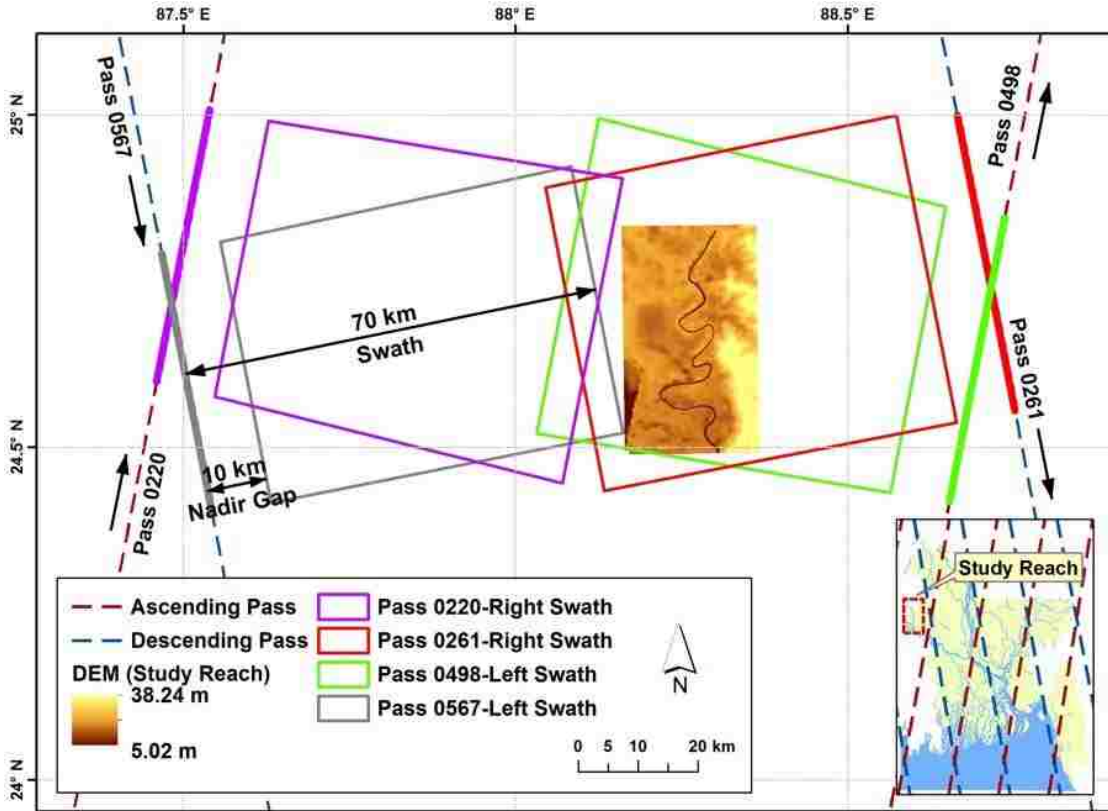
Figure 5.10. SWOT orbital pass and coverage over the Mohananda river reach. The lower right panel in the inset shows the SWOT coverage with a 21 day repeat cycle at 77.6 degree inclination.

5.3.3 *At-Many-Stations Hydraulic Geometry (AMHG)*

The AMHG algorithm proposed by Gleason, Smith, and Lee (2014) and Gleason and Wang (2015)is based on the hydraulic geometry relationship between river width (w) and flow rate (Q) given by Equation 5.1, or at-a-station hydraulic geometry (AHG) (Leopold and Maddock 1953). Gleason and Hamdan (2017) have also previously applied this method to the Ganges river using Landsat imagery in a proof-of-concept experiment, finding 28% RRMSE between estimated and observed dry-season flows.

$$w = aQ^{b} \tag{5.1}$$

146

Where w is the width of river surface at any cross section at any point in time, Q is the river discharge, and a and b are the hydraulic geometry parameters, which are unique to each cross section along a river. Gleason, Smith, and Lee (2014) first showed that a previously unknown relationship between a and b parameters existed, and termed this relationship as AMHG, given by Equation 5.2.

$$b = -AMHG \times \log(a) + AMHG \times \log(w_{glob}) \tag{5.2}$$

Where, w_{glob} is the mean of all observed widths in a study reach over space and time, *AMHG* is the slope of the $b - \log(a)$ relationship, and a and b are the hydraulic geometry parameters. AMHG thus relates cross sectional AHG parameters in space. A proxy for the slope of a river's AMHG which only requires repeated width measurements of the river reach, given by Equation 5.3, has been used to determine AMHG in the past.

$$\log(\max(w_{x1,x2,...xn})) = \frac{1}{AMHG} \log\left(\max(w_{x1,x2,...xn})^2 - \min(w_{x1,x2,...xn})^2\right) + p \tag{5.3}$$

Where, *AMHG* is slope of the $b - \log(a)$ relationship, $w_{x1,x2,...xn}$ is the width of river corresponding to each cross section of the reach and p is an empirical regression parameter. This relationship is not guaranteed to perfectly predict a river's AMHG. Gleason and Wang (2015) found this relationship to be unreliable, however it is assumed to apply to the rivers studied here. An exploration of the impact of using this proxy on discharge estimation is presented in Section 5.4.4.

Using Equation 5.3, the AMHG can be calculated for a given reach via linear regression, allowing the relationship between a cross section's a and b to be known. The p term represents the intercept of the linear regression and is not used in determining the AMHG. Next, an optimization routine (in this case a genetic algorithm (Gleason, Smith, and Lee 2014)is used to

147

determine the *a* and *b* parameters for each cross section in the river reach by minimizing the difference in flow rates between each cross section. The optimization routine is constrained in its search by AMHG and by discharge constraints proposed by Gleason, Smith, and Lee (2014). The genetic algorithm is here run 50 times for 50 generations each, with random start points and an average of all the resulting flow rates is output as the river reach's discharge. The results were insensitive to the number of genetic algorithm runs (this is consistent with the sensitivity analysis performed in Gleason and Wang (2015)) and 50 runs of 50 generations were used, because this matched the procedure used in Gleason, Smith, and Lee (2014). Figure 5.11 shows a flow chart breakdown of the implementation of the AMHG algorithm.

AMHG Algorithm Flowchart

Inputs: Time Series of River Width

Calculate AMHG slope from width proxy

Genetic Algorithm finds optimal *a-b* pairs for one pair of cross sections

Repeat for all possible unique cross section pairs

Use *a-b* pairs to obtain many estimates of Q from $w = aQ^b$

Estimates of Q averaged to obtain river reach discharge

MFG Algorithm Flow Chart

Long Term Observed:
Avg. Height (H_o)
Avg. Width (W_a)
Mean Annual Discharge (Qa)

Estimated Manning's *n*

Daily Data:
Width (W)
Height (H)

Constant:
Prior Manning's *n* (n_a)
Slope (S)
Shape Factor (B)

Calibration: H_0 c1, x1

Estimated Discharge

Average Discharge

Metropolis Manning Algorithm Flowchart

Time Series of river width, height, and slope

Prior values of A_0, n and standard deviations of each

$$\delta A = \frac{w(r,t) + w(r,t+1)}{2} * (h(r,t+1) - h(r,t))$$

Error Function
$$\Theta(r,t) = \delta\bar{Q} + \frac{\delta A(r,t) - \delta A(r,t-1)}{\Delta t} - \bar{q}(r,t)$$

Minimize error function using the stochastic sampling algorithm, Metropolis Algorithm

Estimates of Q for each reach

Figure 5.11. Flow chart of steps to calculate discharge using the AMHG algorithm (top), the MFG algorithm (middle) and the Metropolis Manning algorithm (bottom).

A brief sensitivity analysis was performed to determine the sensitivity of the AMHG method to the number of cross sections used to calculate discharge. It was found that the method was insensitive to this parameter as long as more than 15 cross sections were used. In this study, we used 25 equally spaced cross sections for each reach to balance the 15 cross section limit found in the sensitivity analysis while maintaining fewer cross sections to achieve reasonable

149

computation speed. The water surface widths at these cross sections were taken from the 10 m water surface DEM generated from HEC-GeoRAS.

5.3.4   *Mean Flow and Geomorphology Algorithm*

The MFG algorithm is developed from conceptual approaches discussed in Bjerklie et al. (2003; 2005). The algorithm assumes a mean value for the Manning friction coefficient that is modified based on the change in cross-sectional flow area, assumes a regular geometric shape for the cross-section such that the change in maximum depth measured by change in stage can be translated into the change in the mean flow depth of the cross-section, and assumes a minimum or zero flow stage. The general relation is given in Equation 5.4.

$$Q = \frac{1}{n}([H - H_o]Y^*)^{\frac{5}{3}}WS^{\frac{1}{2}} \tag{5.4}$$

Where, n is the estimated Manning's resistance coefficient, W is the observed width, H is the observed height, S is the mean slope of the river (water surface assuming equivalent to energy slope), Y^* is the fraction to derive mean cross section depth, equal to $1 - \frac{1}{1+B}$, where B is the shape factor (2 for parabolic cross section and 10 for Rectangular cross section) and H_o is the zero flow depth, which is individually calibrated with mean annual flow.

The mean water surface slope was derived from the HEC-RAS model output for the year 2000. A rectangular cross section was assumed in calculating Y^* (with B equal to 10). The Manning *n* value is assumed to be associated with the mean value of channel width and stage. This Manning n value is varied according to the change in channel cross-section as indexed by Equation 5.5.

$$n = c1\left(\frac{WH}{W_aH_a}\right)^{x1}n_a \tag{5.5}$$

150

Where W_a is the long term average of observed width, H_a is the long term average of observed height and n_a is the input average Manning's n

The long term width and height observations were taken from the daily output from the HEC-RAS model for the year 2000. The input average Manning's n used here was 0.025. Section 5.4.5 shows that this method is relatively insensitive to the Manning roughness input. The coefficients, $c1$ and $x1$, remain constant through time and were calibrated based on daily water surface elevation and mean annual discharge from the same HEC-RAS model output for the year 2000. While an entire year of daily data was used here, the calibration of these coefficients can proceed using limited time series of stage or general relationships developed on rivers in a similar setting and then further calibration can be performed as more satellite observations become available. For the three rivers studied here, the difference between annual average height, width, slope, and discharge calculated from daily values and calculated from a more limited time series (the 5th, 15th, and 25th of each month) were less than 0.1%, ultimately leading to no difference in discharge estimation. It is anticipated that initial empirically derived default values for B, n_a, $c1$ and $x1$ can be optimized over time based on validation time series, and improved understanding of the relation between the coefficient values and river characteristics.

The value for the minimum flow depth H_0 is optimized by calibrating the time series of observed width, stage and slope to the mean discharge for the river, and as such is dependent on knowledge of the mean discharge. It is assumed that the mean discharge is available from various global data bases, or from global circulation and hydrologic models, or from other sources. The parameterization of Manning n cannot address tidal flux, because in these environments the relation between change in Manning n and change in cross-section does not

necessarily have any validity. This is because the flow resistance is dominated by backwater effects and varies substantially during periods of adverse (upstream) slope (incoming flood tide) and downstream slope (outgoing ebb tide). However, a modified relation between cross-sectional change and slope could be developed to account for this deficiency.

The MFG algorithm relies on the prior estimation of average Manning's n (n_a) and mean annual flow to calibrate the H_o. The sensitivity of the algorithm to prior estimations of these parameters is explored in Section 5.4.5. This discharge estimation algorithm can be applied to calculate cross sectional discharge as well as reach averaged discharge. In this study, reach averaged observations were used for this method resulting in reach averaged discharge. Figure 5.11 shows the algorithm structure for calibrating $c1$, $x1$ and H_0 and estimating discharge.

5.3.5   *Metropolis-Manning Algorithm*

The Metropolis Manning algorithm also uses a form of Manning's equation paired with mass conservation as a basis for determining discharge (Durand et al. 2014). Equation 5.6 shows Manning's equation as used by this algorithm. Note that the bar signifies reach averaged quantities.

$$\overline{Q}(r,t) = \frac{1}{n(r)}\left[\overline{A}_0(r) + \delta\overline{A}(r,t)\right]^{5/3} w(r,t)^{-2/3}\overline{S}(r,t)^{1/2} \tag{5.6}$$

Where, *r* denotes reach, *t* denotes time step, *n* is Manning's n, A_0 is the base flow area, δA is the deviation in flow area from base flow area, *w* is the river top width, *S* is the river slope, and *Q* is the river discharge. Equation 5.7 gives the mass conservation of the river.

$$\frac{\partial\overline{Q}}{\partial x}(r,t) + \frac{\partial\overline{A}}{\partial t}(r,t) = \overline{q}(r,t) \tag{5.7}$$

152

Where, $\dfrac{\partial \overline{Q}}{\partial x}$ is the partial derivative of flow rate with respect to the downstream direction, $\dfrac{\partial \overline{A}}{\partial t}$ is

the partial derivative of flow area with respect to time and $\overline{q}$ is the reach averaged lateral

inflows. Discretizing Equation 5.7 between two remote sensing overpasses gives Equation 5.8.

By minimizing Equation 5.8, the optimal Manning's n and base flow area can be obtained.

$$\Theta(r,t) = \delta_{r,t}\overline{Q}_{r,t} + \frac{\delta\overline{A}(r,t) - \delta\overline{A}(r,t-1)}{\Delta t} - \overline{q}(r,t) \qquad (5.8)$$

Where, $\Theta(r,t)$ is the error for reach *r* at time *t* and $\delta_{r,t}$ is a constant dependent on length of reach,

see Durand et al. (2014)for more details

The error term in Equation 5.8 is minimized using a stochastic sampling algorithm known

as the Metropolis algorithm that uses a Bayesian probability updating scheme to create a Markov

chain of the unknown parameters, *n* and A_0. The Markov chain is run for 100,000 iterations and

the end result is likely values for the Manning's n and base flow area. With these parameters

known, Equation 5.6 is solved to provide discharge.

In this study, lateral inflow (q) was assumed to be 0. This is valid for the synthetic

experiment in this study , because the HEC-RAS model does not take into account smaller

tributaries, distributaries or groundwater effects. In application, this assumption would likely

decrease the accuracy of this method. The prior base flow area (A_0) was estimated using

minimum river width and discharge from the year 2000 calibration data set and assuming a water

depth of 1m. The standard deviation of this base flow area estimate was set as 20% of the base

flow area estimate. The initial estimate of Manning's *n* was taken as 0.025 with a standard

deviation of 0.01. The standard deviation of slope, height and width for all reaches were defined

as 0.5 cm/km, 1 cm and 1 m, respectively. These values represent the uncertainty in the

observations. To test the algorithmic uncertainty of the Metropolis Manning algorithm, the

observations are assumed to be perfect. However, this algorithm requires these values to be non-zero. For this reason, relatively small standard deviations of the observations were selected.

This algorithm was designed to operate using more than three river reaches. Here, the study reaches were discretized further, similar to the manner Durand et al. (2014) further discretized their study reach of the River Severn. In this past study, river sub-reaches ranged from 6.7 km to 8.2 km. Here, we partitioned each study reach in an attempt to match the reach length used in Durand et al. (2014). However, this was balanced against the increasing computational expense caused by increasing the number of reaches. The Ganges was split into nine sub-reaches (each approximately 20 km in length), the Mohananda was split into six sub-reaches (each approximately 10 km in length) and the Arial-Khan was split into five sub-reaches (each approximately 20 km in length). All sub-reaches maintained the 100 m spacing between width and height observations described in Section 5.3.2. Since this algorithm provides reach averaged discharge, length weighted average discharges were calculated which correspond to the original study reaches defined in Section 5.2 for comparison to the other two algorithms.

154

5.4 RESULTS

5.4.1 *Ganges River Results*

Figure 5.12 shows the reach averaged discharge estimated by the discharge algorithms on the two sub reaches of the Ganges River and Table 5.1 provides root mean squared error (RMSE), relative root mean squared error (RRMSE), bias, and percentage of error that is bias for each algorithm. The RRMSE is the RMSE relative to the average observed discharge (from HEC-RAS model) and expressed as a %. All three algorithms provided satisfactory results during the dry season (48% to 54% RRMSE) for the first reach (0.4km to 122.5km). The Metropolis Manning algorithm showed much greater accuracy on the dry season of the second reach (17.9% RRMSE) with the other two algorithms showing performance similar to their first reach performance. The AMHG algorithm significantly reduces in skill during the wet season when compared to the other two algorithms. This is in contrast to previous application of AMHG in the basin, as Gleason and Hamdan (2017) used Landsat imagery to demonstrate AMHG for the Ganges near Hardinge Bridge, and they found an RRMSE of 28% for dry season flows when compared to discharge measured on the same day as the Landsat images. However, a difference is expected because Gleason and Hamdan (2017) used real observations and assumed an AMHG parameter that matched with observations. The Metropolis Manning algorithm also showed a decrease in accuracy during the wet season on both reaches which corresponds to an increase in error associated with bias. The MFG algorithm performed better in the wet season than the dry season with 10% to 15% lower RRMSE. This increase in performance is accompanied by a large decrease in the error associated with bias. Overall, the MFG algorithm outperforms the Metropolis Manning and AMHG algorithms in the wet season, while each algorithm appears to perform well in the dry season.
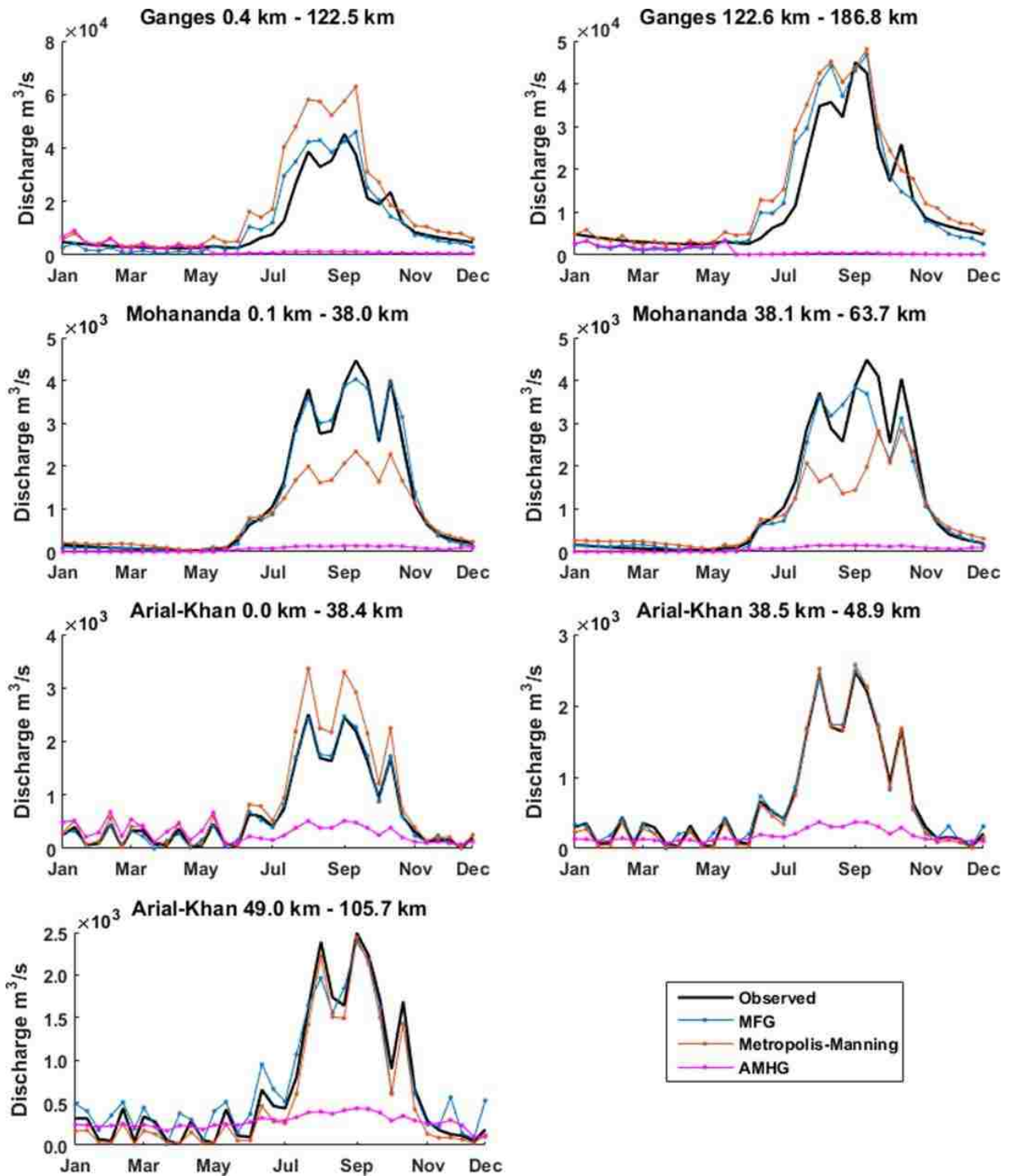
Figure 5.12. Comparison of performance of each algorithm on the Ganges, Mohananda, and Arial-Khan Rivers during the independent validation period of 2001.

Table 5.1. Error statistics of the discharge algorithms for Ganges River during the study period of 2001.

Ganges 0.4km - 122.5km						
	MFG		Metropolis-Manning		AMHG	
	Dry	Wet	Dry	Wet	Dry	Wet
RMSE [m^3/s]	1592	5741	1745	13159	1779	20530
RRMSE [%]	48.4	34.4	53.1	78.8	54.1	122.9
Bias [m^3/s]	1542	2191	1110	9387	812	15244
% of Error from Bias	96.8	38.2	63.6	71.3	45.6	74.3
Ganges 122.6km - 186.8km						
RMSE [m^3/s]	1574	5384	589	6998	1310	21217
RRMSE [%]	47.8	32.2	17.9	42.0	39.8	126.8
Bias [m^3/s]	1594	1961	137	4890	1307	15566
% of Error from Bias	97.7	36.6	23.2	69.9	96.2	73.5

5.4.2   *Mohananda River Results*

Figure 5.12 shows the results of the discharge algorithms on the two sub-reaches of the Mohananda River and Table 5.2 provides RMSE and RRMSE for each algorithm. The MFG algorithm showed skill in both seasons, with better performance in the wet season than the dry season. The Manning Metropolis algorithm also performed better in the wet season than the dry season, but the extracted discharge estimates were much worse than those of the MFG algorithm. A large percentage of the Metropolis Manning's error during the dry season was associated with bias. The AMHG was unable to extract skillful discharge estimates during both dry and wet seasons for both river segments. A possible cause of this is the inability of the width proxy to accurately estimate the Mohananda River's AMHG parameter for both dry and wet seasons. This

157

idea is explored further later in this section. The MFG algorithm shows a clear performance

advantage over the other two algorithms on the Mohananda River.

Table 5.2. Error statistics of the discharge algorithms for Mohananda River during the study
period of 2001

Mohananda 0.1km – 38.0km						
	MFG		Metropolis-Manning		AMHG	
	Dry	Wet	Dry	Wet	Dry	Wet
RMSE [m³/s]	29	197	66	1049	90	2412
RRMSE [%]	35.9	10.5	81.7	55.9	110.8	128.5
Bias [m³/s]	19	6	58	644	80	1702
% of Error from Bias	66.5	3.1	88.2	61.4	89.2	74.0
Mohananda 38.1km – 63.7km						
RMSE [m³/s]	47	480	119	1034.7	90	2406
RRMSE [%]	58.0	25.6	146.0	55.2	109.7	128.4
Bias [m³/s]	19	192	116	570	80	1697
% of Error from Bias	39.7	39.9	97.0	55.1	89.6	74.0

5.4.3   *Arial Khan River Results*

Figure 5.12 shows the results of the discharge algorithms on the three sub reaches of the

Arial Khan River and Table 5.3 provides RMSE and RRMSE for each algorithm. It is important

to note that the AMHG and MFG algorithms are unable to vectorize flow as Metropolis Manning

algorithm (positive flow is flow along the downstream direction; negative flow is flow in the

upstream direction), but should still properly capture the magnitude of the flow when a river

switches flow direction. The output of these two algorithms were therefore compared with the

absolute value of the observed discharge for a more accurate error analysis during the dry season

with heavy tidal effects (i.e., during high tide). This is realistic because while the algorithms

158

themselves have no method of determining flow direction, it can easily be determined form SWOT observations of river slope. Figure 5.12 shows the absolute value of the observed discharge and the absolute value of the Manning Metropolis estimated discharge to show a fairer comparison between each algorithm output.

Table 5.3. Error statistics of the discharge algorithms for Arial Khan River during the validation period of 2001.

Arial-Khan 0.0km – 38.4km						
	MFG		Metropolis-Manning		AMHG	
	Dry	Wet	Dry	Wet	Dry	Wet
RMSE [m³/s]	64	64	75	408	187	957
RRMSE [%]	29.7	6.9	35.0	43.9	86.8	102.8
Bias [m³/s]	7	18	57	288	170	639
% of Error from Bias	10.4	27.8	75.2	70.7	90.7	66.8
Arial-Khan 38.51km – 48.9km						
RMSE [m³/s]	86	68	60	54	168	1072
RRMSE [%]	42.2	7.3	29.4	5.8	82.1	115.0
Bias [m³/s]	23	24	49	22	74	700
% of Error from Bias	26.1	35.4	81.1	41.2	43.8	68.5
Arial-Khan 49.0km – 105.7km						
RMSE [m³/s]	182	215	114	163	146	1023
RRMSE [%]	94.5	23.0	58.9	17.5	75.7	109.6
Bias [m³/s]	125	37	80	144	46	610
% of Error from Bias	68.4	17.2	70.6	88.3	31.6	62.5

For all three reaches of the Arial-Khan River, both the MFG and Metropolis Manning algorithms showed high skill during the wet season (6.9% to 23.0% RRMSE). Dry season discharge estimation was more challenging for all three approaches than wet season, possibly

159

due to the high tidal effects on the river causing diurnal change in flow regime from within-bank to floodplain flow quite frequently. The Metropolis Manning algorithm was the only one to consistently provide accurate discharge estimations during the dry season. The Metropolis Manning algorithm showed high error associated with bias while the MFG algorithm's error showed less bias. Once again, the AMHG algorithm failed to produce skillful discharge estimates, possibly caused by the method's width proxy inaccurately estimating the AMHG parameter.

5.4.4   *Improving the AMHG Algorithm*

To better understand where the large errors from the AMHG may be originating from, estimation of the AMHG slope was examined via the width proxy. The AMHG for each river for the year 2001 for both dry and wet seasons were obtained from the river width proxy (Equation 5.3) and compared to the AMHG calculated directly from the HEC-RAS model widths and discharge that represent the river's true AMHG. Table 5.4 shows these AMHG parameters, as well as the R^2 statistic of the directly calculated AMHG as a measure for how tight the a-b relationship for the river is. The table also shows the percent difference between the proxy estimated AMHG and the directly calculated AMHG.

Table 5.4. Comparison between proxy AMHG and Observed 'true' AMHG.

River	Reach	Directly Calculated AMHG	Direct AMHG R^2	Proxy Estimated AMHG	% Difference between Proxy and Direct
Ganges Dry	0.4km – 122.5km	-0.1189	0.99	-0.0901	27.6
	122.6km – 186.8km	-0.1208	0.97	-0.4502	115.4
Ganges Wet	0.4km – 122.5km	-0.0965	0.99	-0.4157	124.6
	122.6km – 186.8km	-0.1052	0.93	-0.2725	88.6
Arial-Khan Dry	0.0km – 38.4km	-0.1095	0.88	-0.2793	87.3
	38.5km – 48.9km	-0.0244	0.04	-0.3141	171.2
	48.9km – 105.7km	-0.0108	0.04	-0.2377	182.6
Arial-Khan Wet	0.0km – 38.4km	-0.1540	0.96	-0.3712	82.7
	38.5km – 48.9km	-0.0449	0.30	-0.0484	7.5
	48.9km – 105.7km	-0.0665	0.56	-0.2708	121.1
Mohananda Dry	0.1km – 38.0km	-0.0883	0.71	-0.4958	139.5
	38.1km – 63.7km	-0.1207	0.68	-0.3741	102.4
Mohananda Wet	0.1km – 38.0km	-0.1048	0.83	-0.4134	119.1
	38.1km – 63.7km	-0.1302	0.89	-0.4081	103.3

As can be seen in Table 5.4, the proxy incorrectly estimated the actual river AMHG for almost all of the river reaches. Furthermore, one of the only AMHG slopes estimated correctly, that of the Arial-Khan Wet 38.5 km – 48.9 km, exhibited a very loose AMHG ($R^2 = 0.3$), which is indicative that the AMHG method may not perform well. The other fairly closely estimated proxy, Ganges Dry 0.4 km – 122.5 km, resulted in more skillful results (54% RRMSE). However, the inaccurately estimated proxy for Ganges Dry 122.6 km -186.8 km resulted in lower uncertainties (39.8% RRMSE), the cause of which is unclear at this time. Nevertheless, the fact that the only reasonably accurate proxy estimate of AMHG resulted in one instance of the AMHG method accurately estimating discharge indicate that more accurate estimations of AMHG could lead to more successful applications of the AMHG method.

Thus, we tested a 'corrective' approach on the Ganges River data. The Ganges River daily discharge and river width data from HEC-RAS for the year 2000 was used to obtain estimates of the AMHG parameters. This width and discharge data was the same data provided to the MFG algorithm for calibration and the Metropolis Manning algorithm for prior parameter estimation. These were fed into the AMHG method with the same width data from the study period of 2001. Figure 5.13 shows the results of this approach of relying on a priori model based hydraulic parameters.
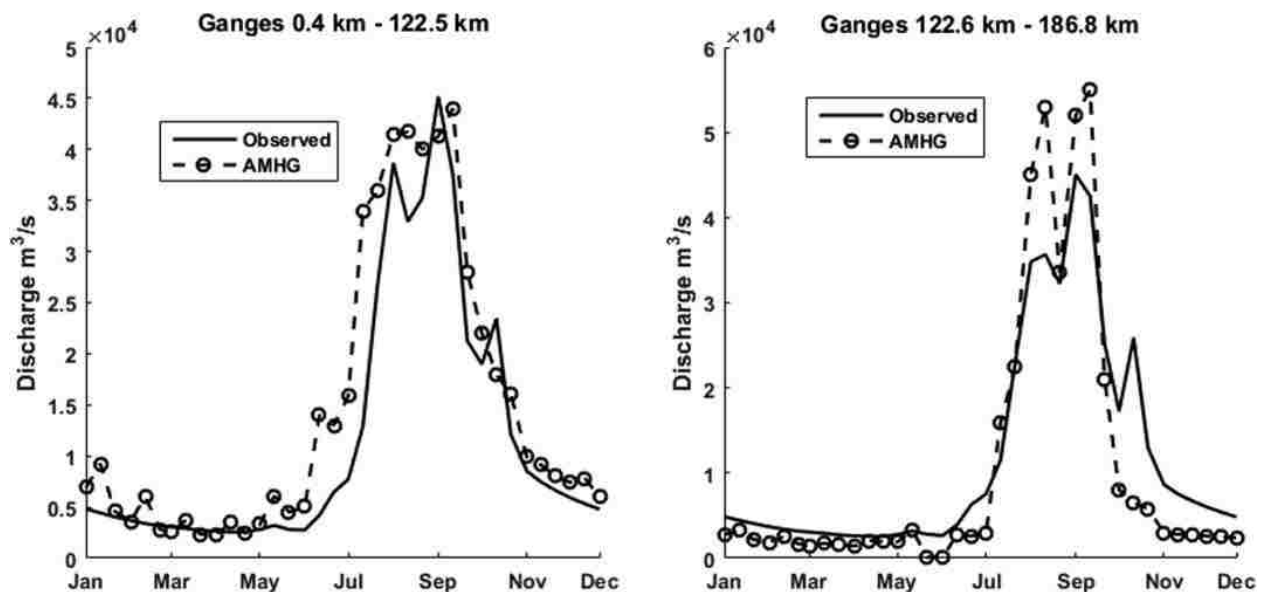
Figure 5.13. The AMHG algorithm performance using a priori AMHG knowledge from HEC RAS Model.

It is clear from Figure 5.13 that the AMHG discharge estimation accuracy is greatly improved for the Ganges River by using prior knowledge of the river's discharge. Table 5.5 shows the Ganges River error statistics using the corrective approach on AMHG values. This shows that the AMHG method can provide skillful discharge estimates with accuracies comparable to the MFG and Metropolis Manning algorithms, even during the wet season. The dependence on the proxy is further confirmed with the good AMHG performance found by

Gleason and Hamdan [2015] for the Ganges, where in their case they did not rely on the proxy but instead assumed an AMHG slope of -0.30, which agrees with observed data. Improving the performance of AMHG without use of a priori knowledge is a key challenge to the AMHG method and an area of active research: the AMHG method has limited utility for the rivers studied here without further refinement.

Table 5.5. Ganges River Error Statistics with corrected AHMG approach relying on a priori information

Ganges 0.4km - 122.5km						
	MFG		Metropolis-Manning		AMHG	
	Dry	Wet	Dry	Wet	Dry	Wet
RMSE [m^3/s]	1592	5741	1361	6724	1703	6776
RRMSE [%]	48.4	34.4	41.4	40.3	51.8	40.5
Ganges 122.6km - 186.8km						
RMSE [m^3/s]	1574	5384	1703	7082	1310	7869
RRMSE [%]	47.8	32.2	51.7	42.3	39.8	47.0

5.4.5   *Sensitivity to Algorithm Parameters*

The Metropolis Manning and MFG methods both require a priori information in order to estimate discharge. The Metropolis Manning method requires estimates for the Manning's roughness parameter as well as an estimate of cross sectional area under minimum flow conditions. The MFG method also requires an estimate of Manning's roughness as well as the average discharge of the river. Here, we tested the sensitivity of the estimated discharge from both algorithms to these input parameters. Each algorithm was run multiple times while varying these input parameters by modifying the original value (i.e. the parameter values used to generate the results in sections 4.1, 4.2, and 4.3) by ±5%, ±10%, ±25%, and ±50%. Only one parameter

was modified at a time and the sensitivities of the methods to changing more than one parameter at one time were not evaluated. The results of the sensitivity analysis are shown in Figure 5.14. For clarity, only the results from the Ganges reach 0.4 km – 122.5 km are shown. The trends shown here are representative of the algorithm sensitivities on all reaches. Figure 5.14 shows that the MFG method is not sensitive to changes in the input Manning's roughness parameter, with RRMSE remaining at a constant 40% for all tested values. The MFG method was sensitive to the input mean discharge, with RRMSE ranging from 39% at -10% of the original input value to 79% at +50% of the original input value. The Metropolis Manning method was also insensitive to changes in the input Manning's roughness parameter, with RRMSE remaining constant at 66% for all tested parameter values. The Metropolis Manning was sensitive to changes in the minimum flow area input, with RRMSE ranging from 62% at -10% of the original input value to 85% at +50% of the original value. For this reach, both methods appear to have a minimum error around -10% of the input parameters. On other reaches, this minimum error occurred at different changes in parameter values ranging from -25% to +10% and were not always in the same location for both algorithms (e.g. the minimum error for the second Ganges reach occurred at -25% for the MFG method, and at -10% for the Metropolis Manning method).
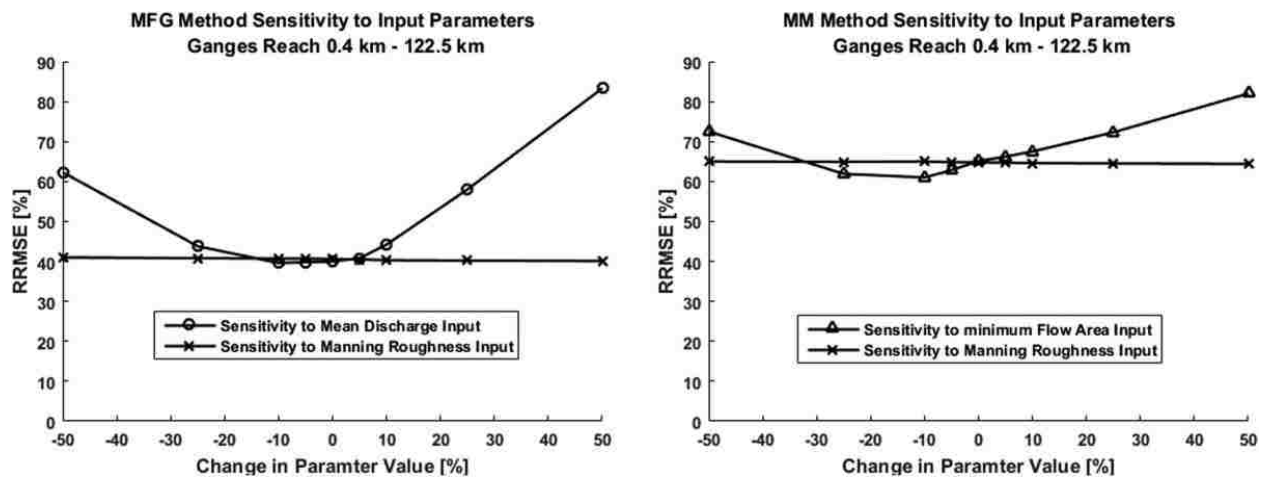
Figure 5.14. Algorithm sensitivities to change in input parameters for the Ganges reach 0.4 km - 122.5 km of the MFG method (Left) and the Metropolis Manning method (Right).

The sensitivity of both algorithms appears to be similar in magnitude. Both algorithms require a record of river observations in order to estimate the necessary input parameters. Repeated measurements of river cross sectional area during a river's dry season are needed to estimate minimum flow for the Metropolis Manning method. At least a one-year record of discharge estimates is required to accurately estimate a river's average discharge for the MFG method. This sensitivity analysis highlights the reliance of these two methods on good estimates for their input parameters, minimum flow area for the Metropolis Manning method and mean discharge for the MFG method.

5.4.6   *Implication for the Planned SWOT Mission*

To gain a basic understanding of the implications of the above results for the SWOT mission, SWOT simulated river height observations of the 36 days in 2001 for the Mohananda River were run through the MFG and Metropolis Manning algorithms along with river widths obtained from the HEC-RAS model. As we had only considered the simulated height from the

165

SWOT simulator (and not SWOT river widths) along with the true width (from HEC-RAS) of the river, the AMHG method's response to SWOT observables could not be tested.

The MFG and Metropolis Manning algorithms were applied using the river height and slope derived from SWOT simulator water level and the width data from the HEC-RAS simulation (the same data used in the previous section to test the algorithmic uncertainty) to calculate the discharge. Two sets of discharge were generated for each date, one by orbit-0261 output and another by orbit-0498 output. The average of these two sets is considered here as the discharge estimated from the SWOT simulator output. Figure 5.15 shows the observed and SWOT simulated algorithm discharge for the MFG and Metropolis Manning algorithms and Table 5.6 shows the corresponding error statistics.
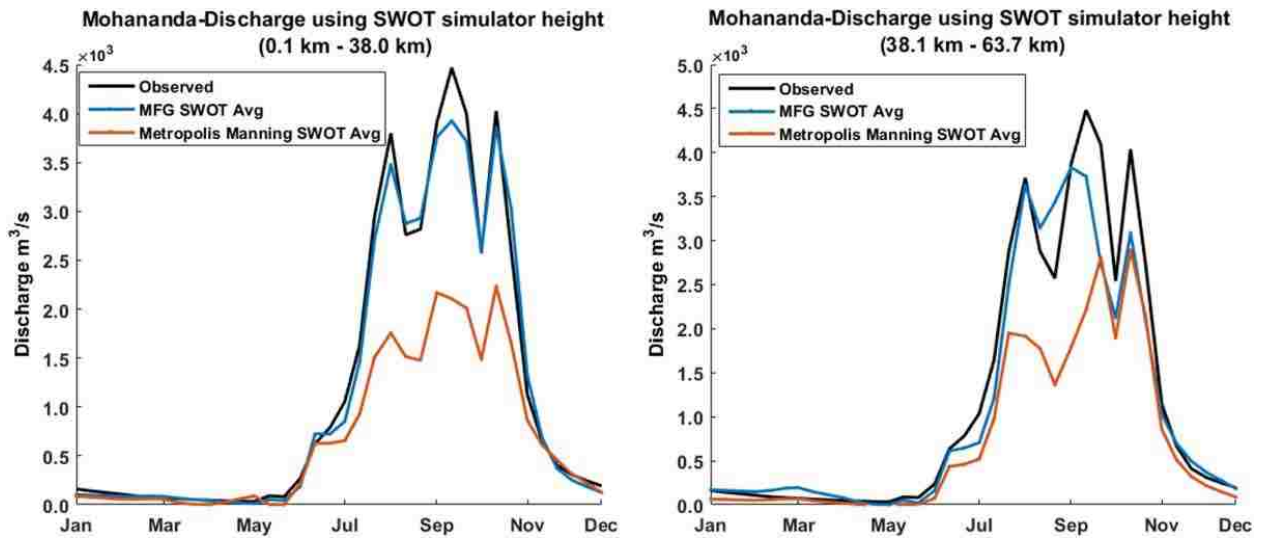

Figure 5.15. Algorithm sensitivities to change in input parameters for the Ganges reach 0.4 km - 122.5 km of the MFG method (Left) and the Metropolis Manning method (Right).

Table 5.6. Comparison of algorithm performance between discharge estimations using reference river observations and discharge estimations using SWOT simulated river observations

		RMSE [m³/s]		RRMSE [%]	
		Reference Observations	SWOT Simulated Observations	Reference Observations	SWOT Simulated Observations
0.1km - 38.0km					
MFG	Dry	29	25	35.9	31.4
	Wet	197	205	10.5	10.9
Metro-Man	Dry	66	51	81.7	62.3
	Wet	1049	1186	55.9	63.2
38.1km - 63.7km					
MFG	Dry	47	60	58	73.3
	Wet	480	487	25.6	26
Metro-Man	Dry	119	52	146.3	63.1
	Wet	1035	1036	55.2	55.3

Propagating remote sensing errors through the algorithms had two significant effects on discharge estimation accuracy. The MFG method in the second reach performed considerable less skillfully during the dry season (RRMSE increased by 15.3%). In contrast, the Metropolis Manning algorithm experienced a large increase in dry season accuracy in both reaches (RRMSE decreased by 19.4% and 83.2%). These accuracy increases could be the result of the SWOT simulated observations forcing the algorithm to search a wider range of parameter values to find the minimum error than the reference data. With the reference data, the Metropolis Manning algorithm could have converged to a local minimum and the introduction of SWOT errors could cause the algorithm to converge to a more optimal minimum. In all other cases, both algorithms performed only slightly worse than with reference observations. These results indicate that the Metropolis Manning algorithm may be more sensitive to uncertainty in remotely sensed river surface elevation. This is most likely due to the unrealistic assumption of no observational

167

uncertainty in river width, which at the time of writing this manuscript, a proper procedure to rationalize extraction of SWOT-river widths from the simulator was absent.

It should be noted that the minimum or zero flow stage in the MFG algorithm is analogous to the minimum flow area in the Metropolis Manning algorithm. Thus, the convergence of the MFG and Metropolis algorithms might be used as an additional objective function for optimizing the discharge estimation. Additionally, the AMHG could be used to derive a mean discharge as a function of width based on general regime theory [*Leopold and Wolman,* 1964] and used to calibrate the MFG zero flow depth and the Metropolis Manning minimum cross-section area. These considerations point to the advantage for synergistic application of multiple algorithms as a 'team'.

An important consideration for application of the algorithms is the reach length over which the slope should be derived, and which average values of width and stage should be assessed. In most cases, this length may be determined from observational data limitations, but in a best case scenario, should be related to a reach length that encompasses repeating geomorphic channel features such as a meander length, or a repeating braiding or multi-channel pattern, or riffle pool sequence.

5.5   CONCLUSIONS

This first tier of assessment of three discharge algorithms designed to work with data from the upcoming SWOT mission, showed that the MFG and Metropolis Manning algorithms generally outperformed the AMHG algorithm. Both the MFG and Metropolis Manning algorithms provided the better performance on different reaches and seasons, with at least one of the two typically producing discharge estimates with less than 50% RRMSE. Furthermore, the study found that the AMHG method can be improved during the wet season using *a priori*

168

information of discharge, and such improvement is needed for operational application of AMHG. The impact of SWOT estimation uncertainty of river height on discharge accuracy appeared insignificant. In general, the MFG method was found to remain relatively more accurate while the Metropolis Manning algorithm appeared more sensitive to SWOT height observation errors. However, the SWOT elevation errors estimated here were limited by excluding errors occurring outside the true water extent. Thus, the error simulated here is an underrepresentation of the overall errors expected from the SWOT mission. Future studies should further explore the effects of SWOT error on discharge estimation as more complete SWOT simulator packages become available.

Overall, the MFG algorithm appeared to be the most stable of the three discharge algorithms in the Ganges river system. However, its dependence on knowledge of prior mean river discharge and various hydraulic flow parameters (width and height etc.) suggests that it is not suited for a completely ungauged river system lacking in historical records. For the vast majority of cases in the developing world, the Metropolis Manning or AMHG method may be the more practical alternative for using satellite water elevation data to estimate discharge. Furthermore, the fact that the Metropolis Manning algorithm and the MFG algorithm seemed to excel in different cases and the region-specific correction improved AMHG performance, a multi-algorithm ensemble approach of algorithms working as a 'team' may be the future of space-borne discharge estimation. Ultimately, this chapter shows that SWOT is expected to provide skillful discharge estimates in tropical monsoonal rivers.

Chapters 4 and 5 have framed our current and near future ability to assess the volumetric impacts of reservoirs on river systems. Chapter 6 examines a different dimension of reservoir impacts, water quality, from a remote sensing perspective.

Chapter 6: Understanding Hydropower's Impact on River Temperature in the 3S River Basin

Note, this chapter has been adapted from a paper submitted to *Geophysical Research Letters*. At the time of writing, this paper is currently in review.

Abstract: Extensive hydropower dam development in the Mekong River Basin (MRB) is rapidly altering the natural state of the region's surface water. Despite efforts to understand these changes, one impact has gone unnoticed, the impact of hydropower dams on downstream river temperatures. This chapter uses thermal infrared observations from 30 years of Landsat satellite imagery and identifies a relationship between dry season water temperature cooling trends and dam development in the 3S Basin, a major tributary of the Mekong River. Rapid decreases in annual average dry season river temperature ranging between $0.7°$ C and $2°$ C occurred within a year of major dams beginning operations on the three major rivers in the 3S basin. Furthermore, in-situ water temperature observations confirmed decreasing river temperature for two major dam development events and showed that the temperature impacts of those dams could be as significant as $6°$ C reduction in some months. Other possible sources of the temperature anomalies investigated were precipitation, air temperature trends and deforestation, but all were are ruled out as potential drivers of the observed river cooling. Finally, this cooling effect was tracked downstream to the Mekong River, again utilizing the long record of Landsat thermal infrared observations. Evidence was found that the 3S outflow has been cooling the Mekong river downstream of the confluence, by as much as $0.8°$ C in recent years. Our study presents a very clear pattern between dam development in the 3S and cooling river temperatures. Given the cooling effects discovered here, understanding the thermal impacts of reservoirs in the MRB is critically important for understanding how fish and aquatic ecosystems will behave in the future.

In the face of continued widespread dam development plans in the MRB, uncovering the transformation by hydropower dams on the thermal regime of the river system should now be a top priority for sustainable water resources development.

6.1   INTRODUCTION

The previous chapters all focused on the impacts of reservoirs on water quantity (timing and magnitude of streamflows). However, reservoirs also have direct impacts on several aspects of water quality. One critical element of the impact of dams on water quality that has gone undetected is the aggregate effects of dams on downstream water temperature.

Hydropower dams tend to cool the downstream water temperature by releasing water from the penstock located at deeper levels of thermally stratified reservoirs (Sherman et al. 2007; Niemeyer et al. 2018). Changes in the thermal regime of rivers in the MRB threaten fish production downstream, a source of food and livelihood for millions (Mekong River Commission 2003; Ahmed et al. 1998). The Tonle Sap Lake, connected to the Mekong River, is home to one of largest inland fisheries in the world (Baran and Myschowoda 2009). Perturbations in the thermal regime of Tonle Sap Lake would have significant impacts on the health of the fish population (Ficke, Myrick, and Hansen 2007) and regional biodiversity (Liermann et al. 2012). The MRB severely lacks in-situ temperature monitoring stations, allowing dam driven temperature change to remain hidden and unexplored. Satellite remote sensing is a powerful and underutilized tool that can be harnessed to illuminate the potential thermal impacts of dams. The Landsat Mission thermal infrared (TIR) sensors are a promising option due to high revisit time (16 days), high spatial resolution (60m-90m), and a long historical record. Landsat TIR data has been used before to monitor river temperatures (Tavares et al.

2019; Dugdale 2016; Ling et al. 2017), but never in the context of the dam development in the MRB. Applying TIR observations to the MRB allows for the monitoring of river temperature in locations that were previously un-monitored, which is key for understanding the thermal impacts of current dams and predicting the impacts of dams that have yet to be built.

This study presents the results of the application of Landsat 5, 7, and 8 TIR observations towards monitoring changes in river temperature in the 3S Basin in an attempt to answer: *Are dams in the 3S Basin causing changes in stream temperature and if so, what are the impacts on the temperature of the Mekong River?*

6.2   STUDY REGION

The 3S Basin, the largest tributary to the Mekong River (Adamson et al. 2009), is a prime location to reveal the hidden thermal impacts of dams. The basin consists of three major rivers (Sekong, Sesan, and Srepok), draining from southern Lao PDR, western Vietnam, and eastern Cambodia before emptying into the Mekong River Figure 6.1. The 3S Basin is a microcosm of dam development in the MRB, with many small, upper tributary dams already built and progressively larger dams planned or under construction on the main rivers. In other words, what is now happening to the lower Mekong River in general has already happened to the 3S Basin since the 2000s and the two basins have strikingly similar hydro-climatic properties. While all three sub-basins are undergoing hydropower development, they are being developed at different rates[2]. Major dams on the Sesan River were constructed in 2001, 2008, and 2009, while major dams on the Sekong River were not installed until 2015 (WLE 2017). Direct comparisons of stream temperature trends between three basins at different stages of development allow for the identification of dam driven temperature changes. Beyond being an ideal testbed, the 3S Basin is

172

also critically important for the health of the greater MRB ((ADB)(Manila) 2006). The 3S Basin contributes 17-20% of the total MRB discharge (Adamson et al. 2009). In relatively close proximity to Tonle Sap Lake and the Mekong Delta with high hydrologic connectivity, the 3S basin is linked to crucial fish and rice production downstream. Understanding how river temperature is changing in the 3S Basin and the source of those changes is critical for better managing rice and fish production downstream (Matti Kummu and Sarkkula 2008; Arias et al. 2014). This is especially true in the coming decades, with more major dams planned for all three rivers.
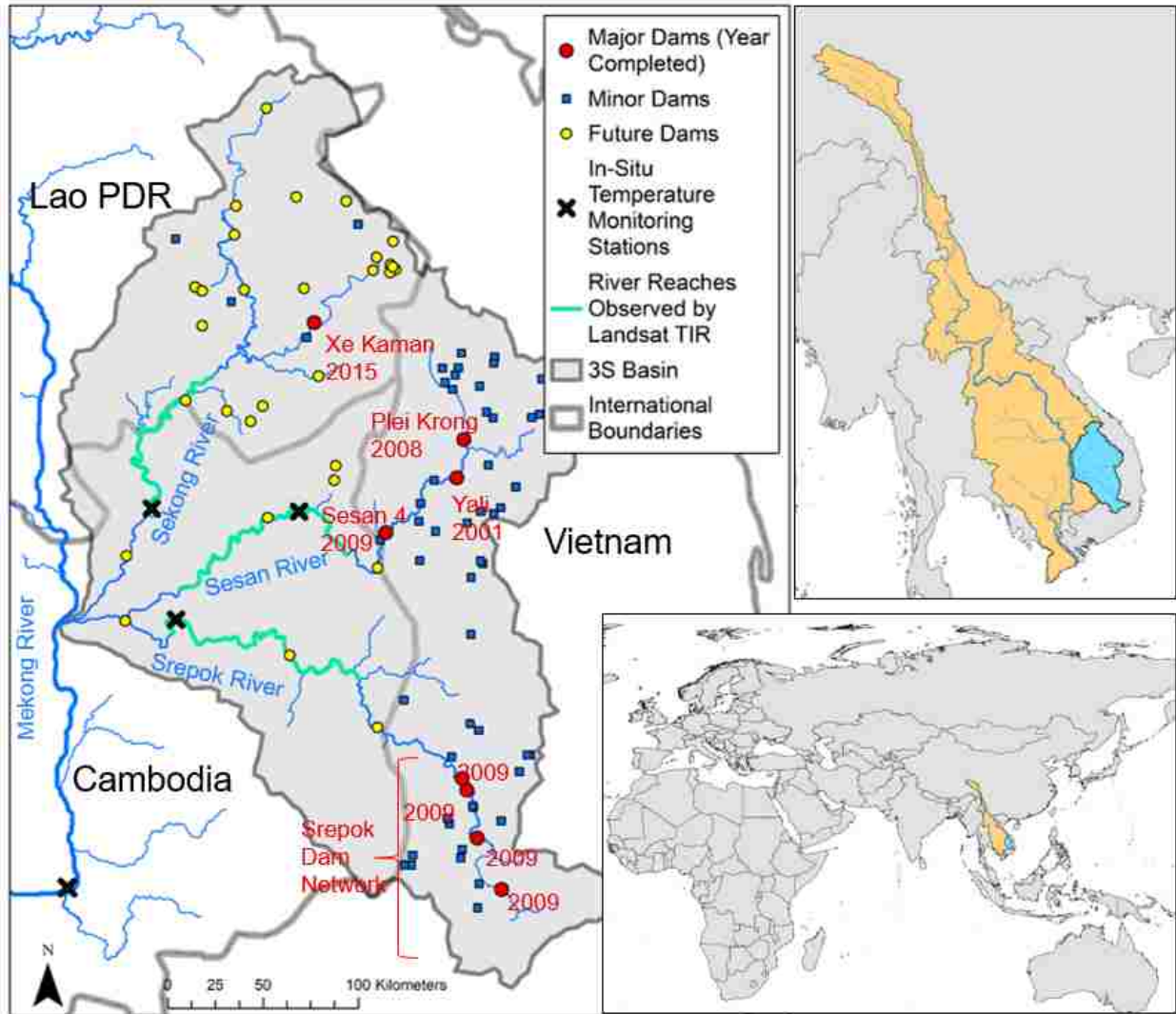
Figure 6.1. Map of 3S Basin showing existing and future (under construction, planned, and proposed) dams as of 2017 as well as the locations of three water quality monitoring stations. A distinction has been made between major and minor dams based on their expected thermal impact. Major dams were defined as dams located on a major river or a tributary with a significant impounded reservoir (>25 km^2 surface area). Minor dams consisted of dams on smaller tributaries, and run-of-the-river style dams on major rivers with no impounded reservoir and unlikely thermal stratification.

174

6.3 METHODS

6.3.1 *Landsat-Based Water Surface Temperature Estimation*

Water surface temperatures of the Sekong, Sesan, and Srepok Rivers were derived from Landsat 4,5, 7, and 8 thermal infrared (TIR) data. A flowchart of the temperature estimation process is shown in Figure 7. All computations were performed in Google Earth Engine. Before temperature estimation, several data screening processes were applied to ensure high quality temperature observations. Only images from January through April (corresponding with the late dry season) were considered because the presence of clouds in the other months resulted in very few useable images. First, visible, near infrared, and TIR images were cropped according to domains consisting of approximately 50 km reaches of each river. These domains were selected by locating the portions of the river wide enough to be reliably observed by Landsat TIR (with at least 3 pixels wide with resolutions ranging from 60 m to 100 m) and then taking the most upstream 50 km. These reaches all encompassed the in-situ water temperature monitoring stations so that Landsat based water temperature estimates could be validated. Water surface temperature estimates were relatively invariant down and up stream of these locations. After the Landsat images were cropped, a simple cloud filter was applied. For every cropped image, the cloud mask was extracted from the quality assessment data. If any pixels within the cropped region were flagged as containing clouds, the entire image was discarded and not used for temperature estimation. Next, the water areas within the image were classified using the Dynamic Surface Water Extent (DSWE) tests for open water body classification (Jones 2015). Pixels classified as open water with high confidence were retained and all other pixels removed.
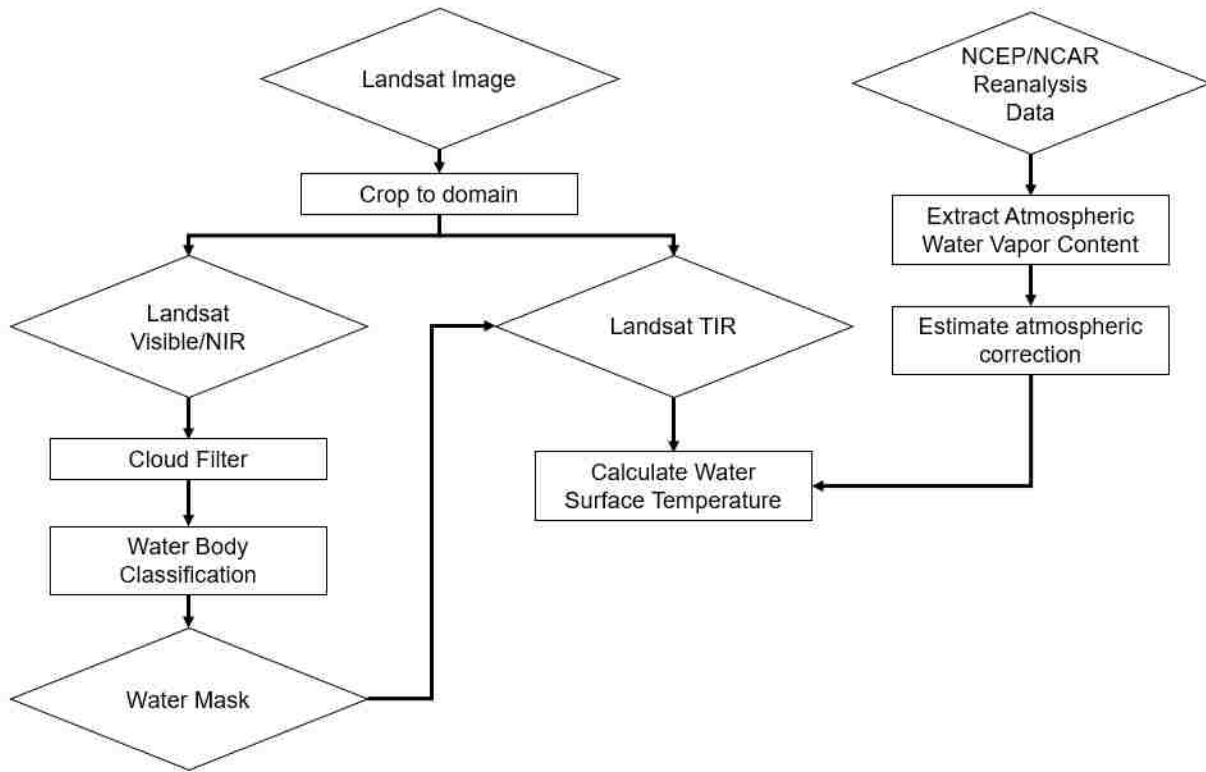
Figure 6.2. Flowchart of water surface temperature from Landsat thermal infrared (TIR) data, using Landsat visible and near infrared (NIR) to inform on the presence of clouds and location of water, and using NCEP/NCAR reanalysis water vapor data to estimate temperature corrections due to atmospheric effects.

Finally, the kinetic temperature of each pixel was estimated from the TIR brightness temperature using a single channel algorithm described in (Jimenez-Munoz et al. 2009). This algorithm applies a correction for atmospheric effects and takes into account the emissivity of water (here assumed to be 0.98) to estimate the kinetic temperature of the water surface. This process is described by Equation 6.1(Jimenez-Munoz et al. 2009):

$$T_S = \gamma \left(\frac{1}{\varepsilon} (\varphi_1 L_{sen} + \varphi_2) + \varphi_3 \right) + \delta \tag{6.1}$$

Where T_S is the kinetic surface temperature, ε is the emissivity of water, L_{sen} is the thermal radiance measured at the satellite sensor, φ_i are atmospheric functions, estimated from

polynomial relationships with atmospheric water vapor content derived in (Jimenez-Munoz et al.

2009), and γ and δ are parameters dependent on Plank's function, described in greater detail in

(Jimenez-Munoz et al. 2009).

Here, atmospheric vapor content for calculation of the atmospheric functions was derived

from National Centers for Environmental Prediction (NCEP) and the National Center for

Atmospheric Research (NCAR) Reanalysis data for days corresponding with sensing data of

each Landsat image (Kalnay et al. 1996). The calculation of the atmospheric functions is

described in Equation 6.2.

$$\begin{bmatrix} \varphi_1 \\ \varphi_2 \\ \varphi_3 \end{bmatrix} = \begin{bmatrix} c_{11} & c_{12} & c_{13} \\ c_{21} & c_{22} & c_{23} \\ c_{31} & c_{32} & c_{33} \end{bmatrix} \begin{bmatrix} w^2 \\ w \\ 1 \end{bmatrix} \tag{6.2}$$

Where c_{ij} are coefficients empirically derived from atmospheric simulations, taken from

(Jimenez-Munoz et al. 2009), and w is the atmospheric water vapor content, taken from the

NCEP/NCAR reanalysis dataset.

The calculated temperatures are then averaged across the domain to provide a single

average temperature estimate for each cloud free image. Images with unrealistically high and low

temperatures (greater than 40 C and less than 0 C) were automatically removed. Images with

anomalously high or low temperatures were manually inspected for the influence of undetected

clouds and other anomalies and removed if deemed inaccurate. The remaining temperatures were

then aggregated across the entire dry season to provide the annual average dry season

temperatures. This same process was applied to the main 3S outflow channel, just upstream of

where it merges with the Mekong River, as well as on the Mekong River itself, both upstream

and downstream of the 3S confluence. For the Mekong River observations, the difference in

kinetic temperature between upstream and downstream was also calculated for each image and then the differences averaged on an annual basis.

The Landsat based temperature estimates were validated for each of the three rivers at the in-situ temperature monitoring stations Figure 6.1, which operated monthly from 2004-2011. These monthly in-situ observations were matched with the most recent Landsat temperature observation (within +/- 10 days). This validation is shown in Figure 6.3. We see good correlation (0.86 correlation coefficient), but with an overall negative bias of around 2° C. These temperatures should be slightly different, because the temperature estimated from the satellite data is actually water surface temperature and the in-situ temperature were estimated from 0.5 m below the water surface. For the applications used here, to observe long term temperature trends, this level of error is acceptable.
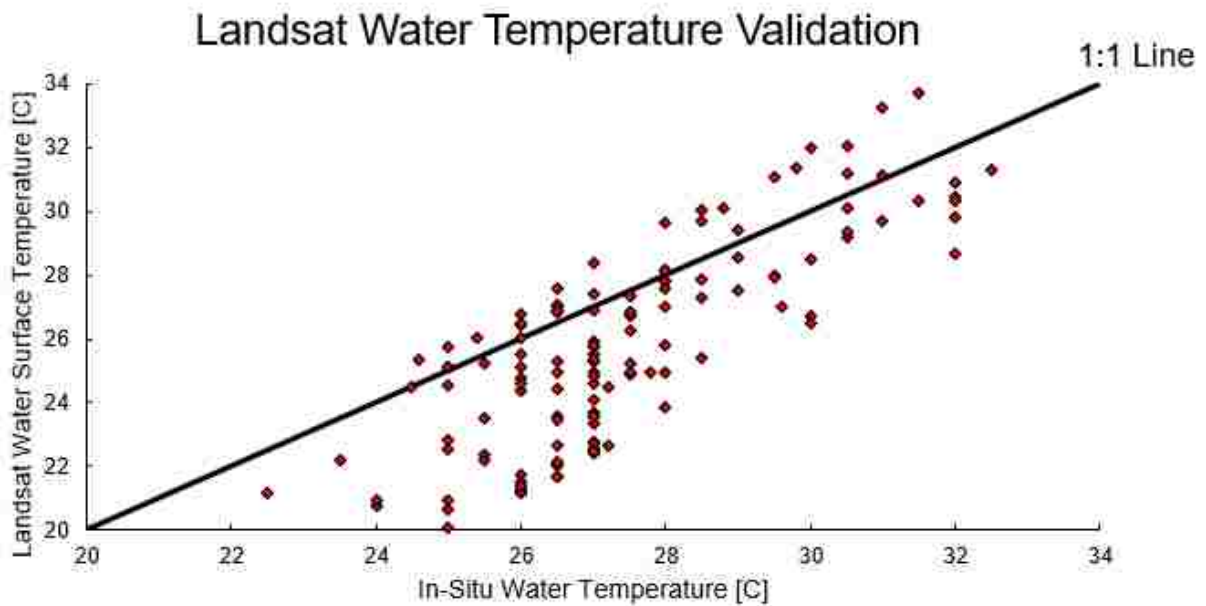

Figure 6.3. Comparison between Landsat based water surface estimates and in-situ water temperature observations at the water quality monitoring stations on each of the major 3S rivers.

6.3.2   *Reservoir Operating Pattern Estimation*

The operating patterns of the major 3S dams were determined using the method employed in
Chapter 3. Here, Sentinel-1 SAR data was used to estimate surface area instead of Landsat
imagery so that wet season reservoir surface area could be easily observed, even in the presence
of cloud cover. This is important for the newer reservoirs, as they have a much shorter record of
Landsat images from which to find cloud free images. Sentinel 1 SAR images of each reservoir
were classified by first applying a speckle filter to reduce random noise and then applying a
simple threshold. Pixels with backscatter coefficients lower than -14 dB were classified as water
and all other pixels were classified as non-water. Domains around each reservoir were visually
defined based on perceived maximum reservoir surface area extent and a 250 m buffer area
beyond that maximum. For each classified SAR image, reservoir surface area was estimated by
summing the number of water pixels within the reservoir domains and multiplying by the SAR
image pixel size (10 m).

These surface areas were then linked to water surface elevations using an area-elevation
relationship derived from the SRTM DEM. All reservoirs except the Yali Reservoir, were
constructed and filled after SRTM operated in 2000 (Yali Dam began operating in 2001, but
filled between 1999 and 2000). This means that the topography beneath the current water surface
was observed by SRTM and is present in the resulting 30 m digital elevation model (DEM). The
area-elevation relationships of these reservoirs were estimated by extracting the DEM in the
domain around each reservoir, and calculating the cumulative surface area of pixels that would
be inundated by increasing water levels. Since the Yali Reservoir was already partially full when
SRTM observed it, all topographical information beneath the water surface at that time is lost. In
this case, we followed the same procedure as the other reservoirs to derive the water surface

179

elevation curve above the water level at the time of SRTM observation. This curve was then fit with a best-fit power curve to estimate surface area of water surface elevations below the SRTM water surface. The derived area-elevation relationships are shown in Figure 6.4.
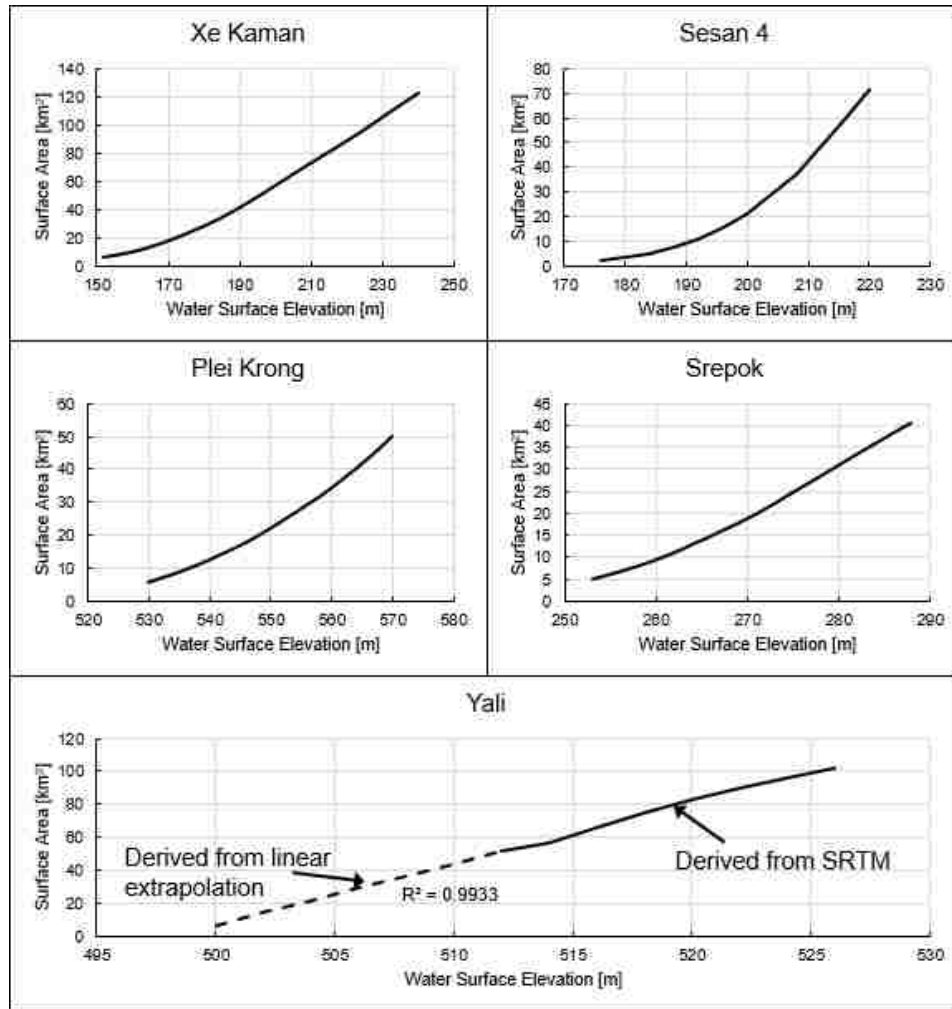
Figure 6.4. Reservoir area-elevation relationships derived from SRTM DEM. Yali Reservoir was already partially filled when observed by SRTM and the bathymetric information at lower elevations is not present in the DEM. The relationship at these lower elevations was estimated by linear interpolating the relationship derived at higher elevations.

These relationships were then used to estimate the water surface elevations of the water surface areas observed in each Sentinel-1 SAR image. With estimates of both water surface area

and water surface elevation, the storage change between subsequent SAR images was calculated

for the entire Setninel-1 time series using the trapezoidal approximation, as described in Chapter

2. These storage change estimates were then converted to total storage by assuming the

maximum reservoir extent observed corresponded with documented maximum reservoir

capacity. Given that Sentinel-1 has only been operating since 2013, this assumption may not hold

and lead to inaccuracies in total storage estimation, but it is sufficient for estimating the shape

and timing of the reservoir operating patter. Finally, the reservoir storage estimates were

averaged by month and normalized by their maximum storage.

6.3.3 *Sub-Basin Precipitation, Land Cover, and Air Temperature Averaging*

All three variables were aggregated using Google Earth Engine. Precipitation data was

taken from the Precipitation Estimation from Remotely Sensed Information using Artificial

Neural Networks-Climate Data Record (PERSIANN-CDR), a global retrospective satellite

remote sensing-based precipitation dataset (Ashouri et al. 2015). Annual precipitation was

calculated by averaging daily precipitation across each sub-basin and then summing by year. Air

temperature was extracted from reanalysis surface air temperature data from NCEP/NCAR. The

air temperature data was averaged by year for each pixel (or partial pixel) within each sub-basin,

then spatially for each year to arrive at average annual temperatures. Deforestation areas were

estimated from the Moderate Resolution Imaging Spectroradiometer (MODIS) annual land cover

product (MCD12Q1.006) (Friedl et al. 2010). Pixels classified as any kind of forest were

grouped and the total number of forest pixels in each sub-basin was summed for each year and

the total area was calculated using the pixel size (500m). The total forested areas were then

normalized by the total surface area of each sub-basin.

6.4 RESULTS

6.4.1 *Landsat-Based River Temperature*

By leveraging thermal infrared data from 1,364 satellite images from Landsat 4, 5, 7, and 8, we constructed annual timeseries of average late dry season (January-April) water surface temperature of the three major 3S rivers, aggregated from the entire river reach downstream of all current dams Figure 6.1, from 1988 through 2018 Figure 6.5. From these timeseries, a dramatic relationship emerges between the construction and operation of major dams (dams on major rivers with >25 km^2 surface area) and downstream river temperature. Major dams, impounding large, deep reservoirs were distinguished from minor dams based on their predicted thermal impact potential. On all three rivers, significant temperature decreases were observed within one year of the beginning of operations of a major dam. These temperature changes were most clearly observed on the Sesan River, which experienced the construction of three major dams. In 2001, the Sesan River dry season water temperature experienced a 1° C decrease, corresponding with the commissioning of the Yali Dam, first major dam on the river (Figure 2, middle panel). The water temperature dropped again between 2008 and 2009, by around 2° C and again, this temperature change corresponds with the timing of two major dams, Sesan 4, and Plie Krong, starting operations (Figure 6.5, middle panel). The Srepok River also experienced dam development in 2009, with a network of 4 dams coming online in 2009. Once again, a sharp decrease in temperature was observed. Between 2007 and 2009, the water temperature dropped by 1.4° C (Figure 6.5, lower panel). The Sekong River experienced a temperature decrease corresponding with the commissioning of the Xe Kaman Dam in 2015, but with less severity than the other two rivers, only dropping by 0.7° C over the course of three years (Figure 6.5, upper panel). This can be attributed to the fact that the Xe Kaman Dam impounds a major

182

tributary of the Sekong River, and not Sekong River itself, meaning that it only influenced the temperature of a portion of the water observed by the satellite data. Unfortunately, the tributary is not wide enough in the dry season to be accurately resolved by the thermal Landsat data, so the thermal impacts of this dam can only be deduced downstream after the impacted water has mixed with relatively free flowing water.
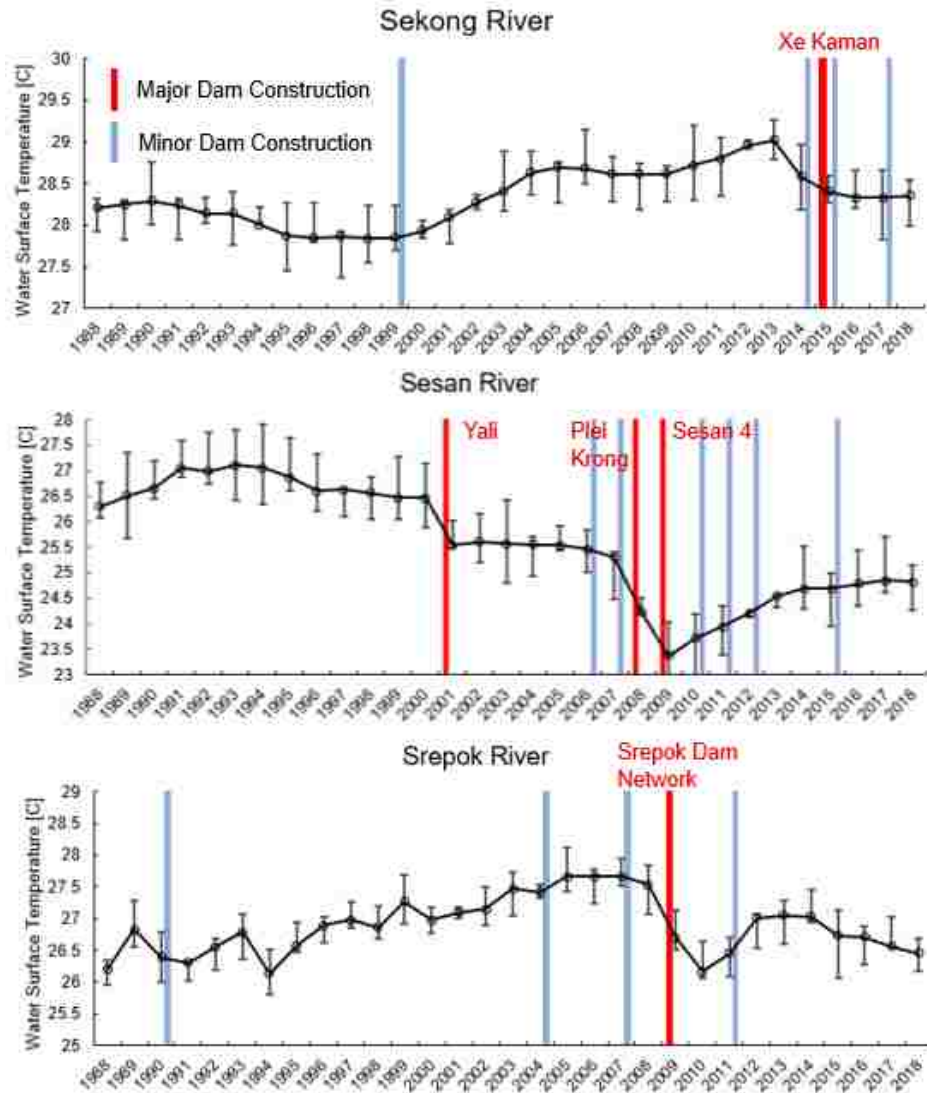

Figure 6.5. Timeline of dam development in each sub-basin and corresponding average annual Landsat based dry season river temperature downstream of dam development. Error bars represent 95 percentile bounds.

Another characteristic of the Landsat temperature time series is that the river surface temperature appears unaffected by the influence of minor dams. Here, dams were classified as minor for one of two reasons. Several of the dams on the main stems of the major rivers are run-of-the-river style impoundments and do not create a sizeable reservoir. This means the water behind the dam does not thermally stratify, resulting in little thermal change to the downstream river. Most of the minor dams however, are located on smaller tributaries and impound only a fraction of the total basin discharge. Despite the presence of numerous minor tributary dams in the Sesan and Srepok Basins, no clear relationship between the timing of minor dam construction and downstream river temperature can be seen. This does not mean that these dams have no thermal impacts on the tributaries they impound, only that any potential impacts do not appear to manifest downstream in the main river channel in a significant way.

A third feature of the satellite-based temperature timeseries is that all three rivers experience temperature changes unrelated from dam development. Each river goes through periods of warming. For the Sekong, and Srepok Rivers, these warming periods last greater than 10 years and overall equal or exceed the temperature decreases apparently caused by reservoirs, resulting in river temperatures ending around the same as they were in 1988, at the beginning of the time series. The Sesan River however goes through shorter periods of warming, which are not enough to offset the temperature drops. Clearly, there are other factors influencing river temperature and some possible sources of warming are explored in following sections.

6.4.2   *River Temperature from Limited Ground Observations*

Fortunately, there are in-situ water temperature observations from water quality monitoring stations on each of the major rivers (see Figure 6.1 for location of in-situ temperature monitoring stations). These stations provided monthly temperature observations but were only in operation

184

from 2004 through 2011. While this time period misses the commissioning of the Xe Kaman Dam in the Sekong River Basin (which occurred in 2015), it does capture the construction of major dams on both the Sesan and Srepok Rivers in 2008 and 2009. Since the monitoring stations were in operation year-round, the observations also provide valuable insight into the seasonality of perceived thermal influence exerted by hydropower dams on the downstream reaches. To that end, we separated the datasets into pre- and post- dam time periods. The Sekong in-situ temperature was also split at 2008 to serve as a reference. From these datasets, we constructed a monthly average water temperature profile for each river during pre- and post- dam construction periods (Figure 6.6).
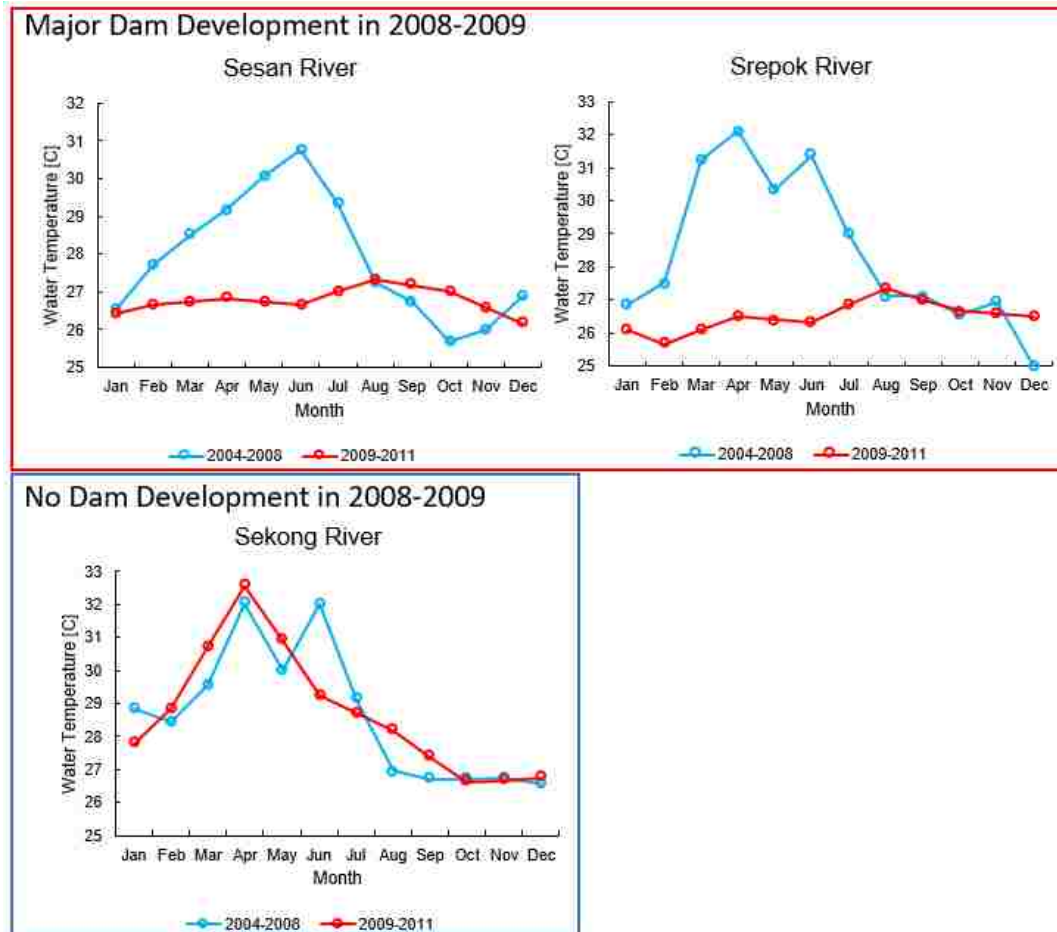
Figure 6.6. Average monthly river temperature from in-situ monitoring stations, separated into pre- and post- dam construction periods. The Sekong River experienced no major development within this time period and the separated time periods are shown as a reference.

The pre- and post- dam differences in monthly water temperature for Srepok and Sesan Rivers are striking, with both experiencing drastic cooling in the late dry season after dam construction. More importantly, these cooling effects linger into the first half of the wet season (May, June, and July), when streamflow significantly increases. This is critical because it represents a stabilization of seasonal water temperature, the elimination of seasonal water temperature variance. These stark post-dam temperature changes are contrasted by an absence of change in water temperature seasonality in the free flowing Sekong River over the same time

186

period. Sesan River temperature post-dam construction was colder throughout the late dry season (February through May and into the beginning of the wet season (June and July), with the difference growing to approximately 4° C in June (Figure 6.6, upper left panel). However, from August through January, there was little change after dam construction. The Srepok River experienced a similar pattern, but peak temperature difference of 6° C occurred earlier in the season in April (Figure 6.6, upper right panel). One explanation for the slight difference in seasonality between the Sesan and Srepok is that the Sesan already had one major dam present during the pre-dam period while the Srepok was relatively free flowing until 2009. This means there was already thermal influence on the Sesan River temperature during the pre-dam time period.

To help explain the seasonality of the temperature effects, we need to look at patterns in the way reservoirs store and release water, otherwise known as operating patterns. Most reservoir operations follow patterns based on seasonally dependent hydrologic conditions (i.e. upstream precipitation and runoff) and objectives (i.e. hydropower production, flood control, water supply, etc.). Since the governing rules that the dam operators in the 3S Basin follow are unknown to us and in-situ reservoir observations of storage or outflow are limited, we used remote sensing observations to derive average monthly storage patterns using a proven approach developed in Chapter 3 (Figure 6.7). This was done using Sentinel-1 satellite mission's Synthetic Aperture Radar (SAR) data to estimate changes in reservoir surface area, and linking these surface area changes to storage estimates using topographical information from the Shuttle Radar and Topography Mission (SRTM). On the Sesan River, the three major rivers all follow the same general pattern, starting relatively full in January and draining throughout the dry season to minimum storage, then filling back up in the early to mid-wet season, with filling beginning

between May and July. During the low inflow dry season months, the reservoirs have the most control over downstream streamflow. Only one reservoir on the Srepok River follows this pattern, with the remaining dams operate at a relatively static level throughout the year. However, this dynamic reservoir is considerably larger than the other Srepok River reservoirs. When inflow increases in the wet season, two things happen. First, reservoir outflow dramatically increases in order to deal with the increased inflow and to maintain low water levels in order to provide flood control if needed. Second, the temperature of the water flowing into the reservoir likely decreases due simply to the abundance of fresh runoff. This is consistent with the cooling observed at the in-situ temperature monitoring stations in the beginning of the wet season (May through July) because during this time, the reservoirs are more rapidly discharging water from the cooler layers, while upstream inflow remains warmer. As the wet season continues into August, the natural streamflow becomes colder, to the point where the reservoir stratification no longer exerts a cooling effect on the river downstream. In other words, the river naturally cools down to the temperature of the stratified reservoir outflow and no temperature change occurs.
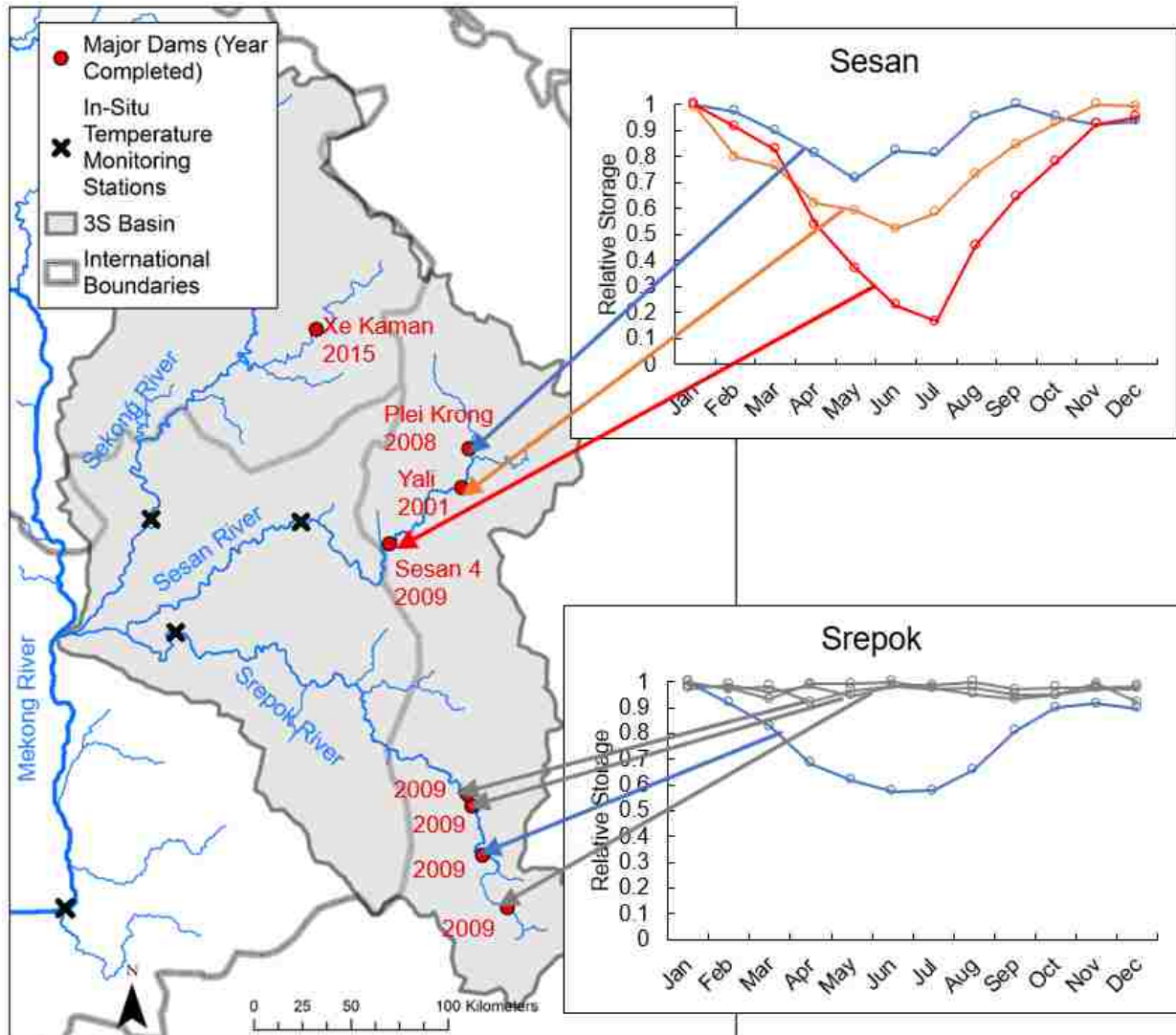
Figure 6.7. Remote sensing derived operating patterns of major dams in Sesan and Srepok Basins.

6.4.3   *Other Potential Drivers of River Temperature Change*

It is clear that there may be other drivers, both natural and artificial, besides dam development that can alter river temperature. Here, we take a closer look at three of these drivers, precipitation and air temperature trends, as well as land cover change, to determine if any of these could have played a role in the cooling effects we observed (Figure 6.8). Annual precipitation for all three

basins remained relatively constant throughout the 30-year period, except for 1999 and 2000, which were anomalously wet years. This roughly corresponds with the sharp cooling seen in the Sesan Basin, and an excess in runoff could cause water temperatures to decrease. However, the Sekong or Srepok River Basins experienced the same high precipitation and neither showed any signs of river temperature cooling around 2000. Annual average air temperature showed a mild warming trend which is similar for all three basins. Interannual air temperature anomalies are small and appear to have little effect on the annual river temperature anomalies. For example, 1998 was a warm year, yet this is not reflected in the river temperature observations. However, the slightly warming air temperature trend could contribute to the long periods of river warming observed. Land cover data was derived from the Moderate Resolution Imaging Spectroradiometer (MODIS), which has been in operation since 2000. The dominant land cover change in the 3S basin over the last 20 years has been deforestation. The forests of all three basins have been rapidly converted to agricultural lands. Deforestation of this scale is often linked with increasing stream temperatures (Nelson and Palmer 2007; Macedo et al. 2013). Given the extent of deforestation occurring in the 3S Basin, it is likely a major driver of stream temperature warming. However, deforestation has been occurring at a fairly steady rate over the past 30 years and is unlikely to be the cause the sharp river temperature declines observed in our study.
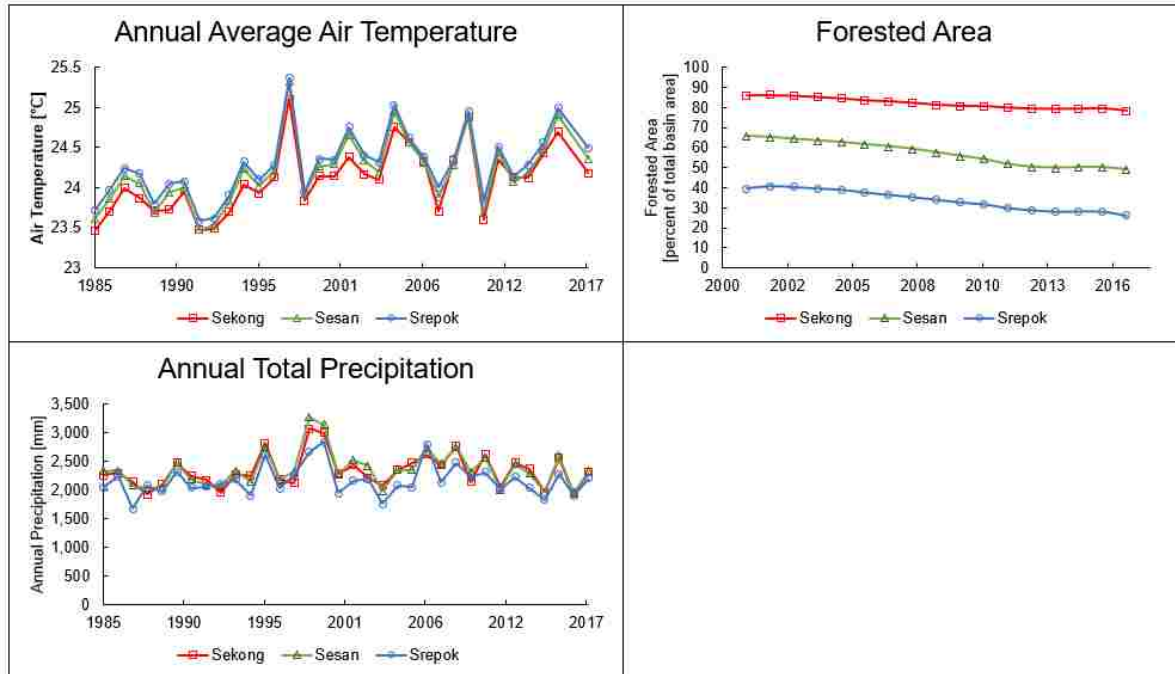
Figure 6.8. Annual average air temperature, annual total precipitation, and annual forested area loss for each of the major sub-basins.

6.4.4   *Impact on the Greater Mekong Basin*

Given that the rivers in the 3S basin are cooling and hydropower dam development is the most plausible driver, a follow up question emerges: *How far downstream does this effect propagate?* To help answer this, we applied the same Landsat monitoring technique to three more locations, the 3S outlet just upstream of where it meets the Mekong River, and the Mekong River just upstream and just downstream of the 3S confluence (Figure 6.9). At the 3S outlet, we see signs of cooling, but rather than the sharp, discrete decreases observed on the individual rivers, the temperature here slowly decreases over the course of the 30-year period. It is difficult to attribute this cooling to any particular dam development episode. However, given that hydropower dams appear to be the primary source of cooling in the major rivers, it is highly likely that this slow,

191

steady temperature decline represents a cumulative of the cooling effects experienced by the major rivers upstream of the Mekong river confluence (Figure 6.9). While this cooling trend is fairly prominent at the 3S confluence, it becomes more ambiguous after mixing with the Mekong River. The Mekong River generally experienced warming at this location within the 30-year period, and none of the thermal characteristics appear to correspond clearly with hydropower dam development in the 3S. However, comparing the temperature of the Mekong River before and after it has mixed with the 3S, reveals the influence of the 3S on Mekong River temperature (Figure 6.9). Before 2000, the 3S generally had a warming effect on the Mekong River when the two rivers mixed, with the downstream 0.2-0.4° C warmer than the upstream. After 2000, this trend shifts with the 3S appearing to cool the Mekong River, by as much as 0.8° C downstream of the confluence. The timing of this shift roughly corresponds with the beginning of operations of the Yali Dam on the Sesan River in 2001. This is where signs of cooling end for now. The cooling signal disappears by the time the water reaches an in-situ temperature monitoring station approximately 100 km downstream of the 3S confluence (see Figure 6.1). This does not mean that the cooling effect has not propagated that far downstream, only that the magnitude of the effect gets lost among other and more localized river temperature effects.

192
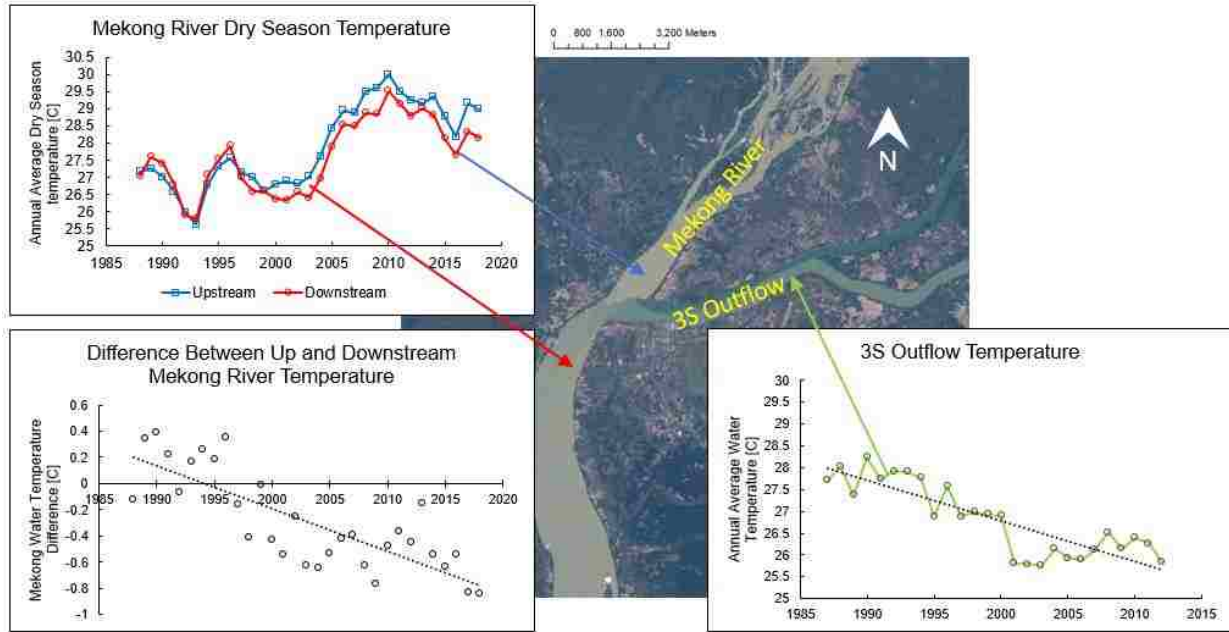
Figure 6.9. Landsat based dry season temperature trends of the 3S Basin outflow, and the Mekong River upstream and downstream of the 3S-Mekong confluence. The difference between the upstream and downstream Mekong River temperature is also shown.

6.5 CONCLUSIONS

By leveraging a long record of Landsat satellite's thermal observations, we deciphered a river temperature cooling trend in the 3S River Basin that was previously undiscovered due to limited in-situ data. We linked these trends with upstream development of major dams by using the varying rates of dam development among the three major sub-basins. The limited in-situ data available suggests that this cooling is not limited to the low streamflow of the dry season, but rather extends several months into the wet season, when streamflow dramatically increases (by at least one order of magnitude), further highlighting the magnitude of the cooling. A consequence of this cooling is the stabilization of the seasonal thermal regime, which has immense implications for ecological health downstream (Olden and Naiman 2010). Other possible

193

sources of river temperature change were investigated but ruled out as a driver of these cooling trends. Finally, this cooling effect was tracked downstream and a noticeable impact on Mekong River water temperature was established. While the impact on the greater Mekong Basin is relatively small for now, this could rapidly change as larger and more numerous dams are planned in the 3S Basin, much further downstream than current hydropower dams. Furthermore, major dams planned on the main stem of the Mekong River in Laos and Cambodia also pose major changes to river temperature (WLE 2017). Understanding and preparing for these changes will be critical in the coming decades for downstream fisheries, which currently provides the protein source for millions of people. Unless in-situ temperature monitoring efforts dramatically increase, the only way to monitor these changes towards sustainable water resources development will be through the use of satellite remote sensing data, like those used here. Even in the face of overwhelming evidence of the negative environmental impacts that dam development has caused and will cause, there are no signs of slowing dam development in the MRB (Orr et al. 2012; Grumbine and Xu 2011; Dugan et al. 2010; Hecht et al. 2019; Y. Pokhrel et al. 2018).

This chapter highlights yet another facet of the environment that will be significantly altered by continued hydropower dam construction. However, in the context of river temperature, the seemingly unstoppable force of dam development in the MRB could be seen as an opportunity, rather than a threat. Many surface waters around the world are warming in step with the global climate(Adrian et al. 2009; Schneider and Hook 2010) and new evidence shows that the MRB's Tonle Sap Lake is no exception (Daly et al. 2019). If more research and careful consideration is given to impacts of future dams on river temperature, their cooling effects could be leveraged to offset the warming effects of global climate change and other human impacts. It

194

may even be possible to tailor the design and operations of future dams towards targeting certain thermal effects, though more research is needed to determine if this is feasible. Ultimately, it is clear that hydropower dams have altered and will continue to alter the temperature of rivers in the MRB, and these impacts need to be carefully considered going forward to minimize the negative livelihood effects on the millions of people downstream who depend on the river ecosystem. Sustainable water resources development for the Mekong nations will have to embrace freely available satellite observations as a practical way forward.

Chapter 7: Conclusion

The main findings of this dissertation are as follows:

- Monthly outflow of reservoirs in humid tropical regions can be reasonably estimated using a satellite data driven mass balance model.

- The mass balance model can be used to evaluate the flow alteration and residence time of reservoirs and systems of reservoirs. This method was applied to reservoirs in the Mekong River Basin and a wide range of flow alteration and residence time impacts were found.

- SWOT is expected to accurately observe reservoir storage change in most cases and that the largest errors are expected to occur for reservoirs set in complex terrain.

- SWOT discharge algorithms can accurately capture river discharge in monsoonal climates, but more work is needed to understand the optimal method of selecting which algorithm(s) to use in such regions.

- Hydropower development in the 3S Basin, a major tributary to the Mekong Basin, has had a cooling effect on downstream river temperature, and this effect was observed using satellite based thermal infrared data.

Developing river basins around the world are going through a transformation due to rapid dam construction. The work presented in this dissertation provides valuable steps towards understanding this transformation. By establishing purely remote sensing based methods for estimating storage change, outflow, flow alteration, and residence time of reservoirs, this work aims to advance our ability to understand anthropogenic alterations to the world's rivers in an age where humans are imposing increasing control over once natural river systems. In the coming decades, dam construction in developing regions will only increase, and the impacts of

196

reservoirs will only intensify. Fortunately, our ability to observe reservoirs and their impacts remotely will improve. Several recently launched and soon to launch satellite platforms will provide valuable hydrologic information, chief among them the SWOT mission. This work demonstrated the usefulness of the SWOT mission for observing both reservoirs and rivers. Other missions such as GRACE-FO (launched in 2018), NISAR (launching 2021), and continuations of the Landsat and JASON missions will all provide useful hydrologic information.

No single satellite will provide all information needed for a clear understanding of reservoir impacts. This is evident by the cooperative, multi-sensor approaches demonstrated by this work. Reservoir storage changes could only be estimated by combining observations of water surface area or elevation with remotely sensed topographical information. When SWOT launches, it will be able to estimate reservoir storage changes on its own. However, it will be joining an already impressive array of satellites, capable of providing the information needed to accurately estimate storage change (see Figure 4.9). Thus, there is likely an optimal method of estimating the most accurate storage changes at the highest frequency based on cooperatively incorporating information from all sensors. This multi-sensor concept also extends to understanding water quality parameters. In Chapter 6, the downstream river temperature patterns observed by Landsat thermal imagery could not be fully understood without understanding the operating patterns of the upstream reservoirs, derived from Sentinel-1 SAR data. Ultimately, the only way to begin to understand the full extent of dam development impacts is through multi-sensor approaches.

The benefits of the remote sensing approaches presented here extend beyond the hydrologic remote sensing community. All satellite data utilized in this work is freely available.

197

With the advent of cloud computing platforms, remote sensing data and the computing power needed to process it are more accessible than ever. The methods applied here can be adopted by water management agencies and stakeholders around the world, providing them with observations of hydrologic variables that would be otherwise unknowable. These methods are particularly applicable in transboundary developing regions like the MRB, where upstream dam development makes downstream decision making increasingly difficult for water managers and policy makers. In such regions, satellite observations allow all nations and agencies access to the same hydrologic information, leading to increased democratization of water management decisions.

While this dissertation provides valuable steps towards understanding the impacts of dam development around the world, there is still much work to be done. Future research needs to be done to determine optimal methods for cooperative utilization of observations from multiple sensors of reservoir surface area and surface elevation, in order to provide the more accurate and more frequent estimates of reservoir storage change and outflow. Such methods should be designed to incorporate data from upcoming missions such as SWOT. Furthermore, additional work must be done to test and apply these methods in regions with different climates. Many developing basins are in tropical monsoon climates like the MRB, but some climates are drastically different (like the Nile River Basin) and the same assumptions used here may not hold everywhere. In order to understand reservoir impacts in these differing regions, region specific alterations to the methods may need to be applied. Finally, satellite based observations of reservoir impacts on river temperature is still in its infancy. At the time of writing, this is the only known study to show the large scale impact of a network of hydropower reservoirs on river temperature using satellite remote sensing. Future research should apply this technique to other

198

sub basins of the MRB and other developing basins around the world as well as incorporate thermal infrared observations from other satellite platforms. In fact, the over 30 year record of thermal infrared imagery from the Landsat mission represents a stockpile of untapped potential for global scale water quality analysis. It is the responsibility of the hydrologic remote sensing to community to leverage our wealth of remote sensing observations to better understand the hydrologic cycle and humanities role in altering it.

Bibliography

(ADB)(Manila), Asian Development Bank. 2006. "Sesan, Sre Pok, and Sekong River Basins Development Study in Kingdom of Cambodia, Lao People's Democratic Republic, and Socialist Republic of Viet."

Ackerman, CT - US Army Corps of Engineers–Hydrologic. 2009. "HEC-GeoRAS–GIS Tools for Support of HEC-RAS Using ArcGIS, User's Manual."

Adamson, Peter T., Ian D. Rutherfurd, Murray C. Peel, and Iwona A. Conlan. 2009. "The Hydrology of the Mekong River." In *The Mekong*, 53–76. Elsevier Inc. https://doi.org/10.1016/B978-0-12-374026-7.00004-8.

Adrian, Rita, Catherine M. O'Reilly, Horacio Zagarese, Stephen B. Baines, Dag O. Hessen, Wendel Keller, David M. Livingstone, et al. 2009. "Lakes as Sentinels of Climate Change." *Limnology and Oceanography* 54 (6 PART 2): 2283–97. https://doi.org/10.4319/lo.2009.54.6_part_2.2283.

Ahmed, M, H Navy, L Vuthy, and M Tiongco. 1998. "Socioeconomic Assessment of Freshwater Capture Fisheries in Cambodia: Report on a Household Survey." http://agris.fao.org/agris-search/search.do?recordID=QW2016000202.

Alsdorf, DE, and NM Mognard. 2011. "Remote Sensing of Surface Water and Recent Developments in the SWOT Mission." *Adsabs.Harvard.Edu*. http://adsabs.harvard.edu/abs/2011AGUFM.H21J..06A.

Alsdorf, Douglas E., Ernesto Rodríguez, and Dennis P. Lettenmaier. 2007. "Measuring Surface Water from Space." *Reviews of Geophysics* 45 (2). https://doi.org/10.1029/2006RG000197.

Altenau, Elizabeth H., Tamlin M. Pavelsky, Delwyn Moller, Christine Lion, Lincoln H. Pitcher, George H. Allen, Paul D. Bates, Stéphane Calmant, Michael Durand, and Laurence C. Smith. 2017. "AirSWOT Measurements of River Water Surface Elevation and Slope: Tanana River, AK." *Geophysical Research Letters* 44 (1): 181–89. https://doi.org/10.1002/2016GL071577.

Ambrosetti, Walter, Luigi Barbanti, and Nicoletta Sala. 2002. "Residence Time in Lakes:Science, Management." *J. Limnol*. Vol. 62.

Andreadis, Konstantinos M., Pascal Storck, and Dennis P. Lettenmaier. 2009. "Modeling Snow Accumulation and Ablation Processes in Forested Environments." *Water Resources Research* 45 (5). https://doi.org/10.1029/2008WR007042.

Arias, M. E., T. Piman, H. Lauri, T. A. Cochrane, and M. Kummu. 2014. "Dams on Mekong Tributaries as Significant Contributors of Hydrological Alterations to the Tonle Sap Floodplain in Cambodia." *Hydrology and Earth System Sciences* 18 (12): 5303–15. https://doi.org/10.5194/hess-18-5303-2014.

Ashouri, Hamed, Kuo Lin Hsu, Soroosh Sorooshian, Dan K. Braithwaite, Kenneth R. Knapp, L. Dewayne Cecil, Brian R. Nelson, and Olivier P. Prat. 2015. "PERSIANN-CDR: Daily Precipitation Climate Data Record from Multisatellite Observations for Hydrological and Climate Studies." *Bulletin of the American Meteorological Society* 96 (1): 69–83. https://doi.org/10.1175/BAMS-D-13-00068.1.

Baran, E., and C. Myschowoda. 2009. "Dams and Fisheries in the Mekong Basin." *Aquatic Ecosystem Health and Management* 12 (3): 227–34. https://doi.org/10.1080/14634980903149902.

Beamesderfer, Raymond C., Bruce E. Rieman, Lewis J. Bledsoe, and Steven Vigg. 1990. "Management Implications of a Model of Predation by a Resident Fish on Juvenile Salmonids Migrating through a Columbia River Reservoir." *North American Journal of*

Fisheries Management 10 (3): 290–304. https://doi.org/10.1577/1548-8675(1990)010<0290:mioamo>2.3.co;2.

Benveniste, J, S Baker, O Bombaci, C Zeli, P Venditti - Frascati, Italy: Eur. Space, and Undefined 2002. 2002. "Envisat RA-2/MWR Product Handbook."

Berthon, L, S Biancamaria, … N Goutal - EGU General, and Undefined 2014. 2014. "Towards the Estimation of Reach-Averaged Discharge from SWOT Data Using a Manning's Equation Derived Algorithm. Application to the Garonne River Between." *Adsabs.Harvard.Edu*. http://adsabs.harvard.edu/abs/2014EGUGA..16.3934B.

Biancamaria, Sylvain, Dennis P. Lettenmaier, and Tamlin M. Pavelsky. 2016. "The SWOT Mission and Its Capabilities for Land Hydrology." *Surveys in Geophysics*. Springer Netherlands. https://doi.org/10.1007/s10712-015-9346-y.

Biemans, H., I. Haddeland, P. Kabat, F. Ludwig, R. W.A. Hutjes, J. Heinke, W. Von Bloh, and D. Gerten. 2011. "Impact of Reservoirs on River Discharge and Irrigation Water Supply during the 20th Century." *Water Resources Research* 47 (3). https://doi.org/10.1029/2009WR008929.

Birkett, C. M. 1994. "Radar Altimetry: A New Concept in Monitoring Lake Level Changes." *Eos, Transactions American Geophysical Union* 75 (24): 273–75. https://doi.org/10.1029/94EO00944.

———. 1995. "The Contribution of TOPEX/POSEIDON to the Global Monitoring of Climatically Sensitive Lakes." *Journal of Geophysical Research* 100 (C12): 25179. https://doi.org/10.1029/95JC02125.

———. 2000. "Synergistic Remote Sensing of Lake Chad: Variability of Basin Inundation." *Remote Sensing of Environment* 72 (2): 218–36. https://doi.org/10.1016/S0034-4257(99)00105-4.

Birkett, C., C. Reynolds, B. Beckley, and B. Doorn. 2011. "From Research to Operations: The USDA Global Reservoir and Lake Monitor." In *Coastal Altimetry*, 19–50. Springer Berlin Heidelberg. https://doi.org/10.1007/978-3-642-12796-0_2.

Bjerklie, David M., S. Lawrence Dingman, Charles J. Vorosmarty, Carl H. Bolster, and Russell G. Congalton. 2003. "Evaluating the Potential for Measuring River Discharge from Space." *Journal of Hydrology* 278 (1–4): 17–38. https://doi.org/10.1016/S0022-1694(03)00129-X.

Bjerklie, David M., Delwyn Moller, Laurence C. Smith, and S. Lawrence Dingman. 2005. "Estimating Discharge in Rivers Using Remotely Sensed Hydraulic Information." *Journal of Hydrology* 309 (1–4): 191–209. https://doi.org/10.1016/j.jhydrol.2004.11.022.

Bonnema, Matthew G., Safat Sikder, Faisal Hossain, Michael Durand, Colin J. Gleason, and David M. Bjerklie. 2016. "Benchmarking Wide Swath Altimetry-Based River Discharge Estimation Algorithms for the Ganges River System." *Water Resources Research* 52 (4): 2439–61. https://doi.org/10.1002/2015WR017296.

Bonnema, Matthew, and Faisal Hossain. 2017a. "Inferring Reservoir Operating Patterns across the Mekong Basin Using Only Space Observations." *Water Resources Research* 53 (5): 3791–3810. https://doi.org/10.1002/2016WR019978.

———. 2017b. "Inferring Reservoir Operating Patterns across the Mekong Basin Using Only Space Observations." *Water Resources Research* 53 (5): 3791–3810. https://doi.org/10.1002/2016WR019978.

———. 2019. "Assessing the Potential of the Surface Water and Ocean Topography Mission for Reservoir Monitoring in the Mekong River Basin." *Water Resources Research* 55 (1): 444–61. https://doi.org/10.1029/2018WR023743.

Bonnema, Matthew, Safat Sikder, Yabin Miao, Xiaodong Chen, Faisal Hossain, Ismat Ara Pervin, S. M. Mahbubur Rahman, and Hyongki Lee. 2016. "Understanding Satellite-Based Monthly-to-Seasonal Reservoir Outflow Estimation as a Function of Hydrologic Controls." *Water Resources Research* 52 (5): 4095–4115. https://doi.org/10.1002/2015WR017830.

Bunn, Stuart E., and Angela H. Arthington. 2002. "Basic Principles and Ecological Consequences of Altered Flow Regimes for Aquatic Biodiversity." *Environmental Management*. https://doi.org/10.1007/s00267-002-2737-0.

Cherkauer, Keith A., and Dennis P. Lettenmaier. 1999. "Hydrologic Effects of Frozen Soils in the Upper Mississippi River Basin." *Journal of Geophysical Research Atmospheres* 104 (D16): 19599–610. https://doi.org/10.1029/1999JD900337.

Cherkauer, Keith A, Laura C Bowling, and Dennis P Lettenmaier. 2003. "Variable Infiltration Capacity Cold Land Process Model Updates." https://doi.org/10.1016/S0921-8181(03)00025-0.

Chow, VT, DR Maidment, and LW Mays. 1988. *Applied Hydrology*. http://documentatiecentrum.watlab.be/imis.php?module=ref&refid=127685&basketaction=add.

Coe, Michael T., and Charon M. Birkett. 2004. "Calculation of River Discharge and Prediction of Lake Height from Satellite Radar Altimetry: Example for the Lake Chad Basin." *Water Resources Research* 40 (10). https://doi.org/10.1029/2003WR002543.

Corp., RL Brooks - Geosci. Res., undefined Salisbury, undefined Md, and undefined 1982. n.d. "Lake Elevations from Satellite Radar Altimetry from a Validation Area in Canada, Report."

Daly, K, F Hossain, S Ahmad, M Bonnema, C Beverridge, B Njissen, and G Holtgrieve. 2019. "Recent Warming of the Tonle Sap Lake, Cambodia: Implications for One of the World's Most Productive Inland Fisheries." *Scientific Reports (in Review)*.

Döll, P., K. Fiedler, and J. Zhang. 2009. "Global-Scale Analysis of River Flow Alterations Due to Water Withdrawals and Reservoirs." *Hydrology and Earth System Sciences* 13 (12): 2413–32. https://doi.org/10.5194/hess-13-2413-2009.

Duan, Zheng, and W. G.M. Bastiaanssen. 2013. "Estimating Water Volume Variations in Lakes and Reservoirs from Four Operational Satellite Altimetry Databases and Satellite Imagery Data." *Remote Sensing of Environment* 134 (July): 403–16. https://doi.org/10.1016/j.rse.2013.03.010.

Dugan, Patrick J., Chris Barlow, Angelo A. Agostinho, Eric Baran, Glenn F. Cada, Daqing Chen, Ian G. Cowx, et al. 2010. "Fish Migration, Dams, and Loss of Ecosystem Services in the Mekong Basin." *Ambio* 39 (4): 344–48. https://doi.org/10.1007/s13280-010-0036-1.

Dugdale, Stephen J. 2016. "A Practitioner's Guide to Thermal Infrared Remote Sensing of Rivers and Streams: Recent Advances, Precautions and Considerations." *Wiley Interdisciplinary Reviews: Water* 3 (2): 251–68. https://doi.org/10.1002/wat2.1135.

Durand, Michael, Jeffrey Neal, Ernesto Rodríguez, Konstantinos M. Andreadis, Laurence C. Smith, and Yeosang Yoon. 2014. "Estimating Reach-Averaged Discharge for the River Severn from Measurements of River Water Surface Elevation and Slope." *Journal of Hydrology* 511 (April): 92–104. https://doi.org/10.1016/j.jhydrol.2013.12.050.

Dyurgerov, Mark B, and Mark F Meier. 2005. "GLACIERS AND THE CHANGING EARTH SYSTEM: A 2004 SNAPSHOT."

Farr, Tom G., and Mike Kobrick. 2000. "Shuttle Radar Topography Mission Produces a Wealth of Data." *Eos* 81 (48): 583–85. https://doi.org/10.1029/EO081i048p00583.

Ficke, Ashley D., Christopher A. Myrick, and Lara J. Hansen. 2007. "Potential Impacts of Global Climate Change on Freshwater Fisheries." *Reviews in Fish Biology and Fisheries* 17 (4): 581–613. https://doi.org/10.1007/s11160-007-9059-5.

Fischer, G, H Van Velthuizen, M Shah, F Nachtergaele - IIASA, Undefined Laxenburg, Undefined Austria, and Undefined 2002. 2008. "Global Agro-Ecological Zones Assessment for Agriculture in the 21st Century: Methodology and Results."

Fjørtoft, Roger, Jean Marc Gaudin, Nadine Pourthié, Jean Claude Lalaurie, Alain Mallet, Jean Francois Nouvel, Joseph Martinot-Lagarde, et al. 2014. "KaRIn on SWOT: Characteristics of near-Nadir Ka-Band Interferometric SAR Imagery." *IEEE Transactions on Geoscience and Remote Sensing* 52 (4): 2172–85. https://doi.org/10.1109/TGRS.2013.2258402.

Friedl, Mark A., Damien Sulla-Menashe, Bin Tan, Annemarie Schneider, Navin Ramankutty, Adam Sibley, and Xiaoman Huang. 2010. "MODIS Collection 5 Global Land Cover: Algorithm Refinements and Characterization of New Datasets." *Remote Sensing of Environment* 114 (1): 168–82. https://doi.org/10.1016/j.rse.2009.08.016.

Fu, K. D., D. M. He, and X. X. Lu. 2008. "Sedimentation in the Manwan Reservoir in the Upper Mekong and Its Downstream Impacts." *Quaternary International* 186 (1): 91–99. https://doi.org/10.1016/j.quaint.2007.09.041.

Fu, Lee-Lueng, Douglas Alsdorf, Ernesto Rodriguez, and Nelly Mognard. 2012. "SWOT: The Surface Water and Ocean Topography Mission Wide-Swath Altimetric Measurement of Water Elevation on Earth."

Gao, H., T. J. Bohn, E. Podest, K. C. McDonald, and D. P. Lettenmaier. 2011. "On the Causes of the Shrinking of Lake Chad." *Environmental Research Letters* 6 (3). https://doi.org/10.1088/1748-9326/6/3/034021.

Gao, Huilin. 2015. "Satellite Remote Sensing of Large Lakes and Reservoirs: From Elevation and Area to Storage." *Wiley Interdisciplinary Reviews: Water* 2 (2): 147–57. https://doi.org/10.1002/wat2.1065.

Gao, Huilin, Charon Birkett, and Dennis P. Lettenmaier. 2012. "Global Monitoring of Large Reservoir Storage from Satellite Remote Sensing." *Water Resources Research* 48 (9). https://doi.org/10.1029/2012WR012063.

Gebregiorgis, Abebe, and Faisal Hossain. 2014. "Making Satellite Precipitation Data Work for the Developing World." *IEEE Geoscience and Remote Sensing Magazine* 2 (2): 24–36. https://doi.org/10.1109/mgrs.2014.2317561.

Gebregiorgis, Abebe S., Yudong Tian, Christa D. Peters-Lidard, and Faisal Hossain. 2012. "Tracing Hydrologic Model Simulation Error as a Function of Satellite Rainfall Estimation Bias Components and Land Use and Land Cover Conditions." *Water Resources Research* 48 (11). https://doi.org/10.1029/2011WR011643.

Gleason, Colin J., and Ali N. Hamdan. 2017. "Crossing the (Watershed) Divide: Satellite Data and the Changing Politics of International River Basins." *Geographical Journal* 183 (1): 2–15. https://doi.org/10.1111/geoj.12155.

Gleason, Colin J., Laurence C. Smith, and Jinny Lee. 2014. "Retrieval of River Discharge Solely from Satellite Imagery and At-Many-Stations Hydraulic Geometry: Sensitivity to River Form and Optimization Parameters." *Water Resources Research* 50 (12): 9604–19. https://doi.org/10.1002/2014WR016109.

Gleason, Colin J., and Jida Wang. 2015. "Theoretical Basis for At-Many-Stations Hydraulic Geometry." *Geophysical Research Letters* 42 (17): 7107–14. https://doi.org/10.1002/2015GL064935.

González-Jorge, Higinio, Luis Miguel González-deSantos, Joaquin Martínez-Sánchez, Ana Sánchez-Rodríguez, and Henrique Lorenzo. 2018. "Automatic Measurement Ofwater Height in the as Conchas (Spain) Reservoir Using Sentinel 2 and Aerial LiDAR Data." *Remote Sensing* 10 (6). https://doi.org/10.3390/rs10060902.

Graf, William L. 2006. "Downstream Hydrologic and Geomorphic Effects of Large Dams on American Rivers." *Geomorphology* 79 (3–4): 336–60. https://doi.org/10.1016/j.geomorph.2006.06.022.

Grill, Günther, Bernhard Lehner, Alexander E Lumsdon, Graham K MacDonald, Christiane Zarfl, and Catherine Reidy Liermann. 2015. "An Index-Based Framework for Assessing Patterns and Trends in River Fragmentation and Flow Regulation by Global Dams at Multiple Scales." *Environmental Research Letters* 10 (1): 15001.

Grill, Günther, Camille Ouellet Dallaire, Etienne Fluet Chouinard, Nikolai Sindorf, and Bernhard Lehner. 2014. "Development of New Indicators to Evaluate River Fragmentation and Flow Regulation at Large Scales: A Case Study for the Mekong River Basin." *Ecological Indicators* 45: 148–59. https://doi.org/10.1016/j.ecolind.2014.03.026.

Grumbine, R. Edward, and Jianchu Xu. 2011. "Mekong Hydropower Development." *Science* 332 (6026): 178–79. https://doi.org/10.1126/science.1200990.

Haddeland, Ingjerd, Dennis P. Lettenmaier, and Thomas Skaugen. 2006. "Effects of Irrigation on the Water and Energy Balances of the Colorado and Mekong River Basins." *Journal of Hydrology* 324 (1–4): 210–23. https://doi.org/10.1016/j.jhydrol.2005.09.028.

Hamlet, Alan F., and Dennis P. Lettenmaier. 1999. "Effects of Climate Change on Hydrology and Water Resources in the Columbia River Basin." In *Journal of the American Water Resources Association*, 35:1597–1623. American Water Resources Assoc. https://doi.org/10.1111/j.1752-1688.1999.tb04240.x.

Hecht, Jory S., Guillaume Lacombe, Mauricio E. Arias, Thanh Duc Dang, and Thanapon Piman. 2019. "Hydropower Dams of the Mekong River Basin: A Review of Their Hydrological Impacts." *Journal of Hydrology*. Elsevier B.V. https://doi.org/10.1016/j.jhydrol.2018.10.045.

Hong, Yang, Robert F. Adler, Faisal Hossain, Scott Curtis, and George J. Huffman. 2007. "A First Approach to Global Runoff Simulation Using Satellite Rainfall Estimation." *Water Resources Research* 43 (8). https://doi.org/10.1029/2006WR005739.

Hou, Arthur Y., Ramesh K. Kakar, Steven Neeck, Ardeshir A. Azarbarzin, Christian D. Kummerow, Masahiro Kojima, Riko Oki, Kenji Nakamura, and Toshio Iguchi. 2014. "The Global Precipitation Measurement Mission." *Bulletin of the American Meteorological Society* 95 (5): 701–22. https://doi.org/10.1175/BAMS-D-13-00164.1.

Huang, Wenli, Ben DeVries, Chengquan Huang, Megan W. Lang, John W. Jones, Irena F. Creed, and Mark L. Carroll. 2018. "Automated Extraction of Surface Water Extent from Sentinel-1 Data." *Remote Sensing* 10 (5). https://doi.org/10.3390/rs10050797.

Huffman, George J., Robert F. Adler, David T. Bolvin, Guojun Gu, Eric J. Nelkin, Kenneth P. Bowman, Yang Hong, Erich F. Stocker, and David B. Wolff. 2007. "The TRMM Multisatellite Precipitation Analysis (TMPA): Quasi-Global, Multiyear, Combined-Sensor Precipitation Estimates at Fine Scales." *Journal of Hydrometeorology* 8 (1): 38–55. https://doi.org/10.1175/JHM560.1.

IEA. 2016. "Extended World Energy Balances: IEA World Energy Statistics and Balances (Database)."

Jimenez-Munoz, Juan C., Jordi Cristobal, José A. Sobrino, Guillem Sòria, Miquel Ninyerola, and

Xavier Pons. 2009. "Revision of the Single-Channel Algorithm for Land Surface Temperature Retrieval from Landsat Thermal-Infrared Data." *IEEE Transactions on Geoscience and Remote Sensing* 47 (1): 339–49. https://doi.org/10.1109/TGRS.2008.2007125.

Jones, John W. 2015. "Efficient Wetland Surface Water Detection and Monitoring via Landsat: Comparison with in Situ Data from the Everglades Depth Estimation Network." *Remote Sensing* 7 (9): 12503–38. https://doi.org/10.3390/rs70912503.

Kalnay, E., M. Kanamitsu, R. Kistler, W. Collins, D. Deaven, L. Gandin, M. Iredell, et al. 1996. "The NCEP/NCAR 40-Year Reanalysis Project." *Bulletin of the American Meteorological Society* 77 (3): 437–71. https://doi.org/10.1175/1520-0477(1996)077<0437:TNYRP>2.0.CO;2.

Kondolf, G. M., Z. K. Rubin, and J. T. Minear. 2014. "Dams on the Mekong: Cumulative Sediment Starvation." *Water Resources Research* 50 (6): 5158–69. https://doi.org/10.1002/2013WR014651.

Kummu, M, XX Lu, JJ Wang, O Varis - Geomorphology, and Undefined 2010. 2010. "Basin-Wide Sediment Trapping Efficiency of Emerging Reservoirs along the Mekong." *Elsevier*. https://www.sciencedirect.com/science/article/pii/S0169555X10001339.

Kummu, Matti, and Juha Sarkkula. 2008. "Impact of the Mekong River Flow Alteration on the Tonle Sap Flood Pulse." *Ambio*. https://doi.org/10.1579/0044-7447(2008)37[185:IOTMRF]2.0.CO;2.

Kummu, Matti, and Olli Varis. 2007. "Sediment-Related Impacts Due to Upstream Reservoir Trapping, the Lower Mekong River." *Geomorphology* 85 (3–4): 275–93. https://doi.org/10.1016/j.geomorph.2006.03.024.

Lambin, Juliette, Rosemary Morrow, Lee Lueng Fu, Josh K. Willis, Hans Bonekamp, John Lillibridge, Jacqueline Perbos, et al. 2010. "The OSTM/Jason-2 Mission." *Marine Geodesy* 33: 4–25. https://doi.org/10.1080/01490419.2010.491030.

Lauri, H., H. de Moel, P. J. Ward, T. A. Räsänen, M. Keskinen, and M. Kummu. 2012. "Future Changes in Mekong River Hydrology: Impact of Climate Change and Reservoir Operation on Discharge." *Hydrology and Earth System Sciences Discussions* 9 (5): 6569–6614. https://doi.org/10.5194/hessd-9-6569-2012.

Lee, Hyongki, Michael Durand, Hahn Chul Jung, Doug Alsdorf, C. K. Shum, and Yongwei Sheng. 2010. "Characterization of Surface Water Storage Changes in Arctic Lakes Using Simulated SWOT Measurements." *International Journal of Remote Sensing* 31 (14): 3931–53. https://doi.org/10.1080/01431161.2010.483494.

Lee, Hyongki, C. K. Shum, Kuo-Hsin Tseng, Jun-Yi Guo, and Chung-Yen Kuo. 2011. "Present-Day Lake Level Variation from Envisat Altimetry over the Northeastern Qinghai-Tibetan Plateau: Links with Precipitation and Temperature." *Terrestrial, Atmospheric and Oceanic Sciences* 22 (2): 169–75. https://doi.org/10.3319/TAO.2010.08.09.01(TibXS).

Lehner, Bernhard, Catherine Reidy Liermann, Carmen Revenga, Charles Vörömsmarty, Balazs Fekete, Philippe Crouzet, Petra Döll, et al. 2011. "High-Resolution Mapping of the World's Reservoirs and Dams for Sustainable River-Flow Management." *Frontiers in Ecology and the Environment*. https://doi.org/10.1890/100125.

Leopold, LB, and T Maddock. 1953. *The Hydraulic Geometry of Stream Channels and Some Physiographic Implications*. https://books.google.com/books?hl=en&lr=&id=K496gE_YsJoC&oi=fnd&pg=PP8&dq=%0ALeopold,+L.+B.,+and+%0AT.+Maddock+Jr.+(1953),+The+hydraulic+geometry+of+str

eam+channels+and+some+physiographic+implications,+U.S.+Geol.+Surv.+Prof.+Pap.,+25 2,+1–57.%0A&ots=FipHBxr3Ch&sig=LzcOrcz7nED_V89_FkcSneN630s.

Liang, X, DP Lettenmaier, … EF Wood - Journal of Geophysical, and Undefined 1994. 1994. "A Simple Hydrologically Based Model of Land Surface Water and Energy Fluxes for General Circulation Models." *Wiley Online Library*. https://agupubs.onlinelibrary.wiley.com/doi/abs/10.1029/94jd00483.

Liermann, Catherine Reidy, Christer Nilsson, James Robertson, and Rebecca Y. Ng. 2012. "Implications of Dam Obstruction for Global Freshwater Fish Diversity." *BioScience* 62 (6): 539–48. https://doi.org/10.1525/bio.2012.62.6.5.

Ligon, Franklin K., William E. Dietrich, and William J. Trush. 1995. "Downstream Ecological Effects of Dams." *BioScience* 45 (3): 183–92. https://doi.org/10.2307/1312557.

Ling, Feng, Giles M. Foody, Hao Du, Xuan Ban, Xiaodong Li, Yihang Zhang, and Yun Du. 2017. "Monitoring Thermal Pollution in Rivers Downstream of Dams with Landsat ETM+ Thermal Infrared Images." *Remote Sensing* 9 (11). https://doi.org/10.3390/rs9111175.

LOHMANN, DAG, RALPH NOLTE-HOLUBE, and EHRHARD RASCHKE. 1996. "A Large-Scale Horizontal Routing Model to Be Coupled to Land Surface Parametrization Schemes." *Tellus A* 48 (5): 708–21. https://doi.org/10.1034/j.1600-0870.1996.t01-3-00009.x.

Loveland, T. R., B. C. Reed, D. O. Ohlen, J. F. Brown, Z. Zhu, L. Yang, and J. W. Merchant. 2000. "Development of a Global Land Cover Characteristics Database and IGBP DISCover from 1 Km AVHRR Data." *International Journal of Remote Sensing* 21 (6–7): 1303–30. https://doi.org/10.1080/014311600210191.

Lu, X. X., Siyue Li, Matti Kummu, Rita Padawangi, and J. J. Wang. 2014. "Observed Changes in the Water Flow at Chiang Saen in the Lower Mekong: Impacts of Chinese Dams?" *Quaternary International* 336 (June): 145–57. https://doi.org/10.1016/j.quaint.2014.02.006.

Lu, X. X., and R. Y. Siew. 2006. "Water Discharge and Sediment Flux Changes over the Past Decades in the Lower Mekong River: Possible Impacts of the Chinese Dams." *Hydrology and Earth System Sciences* 10 (2): 181–95. https://doi.org/10.5194/hess-10-181-2006.

Macedo, Marcia N., Michael T. Coe, Ruth DeFries, Maria Uriarte, Paulo M. Brando, Christopher Neill, and Wayne S. Walker. 2013. "Land-Use-Driven Stream Warming in Southeastern Amazonia." *Philosophical Transactions of the Royal Society B: Biological Sciences* 368 (1619). https://doi.org/10.1098/rstb.2012.0153.

Mason, IM, AR Harris, CM Birkett, W Cudlip, CG Rapley - Proc. 16th Ann. Conf, and undefined 1991. n.d. "Remote Sensing of Lakes for the Proxy Monitoring of Climatic Change."

Maswood, Mehedi, and Faisal Hossain. 2016. "Advancing River Modelling in Ungauged Basins Using Satellite Remote Sensing: The Case of the Ganges–Brahmaputra–Meghna Basin." *International Journal of River Basin Management* 14 (1): 103–17. https://doi.org/10.1080/15715124.2015.1089250.

McFeeters, S. K. 1996. "The Use of the Normalized Difference Water Index (NDWI) in the Delineation of Open Water Features." *International Journal of Remote Sensing* 17 (7): 1425–32. https://doi.org/10.1080/01431169608948714.

Mekong River Commission. 2003. "State of the Basin Report." Phenom Penh.

Molle, François, Tira Foran, and Mira Käkönen. 2009. "Contested Waterscapes in the Mekong Region Hydropower, Livelihoods and Governance London • Sterling, VA Publishing for a Sustainable Future."

Moller, D, E Rodriguez, … J Carswell - … Geoscience and Remote, and undefined 2011. n.d.

"AirSWOT—A Calibration/Validation Platform for the SWOT Mission."

Monsen, Nancy E., James E. Cloern, Lisa V. Lucas, and Stephen G. Monismith. 2002. "A Comment on the Use of Flushing Time, Residence Time, and Age as Transport Time Scales." *Limnology and Oceanography* 47 (5): 1545–53. https://doi.org/10.4319/lo.2002.47.5.1545.

Morris, Charles S., and Stephen K. Gill. 1994. "Evaluation of the TOPEX/POSEIDON Altimeter System over the Great Lakes." *Journal of Geophysical Research* 99 (C12): 24527. https://doi.org/10.1029/94JC01642.

Muala, Eric, Yasir A. Mohamed, Zheng Duan, and Pieter van der Zaag. 2014. "Estimation of Reservoir Discharges from Lake Nasser and Roseires Reservoir in the Nile Basin Using Satellite Altimetry and Imagery Data." *Remote Sensing* 6 (8): 7522–45. https://doi.org/10.3390/rs6087522.

Nelson, Kären C., and Margaret A. Palmer. 2007. "Stream Temperature Surges under Urbanization and Climate Change: Data, Models, and Responses." *Journal of the American Water Resources Association* 43 (2): 440–52. https://doi.org/10.1111/j.1752-1688.2007.00034.x.

Niemeyer, Ryan J., Yifan Cheng, Yixin Mao, John R. Yearsley, and Bart Nijssen. 2018. "A Thermally Stratified Reservoir Module for Large-Scale Distributed Stream Temperature Models With Application in the Tennessee River Basin." *Water Resources Research* 54 (10): 8103–19. https://doi.org/10.1029/2018WR022615.

Okeowo, Modurodoluwa Adeyinka, Hyongki Lee, Faisal Hossain, and Augusto Getirana. 2017. "Automated Generation of Lakes and Reservoirs Water Elevation Changes from Satellite Radar Altimetry." *IEEE Journal of Selected Topics in Applied Earth Observations and Remote Sensing* 10 (8): 3465–81. https://doi.org/10.1109/JSTARS.2017.2684081.

Olden, Julian D., and Robert J. Naiman. 2010. "Incorporating Thermal Regimes into Environmental Flows Assessments: Modifying Dam Operations to Restore Freshwater Ecosystem Integrity." *Freshwater Biology* 55 (1): 86–107. https://doi.org/10.1111/j.1365-2427.2009.02179.x.

Orr, Stuart, Jamie Pittock, Ashok Chapagain, and David Dumaresq. 2012. "Dams on the Mekong River: Lost Fish Protein and the Implications for Land and Water Resources." *Global Environmental Change* 22 (4): 925–32. https://doi.org/10.1016/j.gloenvcha.2012.06.002.

Pavelsky, Tamlin, and Michael Durand. 2012. "Developing New Algorithms for Estimating River Discharge from Space." In *Eos*, 93:457. https://doi.org/10.1029/2012EO450006.

Pekel, Jean François, Andrew Cottam, Noel Gorelick, and Alan S. Belward. 2016. "High-Resolution Mapping of Global Surface Water and Its Long-Term Changes." *Nature* 540 (7633): 418–22. https://doi.org/10.1038/nature20584.

Peral, E., E. Rodriguez, D. Moeller, M. McAdams, M. Johnson, and K. Andreadis. 2014. "SWOT Simulator Quick User Guide."

Pham-Duc, Binh, Catherine Prigent, and Filipe Aires. 2017. "Surface Water Monitoring within Cambodia and the Vietnamese Mekong Delta over a Year, with Sentinel-1 SAR Observations." *Water (Switzerland)* 9 (6). https://doi.org/10.3390/w9060366.

Pokhrel, Yadu, Mateo Burbano, Jacob Roush, Hyunwoo Kang, Venkataramana Sridhar, and David W. Hyndman. 2018. "A Review of the Integrated Effects of Changing Climate, Land Use, and Dams on Mekong River Hydrology." *Water (Switzerland)*. MDPI AG. https://doi.org/10.3390/w10030266.

Pokhrel, Yadu N., Naota Hanasaki, Pat J.F. Yeh, Tomohito J. Yamada, Shinjiro Kanae, and

Taikan Oki. 2012. "Model Estimates of Sea-Level Change Due to Anthropogenic Impacts on Terrestrial Water Storage." *Nature Geoscience* 5 (6): 389–92. https://doi.org/10.1038/ngeo1476.

Pringle, Catherine. 2003. "What Is Hydrologic Connectivity and Why Is It Ecologically Important?" *Hydrological Processes* 17 (13): 2685–89. https://doi.org/10.1002/hyp.5145.

Rodriguez, E, and D Moller. 2004. "Measuring Surface Water from Space." *Adsabs.Harvard.Edu*. http://adsabs.harvard.edu/abs/2004AGUFM.H22C..08R.

Rueda, F, E Moreno-Ostos, J Armengol - Ecological Modelling, and Undefined 2006. 2006. "The Residence Time of River Water in Reservoirs." *Elsevier*. https://www.sciencedirect.com/science/article/pii/S0304380005002760.

Schneider, Philipp, and Simon J. Hook. 2010. "Space Observations of Inland Water Bodies Show Rapid Surface Warming since 1985." *Geophysical Research Letters* 37 (22). https://doi.org/10.1029/2010GL045059.

Sheffield, Justin, Gopi Goteti, and Eric F. Wood. 2006. "Development of a 50-Year High-Resolution Global Dataset of Meteorological Forcings for Land Surface Modeling." *Journal of Climate* 19 (13): 3088–3111. https://doi.org/10.1175/JCLI3790.1.

Sherman, Bradford, Charles R. Todd, John D. Koehn, and Tom Ryan. 2007. "Modelling the Impact and Potential Mitigation of Cold Water Pollution on Murray Cod Populations Downstream of Hume Dam, Australia." *River Research and Applications* 23 (4): 377–89. https://doi.org/10.1002/rra.994.

Siddique-E-Akbor, A. H. M., Faisal Hossain, Safat Sikder, C. K. Shum, Steven Tseng, Yuchan Yi, F. J. Turk, and Ashutosh Limaye. 2014. "Satellite Precipitation Data–Driven Hydrological Modeling for Water Resources Management in the Ganges, Brahmaputra, and Meghna Basins." *Earth Interactions* 18 (17): 1–25. https://doi.org/10.1175/ei-d-14-0017.1.

Siddique-E-Akbor, A. H.M., Faisal Hossain, Hyongki Lee, and C. K. Shum. 2011. "Inter-Comparison Study of Water Level Estimates Derived from Hydrodynamic-Hydrologic Model and Satellite Altimetry for a Complex Deltaic Environment." *Remote Sensing of Environment* 115 (6): 1522–31. https://doi.org/10.1016/j.rse.2011.02.011.

Sikder, Md Safat, and Faisal Hossain. 2015. "Understanding the Geophysical Sources of Uncertainty for Satellite Interferometric (SRTM)-Based Discharge Estimation in River Deltas: The Case for Bangladesh." *IEEE Journal of Selected Topics in Applied Earth Observations and Remote Sensing* 8 (2): 523–38. https://doi.org/10.1109/JSTARS.2014.2326893.

Smith, Laurence C., and Tamlin M. Pavelsky. 2009. "Remote Sensing of Volumetric Storage Changes in Lakes." *Earth Surface Processes and Landforms* 34 (10): 1353–58. https://doi.org/10.1002/esp.1822.

Solander, Kurt C., John T. Reager, and James S. Famiglietti. 2016. "How Well Will the Surface Water and Ocean Topography (SWOT) Mission Observe Global Reservoirs?" *Water Resources Research* 52 (3): 2123–40. https://doi.org/10.1002/2015WR017952.

Swenson, Sean, and John Wahr. 2009. "Monitoring the Water Balance of Lake Victoria, East Africa, from Space." *Journal of Hydrology* 370 (1–4): 163–76. https://doi.org/10.1016/j.jhydrol.2009.03.008.

Tavares, Matheus Henrique, Augusto Hugo Farias Cunha, David Motta-Marques, Anderson Luís Ruhoff, J. Rafael Cavalcanti, Carlos Ruberto Fragoso, Juan Martín Bravo, Andrés Mauricio Munar, Fernando Mainardi Fan, and Lucia Helena Ribeiro Rodrigues. 2019. "Comparison of Methods to Estimate Lake-Surface-Water Temperature Using Landsat 7 ETM+ and

MODIS Imagery: Case Study of a Large Shallow Subtropical Lake in Southern Brazil." *Water (Switzerland)* 11 (1). https://doi.org/10.3390/w11010168.

Tian, Yudong, and Christa D. Peters-Lidard. 2010. "A Global Map of Uncertainties in Satellite-Based Precipitation Measurements." *Geophysical Research Letters* 37 (24). https://doi.org/10.1029/2010GL046008.

Todini, E. 1996. "The ARNO Rainfall-Runoff Model." *Journal of Hydrology* 175 (1–4): 339–82. https://doi.org/10.1016/S0022-1694(96)80016-3.

Umar, M., Bruce L. Rhoads, and Jonathan A. Greenberg. 2018. "Use of Multispectral Satellite Remote Sensing to Assess Mixing of Suspended Sediment Downstream of Large River Confluences." *Journal of Hydrology* 556 (January): 325–38. https://doi.org/10.1016/j.jhydrol.2017.11.026.

Verron, Jacques, Pierre Sengenes, Juliette Lambin, Jocelyne Noubel, Nathalie Steunou, Amandine Guillot, Nicolas Picot, et al. 2015. "The SARAL/AltiKa Altimetry Satellite Mission." *Marine Geodesy* 38 (September): 2–21. https://doi.org/10.1080/01490419.2014.1000471.

Vörösmarty, C., D. Lettenmaier, C. Leveque, M. Meybeck, C. Pahl-Wostl, J. Alcamo, W. Cosgrove, et al. 2004. "Humans Transforming the Global Water System." *Eos* 85 (48). https://doi.org/10.1029/2004EO480001.

Vörösmarty, C., and Dork Sahagian. 2000. "Anthropogenic Disturbance of the Terrestrial Water Cycle." *BioScience* 50 (9): 753. https://doi.org/10.1641/0006-3568(2000)050[0753:adottw]2.0.co;2.

Vorosmarty, C. 1997. "The Storage and Aging of Continental Runoff in Large Reservoir Systems of the World." *Ci.Nii.Ac.Jp*. https://ci.nii.ac.jp/naid/80009822214/.

Vörösmarty, Charles J., James Syvitski, D. A.Y. John, Alex De Sherbinin, Liviu Giosan, and Chris Paola. 2009. "Battling to Save the World's River Deltas." *Bulletin of the Atomic Scientists* 65 (2): 31–43. https://doi.org/10.2968/065002005.

Wenger, Seth J., Charles H. Luce, Alan F. Hamlet, Daniel J. Isaak, and Helen M. Neville. 2010. "Macroscale Hydrologic Modeling of Ecologically Relevant Flow Metrics." *Water Resources Research* 46 (9). https://doi.org/10.1029/2009WR008839.

Wheeler, Kevin G., Mohammed Basheer, Zelalem T. Mekonnen, Sami O. Eltoum, Azeb Mersha, Gamal M. Abdo, Edith A. Zagona, Jim W. Hall, and Simon J. Dadson. 2016. "Cooperative Filling Approaches for the Grand Ethiopian Renaissance Dam." *Water International* 41 (4): 611–34. https://doi.org/10.1080/02508060.2016.1177698.

Winemiller, K. O., P. B. McIntyre, L. Castello, E. Fluet-Chouinard, T. Giarrizzo, S. Nam, I. G. Baird, et al. 2016. "Balancing Hydropower and Biodiversity in the Amazon, Congo, and Mekong." *Science*. American Association for the Advancement of Science. https://doi.org/10.1126/science.aac7082.

WLE. 2017. "Dataset on the Dams of the Irrawaddy, Mekong, Red and Salween River Basins." Vientiane, Lao PDR: CGIAR Research Program on Water, Land and Ecosystems - Greater Mekong. 2017.

Woodward, DE, RH Hawkins, … R Jiang - World water &, and Undefined 2003. 2003. "Runoff Curve Number Method: Examination of the Initial Abstraction Ratio." *Ascelibrary.Org*. https://ascelibrary.org/doi/abs/10.1061/40685(2003)308.

Wu, Huan, John S. Kimball, Nate Mantua, and Jack Stanford. 2011. "Automated Upscaling of River Networks for Macroscale Hydrological Modeling." *Water Resources Research* 47 (3). https://doi.org/10.1029/2009WR008871.

Yoon, Yeosang, and Edward Beighley. 2015. "Simulating Streamflow on Regulated Rivers Using Characteristic Reservoir Storage Patterns Derived from Synthetic Remote Sensing Data." *Hydrological Processes* 29 (8): 2014–26. https://doi.org/10.1002/hyp.10342.

Yunus D. Salami. 2012. "Reservoir Storage Variations from Hydrological Mass Balance and Satellite Radar Altimetry." *International Journal of Water Resources and Environmental Engineering* 4 (6). https://doi.org/10.5897/ijwree11.140.

Zarfl, Christiane, Alexander E. Lumsdon, Jürgen Berlekamp, Laura Tydecks, and Klement Tockner. 2014. "A Global Boom in Hydropower Dam Construction." *Aquatic Sciences* 77 (1): 161–70. https://doi.org/10.1007/s00027-014-0377-0.

Zhang, Jiqun, Kaiqin Xu, Yonghui Yang, Lianhui Qi, Seiji Hayashi, and Masataka Watanabe. 2006. "Measuring Water Storage Fluctuations in Lake Dongting, China, by Topex/Poseidon Satellite Altimetry." *Environmental Monitoring and Assessment* 115 (1–3): 23–37. https://doi.org/10.1007/s10661-006-5233-9.

Zhang, Shuai, Huilin Gao, and Bibi S. Naz. 2014. "Monitoring Reservoir Storage in South Asia from Multisatellite Remote Sensing." *Water Resources Research* 50 (11): 8927–43. https://doi.org/10.1002/2014WR015829.

Zhao, RJ, YL Zhang, LR Fang, XR Liu, and QS Zhang. 1980. "The Xinanjiang Model Hydrological Forecasting Proceedings Oxford Symposium, IASH."

Zhou, Tian, Bart Nijssen, Huilin Gao, and Dennis P. Lettenmaier. 2016. "The Contribution of Reservoirs to Global Land Surface Water Storage Variations." *Journal of Hydrometeorology* 17 (1): 309–25. https://doi.org/10.1175/JHM-D-15-0002.1.

Zhu, Chunmei, and Dennis P. Lettenmaier. 2007. "Long-Term Climate and Derived Surface Hydrology and Energy Flux Data for Mexico: 1925-2004." *Journal of Climate* 20 (9): 1936–46. https://doi.org/10.1175/JCLI4086.1.

Ziv, Guy, Eric Baran, So Nam, Ignacio Rodríguez-Iturbe, and Simon A. Levin. 2012. "Trading-off Fish Biodiversity, Food Security, and Hydropower in the Mekong River Basin." *Proceedings of the National Academy of Sciences of the United States of America* 109 (15): 5609–14. https://doi.org/10.1073/pnas.1201423109.